MODELLING OF AIRFLOW AND AEROSOL PARTICLE MOVEMENT IN BUILDINGS

Weizhen Lu

B.Eng.(Hons) M.Eng.

Thesis submitted to

De Montfort University

for the degree of

Doctor of Philosophy

October 1995

CONTENTS

	Page
Abstract	i
Acknowledgement	iii
List of Figures	iv
List of Symbols	xi
List of Tables	xv

CHAPTER I INTRODUCTION

Abstract

§1.1 Preamble	I-1
§1.2 An Overview of Contaminant Sources in Building	I-3
§1.2.1 Sick building syndrome	I-3
§1.2.2 The sources of indoor air pollution	I-6
§1.3 Methods and Objectives of Study	I-13
§1.3.1 Methods of Study	I-13
§1.3.2 Objectives of Study	I-16

CHAPTER II PREVIOUS RESEARCH

Abstract

§2.1 Introduction	II-1
§2.2 Review of Experimental Study of Aerosol Particle Flow in Buildings	II-3

§2.3 Review of Numerical Analysis in Building Engineering II-9

§2.3.1 The characteristics of flow phenomena in building engineering II-9

§2.3.2 Previous research of CFD simulation in building engineering II-11

§2.4 Conclusions II-24

CHAPTER III PARTICLE DYNAMICS

Abstract

§3.1 Introduction III-1

§3.2 The basic theory of particle settling in continuous fluid III-2

§3.2.1 Stokes equation III-2

§3.2.2 Stokes solution III-8

1. Diagrams of spherical particle motion within infinitive fluid at low R_{ep}
2. Drag force and drag coefficient

§3.3 Numerical Analysis of Solid Particle Settling in Static Air III-17

§3.3.1 The problem definitions III-17

§3.3.2 The equation set III-20

§3.3.3 The analysis of numerical solutions III-22

§3.4 Conclusions III-27

CHAPTER IV MATHEMATICAL DESCRIPTION

Abstract

§4.1 Fluid Motion and Its Description IV-1

§4.1.1 Methods of defining fluid IV-1

§4.1.2 Eulerian and Lagrangian descriptions IV-3

§4.2 Mathematical Description of continuous fluid flow IV-7

§4.2.1 The general governing equation IV-7

§4.2.2 The equation set of laminar flow IV-9

§4.2.3 The equation set of turbulent flow IV-13

I. Definition of turbulence

II. The Reynolds-averaged equation

§4.2.4 Turbulence models IV-19

I. Boussinesq Approximation

II. Prandtl mixing length model (Zero-equation model)

III. Kolmogorov-Prandtl model (One-equation model)

IV. Standard k-ε model (Two-equation model)

§4.3 Solution of The Flow Equations IV-27

§4.3.1 Integration and discritisation IV-30

§4.3.2 Differencing schemes IV-32

I. Central differencing scheme (CD).

II. Upwind differencing scheme.

III. Hybrid differencing scheme (HYB).

IV. Power-law differencing scheme (PLDS).

§4.3.3 Treatment of source terms IV-41

§4.3.4 The non-staggered grid and the pressure-correction equation IV-43

I. Rhie-Chow interpolation algorithm.

II. Pressure-correction equation.

§4.3.5 Implementation of boundary conditions IV-49

I. Flow boundaries.

II. Symmetry plane.

III. Wall boundaries.
§4.3.6 Solution of the algebraic discritisation equations IV-58
I. SIMPLE and SIMPLEC algorithms
II. Co-ordinate transformation between physical and computational spaces
§4.3.7 Convergence criterion and convergence control techniques IV-64
I. Convergence criterion
II. Convergence control techniques
§4.4 Particle Transport Model IV-70
§4.4.1 Equation set of particle transport model IV-70
I. Basic assumptions
II. Equation set
III. Particle tracking process
§4.4.2 Boundary conditions and solutions of particle tracking IV-76
I. Boundary conditions
II. Iterations of fluid flow and particle tracking
§4.5 Conclusions IV-79

CHAPTER V FLOW CHARACTERISTICS IN VENTILATED SPACE

Abstract
§5.1 Introduction V-1
§5.2 Free Air Jet Flow V-3
§5.2.1 Description of free air jet V-3
§5.2.2 The analytical solutions for free circular and plane jet flows V-4

a. Solutions of circular jet

b. Solutions of plane jet

§5.3 Turbulent Wall Jet Flow V-7

§5.3.1 Plane wall jet V-7

§5.3.2 Three-dimensional wall jet V-9

§5.4 Numerical Solutions of Wall Jet Flows V-11

§5.4.1 Test cases V-12

I. Geometrical configuration
II. Defining the flow phenomenon
III. Mesh schemes and computational details

§5.4.2 Results and discussions V-20

I. Airflow patterns and comparisons of computations with measurements
II. Convergence control methods

§5.5 Conclusions V-43

CHAPTER VI MODELLING OF AIR AND PARTICLE FLOW IN VENTILATED ONE-ZONE ROOM

Abstract

§6.1 Introduction VI-1

§6.2 Particle Deposition VI-4

§6.2.1 Particle deposition in still air VI-4

§6.2.2 The effects of aerosol particles in ventilated space VI-6

I. Health effects

II. Soiling problem

§6.2.3 Aerosol particle removal VI-9

I. Factors affecting particle movement

II. Particle extraction through ventilation

§6.3 Case Study VI-12

§6.3.1 Case description VI-12

I. Geometrical configuration

II. Particle parameters

§6.3.2 Boundary conditions VI-15

I. Boundary conditions for the airflow

II. Boundary condition for particle tracking

§6.3.3 Results and discussions VI-18

I. Convergence control

II. Air movement in the room

III. Aerosol particle movement and distribution in room

§6.4 Conclusions VI-38

CHAPTER VII AIRFLOW AND PARTICLE MOVEMENT IN VENTILATED TWO-ZONE ROOM

Abstract

§7.1 Introduction VII-1

§7.2 Numerical Analysis of Airflow and Aerosol Particle Movement in Ventilated Two-Zone Chamber VII-5

§7.2.1 Case Description VII-5

I. Geometrical and flow parameters

II. Experimental procedures

III. Initial and boundary conditions

§7.2.2 Results and Analysis VII-15

I. The convergence history of cases

II. The airflow patterns in the two-zone area

III. The particle deposition, migration & distribution in two-zone chamber

1. Average particle concentration decay in zone 1

2. Average particle concentration decay in zone 2

3. Particle deposition, migration & distribution in two-zone room

4. Average particle deposition, exchange & extraction rates

5. sample particle tracking routes

§7.3 Conclusions VII-45

CHAPTER VIII MODELLING OF AIR AND PARTICLE MOVEMENT UNDER BUOYANCY INFLUENCE

Abstract

§8.1 Introduction VIII-1

§8.1.1 Characters of Buoyancy-affected Flows VIII-2

I. Thermal plumes in a displacement ventilated room

II. Buoyancy influence of non-isothermal wall jet flow

§8.1.2 The Objectives of Study VIII-9

§8.2 Modelling of Airflow and Aerosol Particle Movement in Buoyancy-Affected Flow VIII-11

§8.2.1 Description of Physical Problem VIII-11

§8.2.2 The CFD Modelling Process VIII-14

I. The influence of buoyancy effect on the equation set

II. Buoyancy conditions imposed on the flow simulation

§8.2.3 Results and Analysis VIII-24

I. The airflow patterns and temperature distributions in the room

II. Particle movement in the room

§8.3 Conclusions VIII-43

CHAPTER 9 GENERAL CONCLUSIONS AND SUGGESTIONS FOR FURTHER STUDY

§9.1 General Conclusions IX-1

§9.2 Suggestions for Further Study IX-5

REFERENCES

PUBLICATIONS BY AUTHOR

APPENDIX A NUMERICAL RESULTS OF SINGLE PARTICLE SETTLING PROCESSES

APPENDIX B SCALARS, VECTORS AND TENSORS

APPENDIX C INTEGRATION OF THE GENERAL EQUATION

APPENDIX D THE EXPONENTIAL SCHEME

APPENDIX E SPECIFICATION OF THERMAL WALL BOUNDARY CONDITIONS

ABSTRACT

This thesis is concerned with Computational Fluid Dynamics modelling of airflow and aerosol particle movement in ventilated spaces and the analysis of indoor air quality in these areas. The simulations are carried out in the cases of mechanically ventilated rooms and buoyancy-affected flows in rooms. The validation work has also been done to verify the computations. The work includes:

i) an overview of indoor contaminated sources in buildings in Chapter I.

ii) a literature review of the experimental study of aerosol particle flow in ventilated rooms and the numerical analysis of air movement in buildings in Chapter II. The objectives of this research are also given.

iii) a study of the single particle settling process in still air in Chapter III. The Stokes' law is also described. A particle transport model for simulating the particle settling process is applied, and a good agreement between the numerical results and the analytical solutions has been obtained. It can be concluded that the particle settling process in still air is mainly related to the particle properties. The gravitational settling phenomenon is an important characteristic of particle movement.

iv) a detailed mathematical description of fluid flow, both Eulerian and Lagrangian methods in Chapter IV. The model will be used for simulating the air flow and particle movement and distribution in ventilated buildings.

v) a CFD simulation of the turbulent flow in a ventilated room by an air jet. The numerical results show good agreement with the relevant experimental data. The work carried out helps to establish confidence to carry out more CFD simulations in later chapters.

vi) numerical analyses of airflow and aerosol particle movement, distribution and extraction in a ventilated single zone in Chapter VI. The simulations are carried out with different ventilation rates. The conclusions are: the ventilation conditions strongly influence the particle movement and distribution in the ventilated area; increasing ventilation rate can

enhance particle concentration decay (i.e., particle deposition) and particle extraction in the ventilated room; the gravitational settling dominates the movement of large particles, while the motion of small particles is influenced by the airflow pattern in the ventilated room and by gravity.

vii)an examination of the influence of the size of interzonal opening, and the ventilation rate, on the aerosol particle movement and airflow in a ventilated two-zone enclosure in Chapter VII. This is done by investigating the air movement and the distribution, migration and extraction of aerosol particles in both zones by using CFD methods. The predicted average particle concentration decay profiles show satisfactory agreement with the measured data. It can be concluded that the interzonal opening significantly affects both particle migration between zones and airflow patterns in the two-zone area, i.e., a large interzonal opening can increase the particle migration between zones. Also, particle depositions are mainly influenced by the airflow patterns, particle properties and ventilation conditions; small particles mainly contribute to the pollutant concentration level in the ventilated spaces and greatly affect the indoor air quality.

viii)a CFD simulation of airflow and particle movement under the influence of buoyancy. The predicted temperature field shows good agreement with the experimental data. The room airflow pattern is affected by the thermal wall jet produced by the heat source. The particle movement is also influenced by the thermal wall jet flow. Particles are entrained to the thermal boundary layer from the particle source and then dispersed into the room space with the hot air flow. Generally, large particles are likely to be deposited on the floor, while small particles may remain suspended in the upper warm region. The area close to the heat source is likely to be contaminated.

All of the above has led to an increased understanding of the way in which small airborne particles, which affect indoor air quality, are distributed and dispersed within ventilated spaces.

ACKNOWLEDGEMENT

I would like to express my sincere thanks and gratitude to Professor Andrew T Howarth for his invaluable advice and support throughout the research and writing stages of the thesis.

Special thanks to the staff and researchers of ECADAP Centre, Institute of Energy and Sustainable Development for their kind help and excellent technical support during the periods of the research.

I wish to acknowledge the technical support from the Institute of Building Technology at University of Nottingham and the financial support of Engineering and Physical Science Research Council, UK.

Finally, I would like to thank my family and parents for their patience and understanding during the preparation of the thesis, especially my husband, Peiran.

LIST OF FIGURES

Figure 1.1 Particle size distributions

Figure 3.1 A free falling particle under the action of gravity and resistance forces

Figure 3.2 A spherical particle in acceleration

Figure 3.3 The co-ordinate systems in Stokes flow

Figure 3.4 Streamlines relative to spherical particle at low R_{ep}

Figure 3.5 Streamlines for motion of sphere through the stagnant fluid at low R_{ep}

Figure 3.6 The drag coefficient diagram for a spherical particle

Figure 3.7 Measured drag coefficients for spheres

Figure 3.8 Variation of C_D vis R_{ep} of single lead particle settling with different sizes

Figure 3.9 The geometry outline of the problem

Figure 3.10 Comparison of analytical solutions and numerical results

Figure 3.11 One lead particle deposition route in stagnant air (d_p=10μm)

Figure 4.1 Position vector locating a fluid particle

Figure 4.2 Computational cell with grid information

a. A single three-dimensional volume

b. An x-array of three-dimensional volume

Figure 4.3 Variation of coefficient a_E with Peclet number

Figure 4.4 The comparisons of different schemes

Figure 4.5 One dimensional non-uniform grid information

Figure 4.6 Control cells

Figure 4.7 Near-wall regions in turbulent flow regime

Figure 4.8 Velocity profile in flat-plate boundary layer

Figure 5.1 Schematic flow pattern in a ventilated room

Figure 5.2 Free jet flow pattern

Figure 5.3 A typical free jet plot

Figure 5.4 Schematic of a plane wall jet plot

Figure 5.5 Three-dimensional wall jet plot

Figure 5.6a, b Geometrical configurations

Figure 5.7a, b Grid nodes of two-dimensional plane wall jet simulation

Figure 5.8a, b Grid nodes of three-dimensional plane wall jet simulation

Figure 5.9a, b Grid nodes of three-dimensional wall jet simulation

Figure 5.10a, b Velocity vectors in two-dimensional simulations of plane wall jet flow

Figure 5.11 Normalised U-velocity contours at plane of z/W=0 (Grid 40x30)

Figure 5.12 Comparisons between computed U-velocity and measured data across the chamber height (2-D simulations)

Figure 5.13 U-velocity distributions along the chamber length (2-D simulations)

Figure 5.14 Shaded contour of U-velocity in centreline plane (Grid nodes 40x30)

Figure 5.15 Comparisons of numerical solutions with experimental data at different planes (three-dimensional simulations of plane wall jet flow)

Figure 5.16 Flow patterns in different planes (3-D simulations of plane wall jet flow)

Figure 5.17 U-velocity profiles in different planes (three-dimensional simulations of plane wall jet)

Figure 5.18 Flow patterns of three-dimensional wall jet flow

Figure 5.19 U-velocity distributions in different planes (three-dimensional wall jet flow simulations)
Figure 5.20 Comparisons of computed U-velocity values with relevant experimental data (3-D wall jet flow simulations)
Figure 5.21 The decay of centreline velocity along the chamber length
Figure 5.22a, b Monitor points of simulations
Figure 5.23 Convergence history of 2-d plane jet simulations (default settings)
Figure 5.24 Convergence history of 3-d plane jet simulations (default settings)
Figure 5.25 Convergence history of 3-d wall jet simulations (default settings)
Figure 5.26 Comparisons of Convergence history of 2-d plane wall jet flow simulations
Figure 5.27 Comparisons of Convergence history of 3-d plane wall jet flow simulations
Figure 5.28 Comparisons of Convergence history of 3-d wall jet simulations
Figure 6.1 The three areas of nasal passages
Figure 6.2 The geometrical configuration
Figure 6.3 The mesh scheme
Figure 6.4 The initial positions of the sample particles
Figure 6.5 The convergence history of cases
Figure 6.6a, b and c Airflow patterns in centreline plane
Figure 6.7 Airflow patterns in room height
Figure 6.8a, b U-velocity profiles along the room length (Case 1)
Figure 6.9a, b U-velocity profiles along the room length (Case 2)
Figure 6.10a, b U-velocity profiles along the room length (Case 3)
Figure 6.11 Mass of suspended particles varying with time (Case 1, 0.5 ACH)
Figure 6.12 Mass of suspended particles varying with time (Case 2, 1 ACH)

Figure 6.13 Mass of suspended particles varying with time (Case 3, 2 ACH)
Figure 6.14 Particles removal from the room (Case 1, 0.5 ACH)
Figure 6.15 Particles removal from the room (Case 2, 1 ACH)
Figure 6.16 Particles removal from the room (Case 3, 2 ACH)
Figure 6.17 Comparison of particles settled on the floor (Case 1, 2 & 3)
Figure 6.18 Comparison of particles settled on internal walls (Case 1, 2 & 3)
Figure 6.19 Comparison of particles settled on roof (Case 1, 2 & 3)
Figure 6.20 Comparison of particle deposited on floor and walls (Case 1, 2 & 3)
Figure 6.21 Comparison of extracted particles with ventilation rates (Case 1, 2 & 3)
Figure 6.22 Average particle deposition and extraction rates (Case 1, 2 & 3)
Figure 6.23 Average particle concentration decay with time (Case 1, 2 & 3)
Figure 7.1a Geometrical configuration for Case 1 & 2
Figure 7.1b Geometrical configuration for Case 3 & 4
Figure 7.1c Geometrical configuration for Case 5 & 6
Figure 7.2 The mesh scheme
Figure 7.3 The initial positions of sample particles
Figure 7.4 The convergence history of Case 1 & 2
Figure 7.5 The convergence history of Case 3 & 4
Figure 7.6 The convergence history of Case 5 & 6
Figure 7.7 Typical planes in the two-zone chamber
Figure 7.8a Vectors in plane of z=0.75 m (Case 1)
Figure 7.8b Vectors in plane of z=1.5 m (Case 1)
Figure 7.8a Vectors in plane of z=0.75 m (Case 1)
Figure 7.9a Vectors in plane of z=0.75 m (Case 3)

Figure 7.9b Vectors in plane of z=0.75 m (Case 3)

Figure 7.9c Vectors in plane of z=2.25 m (Case 3)

Figure 7.10a Vectors in plane of z=0.75 m (Case 5)

Figure 7.10b Vectors in plane of z=1.5 m (Case 5)

Figure 7.10c Vectors in plane of z=2.25 m (Case 5)

Figure 7.11 Comparison of average particle concentration decay (Case 1)

a. Particle concentration decay in zone 1 (Case 1, 11.484 ACH)

b. Particle concentration decay in zone 2 (Case 1, 11.484 ACH)

Figure 7.12 Comparison of average particle concentration decay (Case 2)

a. Particle concentration decay in zone 1 (Case 2, 14.004 ACH)

b. Particle concentration decay in zone 2 (Case 2, 14.004 ACH)

Figure 7.13 Comparison of average particle concentration decay (Case 3)

a. Particle concentration decay in zone 1 (Case 3, 11.566 ACH)

b. Particle concentration decay in zone 2 (Case 3, 11.566 ACH)

Figure 7.14 Comparison of average particle concentration decay (Case 4)

a. Particle concentration decay in zone 1 (Case 4, 12.708 ACH)

b. Particle concentration decay in zone 2 (Case 4, 12.708 ACH)

Figure 7.15 Comparison of average particle concentration decay (Case 5)

a. Particle concentration decay in zone 1 (Case 5, 9.216 ACH)

b. Particle concentration decay in zone 2 (Case 5, 9.216 ACH)

Figure 7.16 Comparison of average particle concentration decay (Case 6)

a. Particle concentration decay in zone 1 (Case 6, 10.26 ACH)

b. Particle concentration decay in zone 2 (Case 6, 10.26 ACH)

Figure 7.17a, b Particle distribution in two-zone area (Case 1)

Figure 7.18a, b Particle distribution in two-zone area (Case 2)

Figure 7.19a, b Particle distribution in two-zone area (Case 3)

Figure 7.20a, b Particle distribution in two-zone area (Case 4)

Figure 7.21a, b Particle distribution in two-zone area (Case 5)

Figure 7.22a, b Particle distribution in two-zone area (Case 6)

Figure 7.23 Average particle deposition, migration & extraction rates (Case 1, & 2)

Figure 7.24 Average particle deposition, migration & extraction rates (Case 3, & 4)

Figure 7.25 Average particle deposition, migration & extraction rates (Case 5, & 6)

Figure 7.26 Five sample particles tracking routes (Case 2)

Figure 7.27 Five sample particles tracking routes (Case 6)

Figure 8.1 The sketch of displacement ventilation system

Figure 8.2 Emergence and development of a thermal plume

Figure 8.3 An isothermal wall jet in a ventilated room

Figure 8.4 Penetration depth of a thermal wall jet

Figure 8.5 Geometrical sketch of the chamber

Figure 8.6 The mesh scheme of the simulation

Figure 8.7 The structure of a wall

Figure 8.8a Typical planes in the room width

Figure 8.8b Typical planes in the room height

Figure 8.8c Typical planes in the room length

Figure 8.9 Airflow patterns in planes along the room width

Figure 8.10 The development of the thermal wall jet flow .

Figure 8.11 Temperature interface in room space

Figure 8.12 Temperature stratification in centreline plane

Figure 8.13 Temperature distributions in planes along the room width

Figure 8.14 Air movement and temperature distributions in planes in the room height

Figure 8.15 Vectors and temperature profiles in planes along the room length
Figure 8.16 V-velocity and temperature profiles in thermal boundary layer
Figure 8.17 U-velocity distributions in centreline plane along the room length
Figure 8.18a Comparison of temperature in centreline plane (x=2.37m)
Figure 8.18b Comparison of temperature in centreline plane (x=4.04m)
Figure 8.19a Comparison of temperature in side plane (x=0.7m, z=2.75m)
Figure 8.19b Comparison of temperature in plane (x=4.04m, z=2.75m)
Figure 8.20a, b, c & d Sample particle tracking routes in the room

LIST OF SYMBOLS

A	Constant
A_r	Archemedes number
A_{rad}	Area (m^2)
a	Radius of spherical particle (m).
B	Constant
B_i	Body force of fluid experienced (N/m^3)
C	Concentration ($\mu g/m^3$), constant or turbulent constant
C_D	Drag coefficient
D	Diameter (m)
d_p	Particle diameter (m or μm)
E	Constant, E≈9.0
F	Forces (N)
f	function
G_i	Turbulent generation term
G_B	Buoyancy term
g	Gravitational acceleration (m/s^2)
H	Enthalpy (J/kg); Height (m)
h	height (m)
K	Coefficient
k	Turbulent kinetic energy (m^2/s^2)
L	Length (m)
l	Length (m)
m	Mass or particle mass (kg)
N	Number of sample particles

N_{pd} Number of deposited particles

N_{pe} Number of extracted particles

N_{pm} Number of migrated particles

n an index, n=0.33~1.0;

p Pressure (N/m^2)

Q Heat flux (W/m^2)

R Resistance force acting on the particle from surrounding fluid (N)

R_a thermal resistance of airgap ($W^{-1}\cdot m^2\cdot K$)

R_d Average particle deposition rate (h^{-1})

R_e Reynolds number ($R_e = \frac{\rho V d}{\mu}$)

R_{ep} Particle Reynolds number ($R_{ep} = \frac{\rho V_R d_p}{\mu}$)

R_{exc} Average particle exchange rate between zones (h^{-1})

R_{ext} Average particle extraction rate (h^{-1})

R_i Thermal resistance of wall structure ($W^{-1}\cdot m^2\cdot K$); Richardson number

R_{si} Thermal resistance of inside surface ($W^{-1}\cdot m^2\cdot K$)

R_{so} Thermal resistance of outside surface ($W^{-1}\cdot m^2\cdot K$)

S_ϕ Source term in governing equation

T Time or tracking periods (s or mins), temperature (K or °C)

T_w Wall temperature (K or °C)

T^+ Scaled wall temperature

t Time (s or mins)

U the fluid velocity vector, **U**=(u, v, w),

U Thermal transmittance ($W\cdot K^{-1}\cdot m^{-2}$), velocity component (m/s)

u Particle velocity vector, **u**=(u, v, w)

u Velocity component (m/s)

u_{in}	Supply velocity component (m/s)
u^+	Scaled velocity parallel to the wall surface
V	Velocity component (m/s); volume of space (m^3)
V_R	Relative velocity between particle and fluid (m/s)
v_{in}	Supply velocity component (m/s)
W	Velocity component (m/s)
w_{in}	Supply velocity component (m/s)
x, y, z	Co-ordinates or distance (m)
y^+	Scaled distance to the wall surface
Φ	Dependent variable of governing equation
Γ_Φ	Diffusive coefficient in governing equation
δ	Size of control volume (m)
ε	Turbulent energy dissipation rate (m^2/s^3)
κ	von Kármán constant, κ=0.4~0.44;
λ	Thermal conductivity of fluid (W/m·K)
μ	Dynamic viscosity of fluid (kg/m·s)
μ_t	Turbulent dynamic viscosity of fluid (kg/m·s)
ν	Kinematics viscosity of fluid (m^2/s)
θ	Polar co-ordinate
ρ	Density of surrounding fluid (kg/m^3)
ρ_p	Density of particle (kg/m^3)
σ	Stress tensor
σ_1	Constant, σ_1=0.71;
σ_H	Prandtl number of H
σ_k	Prandtl number of k

σ_L Prandtl number, $\left(\sigma_L = \frac{\mu C_p}{\lambda}\right)$;

σ_T Turbulent Prandtl (Schmidt) number.

σ_ε Prandtl number of ε

τ_w Wall shear stress (N/m^2)

LIST OF TABLES

Table 3.1 Analytical solutions of lead particles settling processes in static air

Table 3.2 Physical properties of particle and fluid

Table 3.3 Numerical results of cases

Table 3.4 Comparison of analytical solutions and numerical results

Table 4.1 The formations of Φ, Γ_Φ and S_Φ in transport equations

Table 4.2 The function $A(|P_e|)$ for different schemes

Table 4.3 The default values of URF in SIMPLE and SIMPLEC

Table 5.1 The geometrical parameters of cases

Table 5.2 Mesh schemes

Table 5.3 Values of URF and FTS for cases

Table 6.1 Settling velocities for various particle sizes and density of particles

Table 6.2 Parameters of cases

Table 6.3 Particle parameters

Table 7.1 Parameters of cases

Table 7.2 The inlet flow parameters of cases

Table 7.3 Particle parameters of case 1 (11.484 h^{-1})

Table 7.4 Particle parameters of case 2 (14.004 h^{-1})

Table 7.5 Particle parameters of case 3 (11.566 h^{-1})

Table 7.6 Particle parameters of case 4 (12.708 h^{-1})

Table 7.7 Particle parameters of case 5 (9.216 h^{-1})

Table 7.8 Particle parameters of case 6 (10.26 h^{-1})

Table 8.1 Parameters of case

Table 8.2 Physical properties of air

Table 8.3 Properties of the test chamber

Table 8.4 source terms for conservation equations in buoyant flow

Table 8.5 The estimated heat losses

CHAPTER I

INTRODUCTION

Abstract

An overview of 'Sick Building Syndrome' and contaminant sources in buildings has been outlined in this chapter. The importance and advantages of Computational Fluid Dynamics Application in buildings, ventilation systems and environmental engineering are also presented herein. The research project of CFD analysis of airflow patterns and pollutant particle distribution in ventilated one- and two-zone areas is proposed in the chapter.

§1.1 Preamble

Indoor air quality (IAQ) has promoted much attention in recent years as the increasing number of health complaints and illness related to buildings has been reported. Today, people spend most of their lives in the indoor environment. An increasing number of complaints and illnesses related to buildings range from complaints on draughts via headache, dry-skin, flu-like symptoms, Environmental Tobacco Smoke (ETS) indoors and allergic diseases such as asthma and rhinitis due to the emissions from building materials, furnishings and decorations. Besides these, there is a world-wide recognised symptom, ' Sick Building Syndrome '. All these concerns have increased the awareness and the study of the air quality of the indoor environment (Fanger, 1990).

There are normally two means of controlling the indoor air quality:

a. Control of contaminant sources

The best way of controlling indoor air quality is to completely avoid harmful contaminants by proper source control, e.g., ' clean room ', low-emitting building materials, etc., but this can be only achieved in buildings which are used for special purposes, e.g., micro-electronics manufacturer, hospital operating room, etc. For normal buildings, i.e., dwellings, schools, offices, etc., it is difficult and costly to achieve high indoor air quality by source control.

b. Ventilation

Ventilation is the method of supplying an acceptable indoor air environment for the occupants through supplying fresh air and diluting contaminants in the ventilated space by either mechanical or natural means.

It is known that the indoor contaminant exposure is dependent on the contaminant, its properties and how it is spread, the amount of air supplied and the distribution of ventilation air within a room. In the past, when designing a ventilation system, the main concern was comfort. However, today such a system should be designed which is both an effective ventilation system and at the same time meets the comfort requirements. The two are closely related. In fact, some difficulties exist in the design of an efficient ventilation system due to the limited knowledge of indoor pollutant movements and distributions, and airflow patterns in the ventilated rooms. The work reported in this thesis deals with the prediction of airflow patterns and aerosol particle deposition. The migration and distribution of particles in ventilation systems are investigated using a Computational Fluid Dynamics methodology. More details will be described in later chapters.

§1.2 An Overview of Contaminant Sources in Buildings

Indoor pollutants have a significant influence on the indoor air quality and the incidence of ' Sick Building Syndrome '. It is therefore necessary to have an investigation of contaminant sources which exist in the indoor environment.

§1.2.1 Sick Building Syndrome

1. The Purpose of Buildings

As dwelling places and major working and social activity spaces, buildings are erected for mainly three reasons. They are:

1) To provide protection of people and their belongings against outdoor climate, illegal entry, etc.;

2) To ensure that adequate functional requirements are met for indoor activities, as a home or as a work, public or leisure space;

3) To constitute value in economical, social as well as psychological terms.

In other words, the purpose of the building is to provide a comfortable, healthy (both physical and psychological) environment for human occupants.

Developments in building technology, building materials and energy technology have been rapid in the last decade. New technologies and new materials have often gained ready acceptance since they conferred technical and economic advantages. But work on quality assurance in construction has not kept pace with this rapid development. There has been less prior control regarding building hygiene aspects. Many new types of pollutants are therefore released into the indoor air (Schneider, 1994) and added to the pollutant category beside the 'old' contaminants given by people, cooking, tobacco smoking, open fires, moulds, bacteria, pollen and house dust mites.

Over the same period, ventilation has been reduced as a consequence of the need for energy conservation. Buildings have become more air tight, with less infiltration/exfiltration as a result, such as modern air-tight buildings. The result is that more pollutants, many new, are released into indoor environments with a low ventilation rate. The IAQ situation is therefore becoming more complex.

2. Sick Building Syndrome

There is no general agreement on the definition of a 'Sick Building'. From most countries in the industrialised western world there are reports about sick buildings or from syndromes such as 'tight building syndrome', 'stuffy office syndrome', 'office illness', 'illness due to work with carbonised copy paper', 'VDU-workers syndrome' and the like. With small differences they are generally described in the same way, with the same type of symptoms. A

common definition is: 'Sick Buildings' are modern buildings in which occupants show symptoms similar to those caused by formaldehyde exposure although the concentrations of formaldehyde are many times below the reaction thresholds. Occupants complain of deteriorating air quality and of subtle medical symptoms that may be related to the indoor air quality. A fairly specific set of reported body perceptions (symptoms) is called the 'Sick Building Syndrome'. The symptoms reported in the sick buildings vary widely but some common features may be recognised.

The main symptoms reported in common seem to be as follows (Lindvall, 1994):

a. irritation of the eyes, the nose, and the throat;

b. sensation of dryness in the mucous and skin;

c. erythema of the skin;

d. mental fatigue;

e. headaches, high frequency of airway infections and coughs;

f. hoarseness, wheezing, itching and unspecified hypersensitivity;

g. nausea, dizziness.

All of the above are the typical symptoms of 'Sick Building Syndrome'. Sick buildings thus fail to satisfy the purpose of buildings due to the poor indoor air quality, and under extreme conditions, they can be harmful to the health of occupants.

§1.2.2 The Sources of Indoor Air Pollution

As the complaints of SBS seemingly have become more frequent over the last 10~15 years, a wide range of investigations of 'Sick Building Syndrome' have been performed. It is believed that 'Sick Building Syndrome' is mainly caused by the poor indoor environment, poor ventilation and the insulation of the building. Odour emission from occupants, contaminants from cooking, tobacco smoking and building materials, radon, formaldehyde, house dust mites, bacteria and pollen comprise the main indoor contaminant sources; these largely influence the quality of the indoor air. It is then helpful to identify these contaminants and their sources within the building as well as the method of removal of such pollutants (Armstrong, et al., 1989).

1. Odour

Odour is associated with occupancy, cooking, bathroom activities and wastes. Odour pollution is related to comfort rather than health. The human sense of smell permits perception of very low concentrations of odours but the sensitivity varies between individuals. People who are exposed to odours for a long period of time become less sensitive to them. Body odour is emitted by all people as a result of sweat and sebaceous secretion through the skin and human digestion system. Odour dilution, to acceptable levels, is usually achieved by supplying outdoor fresh air to the occupied space.

2. Tobacco Smoke

Tobacco smoke produces undesirable odour, particularly to the non-smoker, and some of the smoke constituents can irritate the eyes and the nasal passages, acrolein in particular. Other products such as tar, nicotine and carbon monoxide can have serious health effects on smokers and also non-smokers exposed to a poorly ventilated environment. There have been recent studies (Walsh, et al., 1984) indicating that indirect or passive smoking can lead to lung cancer. The high concentrations of tobacco smoking in localised smoke plumes could be responsible for eye irritation effect. The average size of tobacco smoking particles is between 0.1μm to 1.0μm. The recommended method to dilute tobacco smoke is to entrain fresh air through the ventilation system.

3. Formaldehyde

Formaldehyde is a chemical that has become ubiquitous in today's technological environments. About half of the formaldehyde currently produced is consumed in the production of urea- and phenol-formaldehyde resins that are used as bonding and laminating agents, as adhesives in compressed wood products, and as plastic foam insulation and packaging products. Formaldehyde resins are widely used in the manufacture of building materials and furnishings. Formaldehyde polymers are also used in the manufacture of wallpaper, carpets and textiles. Formaldehyde is also present in consumer products such as paper products, cosmetics, toiletries, glues and room deodorisers. The emission of formaldehyde from a UF foam or F-

polymers is characterised by an initial peak release followed by a low-level continuous release. The initial high release rate is attributed to the presence of free formaldehyde in the foam and methyl. Upon exhaustion of these two sources a further but chronic release of formaldehyde is associated with the degradation of the UF polymer.

Formaldehyde can enter the human body through inhalation, ingestion or skin adsorption. Most of that inhaled is absorbed in the upper respiratory tract. Once in the body, formaldehyde rapidly reacts with tissues containing hydrogen in the form of amino acids, proteins, DNA and others to form stable and unstable products and subsequently to damage the body tissues, i.e., it is genotoxic. Formaldehyde is a strong irritant that produces a variety of symptoms depending on the mode, duration and concentration of the exposure. However, the available data seems to suggest that formaldehyde is a direct-acting carcinogen and likely to pose a carcinogenic risk to humans also. The removal of formaldehyde is also reliant on the ventilation systems.

4. Radon

Radon (R_n) is a naturally occurring radioactive gas which arises from the decay of radium (R_a) present in small amounts in the earth's upper crust and in building materials. Radium originates from the decay chain of uranium (U). Radon itself produces a series of short-lived radioactive decay 'daughters', two of which, $^{222}R_n$ and $^{220}R_n$, emit alpha particles. If radon and its progeny are inhaled, the alpha particles emitted may damage the lining of the lungs and pose the risk of lung cancer. Most of the health damage is caused by the

radon daughters (radioactive) and not radon itself which is an inert gas. The daughters, which are electrically charged ions, attach themselves to dust particles in the air which may then be deposited in the lungs if inhaled. Lung cancer related to radon-exposure is a very serious illness and is closely linked to the building environment. The risk of such disease is enhanced if there is a combined exposure to radon and environmental tobacco smoking(ETS). It is estimated that in temperate climate regions the annual incidence of 10-40 cases of lung cancer per million inhabitants is attributable to radon daughter exposure.

5. Particulates

Particulates can be in the form of dust, fumes, mist or biogenic matter and include viruses, smoke, tobacco smoke, bacteria, alkali fume, pigments, fog, moulds, ash, pollen, heavy industrial dusts, etc. Their sizes range from 0.01μm-1mm. Human occupants are significant particle generators. The complete outer skin layer is shed within 3-4 days. The release of skin scales is largest after showering and at high activity levels. Coughing, and in particular sneezing, generates a large number of bacteria carrying droplets. One sneeze generates the order of 1,000,000 droplets. Other sources of particulates come from the outdoor air pollution, industrial wastes, etc. The largest of the particulates settle on the floor, but a significant amount are reduced in size by the very rapid evaporation and remain airborne for prolonged periods. Statistically, particles of diameter greater than 75μm settle down rapidly and are termed grit, but particles smaller than 50μm may remain suspended in air and constitute aerosol particles. An aerosol is a liquid or solid particle which

is in a quasi-stable suspension status in air. Figure 1.1 shows the particle size distributions based on the statistical results (Owen et al, 1992).

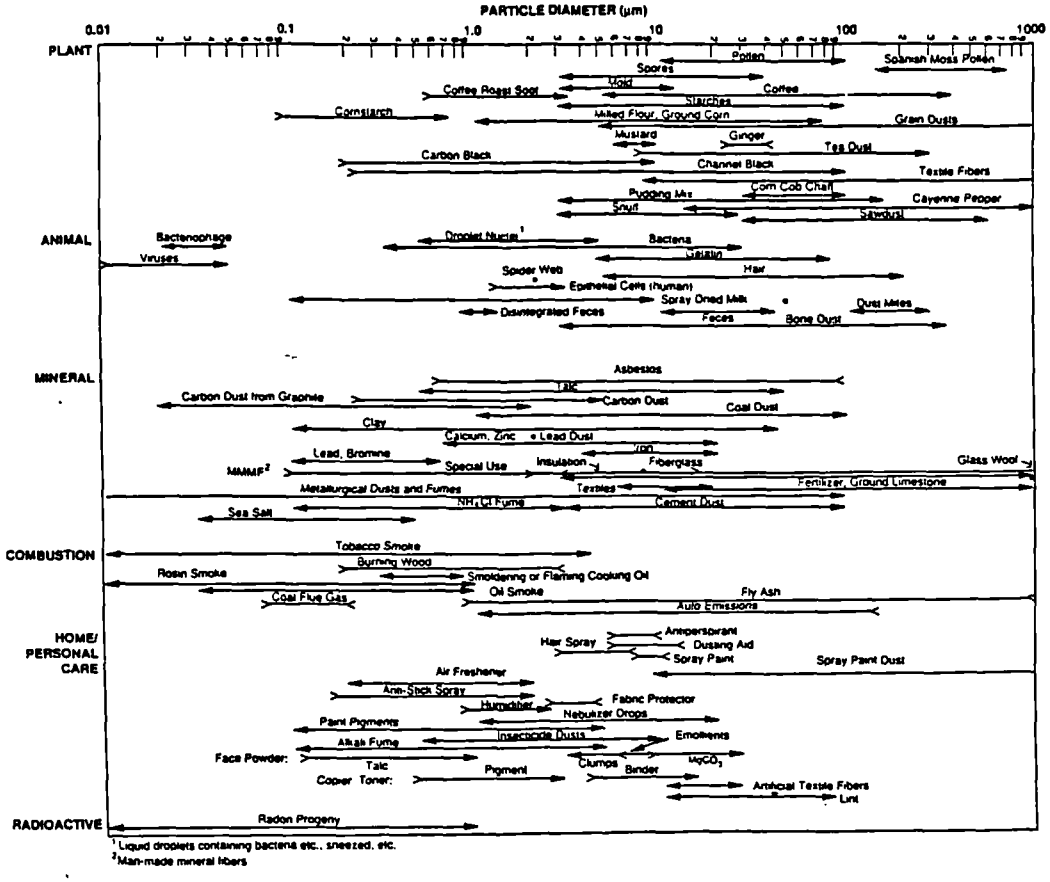

Figure 1.1 Particle sizes distributions

The effect of airborne particulates on health is mainly due to biogenic pollutants such as fungi, moulds, mites, bacteria, viruses and pollens. Indoor dust, which is a mixture of human and animal dander (skin flakes), fibrous material from textiles, organic particles and mites, is also a potential allergen and a cause of bronchial asthma and allergic rhinites. Pollens are the most widespread allergens which cause hay fever seasonally. The main sources of pollen are outdoor vegetation via air infiltration. Similarly, outdoor pollution sources are the major contributors to indoor fungi spores through penetration air from outdoor to indoor and also via ventilation systems.

6. Nitrogen dioxide (NO_2), carbonmonoxide (CO) and carbon dioxide (CO_2)

Combustion processes are the primary sources of both NO_2 and CO and a major pollutant source in residential buildings. The particles generated by combustion processes are almost entirely fine particles (less than 2.5 μm in diameter). The combustion sources involve furnace, oven, microwave equipment, gas heater, etc. Under certain conditions, furnaces and other natural draft combustion appliances may experience flue gas spillage. Flue gas spillage occurs when house depressurization prevents the buoyancy forces developed between the flue gases and the outside air from removing the combustion products. House air-tightness and exhaust ventilation equipment can increase the potential of flue gas spillage.

Carbon dioxide (CO_2) is mainly produced by human respiration and cooking activities. The concentration of CO_2 in a room relates to the population

density, outdoor air flow rate and the efficiency of the ventilation system. Unlike other contaminants (e.g. tobacco smoke), NO_2, CO and CO_2 cannot be filtered. Removal of such contaminants can be achieved via a suitable ventilation system.

It is known (Owen, et. al. 1992; Schneider, 1994; Lindvall, 1994, etc.) that contaminants found in buildings and ventilation systems are mainly composed of pollutant particles. They can have damaging effects on the health of occupants. Indoor aerosol particles are not only associated with outdoor sources (e.g., car exhaust emissions, coal and oil combustion, road dust, etc.) but also arise from a number of indoor sources (e.g., cigarette smoking, building materials, bio-effluents, etc.). Aerosol particles can transport viruses and bacteria. They may be deposited on ventilation ducts and interior surfaces of rooms or can be transported between zones. This can have a serious effect in hospitals and buildings which are used by the micro-electronic and pharmaceutical industries. Deposition of aerosol particles in museums and galleries can lead to perceptible soiling, within short periods, and ultimately result in damage to works of art. The indoor air quality in rooms or buildings can become unacceptable from the existence of the above pollutants within the spaces. A satisfactory and comfortable indoor environment can be achieved through suitable ventilation systems.

§1.3 Methods and Objectives of Study

Despite the increasing interest in indoor air quality problems, only limited research to date has been conducted and this mainly concerns the analysis of indoor pollutant sources. A great deal of study, including computer simulation, laboratory testing and field testing, is required to analyse and quantify the air distribution and aerosol particle movements and distributions in buildings and their ventilation systems.

§1.3.1 Methods of Study

The study of indoor airflow patterns and pollutant particle distributions within a building can be achieved by two approaches: experimental investigation and numerical analysis.

The most realistic information concerning indoor air movement and aerosol particle distribution is, in principle, given by direct measurements. An experimental study of airflow and contaminant distribution requires a full-scale climate room in order to reveal air velocity, temperature, turbulence intensity and pollutant concentrations. Such full-scale tests are, in most cases, expensive and some of the measurements present serious difficulties in many situations. These include the measurement of the flow direction at very low velocity and low turbulence intensity. Previous researchers have noticed that it is impossible to develop a scale model for room air motion where there is

thermal heat production within the room, because similarity of Reynolds number (ratio of inertial force to viscous force) and Archimedes number (ratio of thermal buoyancy force to inertial force) — both important dimensionless terms in determining room air movement — cannot be achieved simultaneously. Moreover, the air movement frequently occurs in multizone areas. In such situations, the airflow is affected by many factors, such as the dimension of the multizone enclosure, the size and the location of interzonal openings, the location of the ventilation supplies and extracts, the heat source condition in the room, etc. It is difficult to deal with all these variations in an experimental investigation. Most of the experimental research to date has employed simplified approaches to studying the air movement and aerosol particle distribution in ventilated spaces. These studies have often focused on the performance of individual pieces of equipment without considering the interactions between the building, the HVAC system and the ambient conditions.

Due to the limitation of the experimental research and the development of digital computer systems, the numerical analysis of indoor airflow and contaminant particle distribution in ventilated rooms has been developed in recent years. There are two types of computer simulation models for studying airflow and pollutant distribution in buildings — multizone models and room airflow models. Multizone airflow and pollutant transport modelling takes a macroscopic view of indoor air quality by evaluating average pollutant concentrations in the different zones of a building as contaminants are transported through the building and its ventilation system. The multizone approach is implemented by constructing a network of

elements describing the flow paths (ventilation ducts, doors, windows, etc.) between the zones of a building.

Room airflow modelling takes a microscopic view of indoor air quality by examining the detailed flow fields and pollutant concentration distributions within a ventilated room (or rooms). Room airflow modelling applies the principles of conservation of mass, momentum and energy (Eulerian system) through the use of the CFD technique. Computational Fluid Dynamics has the advantage of studying the turbulent convective heat and mass transfers within and between full-scale zones. A validated numerical model not only allows investigations to be carried over a short period of time, at less expense, but also provides detailed information on the field distributions of all of the important factors.

§1.3.2 Objectives of Study

CFD simulation provides a valuable insight into processes which are difficult to study experimentally. So far, an extensive literature survey has revealed that the majority of CFD analysis in building engineering is concentrated on the prediction of air velocity, temperature distribution and turbulence intensity in rooms and buildings. Little work has been found in the area of aerosol particle movement and distribution within ventilated rooms and/or buildings. The research proceeded herein is to apply both Eulerian and Lagrangian methods for analysing the airflow patterns and the deposition and distribution of aerosol particles in single- and two-zone ventilation systems by using a CFD code. The objectives of the project are listed below:

1. To validate a particle transport model which can be used to predict the movement of particles in still air and in the ventilated space.

2. To simulate the airflow patterns and analyse the distribution and deposition of aerosol particles in a one-zone mechanically ventilated enclosure.

3. To predict the air movement and analyse the migration, distribution and deposition of aerosol particles in and between two adjoining rooms with mechanical ventilation. The comparison between -computations and experiments will also be analysed where available. Various heights of interzonal opening will be examined.

4. To analyse the aerosol particle distribution and deposition in a buoyancy-affected flow.

5. To develop strategies for improving indoor air quality as affected by aerosol particle concentrations.

With CFD techniques, it is possible to study the influence of ventilation performance and geometry parameters on the field distributions of air velocity, temperature, turbulence intensity and particle concentration in the ventilated space, and consequently, on thermal comfort and the indoor air quality.

CHAPTER II

PREVIOUS RESEARCH

Abstract

This chapter reviews previous experimental investigations about aerosol particle movement in ventilation systems. A literature survey of the application of CFD analysis in building engineering is also presented. The potential of CFD simulation of indoor airflow and pollutant particle distribution in ventilated spaces is outlined in this chapter.

§2.1 Introduction

Indoor air movement is an important research area because it largely affects the air quality, thermal comfort and even more influences the distribution of contaminant particles in the room. Increasingly, concern is being expressed about the quality of the indoor environment, where failure to provide satisfactory conditions has produced many reports of discomfort and ill-health. The concern relates to all building types ranging from domestic houses to office spaces, from atria to auditoria, and includes industrial buildings, processes and medical facilities. However, our understanding of room air flow and pollutant particle movement is limited.

The air movement and aerosol particle flow in ventilated spaces are very complicated phenomena which include heat, momentum and mass (if required) transfer processes. Normally, they are influenced by the geometry, diffuser configuration and location, exhaust location, air velocity and direction at the diffuser, ventilation rate, internal obstructions, particle properties and thermal buoyancy due to the heat generated by occupants and/or equipment. Methods commonly used for the study of room airflow and particle movements are experimental investigation and numerical analysis. Experimental study is important for identifying new phenomena for evaluating the accuracy of other methods and providing a direct knowledge of the process which is being studied, but it is generally too expensive and inconvenient for studying the effects of a full range of external environments, of internal heat and moisture loads, and of internal obstructions in a full-scale building. Numerical analysis

(CFD) has been used intensively to predict the airflow pattern in buildings and ventilation systems. As mentioned before, it is normally less costly and short periods.

Both methods are important for studying and understanding the indoor air movement and pollutant particle deposition and distribution in building and ventilation systems.

§2.2 Review of Experimental study of Aerosol Particle Flow in Buildings

Chapter I has demonstrated that the existence of aerosol particles in building and ventilation systems greatly influences the indoor air quality and the incidence of building sickness. The recent studies described below show that people's dissatisfaction with the indoor environment mainly results from high indoor pollutant concentration and poor ventilation. On the other hand, the poorly maintained ventilation plants contribute to the indoor pollutant concentration and the incidence of building sickness. Therefore, it is necessary to investigate the characteristics of aerosol particles in building and ventilation system. A limited amount of experimental research of aerosol particle behaviour in ventilation systems has been found to date.

The aerosol characteristics from smouldering sources was reported by Mulholland, et al. (1982). The aerosol generated by the large-scale smouldering source is significantly different from that produced by small sources like cigarette smoke. The main difference is in the particle size. The mass mean particle size of the aerosol is 2-3 μm, roughly five times larger than that for cigarette smoke. The coagulation in the source plume may cause further increase in particle size. The coagulation procedure mainly happened within the plume region and appeared to be ignored outside the source plume.

Crump, et al. (1983) studied aerosol particle wall loss rates in a spherical stirred vessel. The experimental results showed that the measurement of particle size and mixing rate agreed well with the theoretical formula of Crump

and Seinfeld (1981). The results demonstrated the utility of the theory in correlating aerosol wall loss data in an experimental apparatus.

Nazaroff et al. (1989) described a mathematical model of indoor aerosol dynamics. The model accounted for the effect of ventilation, filtration, deposition onto surfaces, direct emission and coagulation. The predicted results were applied to explain the data of an experiment in which the evolution of cigarette smoke in a poorly ventilated room. The model was shown to be reasonably successful and may be also applied to the analysis of the soiling of surfaces due to the deposition of airborne particles and control of human exposure to environmental tobacco smoke.

Nazaroff et al. (1990) also studied the airborne particle deposition in museum surfaces theoretically and experimentally with particle size range of 0.05~2.1 μm. Consequently, the general concurrence of modelling and measurement results observed in this study is encouraging. The study shows that those aerosol particles with diameters in the range 0.05~2.1 μm pose a significant soiling hazard, because most of the elemental carbon that is responsible for the blackness of atmospheric aerosols is found in these sizes.

Schneider (1991) presented a measurement and analysis of aerosol particle deposition on interior surfaces. It is said that the rates of aerosol particle removal by surface deposition can be as large or larger than common room ventilation rates. Large particles (d_p>2μm) deposit faster than small particles. So small particles mainly contribute to the contaminant particle concentrations

in the room. It also suggests that cleaning of room surfaces is thus as important as ventilation in controlling particle contamination in the indoor air.

A summarisation of indoor aerosol particle sources, sizes, concentrations and compositions was reported by Owen et al. (1992). The study showed that particle sizes produced indoors or outdoors vary from sub-micrometer to larger than 10 μm. Particle size significantly influences particle deposition and distribution in indoor environment. Understanding indoor aerosols is very important so that control techniques may be implemented to reduce damaging health effects, soiling problems and further more to improve the indoor air quality.

Byrne et al. (1993) measured aerosol particle deposition rates for furnished or unfurnished rooms under different air exchange rates. The results demonstrated that particle deposition rates are governed mainly by particle characteristics and also by the existence of a variety of sinks which the indoor environment provides, such as furnishings, electronic sources, etc. The deposition rates in furnished rooms are larger than those in unfurnished ones. The data also showed that, at high air exchange rates, the role of aerosol deposition is limited, while at low air exchange rates, it becomes the dominant process in the particle movements.

Adam et al. (1993) presented an experimental study of aerosol particle flow in a ventilated chamber lined with different types of materials by using a tracer-gas technique. The conclusions are: a. particle deposition rate was found to be dependent on the size of particles and on the type of lining material used; b.

ventilation rate in room has a strong effect on deposition of particles; c. particle exchange rates were higher than tracer-gas exchange rates due to the deposition effect of particles on the surfaces of the room.

An experimental study of tobacco smoke particles deposition in a low ventilation room was presented by Xu et al. (1994). The results showed that deposition on interior surfaces is an important removal mechanism for tobacco smoke particles, especially at low ventilation rates. A significant amount of ETS particles may deposit on the internal surfaces at the normal ventilation rate of a residence. These deposited particles might be a secondary source of indoor air pollutants.

Cheong et al. (1994) measured aerosol particle flow in a two-zone environmental chamber using tracer gas and aerosol particles. The effect of parameters such as interzone temperature differences and size of interzonal openings on the movement of aerosol particles has been investigated. The coefficient of discharge was found to be random for particle flow. The deposition rate was found to increase with increasing particle size.

Riffat, et. al. (1994) reported an experimental study of aerosol particle flow in a two-zone environmental chamber. A series of measurements of interzonal flow was carried out using tracer-gas and aerosol particles. The effect of parameters such as interzone temperature difference and size of opening on the flow of tracer-gas and aerosol particles has been investigated. The deposition rate of particles on the surfaces of the chamber together with algorithms for interzonal heat and mass transfer through the openings were determined.

Raw (1994) addressed the relative importance for sick building syndrome of internal surfaces pollution and airborne particle pollution. The evidences of indoor surfaces pollution is one of the cause of sick building syndrome have been given in the paper. It is concluded that the ISP includes contaminants such as dust, fibres and micro-organisms which are deposited on building surfaces and in office furnishings.

A field monitor procedure of indoor air particulate in a hospital was reported by MaLaughlin, et. al. (1994) due to the complaints of 'dry eyes' and irritated eyes and skin in that environment. From an intensive indoor air quality assessment, these complaints were identified as being due to air-borne particulates from three sources: construction residual dust, fibreglass ceiling tiles and laundry lint. The paper describes the monitoring undertaken to identify the sources, the mechanisms for the dust distribution and provides useful information for the removal of contaminant pollution.

A laboratory-based study of the performance of a floor-based task ventilation system designed for use in office buildings has been described by Faulkner, et. al. (1995). The experiments were performed to measure the airflow pattern, the age of air at multiple indoor locations using tracer-gas and the transport and concentration of tobacco smoke particles at multiple indoor location. The major founding are: a. Deviations from a uniform age of air, and a uniform particle concentration, were generally less than 30%; b. With two floor-supply units operating and supply air directed toward the occupant, the age of air in the breathing zone was about 20-40% less than the age of air that would occur in the room if the air was perfectly mixed.

The above literature survey of experimental studies of aerosol particle flow in buildings shows that the knowledge of aerosol particle characteristics in buildings and ventilation systems is still limited though some investigations have been produced to date. It is necessary to carry out more research in that area both in experiment and theory.

§2.3 Review of Numerical Analysis in Building Engineering

In recent years, there have been extensive activities in the use of existing general computational fluid dynamics (CFD) software and in developing special computer programs for room and/or building airflow applications. These investigations range from the prediction of air jet diffusion, air velocity and temperature distribution in rooms, spread of contamination in enclosure, to fire and smoke spread inside buildings. In some cases the predicted results are satisfied when compared with available experimental data.

§2.3.1 The Characteristics of Flow Phenomena in Building Engineering.

The air movement in a ventilated space is a very complicated phenomenon which includes heat, momentum and mass (if required) transfer processes. Normally, the temperature ranges from 12°C to 35°C with the operation of supply air systems for cooling and/or heating. Boundary conditions from radiative and convective sources have proved difficult to model. The combined radiative and convective heat flux from surfaces varies from window surfaces (including both single and double glazing) to hot water radiator exposures (ranging from single-panel to double-panel radiators). At small temperature

differences, the ratio of heat transferred from a surface by radiation to that by convection can range from about 0.7 to 5.0 depending on surface emissivity and orientation.

In building applications, CFD codes must be able to predict typically within 2 orders of magnitude down (i.e. 0.05 ms^{-1} and 0.5°C) from any sources of heat and momentum in the space. In addition, there is a requirement to be able to model physical blockages that influence air movement such as partitions, architectural features, furniture and office equipment. In fact, CFD modelling of air movement in building engineering is a very difficult subject and there a large amount of research is required.

§2.3.2 Previous Research of CFD Simulation in Building Engineering

Most of the room air movement simulation programs currently in use are based on the premier works carried out at Imperial College by Spalding (1980), Patankar et al. (1972, 1980), Gosman et al. (1969) and their co-workers.

Nielson (1974) was one of the first to predict air movement and heat transfer in buildings using CFD methods. He developed a calculation procedure based on a stream function approach for predicting two-dimensional flow patterns in ventilated rooms. Later, Nielson et al. (1978, 1979) used a finite volume solution of the 2-D equations for the conservation of mass, momentum and energy as well as the two equations for turbulence energy and its dissipation rate in the k-ε turbulence model. The solution procedure was then extended for solving a 3-D isothermal flow in ventilated rooms. The numerical predictions produced reasonable correlations with experimental data.

Gosman et al. (1980) used a three-dimensional model to study velocity distributions in different geometrical arrangements. Using the k-ε model, it was found that the kinetic energy of turbulence and the length scale were largely uniform in the room.

Timmons et al. (1980) solved an inviscid flow model using equations in stream function and vorticity form. The approach combined fundamental equations with semi-empirical relationships for vorticity distribution. An advantage claimed was the rapid execution speed. The accuracy was found to be

acceptable except near boundaries where, not surprisingly, the inviscid assumption resulted in some errors.

Ideriah (1980) used a numerical procedure to calculate the velocity and temperature fields in a ventilated 2-D square cavity with a heated ceiling. The predicted results showed a good comparison with experimental data.

Howarth (1980) proposed a simplified zonal model to predict the temperature distribution in naturally ventilated rooms with convective heating. The comparisons between theoretical analysis and experimental measurement show good agreement. The zonal model provides a simple and quick method to assess the room temperature variations.

Holmes (1982) studied a number of flow configurations of interest to environmental designers. They comprised a downward projected vertical jet, air flow over a ceiling-beam obstruction, and a full numerical prediction of air movement in a theatre. The correspondence between prediction and experiment was sufficiently close for further investigating work to be recommended.

In 1984, Markatos et al. (1984) obtained a solution to the natural convective flow in a square cavity with two differently heated vertical walls and adiabatic horizontal floor and ceiling using the turbulence model. A satisfactory correlation was with published experimental data for both laminar and turbulent convection within the cavity. Markatos also solved the 2-D steady-state flow equations to predict the spread of fire in a room by representing the fire source

by a heat source and adding additional terms to the equations for k and ε to prescribe the highly buoyant flows being simulated.

Ventilation effectiveness studies using numerical computation were undertaken in 1984 by Ishizu et al. (1984). A two-dimensional stream function and velocity code was used to predict contaminant distribution. A simplified model of ventilation efficiency was derived based on the main numerical predictions.

Detailed calculations of air velocity and temperature distributions in a room were described by Reinartz and Renz (1984). The flow from a circular diffuser was modelled using a two-dimensional code. The calculation performed also modelled the flow within the diffuser and in the initial jet development region.

Awbi and Setrak (1986) developed a numerical solution procedure based on the Imperial College CFD code, TEACH, to predict the diffusion of an isothermal and non-isothermal plane wall jet. The effect of surface mounted rectangular obstacles of different dimensions on the diffusion of the wall jet was also studied and a good agreement with experimental data was obtained. The deflection of the jet and its separation from the surface was accurately predicted by the numerical solution.

In 1987, Whittle (1987) used a TEACH code to generate predictions of air movement and temperature distribution in a perimeter office space subjected to winter design conditions. A focus of interest was the convective and radiative heat transfer processes at the cold glazing and the resulting down draught. The

flow pattern was well predicted and good agreement was obtained for variation of averaged air velocity and temperature with height in the space.

Jones and Reed (1988) reported the use of CFD methods for predicting air movement and temperature gradients in large factory spaces. A body fitted co-ordinate system was used to more realistically model the roof profile and other non-rectangular building features. On the whole, the correspondence between prediction and measurement was satisfactory.

In 1988, Chen et al. (1988) used CFD method to study the combined problem of energy analysis, indoor airflow and air quality by combining CFD and thermal modelling codes.

Awbi (1989) presented the results of a numerical simulation developed for solving two- and three-dimensional ventilation problems. The program solves, in finite difference form, the steady-state conservation equations of mass, momentum and thermal energy. The CFD solution produced reasonably good predictions of the air velocity and temperature distribution in a test room cooled by a ceiling jet. Other predictions involving the heating and cooling of a room and the flow of a wall jet over an obstacle appear to be physically plausible. The role of CFD solutions in room ventilation design has been shown to provide an enhancement of the design process.

In 1989, Davidson (1989) used a CFD code to simulate the flow pattern in a displacement ventilation system. The calculated results presented the typical, for displacement flow systems, division of the flow into two zones: one lower

ventilation zone, and one upper zone where warm fluid is recirculating. The predicted flow pattern was shown to agree reasonably well with experiments.

Chen et al. (1990) studied a numerical analysis of using low-Reynolds-number k-ε turbulence model for predicting natural convection flow in cavities with Rayleigh numbers on the order of 10^{10}. The Boussinesq approximation was used for buoyancy, and the buoyancy production terms in the k and ε equations were also studied. The results indicate that the computed velocity and temperature profiles and convective heat exchanges by the model are in rather good agreement with the measurements. The influence of the buoyancy production is small on velocity and temperature distributions but is considerably large on the kinetic energy distributions. For the indoor airflow computation, use of low-Reynolds-number model with buoyancy production term is recommended so that correct indoor air velocity fields, air temperature distributions, convective heat transfer coefficients, and comfort parameters can be obtained.

A numerical study of three-dimensional airflow patterns and contaminant dispersal in a ventilated two-zone enclosure was reported by Haghighat et al. (1990). Two types of boundary condition for air supply are considered: (1) the outside air uniformly infiltrates through an end-wall at ceiling-level into the enclosure and leaves through a ceiling-mounted exhaust opening; and (2) the ventilation air flows into the enclosure through a rectangular supply opening near the floor on one of the end-wall and leaves the enclosure through the exhaust opening. The two zones are separated by a partition with a door opening at different positions. The effects of the door location on the airflow

pattern and on the contaminant dispersion induced by natural and mechanical ventilation in a two-zone enclosure have been investigated. The door location not only guides the direction of the airflow but also affects the strength of the air circulation. Besides, since air serves not only as a dilute but also as a carrier of contaminants such as smoke, dust, odours, and so on, the distribution of the contaminant concentration inevitably depends on the door location. The conclusions are: a. The flow pattern in the upstream zone is not significantly influenced by the door location, while in the downstream zone, both the direction and the magnitude of the air circulation are dependent on the door location; b. When the contaminant source is in the upstream zone, a partition combined with a local exhaust can efficiently protect the downstream zone from any contamination no matter where the door opening is; c. When the contaminant source is in the downstream zone, the door location greatly affects the distribution of contaminant concentration in this zone. The buoyancy effect is not taken into consideration in above analysis. The results obtained from the study have a practical relevance and give a clear and qualitative information about the ventilation air circulation and contaminant distributions in two-zone enclosure.

Jones (1990) investigated room air distribution in air conditioned offices by using CFD. He also studied the ventilation effectiveness in such situation which is related to the pollutant concentration level, thermal comfort, etc. The research shows that CFD is a useful tool for the design of room air distribution.

An investigation on validation of CFD procedures for room air motion prediction was reported from Baker et. al. (1990). The authors give an

overview of mathematical theory, closure modelling, and code validation issues of pertinence to room air motion CFD prediction. A series of critical benchmark problem predictions are highlighted and discussed that serve assessment needs for code validation. Specific emphasis has been placed on identification of error mechanics that exists at every turn to pollute a CFD solution. The authors strongly notify that the indoor environmental analysis community must strive to become literate users of CFD methodology so that the inherent limitations are understood and fully appreciated. The paper also issues extensive knowledgeable use of CFD technique for prediction of room air fluid/thermal flow fields.

In 1991, Chen et al. (1991) presented an investigation of field distributions of air velocity, temperature, contaminant concentration, and thermal comfort in an office with displacement ventilation for different air supply parameters such as the effective area, shape, and dimension of the diffuser and the turbulence intensity of supply air, flowrate, and supply air temperature. The research was conducted numerically by using a CFD program based on a low-Reynolds-number k-ε model of turbulence. It can be concluded that the geometry of the diffuser and the turbulence intensity of the air supplied have little contribution to room air diffusion except at the floor level. The influence of the flowrate and temperature of the air supplied is very significant on the air diffusion as well as on the thermal comfort and indoor air quality.

Haghighat et al. (1991) analysed the contaminant removal and air freshness in a ventilated two-zone enclosure by using a numerical k-ε turbulence model. The average contaminants distribution in each zone under variable position of door,

supply and exhaust are compared. It is found that the supply and door positions affect the contaminant concentration in the upstream zone significantly, while the exhaust location does not seem to influence the average concentration in either the upstream or the downstream zone.

A numerical simulation of airflow pattern, temperature distribution, and percentage of dissatisfied people in a two-zone enclosure with mixed concentration conditions was presented by Jiang et al. (1992). The effects of door location on flow properties and thermal comfort are examined by placing the door opening at three different positions. The results indicated that temperature is quite uniform for the most part throughout the enclosure, except in the region near the floor in downstream zone; that the percentage of dissatisfied people in most areas is less than 10%; and that average concentration values in both zones are at their lowest values when the door is in the middle of the partition, and are not sensitive to the supply air temperature.

Allard et. al. (1992) reviewed the application of zonal models for predicting thermal behaviour and heat transfer in heated or ventilated rooms. Zonal models are simplified thermal models based on two main assumptions: first, it can predict the main driving flow by balancing the mass and heat transfer within boundary layer, wall jet and thermal plume; second, it needs a sufficiently good empirical knowledge of zonal structures to calculate the main characteristics. The authors compared the results of three zonal models with that of CFD analysis and pointed out that the usefulness of such an approach by using zonal model can get a quick estimate of the non-isothermal behaviour of a room with

heating or ventilating systems. Furthermore the existing comparison with CFD codes or real scale experiments show that most of the time zonal models are able to predict with a reasonable accuracy air flow rates and heat transfer within a room. More details about zonal model can be seen in Howarth (1985).

Moser (1992) reviewed CFD application in numerical simulation of room thermal convection with IEA Annex-20 project. The paper focused on conclusions and recommendations resulting from the numerical simulation of five cases studies that were supported by independent measurements by different countries in identical test chambers. The three-dimensional turbulent air flow patterns were predicted by nine different CFD codes and compared with measurements. The work has shown the state of the art (CFD) in building air flow simulation. Literate CFD users in the field have an opportunity to try out their methods at different cases and to make improvements of their models.

Murakami (1992) outlined new methods for evaluating ventilation efficiency in a room. This evaluation must be based on analysis of the flow field of the room. New scales for ventilation efficiency based on the flow field analysis by numerical simulation process are proposed. These new scales are applied to room models and their effectiveness is confirmed.

Jones, et al. (1992) summerised the histroy of CFD applications in building engineering since the pioneer work carried out by Nielson in 1974. The paper gave a benchmark review of CFD development in building engineering. It also proposed the limitations and shortcomings of current CFD techniques and

outlined the suggestions for further studies. It is concluded that CFD is a cost-effective method for the study of air movement and pollutant distribution in buildings and hopefully to be used as a additional design tool for building engineers in future.

Beghein, et al. (1993) presented a numerical simulation of airflow and temperature distribution in a thermally driven square cavity. The computational results show good agreement with the relevant experimental data.

Li, et al. (1993) used a local grid-refinement method to simulate an indoor airflow pattern in a large room with a small ventilation opening. A multi-grid algorithm, which turns out to be an efficient and accurate solver, is used to solve the discrete system of equations on both global and local grids. The validation shows satisfied agreement between computations and measurements.

J. van der Kooi et al.(1993) presented a numerical simulation of the airflow pattern and contaminant concentration in an operating room. The purpose of analysis is to find out the optimum airflow pattern for reducing the risk of infection in the operating room. The calculations show that the air flow field with exponential inlet velocity profile under the inlet area gives better results. The computations showed a fairly good agreement with experiments.

Vazquea et al. (1993) predicted a forced convective flow across a two-dimensional cross section of an auditorium. The aim of the study was to determine the flow patterns and temperature fields produced by the ventilation

and assess their effect on the wall heat transfer and the thermal comfort conditions inside the auditorium. The k-ε model was used for representing turbulence. The flowrate through the outlet was varied to obtain Reynolds numbers from 1000 to 150,000. In all cases calculated the body heat generated by the occupants of the auditorium was modelled. The effects of the location of the air inlets, of the size of the air outlets and of the outlet velocity on the flow patterns were investigated.

A numerical analysis of buoyant air flow in livestock buildings was reported by Svidt (1993). The effect of room geometry, obstacles and heat sources on the flow field was also simulated. Good agreement was found when results of calculation were compared with measurements.

Jacobsen et al. (1994) presented an investigation of the airflow in a room with displacement ventilation system. The study is aiming at testing the model and conducting numerical simulation to provide a detailed description of the air current along the floor. It also investigated if the model comply with the test.

Brohus, et al. (1994) reported a CFD simulation of air movement and contaminant distribution in a room ventilated by displacement ventilation. The research deals with some of the effects of persons present in the displacement ventilated room, especially the effect on the contaminant distribution. The study shows that the exposure of a sitting and a standing person is in proportion to the stratification height. It is found that the flow in the boundary layer along a person to a great extent is able to entrain air from below the

breathing zone. It also demonstrated that the possible disadvantage when contaminant sources are located in the lower part in the room.

Fontaine, et al. (1994) described a numerical analysis of airflow and pollutant distribution in a ventilated workshop with a high level air supply and a low level large extraction. The system produces, in isothermal conditions, a displacement type of flow. Interactions between the downward flow and the walls induces nevertheless weak recirculation vortices and upward flows. This effect is more pronounced when high velocity jets were added to the area. The jets contribute to increase velocities in the working zone and to enhance the reverse flow. The upward flow leads to a contaminant concentration distribution in the breathing zone which is less satisfactory than in the absence of the jets.

A CFD prediction of air movement in a large enclosure equipped with HVAC system was reported by Buchmann, et al. (1994). Energy consumption, thermal comfort, overheating and thermal stratification are often encountered in such system due to the inappropriate design and dimensioning of the HVAC system. Therefore, airflow predictions are expected to give recommendations. Both standard k-ε turbulence model and low Reynolds number k-ε turbulence model were used in the study. The CFD simulation results show that a low Reynolds number turbulence model improves the predictions of thermal losses, thermal stratification and velocities and temperature fields.

Alamdari, et al. (1994) presented a CFD prediction of airflow and temperature distribution in an office building space with displacement ventilation system.

Measurements of velocity and temperature fields have used to verify the predicted data obtained by CFD model. Acceptable conditions were predicted and measured within the space considered in the study. Both computations and measurements indicated that secondary sir flows resulting from infiltration and cold surfaces can adversely affect the ventilation performance and reduce thermal comfort.

Jiang, et al. (1995) studied the impact of office partitions on indoor contaminant control in large partitioned office equipped with a displacement ventilation system. The investigation is conducted by numerical simulation of three-dimensional turbulent flow using the k-ε turbulence model. Five partition layouts were considered in the study. The air quality in the office is assessed by the overall level of contaminant concentration in the office and the average contaminant concentration in each zone. It is found that, comparing to a conventional ventilation system, displacement ventilation provides a fresher air to all zones, but in general it is not suitable for partitioned offices if the contaminant source is located in a chamber where it is exposed directly to the supply air. The buoyancy effect significantly influences the contaminant level in the occupied zone.

From the above literature search, the role of CFD simulation in room and/or building ventilation system has been presented to provide an enhancement of the design process. A CFD solution produces considerably qualitative information about the air flow field in the spaces concerned with especially in low velocity turbulent flows. For such cases, the full-scale experimental study is proved to be expensive and difficult to proceed.

§2.4 Conclusions

To date, the CFD technique has been extensively applied in building and environmental engineering and a number of qualitative results have been obtained. Most CFD codes are capable of predicting airflow within buildings. Most codes use the finite volume method and essentially solve similar numerical forms of the equations for mass, momentum and energy conservations. The options of different turbulence models, such as k-ε model, algebraic stress model, full Reynolds stress model, etc., are available in most CFD codes. Most codes are able to accommodate curvilinear co-ordinate systems (body-fitted co-ordinates) for the flexibility of mesh generation to match the complicated geometry encountered in building applications. The flexible pre- and post-processors are efficient presentation tools when compared with available experimental data.

However, numerical modelling of airflow patterns in building engineering is still at an early stage of development and a considerable amount of research and development work will be needed. Major technical limitations and shortcomings exist in most CFD codes are:

1) turbulence modelling, especially the understanding of the nature of turbulence in buildings is still incomplete;
2) need for surface-to-surface radiation models;
3) lack of interaction with thermal model;

4) need for better coupling of Euler equation and Lagrangian trajectory equation which can be used for tracing contaminant particulates within ventilation systems;

5) need for faster convergence for buoyant flows;

6) need for dealing with non-othorganol meshes;

7) requirement for fundamental research in new area of particle tracking model which will be used to monitor the contaminated particles within ventilated space.

The research project proceeded in this thesis is to predict the airflow patterns and pollutant aerosol particle deposition, migration and distribution in heating, ventilation and air-conditioning system using both Eulerian continuous fluid method and Lagrangian particle tracking method.

CHAPTER III

PARTICLE DYNAMICS

Abstract

A description of particle characteristics in continuous fluids has been given in this chapter. A numerical model, i.e. particle transport model, for simulating particle settling process in stagnant air is also presented herein. A good agreement between numerical results and analytical solutions has been obtained. It can be concluded that the particle deposition procedure is mainly related to the properties of particle and continuous fluids. Particle deposition is an important characteristics of particle movement in indoor environment.

§3.1 Introduction

Particle and fluid mixed flows are of frequent occurrences in nature and in industry. Rainfall, snowdrifts and sandstorms in nature are all examples of particle-fluid mixed flows or of its results. A brief extract of such mixed flows in which particles play a primary role in industry is listed as follows:

1. Steam-water flows in boilers, condensers, turbines, cavitating pumps, pipes and valves in which particles act in the form of steam bubbles;
2. Dusty-gas flows in heating, ventilation and air-conditioning systems, coal mines, cyclone separators, sand-blast cleaners, fluidised-bed combustors, electrostatic precipitators, rocket-exhaust plumes;
3. Spray-suspension flows in diesel engines, furnaces, gas-turbine combustors, rocket motors, powdered-milk dryers, distillation columns;
4. Liquid-solid flows in coal-transportation pipelines, sewage plants;
5. Liquid-liquid flows in settling tanks, emulsifiers, petroleum winning processes;
6. Oil mixture transport and off-shore oil industry examples.

In all these phenomena and processes, particles are of fundamental importance, and there is relative motion between particles and surrounding fluid. In many cases, mass and/or heat transfer is also of importance. Study of interactions between particles and fluid forms the main purpose of this chapter, i.e., to give a comprehensive description of the fluid dynamics of particle movement within a surrounding fluid — particle dynamics.

§3.2 Basic Theory of Particle Settling Process in Continuous Fluid

Particle is, by definition, a self-contained body with dimension up to 10 cm, separated from the surrounding medium by a recognisable interface. The material forming the particle is termed 'dispersed phase'. Here, we refer to particles whose dispersed phases are composed of solid matter as 'solid particles' or 'rigid particles'. If the dispersed phase is in liquid state, the particle is called a 'drop'. Those particles whose phases are in gas state are referred as bubbles. In this research, attention is concentrated on 'solid particles' which are biologically inert, which are free to move through the continuous fluids under the action of body forces such as gravity and whose size scales are large enough to ignore the scale of Browning molecular motion in the dispersed phase. Particle dynamics is a branch of general mechanics dealing with relative motion and interactions between a particle (solid or liquid) and surrounding fluid (gas or liquid), regardless of the particle moving in a stationary fluid or suspended in a moving fluid.

§3.2.1 Stokes Equation

The system considered in this chapter is a solid particle moving in an infinitely large volume of fluid. The particle Reynolds number is sufficiently low ($0 \le R_{ep} \le 0.2$) that there is no wake at the rear of the particle. Here, the particle Reynolds number is defined as:

$$R_{e_p} = \frac{\rho V_R d_p}{\mu} \qquad (3\text{-}1)$$

In this circumstance, the Stokes law of drag force is applied. For the sake of simplicity, however, the particle is assumed to be spherical throughout the chapter. Under such an extraneous condition, the particle enjoys complete freedom in its motion, unlike a situation in which a very large number of particles are crowded into a limited space. This motion is referred as free motion, generally, or free falling (i.e., free deposition), in particular, when the motion is under the influence of gravity. Otherwise the motion is said to be hindered. In hindered motion the particles interfere with each other with the effect that their settling (or deposition) rates are reduced considerably.

The theory of particle deposition in a stagnant fluid finds an extensive application in a number of industrial processes. If the concentration of particles is at low level, their behaviour may not be very different from that of a single particle. It can be assumed then, that the particles have sufficient freedom in their motion to enable them to behave in nearly the same manner as does the single particle to which the theory applies. It will be therefore helpful to fully understand the phenomenon of single particle settling (or deposition) in an infinitely large volume of fluid.

Consider a solid particle falling from rest in a stationary fluid under the action of gravity. It is assumed that the particle is a rigid spherical one and the surface tension effects can be ignored. The particle will at first accelerate as it does in a vacuum, but unlike in a vacuum, its acceleration will be retarded due to friction with surrounding fluid. As the frictional force, i.e. the resistance force,

increases with the velocity, this force will eventually reach a value equal to that of the gravitational force, see figure 3.1. From this point on, the two forces will be balanced and the particle will continue to fall with constant velocity. Since this velocity is attained at the end of the acceleration period, it is called terminal settling velocity, see figure 3.2. According to Newton's second law, the equation of particle free falling is as follows:

$$m\frac{dV}{dt} = F - R \tag{3-2}$$

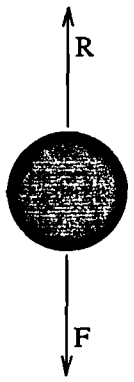

Figure 3.1 A free falling particle under the action of gravity and resistance forces

The gravitational force (F) acts on the particle even when it is at rest, and remains constant during the whole period of fall. In practice, the acceleration period is of a very short duration, often of the order of a small fraction of a second. It is therefore reasonably to ignore this period in particle settling processes, and the terminal settling velocity then becomes the only important factor in this kind of problem. Its magnitude is closely related to the physical properties of the fluid and the particle, and the relationship can be obtained from a balance of the two forces involved. For a particle settling at its terminal

velocity, the two opposing forces are in a balance, $a = dV/dt = 0$, so equation (3-2) becomes:

$$F - R = 0 \tag{3-3}$$

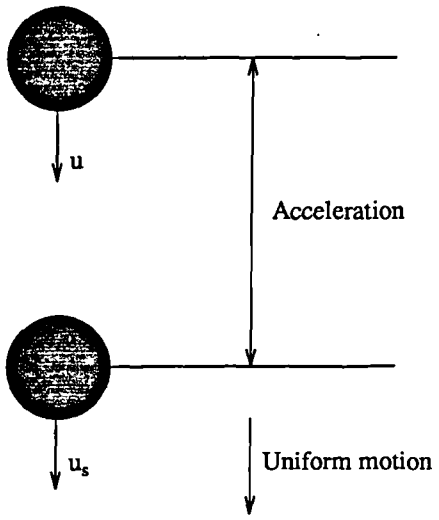

Figure 3.2 A spherical particle in acceleration

Let D_p be the diameter of the particle, then $(\pi D_p^3/6)$ is its volume, and $(\pi D_p^3 \rho_p/6)$ its mass. From Newton's second law of motion, using the absolute systems of units, then,

$$F = \frac{\pi D_p^3 \rho_p}{6} g - \frac{\pi D_p^3 \rho}{6} g = \frac{\pi D_p^3}{6}(\rho_p - \rho) g \tag{3-4}$$

The last term of equation (3-4) represents the buoyancy effect. This effect may be ignored if the density of the fluid is negligibly small compared with the density of the solid particle, e.g. lead particle.

The resistance force is generally referred to as the drag. Its magnitude is assumed to be a function of the diameter of the particle D_p, its relative velocity to the fluid V_R, and physical properties of the surrounding fluid such as its density ρ and viscosity μ. Based on these assumptions, the following proportionality can be set up (Clift, R, et al., 1978; Warsi, Z U A, 1993):

$$R \propto D_p^x \rho^y V_R^z \mu^t \tag{3-5}$$

or

$$R = k D_p^x \rho^y V_R^z \mu^t \tag{3-6}$$

Substituting the dimensions for each variable of equation (3-6),

$$ML\theta^{-2} = L^x \left(ML^{-3}\right)^y \left(L\theta^{-1}\right)^z \left(ML^{-1}\theta^{-1}\right)^t \tag{3-7}$$

Following Reyleigh's method of dimensional analysis, the dimensions will be separated into the following equations by equating the indices for

Mass (M)	$1 = y + t$	(a)
Length (L)	$1 = x - 3y + z - t$	(b)
Time (θ)	$-2 = -z - t$	(c)

Solving these three equations simultaneously in terms of t, obtaining

$$x = 2 - t \tag{d}$$

$$y = 1 - t \tag{e}$$

$$z = 2 - t \tag{f}$$

Therefore equation (3-6) becomes

$$R = k\left(D_p\right)^{2-t}\left(V_R\right)^{2-t}\left(\rho\right)^{1-t}\left(\mu\right)^t = k D_p^2 V_R{}^2 \rho \left[\frac{\rho V_R D_p}{\mu}\right]^{-t} \tag{3-8}$$

The above exponential equation does not avail itself for immediate use, except for the condition at which the exponent (t) is clearly determinable. Such a condition exists for laminar flow. The term ($\rho V_R D_p/\mu$) is the particle Reynolds number defined in equation (3-1) based on the particle diameter.

For spherical particles, the accepted range of laminar motion is up to R_{ep}=0.2, approximately. For this range, t=1. The constant k has been determined experimentally for a number of shapes. For spherical particles, it has a value of 3π, so that equation (3-8) takes the form as below:

$$R = 3\pi\mu D_p V_R \tag{3-9}$$

This equation was derived in 1851 by Stokes (Clift, R, et al., 1978) by the application of one of the so-called Navier-Stokes equations of viscous motion in steady flow past a sphere (details in §3.2.2). It is known as the Stokes equation.

For a particle settling at its terminal velocity, let u_s be the terminal settling velocity, the equation (3-3) becomes:

$$\frac{\pi D_p^3}{6}(\rho_p - \rho)g = 3\pi\mu D_p u_s \tag{3-10}$$

then

$$u_s = \frac{D_p^2(\rho_p - \rho)g}{18\mu} \tag{3-11}$$

This equation is also called the Stokes equation. It is suitable for single particle deposition in static fluid in laminar flow regime.

§3.2.2 The Stokes Solution

1. Streamline and velocity diagrams of spherical particle and infinite fluid at low R_{ep}.

As mentioned above, the case of flow past a sphere within an unbounded fluid at low R_{ep} was first considered by Stokes. Such a system is also called the Stokes system. Here, the origin of the spherical-polar co-ordinates is chosen at the centre of the sphere and the axis $\theta=0$ in the direction of incident velocity U, see Figure 3.3. The particle surface tension effect is ignored. For axisymmetric flows of incompressible fluids, we define a stream function, ψ, called the Stokes stream function. The problem can be treated in terms of the stream function ψ. The set of equations reduces to one equation in ψ as:

$$\nabla^4\psi = 0 \tag{3-12}$$

where: $$\nabla^2 = \frac{\partial^2}{\partial r^2} + \frac{1}{r^2}\frac{\partial^2}{\partial \theta^2} - \frac{\cot\theta}{r^2}\frac{\partial}{\partial \theta}$$

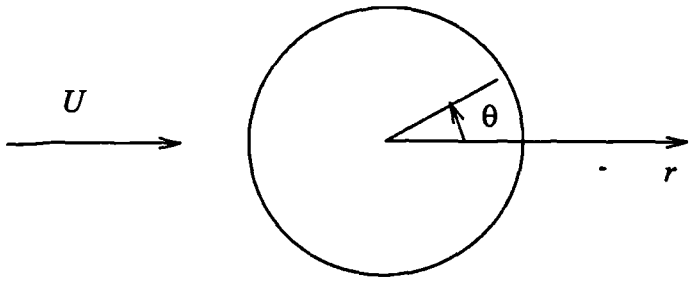

Figure 3.3 The co-ordinate systems in Stokes flow

The velocity components along the radius and the tangential angles are related to ψ (i.e., u_r and u_θ, respectively) in spherical-polar co-ordinates by

$$u_r = \frac{1}{r^2 \sin\theta}\frac{\partial\psi}{\partial\theta}, \qquad u_\theta = \frac{-1}{r\sin\theta}\frac{\partial\psi}{\partial r} \tag{3-13}$$

The boundary conditions for the fourth order equation (3-12) are obtained from the following conditions:

at $r = a$, $$u_r = u_\theta = 0 \tag{3-14}$$

at $r \to \infty$ $$u_r = U\cos\theta, \quad u_\theta = -U\sin\theta \tag{3-15}$$

as $r \to \infty$ $$\psi = \frac{1}{2}Ur^2\sin^2\theta \tag{3-16}$$

The solution of equation (3-12) with boundary conditions (3-14) ~ (3-16) can be found in a number of standard texts (Batchelor, G K, 1967; Warsi, Z U A, 1993) and is described below:

$$\psi = \frac{r^2}{2}U\sin^2\theta\left(1-\frac{3a}{2r}+\frac{a^3}{2r^3}\right) \tag{3-17}$$

The corresponding velocity components are

$$u_r = U\cos\theta\left(1-\frac{3a}{2r}+\frac{a^3}{2r^3}\right) \tag{3-18}$$

$$u_\theta = -U\sin\theta\left(1-\frac{3a}{4r}-\frac{a^3}{4r^3}\right) \tag{3-19}$$

Figure 3.4 represents the streamlines relative to static spherical particle at low R_{ep}. It can be seen that the flow is axisymmetric about the axis of θ=0.

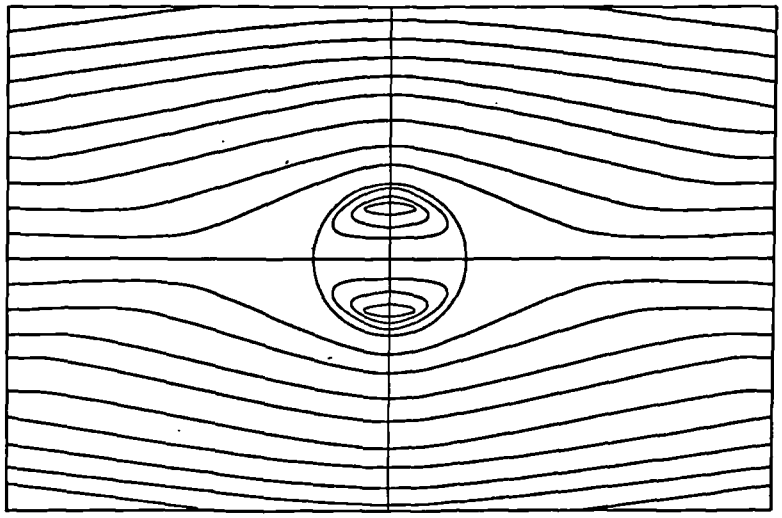

Figure 3.4 Streamlines relative to spherical particle at low R_{ep} (Clift, 1978)

The above solutions are for the situation when the sphere is at rest and the velocity of the fluid at infinity is U. To obtain the solution when the fluid is at rest at infinity while the sphere is moving with velocity $-U$, subtracting $U\cos\theta$ and $-U\sin\theta$ from equations (3-18) and (3-19), respectively, and have:

$$u_r = -U\cos\theta\left(\frac{3a}{2r} - \frac{a^3}{2r^3}\right) \tag{3-20}$$

$$u_\theta = U\sin\theta\left(\frac{3a}{4r} + \frac{a^3}{4r^3}\right) \tag{3-21}$$

The corresponding stream function is then:

$$\psi = -\frac{3Uar}{4}\sin^2\theta\left(1 - \frac{a^2}{3r^2}\right) \tag{3-22}$$

The streamlines for motion of spherical particle through stagnant fluid at low R_{ep} are shown in figure 3.5.

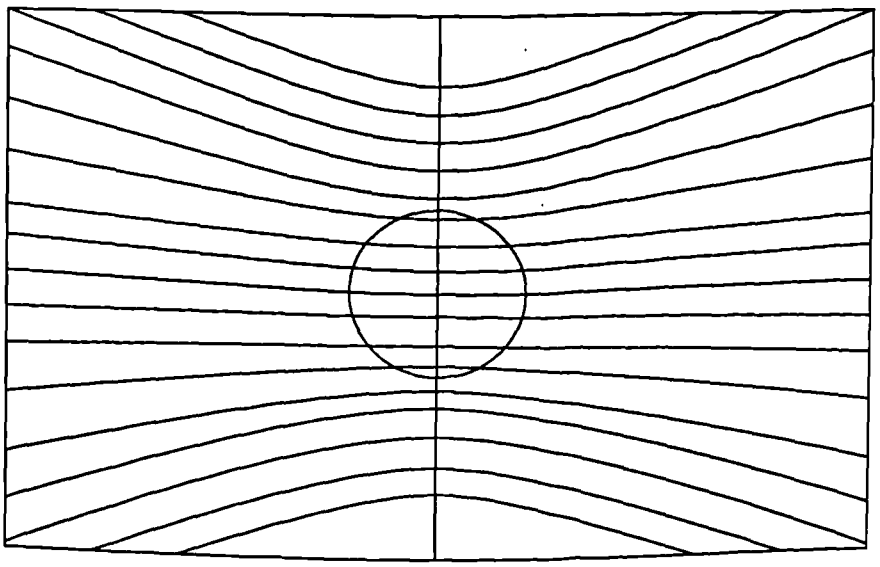

Figure 3.5 Streamlines for motion of sphere through the stagnant fluid at low R_{ep} (Clift, 1978)

2. Drag force and drag coefficient

a. Drag force

Having obtained the velocity distribution, it can be found that the pressure p over the particle surface by using steady, laminar, incompressible Navier-Stokes equation, i.e.,

$$grad(p) = \mu \nabla^2 u \tag{3-23}$$

For Stokes flow, equation (3-23) has the exact solution as below:

$$p = p_\infty - \frac{3\mu U a \cos\theta}{2r^2} \tag{3-24}$$

where p_∞ is the pressure at infinity($r=\infty$). The pressure distribution described in equation (3-24) is an odd function of θ, so that the particle experiences a net pressure force or 'drag'. Integration of the pressure over the surface of the particle leads to an overall drag force of particle which is presented in equation (3-25):

$$R = 6\pi\mu Ua = 3\pi\mu UD_p \tag{3-25}$$

The force R is the drag acting on a sphere due to the streaming flow past it with velocity U. It can be concluded that, first, the drag force is caused due to the viscosity of the fluid; second, note that the streamlines are axisymmetrically distributed about the direction of the streaming flow, thus there is no wake behind the sphere.

b. Drag coefficients

From the drag force, we can obtain the drag coefficient C_D which is a nondimensional coefficient defined as the drag force divided by $\frac{1}{2}\rho U^2$ and by the area of the body projected on a plane normal to the direction of the velocity U. Thus the drag coefficient for a spherical particle becomes:

$$C_D = \frac{R}{\frac{1}{2}\rho U^2 \frac{\pi D_p^2}{4}} = \frac{3\pi\mu UD_p}{\frac{1}{8}\pi\rho U^2 D_p^2} = \frac{24}{R_{ep}} \tag{3-26}$$

The above equation is suitable for a spherical particle in laminar flow at $R_{ep} \leq$ 0.2. When the Reynolds number increases, i.e., the incident velocity U increases, the flow regime changes from laminar to turbulent. Figure 3.6 shows logarithmic plot of C_D varying via Reynolds number. Three zones can be

distinguished on the diagram. The laminar zone, also called the stream or viscous zone, for Reynolds numbers up to 0.2, approximately; the transition zone, for Reynolds numbers from 0.2 to 500, approximately; and the turbulent zone, for Reynolds numbers up to about 100,000. These three zones are often referred as the Stokes, Allen, and Newton zones, respectively.

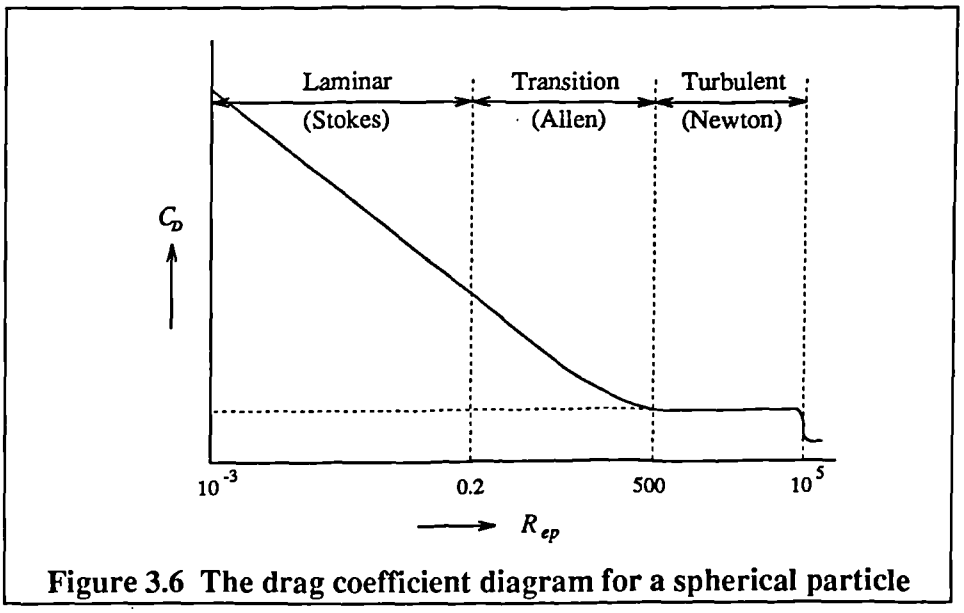

Figure 3.6 The drag coefficient diagram for a spherical particle

For the laminar range (Stokes zone), there is a relation between C_D and R_{ep} as described in equation (3-26). No regular relationship exists between C_D and R_{ep} for the transition range (Allen zone). For this range, the recommended drag coefficient correlations are listed below:

for $0.2 \le R_{ep} \le 20$, $$C_D = \frac{24}{R_{ep}}\left[1 + 0.1315 R_{ep}^{(0.82 - 0.05 \log_{10} R_{ep})}\right] \qquad (3\text{-}27)$$

for $20 \le R_{ep} \le 260$, $$C_D = \frac{24}{R_{ep}}\left[1 + 0.1935 R_{ep}^{0.6305}\right] \qquad (3\text{-}28)$$

for $260 \le R_{ep} \le 1500$,

$$C_D = 1.6435 - 1.1242 \log_{10} R_{ep} + 0.1558 \left(\log_{10} R_{ep}\right)^2 \qquad (3\text{-}29)$$

In turbulent regime (Reynolds zone), the drag coefficient C_D keeps nearly constant and has a value of 0.44, approximately (see figure 3.6 and 3.7).

The conventional curve for drag coefficient on a sphere in steady motion is shown in Figure 3.7, called the 'standard drag curve', where C_D is plotted as a function of R_{ep}. Many empirical or semi-empirical equations have been proposed to approximate this curve. The most commonly used relation is described in (Clift, C, et al., 1978) which is proposed by Schiller and Nauman in 1933, having the formation as:

$$C_D = \frac{24}{R_{ep}}(1 + 0.15R_{ep}^{0.687}) \qquad (3\text{-}30)$$

Equation (3-30) is widely used in engineering to calculate the drag coefficient. The range of deviation of this correlation is between -4~5%.

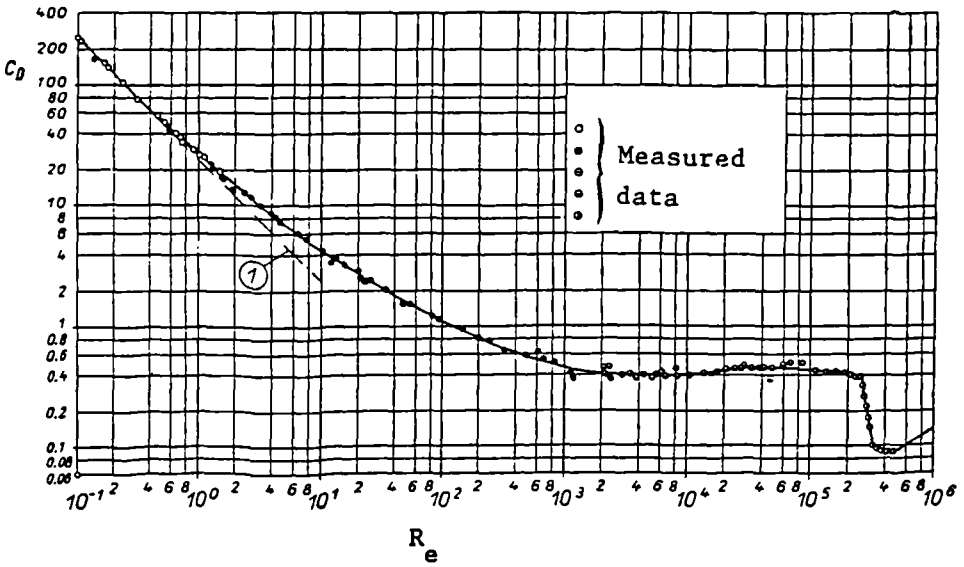

Figure 3.7 Measured drag coefficients for spheres
(① Stokes relation, Warsi, 1993)

There also have approximate equations for calculating the terminal settling velocity of a spherical particle in transition and turbulent ranges. These equations are listed below:

for the transition zone:
$$u_s = \left[\frac{4}{3C_D}\frac{D_p(\rho_p - \rho)g}{\rho}\right]^{1/2} \tag{3-31}$$

for the turbulent zone: $C_D \approx 0.44$, and it is approximately constant between $R_{ep}=500$ and $R_{ep}=100{,}000$, so

$$u_s = \left[1.73\frac{D_p(\rho_p - \rho)g}{\rho}\right]^{1/2} \tag{3-32}$$

According to equations (3-11), (3-26) ~ (3-29), (3-31) and (3-32), it can be seen that the exact solutions of single particle settling (or deposition) procedure in stagnant fluid can be obtained directly for laminar flow region, i.e., calculating the terminal settling velocity u_s from equation (3-11) and drag coefficient C_D from equation (3-26). Table 3-1 shows the analytical solutions of a number of heavy particles (e.g. lead particle, ρ_p=10000 kg/m^3) deposition procedures in a large volume of static air (i.e., ρ=1.209 kg/m^3, μ=1.812×10^{-5} kg/m·s).

All cases listed in Table 3.1 belong to laminar and transient regimes. The drag coefficient C_D decreases rapidly as the particle size increases. The logarithmic plot of the variation of drag factors C_D with particle Reynolds number R_{ep} is shown in Figure 3.8. It can be seen that a linear relation exists between logC_D and logR_{ep} for laminar regime. For transition and turbulent regimes, the

deposition procedures can be solved by iterations, i.e., assuming an initial R_{ep}, iterating the equations (3-27) ~ (3-32) until the two adjacent values are closed within an acceptable range.

Table 3.1 Analytical solutions of lead particles settling processes in static air

Case No	Particle size (μm)	Particle mass (kg)	Settling velocity u_s (m/s)	Particle Reynolds number R_{ep}	Drag factor C_D
1	1	5.236E-15	3.007E-4	0.0000201	1196216.3
2	5	6.545E-13	7.5148E-3	0.00251	9561.753
3	8	2.681E-12	1.925E-2	0.01027	2335.73
4	10	5.236E-12	3.007E-2	0.020063	1196.216
5	20	4.189E-11	1.203E-1	0.1605	149.502
6	30	1.414E-10	2.517E-1	0.503817	51.1706
7	50	6.545E-10	6.097E-1	2.03402	14.5464
8	100	5.236E-9	1.6455	10.9791	3.996

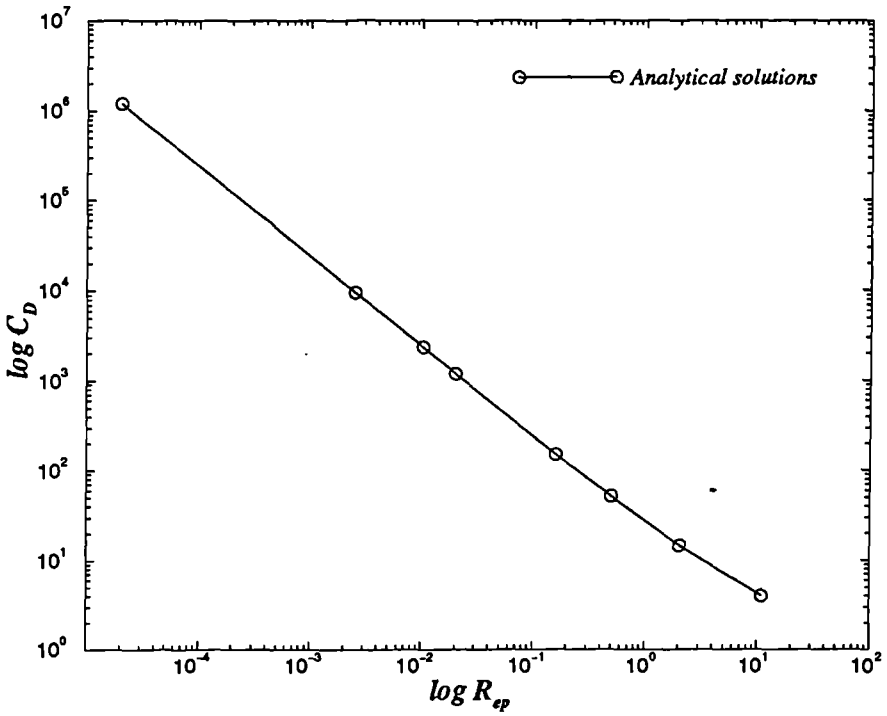

Figure 3.8 Variation of C_D vis R_{ep} of single lead particle settling with different sizes

§3.3 Numerical Analysis of Solid Particle Settling in Still Air

The analytical solutions of a spherical solid particle moving in stationary fluid at laminar condition have been deducted by Stokes and take the forms in equations (3-11) and (3-20) ~ (3-26). The equations (3-27) ~ (2-32) have been obtained for the transition and turbulent ranges. In this section, we are using CFD techniques (is now refereed to as the state of the art of engineering) to simulate single particle deposition procedure in infinite static air within different flow regimes.

§3.3.1 Problem Definitions

The cases considered herein are a single solid particle (e.g., lead particle) falling through the stagnant air in a large three-dimensional space. For the purpose of covering the particle size ranges as wide as possible within the limitation of CFD model, a group of particle sizes between 1μm and 100μm has been chosen in the simulation. The details of cases are listed below.

a. Fluid and particle properties:

The physical properties of particles and fluid are listed in Table 3.2.

Table 3.2 Physical properties of particles and fluid

Case No.	Fluid density ρ (kg/m^3)	Particle density ρ_p (kg/m^3)	Particle size D_p (μm)	Particle mass (kg/s)
No. 1	1.209	10000.0	1	5.236E-15
No. 2	1.209	10000.0	5	6.545E-13
No. 3	1.209	10000.0	8	2.681E-12
No. 4	1.209	10000.0	10	5.236E-12
No. 5	1.209	10000.0	20	4.189E-11
No. 6	1.209	10000.0	30	1.414E-10
No. 7	1.209	10000.0	50	6.545E-10
No. 8	1.209	10000.0	100	5.236E-09

b. Geometry size:

The considered space has a size of 4.0m(length)×3.0(width)×2.8m(height), see figure 3.9.

c. Other conditions:

- all particles start moving from the position shown in figure 3.9;
- no heat and mass transfer exists between fluid and particles;
- the geometric space is infinite compared with the particle size;
- both gravity and resistance forces act on the particles;
- the initial velocities of particles and fluid are zero;
- the fluid is in static state.

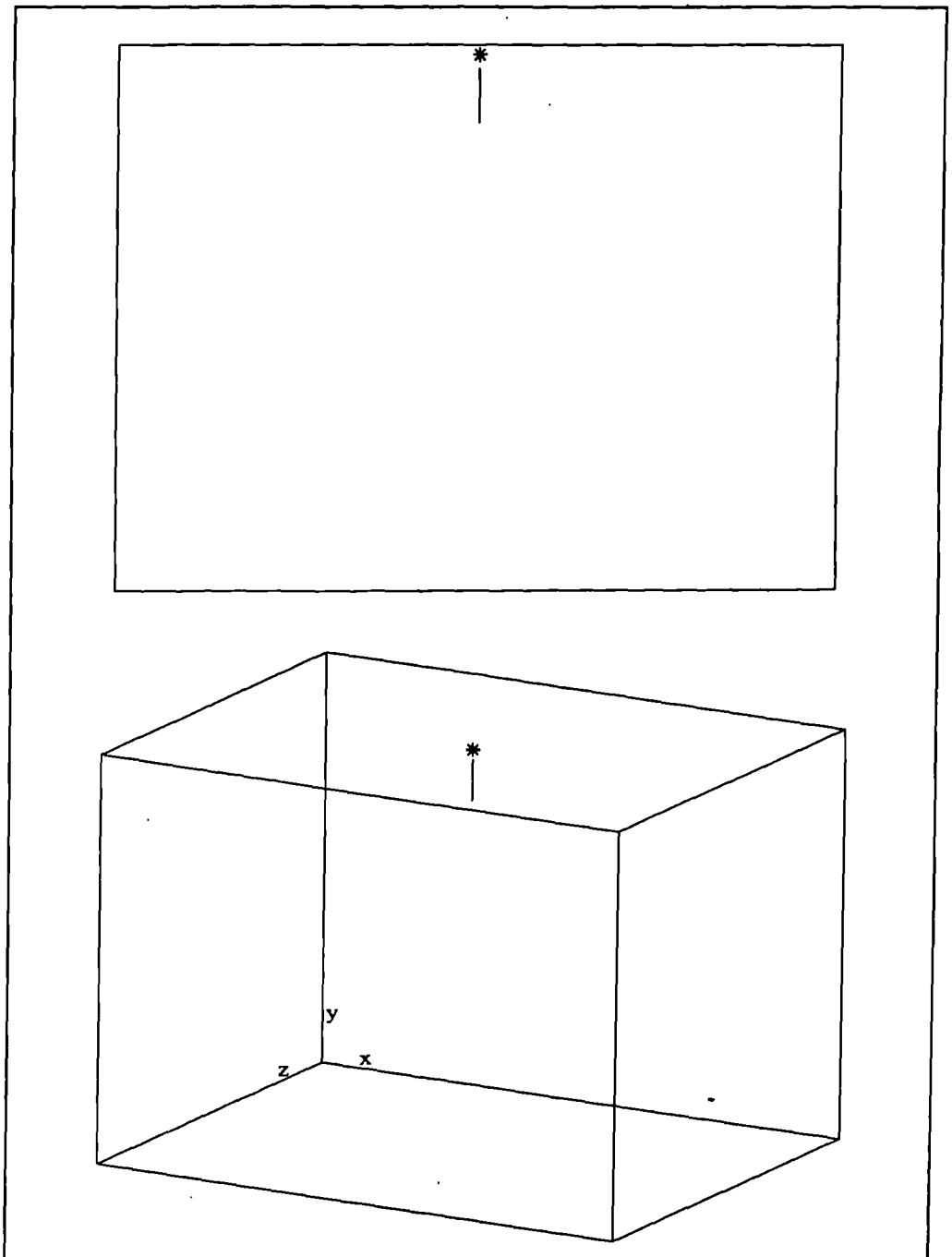

Figure 3.9 The geometrical outline of the problem

§3.3.2 The Equation Set

The CFD code applied in the current research is the CFDS-FLOW3D commercial package. Its main advantage is that the code includes the particle transport model which can be used to trace the particle movement through the space and it can also provide a detailed description of particle routes through the area. In this project, the prediction of particle tracking routes in buildings and ventilation systems is the primary purpose and the most interesting topic after all.

The particle transport model contained in FLOW3D uses the Lagarangian method to split the particle phase into a set of representative sample particles, track these particles through the flow domain of interest. Thus, for the case of single particle settling in a large volume of static air described in this chapter, it can simulate a complete particle deposition process including the acceleration period and the settling period.

For the single particle moving in the infinite static air, only momentum transfer exists between particle and air, the equations of the particle motion are listed as follows:

$$m\frac{dV}{dt} = F - R \qquad (3\text{-}33)$$

$$F = \frac{\pi D_p^3}{6}(\rho_p - \rho)g \qquad (3\text{-}34)$$

$$R = \frac{1}{8}\pi D_p^2 \rho C_D |V_R| V_R \qquad (3\text{-}35)$$

$$C_D = \frac{24}{R_{ep}}\left(1 + 0.15R_{ep}^{0.687}\right) \tag{3-36}$$

$$R_{ep} = \frac{\rho|V_R|D_p}{\mu} \tag{3-37}$$

where m, V, F, R, C_D, D_p, t, ρ, ρ_p, μ have the same meanings as defined in §3.1 and §3.2. R_{ep} is particle Reynolds number. V_R is the relative velocity between the particle and the fluid.

The numerical solutions of the above cases can be obtained by solving these equations by using FLOW3D. FLOW3D involves only one correlation for calculating the drag factor, i.e., equations (3-36) and (3-30). The examination of the deviations caused by this equation will be assessed by comparing the numerical results with the analytical solutions obtained from equation (3-26) for laminar regime and equations (3-27) ~ (3-29) for transition regime, etc.

§3.3.3 The Analysis of Numerical Solutions

The numerical solutions of the cases in Table 3.2 have been obtained by solving equations (3-33) ~ (3-37) using FLOW3D. The results are listed in Table 3.3 as below:

Table 3.3 Numerical results of cases

Case No.	Particle size (μm)	Particle mass (kg)	Particle Reynolds number R_{ep}	Flow regime	Settling velocity u_s (m/s)	Settling time T (s)	Drag factors C_D	Average acceleration (m/s^2)
No. 1	1	5.236E-15	0.00002	Laminar	0.000301	9110.8	1195146.9	0.00000256
No. 2	5	6.545E-13	0.0025	Laminar	0.00751	366.0	9602.77	0.001124
No. 3	8	2.681E-12	0.0102	Laminar	0.0191	144.0	2205.86	0.00729
No. 4	10	5.236E-12	0.0199	Laminar	0.0298	92.3	1219.33	0.0177
No. 5	20	4.189E-11	0.1548	Laminar	0.116	23.8	161.499	0.2613
No. 6	30	1.414E-10	0.4964	Transition	0.248	11.1	52.829	1.0973
No. 7	50	6.545E-10	2.0183	Transition	0.605	4.6	14.78	1.2845
No. 8	100	5.236E-9	11.209	Transition	1.68	1.78	3.8307	2.176

According to Table 3.3, cases 1~5 are located in the laminar zone, while cases 6~8 belong to the transition range. The terminal settling velocity of the particle decreases as the particle size is reduced. The total settling time which is taken by the particle from the starting point to the bottom of the space increases as the particle becomes smaller. This is because the terminal settling velocity of small particles is smaller than that of large particles, so the small particle takes a longer time to go through the same space than the large particle does.

The particle is accelerated at the start of the falling process before its velocity arrives at its terminal velocity (i.e., the balance status of gravitational force and

resistance force), then it maintains constant velocity (i.e., terminal settling velocity) and falls continuously until it arrives at the ground surface of the volume. Finally, the particle velocity reduces to zero rapidly after it hits the ground surface.

From Table 3.3, it can be seen that the average acceleration velocity increases as the particle size increases. This is because the large particle experiences a larger gravitational force (i.e., mg) than that of small particle does at rest and during the deposition periods, while the resistance force depends on the particle velocity and particle properties, i.e., relating to the acceleration speed, so the gravitational force plays a dominant role during the acceleration period. When the resistance force increases to balance the gravitational force, the acceleration stops and the particle moves at constant speed under such a balanced system. So the large particle acquires relative large acceleration velocity.

Table 3.4 lists both the analytical solutions of terminal settling velocities and drag factors of the above cases calculated from equations (3-11), (3-26), (3-27) and (3-31). The comparisons between both data show good consistency. The relative errors between corresponding analytical data and numerical results are defined as follow:

$$\left|\varepsilon_{u_s}\right| = \left|\frac{u_{sa} - u_{sn}}{u_{sa}}\right| \times 100\% \qquad (3\text{-}38)$$

$$\left|\varepsilon_{C_D}\right| = \left|\frac{C_{D_a} - C_{D_n}}{C_{D_a}}\right| \times 100\% \qquad (3\text{-}39)$$

The relative errors between both data become larger as the particle size increases in the laminar region. This is because the role of the second term in equation (3-36) becomes more important as R_{ep} increases. It also increases the deviations between equation (3-26) and (3-36) and finally influences the terminal settling velocity. The errors in the transition regime become random because there is no regular relation between the drag factor C_D and particle Reynolds number R_{ep}.

Table 3.4 Comparison of analytical solutions and numerical results

Case No.	Analytical data u_{sa} (m/s)	Numerical results u_{sn} (m/s)	Relative error ε_{us} (%)	Analytical solution C_{Da}	Numerical results C_{Dn}	Relative error ε_{CD} (%)
1 (1μm)	3.007E-4	3.01E-4	0.0998	1196216.3	1195146.9	0.0908
2 (5μm)	7.5184E-3	7.51E-3	0.1117	9561.753	9602.776	0.429
3 (8μm)	1.925E-2	1.91E-2	0.7792	2335.7298	2205.86	1.4338
4 (10μm)	3.007E-2	2.98E-2	0.8979	1196.216	1219.326	1.93
5 (20μm)	1.203E-1	1.16E-1	3.5744	149.502	161.499	8.0248
6 (30μm)	2.517E-1	2.48E-1	1.47	51.1706	52.8294	3.2417
7 (50μm)	6.097E-1	6.05E-1	0.7709	14.5464	14.7806	1.61
8 (100μm)	1.6455	1.68	2.0966	3.996	3.8307	4.1366

According to engineering principles, the above errors can be ignored. The numerical simulation results of the above solid particle settling cases are quite satisfactory. It can be concluded that the particle transport model in FLOW3D can predict particle movement efficiently and correctly. The detailed numerical results can be found in Appendix A. Figure 3.10 presents the comparison of analytical solutions with numerical data. The tracking route of particle with size of 10μm has been shown in figure 3.11.

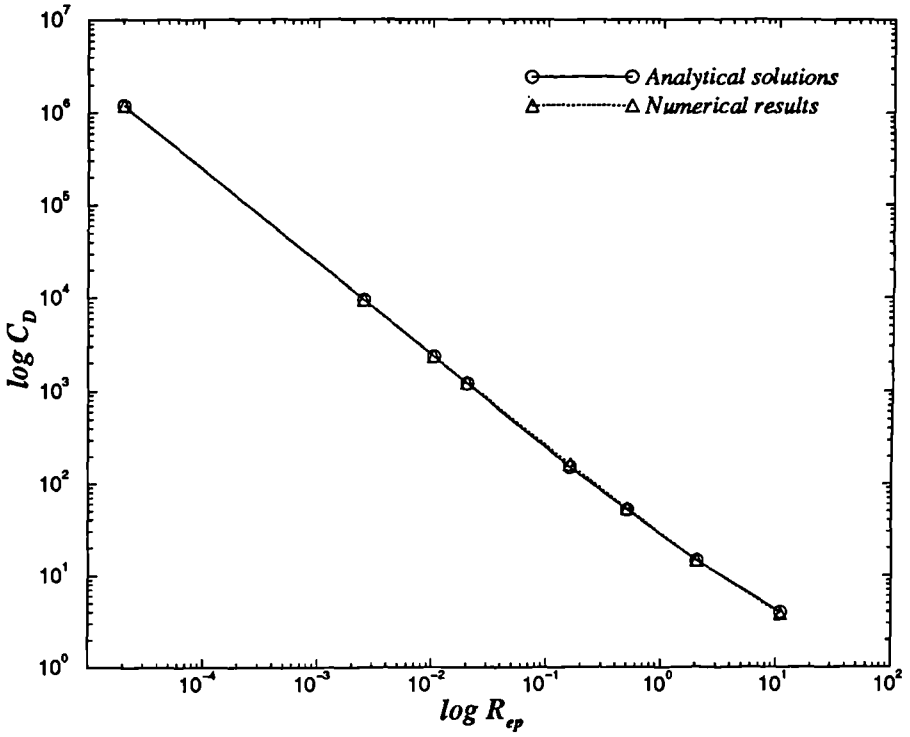

Figure 3.10 Comparison of analytical solutions with numerical results

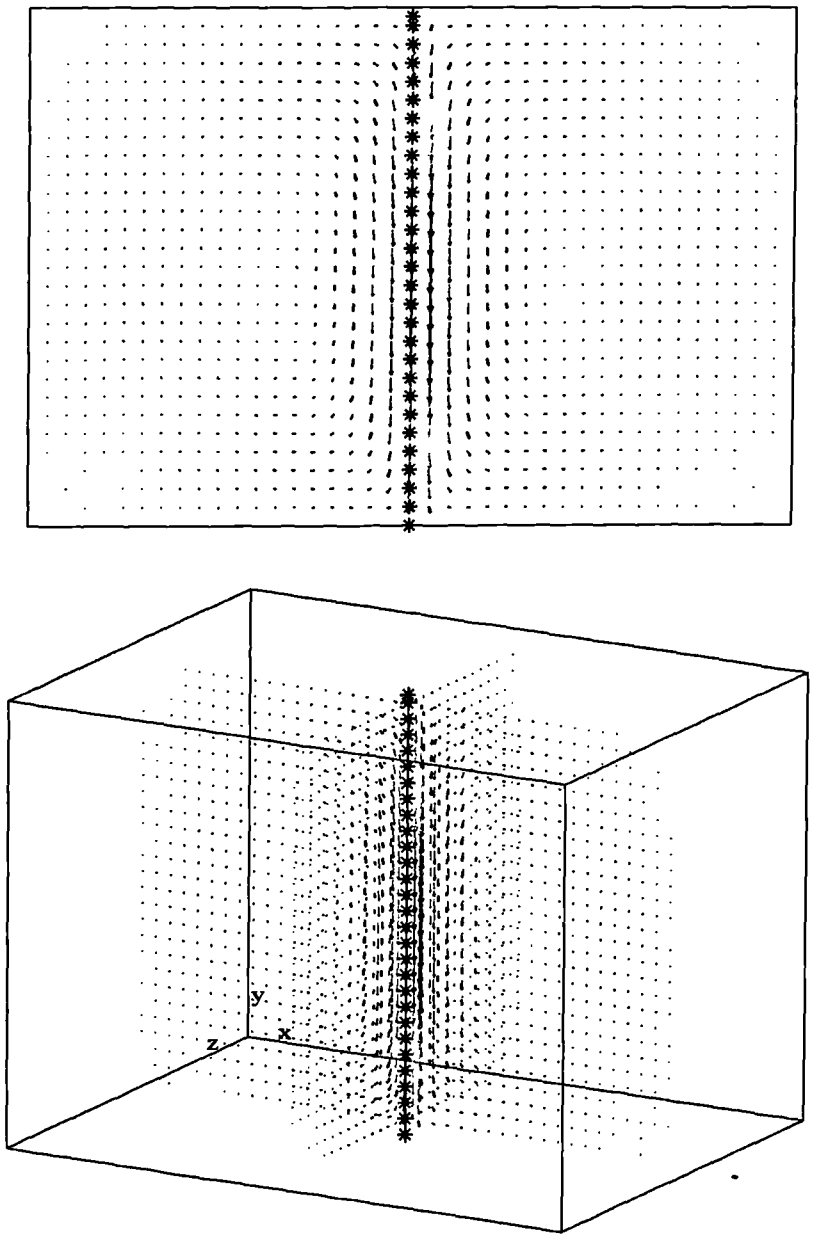

Vector scale: → 1E-4 m/s

Figure 3.11 One lead particle deposition route in stagnant air (d_p=10μm)

§3.4 Conclusions

Stokes theory of the particle deposition process through stagnant fluid has been described in this chapter. A numerical model, i.e., particle transport model, for predicting such phenomena is also presented here. The comparisons between analytical solutions and numerical results have show good agreement. It can be concluded as follows:

1. The particle free deposition process is strongly related to the properties of particle and fluid surrounded;
2. The terminal settling velocity of particle is mainly dependent on the particle size;
3. The gravitational force dominates the particle deposition process, especially in the acceleration periods. The drag force is proportional to the particle velocity and arrives a balance status to the gravity when the particle velocity reaches its terminal settling velocity;
4. The particle transport model is able to simulate the particle deposition process, the numerical results are well consistent with the analytical solutions;
5. Particle settling phenomenon is a basic process of particle movement. As mentioned at the beginning of the chapter, particle deposition procedure strongly influences the particle concentration in building and ventilation systems and further more affects the indoor environment;
6. Particle transport model provides a useful method to analyse the particle deposition, migration and distribution in buildings and ventilation systems.

CHAPTER IV

MATHEMATICAL DESCRIPTION

Abstract

This Chapter is devoted to the theory and solutions of Computational Fluid Dynamics. The basic theory of fluid mechanics, Eulerian and Lagrangian methods, has been described in this chapter. A detailed mathematical description of fluid flow, both laminar and turbulent, has been given in §4.2. The model will be used for simulating the air movement in ventilation systems. Discussions and comparisons of several turbulence models are proceeded herein. A step-by-step CFD numerical solution procedure, including a description of integration, discretisation, differencing schemes and their comparisons, linearization of source terms, pressure-velocity coupling process, implementation of boundary conditions, SIMPLE and SIMPLEC algorithms, and convergence criterion and control techniques, has also been provided in this chapter. A particle transport model, the Lagrangian tracking method, is proposed for tracking the individual contaminant particle movements in ventilation spaces. The corresponding coupling simulation process between continuous phase and particle phase is employed for the fluid-particle iterations. It can be concluded that the CFD technique, state-of-the-art in engineering, is an effective and less costly method of predicting complicated fluid flow phenomena and can be applied to simulate the air and pollutant movements in building engineering. In the current research, both the continuous fluid flow model and the particle transport model are employed in modelling the airflow patterns and particle movements in buildings and ventilation spaces.

§4.1 Fluid Motion and Its Description

This section is devoted to the description of Computational Fluid Dynamics method and its solutions. The basic theory of fluid mechanics and the descriptions of fluid flow are also presented in this section (Launder, et al., 1974, 1989; Patankar, et al. 1972, 1980; Spalding, 1982; CFDS-FLOW3D menu, 1993). Both Eulerian and Lagragian methods are described herein.

§4.1.1 Methods of Defining Fluid

The so-called ' fluid ' (liquid or gas) is composed of a large number of molecules. The physical properties of a fluid are not continuously distributed in space and time because spaces exist between these molecules from a microscopic view. However, the basic unit of space studied in fluid mechanics (i.e., the bulk properties), is much larger than the average aspect of molecular motions, so a continuum hypothesis is introduced to the area of fluid mechanics. It implies the postulate: ' Matter is continuously distributed throughout the region under consideration with a large number of molecules even in macroscopically small volumes ' (Warsi, 1993).

Such a hypothesis assumes that the body of fluid under consideration forms a physical continuum. A physical continuum is a medium filled with a continuous matter such that every part of the medium, however small, is itself a continuum

and entirely filled with the matter. The hypothesis implies that a very small volume will contain a large number of molecules. For example, 1 cm^3 air contains 2.687×10^{19} molecules under normal conditions. So the continuum method of defining fluid is valid for an actual fluid only when the variation of the fluid properties in space is negligible over distances of the order of the average distance between molecules. In most cases, however, an ordinary fluid can be treated as a continuum, or a substance whose properties vary continuously from point to point in space.

Another concept that is very useful in fluid mechanics is the fluid particle. It can be considered to consist of the fluid contained inside an element of volume that is so tiny that the properties of the fluid within it are essentially constant over the entire element. The dimensions of the element are assumed to be so small that the moment of inertia of the particle about any direction passing through it is negligible, and it, therefore, behaves dynamically like the " point mass " of elementary mechanics. Often it is convenient to treat a finite, or " macroscopic ", mass of fluid as a collection of fluid particles whose properties vary in space, and which remain in unbroken contact with one another according to continuum theory as the macroscopic mass of fluid deforms. Fluid Dynamics, a branch of Fluid Mechanics, studies the motion of fluid particles or a collection of such particles and their physical properties varying with space and time.

§4.1.2. Lagrangian and Eulerian Descriptions

1. The motion of fluid particle

Fluid motion can be described in terms of the motion of fluid particles. A convenient way of describing the motion of a fluid particle is in terms of a position vector defined with respect to, e.g., a Cartesian co-ordinate system, as shown in Figure 4.1. The position of the particle is specified by the vector **r** with its tail at the origin of the co-ordinate system and its head at the point occupied by the particle.

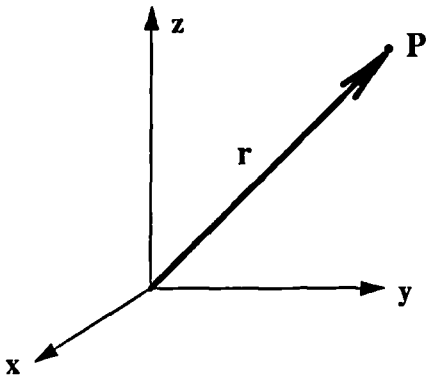

Figure 4.1 Position vector locating a fluid particle

For a given particle, **r** is a function of time unless the particle is stationary, in which case **r** is constant. The basic kinematic definition of the velocity of a point is that it is the time rate of change of the position vector of the point. In this case the velocity V of the fluid particle is defined by the relation:

$$\mathbf{V} = \frac{d\mathbf{r}}{dt} \tag{4-1}$$

in which

$$\frac{d\mathbf{r}}{dt} = \lim_{\Delta t \to 0} \frac{\mathbf{r}(t+\Delta t) - \mathbf{r}(t)}{\Delta t} \tag{4-2}$$

Similarly, the acceleration **a** of the particle is specified by

$$\mathbf{a} = \frac{d\mathbf{V}}{dt} \tag{4-3}$$

or

$$\mathbf{a} = \frac{d^2\mathbf{r}}{dt^2} \tag{4-4}$$

In terms of their components,

$$\mathbf{r} = x\mathbf{i}_x + y\mathbf{i}_y + z\mathbf{i}_z \tag{4-5}$$

$$\mathbf{V} = \frac{dx}{dt}\mathbf{i}_x + \frac{dy}{dt}\mathbf{i}_y + \frac{dz}{dt}\mathbf{i}_z \tag{4-6}$$

or

$$\mathbf{V} = u\mathbf{i}_x + v\mathbf{i}_y + w\mathbf{i}_z \tag{4-7}$$

and

$$\mathbf{a} = \frac{d^2x}{dt^2}\mathbf{i}_x + \frac{d^2y}{dt^2}\mathbf{i}_y + \frac{d^2z}{dt^2}\mathbf{i}_z \tag{4-8}$$

or

$$\mathbf{a} = \frac{du}{dt}\mathbf{i}_x + \frac{dv}{dt}\mathbf{i}_y + \frac{dw}{dt}\mathbf{i}_z \tag{4-9}$$

Here x(t), y(t) and z(t) are the co-ordinates of the fluid particle or the components of the position vector; u, v and w are the components of the velocity vector; and $\mathbf{i}_x$, $\mathbf{i}_y$ and $\mathbf{i}_z$ are unit vectors pointing in the positive directions along the three co-ordinates axes.

2. Lagrangian and Eulerian Methods

Two principle methods for studying the motion of a fluid flow field, or volume of space filled with moving fluid, have been developed.

The Lagrangian method is essentially a study of the individual fluid particles as they move. The general position vector **r** for the flow field is considered to depend both on the particular fluid particle with which it is associated and on time. This dependence can be expressed mathematically as

$$\mathbf{r} = \mathbf{r}(\mathbf{r}_0, t) \tag{4-10}$$

The position vector is related to a specific particle as follows: At an " initial " time t_0 the position vector of each particle is defined as $\mathbf{r}_0$, so that at any following time t a given particle can be specified by the value $\mathbf{r}_0$ of the position vector it had at the initial time t_0. Thus the general position vector **r** is expressed in Equation (4-10) as a function of $\mathbf{r}_0$ as well as of time t. Similarly, the dependence of any general scalar function of the flow and any general vector flow property **c** on the particle with which they are associated and on time can be expressed by the relations:

$$f = f(\mathbf{r}_0, t) \tag{4-11}$$

and

$$\mathbf{c} = \mathbf{c}(\mathbf{r}_0, t) \tag{4-12}$$

Any description of fluid motion using the Lagrangian method $\mathbf{r} = \mathbf{r}(\mathbf{r}_0, t)$ is called a description in the sense of Lagrange.

Although the Lagrangian method of treating fluid flow is appropriate in some situations, in many cases it is desired not to know flow properties associated with individual particles, but rather to find values of these properties at different points in space. The Eulerian method of treating fluid flows considers flow properties depend on points in space and time. According to this, the dependence of a general scalar flow property and a general vector flow property **c** on space and time can be expressed as functions of location in space and of time by the following equations:

$$f = f(x,y,z,t) \tag{4-13}$$

and

$$\mathbf{c} = \mathbf{c}(x,y,z,t) \tag{4-14}$$

in which x, y and z are the Cartesian co-ordinates of a point in space. The descriptions presented in equations (4-13) and (4-14) are called in the sense of Euler.

In a given flow situation, the determination, by experiment or theory, of the properties of the fluid as a function of position in space and of time is considered to be the solution to the problem. In many cases, the emphasis is on the space-time distribution of the fluid properties. So the Eulerian method is used nowadays much more widely than the Lagrangian method. In general, the Eulerian method is normally applied to describe a continuous fluid flow, while the Lagrangian method is used when one wants to study the individual particle motion in a space. In the current project, both Eulerian and Lagrangian methods will be applied for simulation of fluid flow fields and aerosol particles tracking through such flow fields.

§4.2 Mathematical Description of Fluid Flows

A detailed mathematical model for describing the continuous fluid flows will be presented in this section. The turbulence models, which are applied to solve the turbulent characters in relevant turbulent regime, will also be described herein. Computational Fluid Dynamics methods, referred to as the state-of-the-art of engineering, will be introduced in this section.

§4.2.1 The General Governing Equation

All fluid flows, regardless of how complex they are, follow the fundamental conservation laws of mass, momentum and energy. The governing equations for fluid flow are described by the Navier-Stokes equations, which essentially are conservation of mass, Newton's second law of motion (momentum conservation), and conservation of energy. All equations are partial differential equations. If the dependent variable is denoted by Φ, then these equations take the following general form:

$$\frac{\partial(\rho\Phi)}{\partial t} + \mathrm{div}(\rho U\Phi) - \mathrm{div}(\Gamma_\Phi \nabla\Phi) = S_\Phi \qquad (4\text{-}15)$$

$$\Downarrow \qquad \Downarrow \qquad \Downarrow \qquad \Downarrow$$

transient convection diffusion source

where ρ, U, Γ_Φ and S_Φ denote the fluid density, the fluid velocity, the diffusion coefficient and the source term, respectively. The four terms in the general

equation are called the transient term, the convection term, the diffusion term, and the source term. The dependent variable Φ can stand for a variety of different quantities, such as mass fraction of a chemical species, a velocity component, the turbulence kinetic energy, or the turbulence energy dissipation rate. Accordingly, for each of these variables, an appropriate meaning will have to be given to the diffusion coefficient Γ_ϕ and the source term S_ϕ.

Equation (4-15) is also called ' the general transport equation '. The dependent variable, Φ, varies when solving different physical processes such as momentum transfer (i.e., velocity u, v, w), heat transfer (i.e., enthalpy H or temperature T), turbulence scales (i.e., k and ε), etc. The convection and diffusion terms are identical for all the transport equations. This characteristic of the transport equations is extremely useful when the equations are discretised (reduced to algebraic equations) and solved numerically since only a solution of the general equation (4-15) is required. As a consequence, it is sufficient to write a general programme of instructions for solving equation. (4-15), which can be repeatedly used for different meanings of Φ along with appropriate expressions for Γ_ϕ and S_ϕ, and, of course, with appropriate initial and boundary conditions. It also provides the possibility of the formulation of a general numerical method and the development of a general purpose computer program, e.g., the CFDS-FLOW3D code is such a general program which can be used to solve various types of fluid flow problems. This code is employed in the current research.

§4.2.2 The Equation Set of Laminar Flow

In this section, the basic equations for the laminar fluid flow based on the above mentioned conservation laws will be presented. All equations will be written both in conservation forms and in index notation in Cartesian co-ordinate system.

The equation set of laminar fluid flow are composed of equations of mass, momentum and, if a non-isothermal flow, energy. These are:

continuity equation
$$\frac{\partial \rho}{\partial t} + \nabla \cdot (\rho \mathbf{U}) = 0 \qquad (4\text{-}16)$$

momentum equation
$$\frac{\partial (\rho \mathbf{U})}{\partial t} + \nabla \cdot (\rho \mathbf{U} \times \mathbf{U}) = \nabla \cdot \sigma + \mathbf{B} \qquad (4\text{-}17)$$

$$\sigma = -p\delta + \mu \left[\nabla \mathbf{U} + (\nabla \mathbf{U})^{T} \right] \qquad (4\text{-}18)$$

energy equation
$$\frac{\partial (\rho H)}{\partial t} + \nabla \cdot (\rho \mathbf{U} H) - \nabla \cdot (\lambda \nabla T) = \frac{\partial p}{\partial t} \qquad (4\text{-}19)$$

where H is the total enthalpy, given in terms of the static (thermodynamic) enthalpy h by:

$$H = h + \frac{1}{2} U^{2} \qquad (4\text{-}20)$$

Here, the definitions of parameters appeared in equations (4-16) ~ (4-20) can be seen in nomencluture.

Equations (4-16) ~ (4-19) include the unknowns **U**, p, T, h, ρ. They are completed by adding two algebraic equations from thermodynamics, the equation of state, relating density to temperature and pressure,

$$\rho = \rho(p, T) \tag{4-21}$$

and the constitutive equation, relating static enthalpy to temperature and pressure,

$$h = h(p, T) \tag{4-22}$$

The above transport equations (4-16) ~ (4-19) are written in co-ordinate free tensor notation. Its main advantage is that it is independent of co-ordinate system. The relevant computations of saclars, vectors and tensors are listed in Appendix B. For completeness, the forms of the main transport equations in Cartesian co-ordinate system are also given below (in index notation):

$$\frac{\partial \rho}{\partial t} + \frac{\partial}{\partial x_i}(\rho U_i) = 0 \tag{4-23}$$

$$\frac{\partial (\rho U_j)}{\partial t} + \frac{\partial}{\partial x_i}(\rho U_i U_j) = \frac{\partial \sigma_{ij}}{\partial x_i} + B_j \tag{4-24}$$

$$\sigma_{ij} = -p\delta_{ij} + \mu\left(\frac{\partial U_j}{\partial x_i} + \frac{\partial U_i}{\partial x_j}\right) \tag{4-25}$$

$$\frac{\partial (\rho H)}{\partial t} + \frac{\partial}{\partial x_i}\left(\rho U_i H - \lambda \frac{\partial T}{\partial x_i}\right) = \frac{\partial p}{\partial t} \tag{4-26}$$

(N. T. Here, summation is used that repeated indices are summed over).

Equations (4-17) and (4-18) can be written as a convection-diffusion equation:

$$\frac{\partial(\rho \mathbf{U})}{\partial t} + \nabla \cdot (\rho \mathbf{U} \times \mathbf{U} - \mu \nabla \mathbf{U}) = -\nabla p + \nabla \cdot \left[\mu (\nabla \mathbf{U})^T\right] + \mathbf{B} \qquad (4\text{-}27)$$

All terms at the r.h.s. belong to the source term, and can be represented by one symbol S_Φ.

The term B represents many forms of the body forces wherever they are available, e.g., buoyancy force $\mathbf{B} = \rho_o \mathbf{g} + (\rho - \rho_o)\mathbf{g}$ for non-isothermal flow (where ρ_o is the reference density), rotational forces (Coriolis and centrifugal forces) $\mathbf{B}=-2\rho\omega\times\mathbf{U}-\rho\omega\times\omega\times\mathbf{r}$ for a flow in a rotating system (where ω is the angular velocity of the rotation about a fixed axis, $\mathbf{r}$ is the distance to the axis), resistance forces $\mathbf{B} = -\mathbf{R} \cdot \mathbf{U}$ obtained from a flow in a porous resistive material (where $\mathbf{R}$ is a resistance to flow in porous medium), etc. Any of these body forces may be used in combination wherever they co-exist in the flow phenomena.

The general governing equation can also be written in index notation in Cartesian co-ordinate system by:

$$\frac{\partial(\rho\Phi)}{\partial t} + \frac{\partial}{\partial x_i}\left(\rho U_i \Phi - \Gamma_\Phi \frac{\partial \Phi}{\partial x_i}\right) = S_\Phi \qquad (4\text{-}28)$$

For laminar flow, the diffusive coefficient Γ_Φ is the molecular viscosity μ which is a physical property of fluid.

A detailed mathematical description of laminar fluid flow has been given in this section. In practice, Most flow phenomena encountered belong to turbulent regime. It is required to establish a mathematical model for presenting the turbulent fluid flow.

The principals applied in the study of turbulent flow are still based on the conservations of mass, momentum and energy. It should be emphasised that the equations for ' laminar flow ' are, in fact, valid for turbulent flow as well. Turbulent flows are just very complex unsteady laminar flows. The detailed discussion about turbulent flows will be given in next section.

§4.2.3 Equation Set for Turbulent Flow

Although laminar flow theory found some applications in practice, the most prevalent forms of fluid flow in nature are found to be turbulent flows. Turbulent flows are extremely complex time-dependent flows. It is characterised by the appearance of random almost chaotic fluctuations in the flow. Contrary to laminar flow, which is believed to be understood exactly, turbulent flow is too complicated to describe exactly and still needs to be studied.

I. Definition of Turbulence

The emergence of turbulence is still a big issue in fluid dynamics and is not yet fully understood. But it is believed that turbulence is generated mainly by shear which is causing an overproduction of vorticity if the Reynolds number is sufficiently high. It is also believed that the transition from laminar to turbulent flow is an instability phenomenon and that turbulent flow is generally unstable.

Taylor (1936) and von Kármán (1937) gave the following definition: ' Turbulence is an irregular motion which in general makes its appearance in fluids, gaseous or liquid, when they flow past solid surface or even when neighbouring streams of the same fluid flow past or over one another '. According to this definition, the turbulent flow has to satisfy the condition of irregularity.

Indeed, such irregularity is a very important feature. Because of this, it is impossible to describe the motion in all details as a function of time and space co-ordinates. But, fortunately, turbulent motion is irregular in the sense that it is possible to describe it by laws of probability. It appears possible to indicate distinct average values of various quantities, such as velocity, pressure, temperature, etc., and this is very important. Therefore, it is not sufficient just to say that turbulence is an irregular motion and to leave it at that. Perhaps a definition might be formulated somewhat more precisely as follows: ' Turbulent fluid motion is an irregular condition of flow in which the various quantities show a random variation with time and space coordinates, so that statistically distinct average values can be discovered ' (Hinze, 1975).

The following is a list of characters which every turbulent flow phenomenon experiences:

- A turbulent flow field is a random field;
- Turbulence is a continuum phenomenon;
- Turbulence is diffusive. Because of this property the rates of mass and momentum transfer are much higher in turbulent flow than in laminar flow;
- Turbulence is dissipative. This is an inherent dissipative mechanism in a turbulence field which means a continuous process of large-scale eddies breaking into small-scale eddies, small-scale eddies split apart into smaller-scale eddies and so on. It must, however, be stated that practically the main energy dissipation of turbulence takes place through the breaking procedures of small- and smaller-scale eddies due to the viscosity effect;
- Turbulence is always three-dimensional.

The above characters are important for a flow to be classified as a turbulent flow. Added to these properties is that, no matter how complex the turbulent flow is, it is at least deterministic and governed by the basic equations of fluid dynamics.

II. The Reynolds-averaged Method

Because of the random behaviour of a turbulent field, we have to devise an averaging process to obtain deterministic quantities from some available experimental or theoretical data. A natural averaging procedure is the one which requires the use of a probability function (i.e., statistical approach). The approach looks upon an ensemble of averaging over a period of time. Corresponding to the approach, Reynolds proposed that the instantaneous variable of turbulent flow may be regarded as a mean and a fluctuating part:

$$\Phi = \overline{\Phi} + \phi' \tag{4-29}$$

where Φ is the instantaneous variable, $\overline{\Phi}$ is the mean part, ϕ' is a fluctuating part.

The Reynolds-averaging quantity can be expressed as follows:

$$\overline{\Phi}_{(t)} = \frac{1}{2\delta t}\int_{t-\delta t}^{t+\delta t}\Phi_{(\tau)}d\tau \tag{4-30}$$

Here, δt is the time scale of averaging period, which is chosen large enough relative to the time scale of turbulence fluctuations and small enough relative to the time scale of fluid flow. We can easily see that Reynolds averaging has the following properties:

a. $\overline{\Phi}=\overline{\Phi}$, $\phi'=0$

b. $\overline{a\Phi+b\Psi}=a\overline{\Phi}+b\overline{\Psi}$, a, b are constants.

c. $\overline{\Phi\Psi}=\overline{\Phi}\,\overline{\Psi}+\overline{\phi'\psi'}$

d. $\overline{\frac{\partial\Phi}{\partial t}}=\frac{\partial\overline{\Phi}}{\partial t}$, $\overline{\frac{\partial\Phi}{\partial x_i}}=\frac{\partial\overline{\Phi}}{\partial x_i}$

For the simplicity, we drop the bars from Reynolds averaged mean quantities for all primitive variables throughout the thesis.

No matter how complicated the turbulent flow is, the flow still follows the basic laws of Fluid Dynamics and can be described by the general governing equation (4-28). For turbulent flow, the dependent variable, Φ, in that equation means the instantaneous turbulent variable.

Applying Reynolds-averaging method to equation (4-28), we obtain:

continuity:
$$\frac{\partial\rho}{\partial t}+\frac{\partial}{\partial x_i}\left[\rho\overline{(U_i+u_i')}\right]=0$$

$$\frac{\partial\rho}{\partial t}+\frac{\partial}{\partial x_i}(\rho U_i)=0 \qquad (4\text{-}31)$$

or
$$\frac{\partial\rho}{\partial t}+\nabla\cdot(\rho U)=0 \qquad (4\text{-}31)'$$

momentum:
$$\frac{\partial\left[\rho\overline{(U_i+u_i')}\right]}{\partial t}+\frac{\partial}{\partial x_i}\left[\rho\overline{(U_i+u_i')(U_i+u_i')}\right]$$

$$-\frac{\partial}{\partial x_i}\left\{\mu\left[\frac{\partial\overline{(U_i+u_i')}}{\partial x_j}+\frac{\partial\overline{(U_j+u_j')}}{\partial x_i}\right]\right\}=-\frac{\partial\overline{(P+p')}}{\partial x_i}+B_i$$

$$\frac{\partial(\rho U_i)}{\partial t}+\frac{\partial}{\partial x_i}(\rho U_i U_j)-\frac{\partial}{\partial x_i}\left[\mu\left(\frac{\partial U_i}{\partial x_j}+\frac{\partial U_j}{\partial x_i}\right)-\rho\overline{u_i' u_j'}\right]=-\frac{\partial P}{\partial x_i}+B_i \quad (4\text{-}32)$$

or $$\frac{\partial(\rho U)}{\partial t}+\nabla\cdot(\rho U\times U)-\nabla\cdot\left[\mu\left(\nabla U+(\nabla U)^T\right)-\rho\overline{u'\otimes u'}\right]=-p\,\delta+B \quad (4\text{-}32)'$$

scalar transport: $$\frac{\partial\left[\rho\overline{(\Phi+\phi')}\right]}{\partial t}+\frac{\partial}{\partial x_i}\left[\rho\overline{(U_i+u_i')(\Phi+\phi')}\right]$$

$$-\frac{\partial}{\partial x_i}\left[\Gamma_\Phi\frac{\partial\overline{(\Phi+\phi')}}{\partial x_i}\right]=S_\Phi$$

$$\frac{\partial(\rho\Phi)}{\partial t}+\frac{\partial}{\partial x_i}(\rho U_i\Phi)-\frac{\partial}{\partial x_i}\left[\Gamma_\Phi\frac{\partial\Phi}{\partial x_i}-\rho\overline{u_i'\phi'}\right]=S_\Phi \quad (4\text{-}33)$$

or $$\frac{\partial(\rho\Phi)}{\partial t}+\nabla\cdot(\rho U\Phi)-\nabla\cdot\left(\Gamma_\Phi\nabla\Phi-\rho\overline{u'\phi'}\right)=S_\Phi \quad (4\text{-}33)'$$

In equation (4-33) or (4-33)', Φ could represents enthalpy (non-isothermal flow), concentration (chemical species), and mass fraction (multi-phase flow), etc.

Comparing the Reynolds-averaged equations with the equation set of laminar flow, we can see that the Reynolds-averaged continuity equation is the same as the equation that has not been averaged. However, the momentum and scalar transport equations contain turbulent flux terms additional to the molecular diffusive fluxes. These are the

$$\text{Reynolds stress} = \sigma_{stress} = \rho\overline{u'\otimes u'} \quad (4\text{-}34)$$

and the $$\text{Reynolds flux} = \sigma_{flux} = \rho\overline{u'\phi'} \quad (4\text{-}35)$$

It should be noted that these terms arise from the non-linear convection term in the non-averaged equations, not the linear diffusion one. They reflect the fact that convective transport due to turbulent velocity fluctuations will act to enhance mixing over and above that caused by thermal fluctuation at the molecular level. At high Reynolds numbers, turbulent velocity fluctuations occur over a length scale much larger than that the molecular fluxes.

The Reynolds-averaged energy equation is as below:

$$\frac{\partial(\rho H)}{\partial t}+\frac{\partial}{\partial x_i}\left(\rho U_i H+\rho\overline{u_i' h'}\right)-\frac{\partial}{\partial x_i}\left(\lambda\frac{\partial T}{\partial x_i}\right)=\frac{\partial p}{\partial t} \qquad (4\text{-}36)$$

or

$$\frac{\partial(\rho H)}{\partial t}+\nabla\cdot\left(\rho UH+\rho\overline{u'h'}-\lambda\nabla T\right)=\frac{\partial p}{\partial t} \qquad (4\text{-}36)'$$

where the mean total enthalpy is given by

$$H=h+\frac{1}{2}U_i^2+\frac{1}{2}\overline{u_i' u_i'} \qquad (4\text{-}37)$$

Note that the total enthalpy contains a contribution from the turbulent kinetic energy, $k=\frac{1}{2}\overline{u_i' u_i'}$, as well as the mean flow kinetic energy.

Now we have obtained the equation set of turbulent fluid flow, equations (4-31) or (4-31)′, (4-32) or (4-32)′, (4-33) or (4-33)′, (4-36) or (4-36)′, by using Reynolds-averaging method. As seen these equations are similar to equations(4-23) ~ (4-26) and (4-28). The equations for conservation of mass for is exactly the same while the equations for conservation of momentum, energy and scalar have additional second order tensor term, i.e., Reynolds

stresses and Reynolds fluxes. That means for solving turbulent flows, we need to establish extra equations to solve these unknown turbulent tensor terms.

§4.2.4 Turbulence Models

The Reynolds-averaging method introduces more unknown terms, i.e., Reynolds stresses and Reynolds flux tensors, to the basic equation set. In Cartesian co-ordinate systems, equations (4-34) and (4-35) can be expressed as follows:

$$\sigma_{stress} = \rho\overline{\mathbf{u}'\otimes\mathbf{u}'} = \begin{bmatrix} \rho\overline{u'u'} & \rho\overline{u'v'} & \rho\overline{u'w'} \\ \rho\overline{v'u'} & \rho\overline{v'v'} & \rho\overline{v'w'} \\ \rho\overline{w'u'} & \rho\overline{w'v'} & \rho\overline{w'w'} \end{bmatrix} \tag{4-38}$$

and

$$\sigma_{flux} = \rho\overline{u'\phi'} = \begin{bmatrix} \rho\overline{u'\phi'} & 0 & 0 \\ 0 & \rho\overline{v'\phi'} & 0 \\ 0 & & \rho\overline{w'\phi'} \end{bmatrix} \tag{4-39}$$

Equations (4-31) or (4-31)′, (4-32) or (4-32)′, (4-33) or (4-33)′ constitute a set of equations which describe turbulent flows, but it is not possible to solve the set of equations because the appearance of the velocity fluctuations, i.e., the above Reynolds stresses and fluxes, make the set incomplete. In order to be able to solve the set of equations it must be made complete by a model of the stresses. This type of turbulence model is described as closure modelling. The closure modelling can, at present, be divided into two groups: x-equation

models and Reynolds stress models. x-equation models are also called eddy-viscosity turbulence models.

I. Boussinesq Approximation

All x-equation turbulence models are based on the famous Boussinesq approximation which first related the Reynolds stresses to a turbulent viscosity which, in contrast to the molecular viscosity, is not a fluid property but depends on the nature of the turbulence. Boussinesq (1877) assumed that the turbulent stresses are proportional to the mean velocity gradients (Rodi, 1980):

$$-\rho\overline{\mathbf{u}'\otimes\mathbf{u}'} = -\frac{2}{3}\rho k\,\delta + \mu_t\left[\nabla\mathbf{U} + (\nabla\mathbf{U})^T\right] \qquad (4\text{-}40)$$

Here μ_t is an additional viscosity, called the eddy viscosity or the turbulent viscosity.

Boussinesq approximation (i.e., eddy viscosity hypothesis) means that the Reynolds stresses can be linearly related to the mean velocity gradients in a manner analogous to the relationship between the stress and strain tensors in laminar Newtonian flow. The basic idea behind the Boussinesq approximation is, as stated above, the analogy between molecular motion and motion of the eddies. This idea cannot be fully correct simply because there is a conceptional difference between turbulence and small ' lumps ' of fluid exchanging momentum. Nevertheless, equation (4-40) has been proven to work well in many flow situations.

Similar to the eddy viscosity hypothesis, we have the eddy diffusivity hypothesis, that Reynolds fluxes of a scalar are linearly related to the mean scalar gradient:

$$-\rho\overline{u'\phi'} = \Gamma_t \Phi \tag{4-41}$$

Here, Γ_t is the eddy diffusivity and defined as below:

$$\Gamma_t = \frac{\mu_t}{\sigma_t} \tag{4-42}$$

where σ_t is the turbulent Prandtl number for Φ.

Subject to these hypotheses, the Reynolds-averaged momentum and scalar transport equations become:

$$\frac{\partial(\rho U)}{\partial t} + \nabla\cdot(\rho U \otimes U) - \nabla\cdot\left\{\mu_{eff}\left[\nabla U + (\nabla U)^T\right]\right\} = -\nabla p' + B \tag{4-43}$$

and

$$\frac{\partial(\rho\Phi)}{\partial t} + \nabla\cdot(\rho U\Phi - \Gamma_{eff}\nabla\Phi) = S \tag{4-44}$$

where μ_{eff} is the effective viscosity, and Γ_{eff} is the effective diffusivity, defined by:

$$\mu_{eff} = \mu + \mu_t, \qquad \Gamma_{eff} = \Gamma + \Gamma_t \tag{4-45}$$

and p' is a modified pressure, defined by:

$$p' = p + \frac{2}{3}\rho k \tag{4-46}$$

Similarly, the Reynolds-averaged energy equation becomes (by introducing $\lambda\nabla T = \frac{\lambda}{C_p}\nabla H$):

$$\frac{\partial(\rho H)}{\partial t}+\nabla\cdot(\rho UH)-\nabla\cdot\left[\left(\frac{\lambda}{C_p}+\frac{\mu_t}{\sigma_H}\right)\nabla H\right]=\frac{\partial p}{\partial t} \qquad (4\text{-}47)$$

where σ_H is the turbulent Prandtl number for H.

By introducing the Boussinesq approximation, the task is reformulated to, instead of finding the Reynolds stresses, to finding the turbulent viscosity. A number of such models has been developed by different researchers and some of them will be discussed in the following paragraphs.

II. Prandtl Mixing Length Model (Zero-equation Model)

The Prandtl mixing length hypothesis was one of the first models of turbulent viscosity. Prandtl (Warsi, 1993) assumed that turbulent viscosity mainly resulted from the mean flow shear stress and can be represented by (in Cartesian co-ordinate system):

$$\mu_t=\rho l^2\left|\frac{\partial U}{\partial y}\right| \qquad (4\text{-}48)$$

and furthermore,

$$-\rho\overline{u'v'}=\rho l^2\frac{\partial U}{\partial y}\left|\frac{\partial U}{\partial y}\right| \qquad (4\text{-}49)$$

Here, l is the ' mixing length ' parameter or turbulent length scale, which is generally assumed to be proportional to the distance from the nearest wall or the width of a shear layer, a wake, a jet, etc.

The Prandtl mixing length model has provided some significant results in the prediction of simple flows, such as the turbulent flow past flat plates with non-supported boundary layers, pipe flows, far regions in wakes and jets, etc. This ' mixing length ' parameter is the main drawback of the model, because it has to be modified for different kinds of flows and it is very difficult to evaluate for more complex types of flows. The model has, however, been used with success in shear- and boundary-layer flows where l can be determined, e.g., Nikuradses experiments in pipes.

III. Kolmogorov-Prandtl model (One-equation Model)

The basis of one-equation turbulence model lies in the suggestion of both Kolmogorov(1942) and Prandtl(1945) that, on physical considerations, the eddy viscosity, μ_t, should depend on the turbulent kinetic energy, k, which has been prescribed before, and besides k, it also depends on the turbulent mixing length scale, l. The expression is as follows:

$$\mu_t = C_D \rho l k^{1/2} \qquad (4\text{-}50)$$

where C_D is an empirical constant (≈ 1.0).

Equation (4-50) is known as the Kolmogorov-Prandtl equation. The distribution of the k field is obtained by solving a transport equation with k as the dependent variable derived from the Navier-Stokes equation. The transport equation for k (in isothermal flow) is:

$$\frac{\partial(\rho k)}{\partial t}+\frac{\partial(\rho U_i k)}{\partial x_i}-\frac{\partial}{\partial x_i}\left(\Gamma_k\frac{\partial k}{\partial x_i}\right)=P_i-C_D\rho\frac{k^{3/2}}{l} \qquad (4\text{-}51)$$

$$P_i=\mu_t\frac{\partial U_i}{\partial x_i}\left(\frac{\partial U_j}{\partial x_i}+\frac{\partial U_i}{\partial x_j}\right) \qquad (4\text{-}52)$$

where $\Gamma_k=\mu+\frac{\mu_t}{\sigma_k}$, σ_k is the Prandtl turbulent number for k (σ_k≈1.0).

Equations (4-50) ~ (4-52) form the so-called ' one-equation model '. Although this model is an improvement on the mixing length hypothesis, it still relies on a value for the length scale l which is not always definable, especially for complex turbulent flows. That is the reason why one-equation model has never become very popular.

IV. k-ε model (two-equation Model)

In attempt to eliminate the need for specification of the length scale parameter throughout the flow regime, it is necessary to establish a two-equation turbulence model which describes both the turbulence velocity and length scale by appropriate transport equations. Harlow, et al. (1965) and Launder, et al. (1974, 1978) independently made proposals for a two-equation model. All of these models use the turbulence kinetic energy, k, same as in the one-equation model, to describe the turbulence velocity. For the determination of the length scale different proposals have been made, but the choice of the dissipation of turbulent kinetic energy, ε, has now become the most widely used and the k-ε model is possibly, currently, the best choice for a turbulence model for most

engineering applications due to its applicability to a wide-range of flow problems and its reasonable computational demand.

In the k-ε model, the kinetic energy dissipation rate, ε, is defined as

$$\varepsilon = \frac{\mu}{\rho}\left(\overline{\frac{\partial u_i'}{\partial x_j}\frac{\partial u_i'}{\partial x_j}}\right) = C_\mu \frac{k^{1.5}}{l} \tag{4-53}$$

then, substituting for $l = C_\mu k^{1.5}/\varepsilon$ and C_D=1.0 in equation (4-50), we obtain:

$$\mu_t = C_\mu \rho k^2/\varepsilon \tag{4-54}$$

It can be seen that the turbulent kinetic energy is a direct measure for the intensity of the velocity fluctuations and the dissipation of the turbulent kinetic energy is equal to the mean-vorticity arising from the velocity fluctuations times the molecular viscosity. The k and ε equations are modelled as follows:

$$\frac{\partial(\rho k)}{\partial t} + \frac{\partial}{\partial x_i}(\rho U_i k) - \frac{\partial}{\partial x_i}\left(\Gamma_k \frac{\partial k}{\partial x_i}\right) = P - C_D \rho \varepsilon + G \tag{4-55}$$

$$\frac{\partial(\rho \varepsilon)}{\partial t} + \frac{\partial}{\partial x_i}(\rho U_i \varepsilon) - \frac{\partial}{\partial x_i}\left(\Gamma_\varepsilon \frac{\partial \varepsilon}{\partial x_i}\right) = C_1 \frac{\varepsilon}{k}(P + C_3 \max(G,0)) - C_2 \rho \frac{\varepsilon^2}{k} \tag{4-56}$$

$$P = \mu_t \frac{\partial U_i}{\partial x_j}\left(\frac{\partial U_i}{\partial x_j} + \frac{\partial U_j}{\partial x_i}\right) \tag{4-57}$$

$$\Gamma_k = \mu + \frac{\mu_t}{\sigma_k} \tag{4-58}$$

$$\Gamma_\varepsilon = \mu + \frac{\mu_t}{\sigma_\varepsilon} \tag{4-59}$$

$$G = G_{buoy} + G_{rot} + G_{res} \tag{4-60}$$

G_{buoy} is a buoyancy term for non-isothermal flow and can be expressed as $G_{buoy} = \frac{\mu_{eff}}{\sigma_T}\beta g \cdot \nabla T$, β is the coefficient of thermal expansion. G_{rot} and G_{res} are terms representing productions of rotation and resistance respectively wherever applicable.

In the forms of second order tensor expression, equations (4-55) ~ (4-60) can be expressed as follows:

$$\frac{\partial(\rho k)}{\partial t} + \nabla \cdot (\rho U k) - \nabla \cdot \left[\left(\mu + \frac{\mu_t}{\sigma_k}\right)\nabla k\right] = P + G - \rho\varepsilon \qquad (4\text{-}61)$$

$$\frac{\partial(\rho \varepsilon)}{\partial t} + \nabla \cdot (\rho U \varepsilon) - \nabla \cdot \left[\left(\mu + \frac{\mu_t}{\sigma_k}\right)\nabla k\right]$$

$$= C_1 \frac{\varepsilon}{k}\left[P + C_3 \max(G,\ 0)\right] - C_2 \frac{\varepsilon^2}{k} \qquad (4\text{-}62)$$

$$P = \mu_t \nabla U \cdot \left[\nabla U + (\nabla U)^T\right] \qquad (4\text{-}63)$$

$$G = \nabla G_{buoy} + \nabla G_{rot} + \nabla G_{res} \qquad (4\text{-}64)$$

The k-ε model described by equations (4-55) ~ (4-60) or (4-61) ~ (4-64) is also referred as standard k-ε model. The parameters C_1, C_2, C_3, C_μ, σ_k, σ_ε are regarded as constants in k-ε model and take the values below:

$$C_1 = 1.44,\ C_2 = 1.92,\ C_3 = 0 \text{ or } 1.0,\ C_\mu = 0.09,\ \sigma_k = 1.0,\ \sigma_\varepsilon = 1.3$$

The standard k-ε model has been applied and proved to be of good predictive accuracy in many engineering applications. This model is being applied in the current research.

§4.3 Solution of the Flow Equations

In general, all equations in the mathematical model are transport equations. These equations can be expressed in a general form which is more comprehensive for the numerical discretisation procedures. The general equation is as below:

$$\frac{\partial}{\partial t}(\rho\Phi)+\frac{\partial}{\partial x_i}(\rho U_i\Phi)-\frac{\partial}{\partial x_i}\left(\Gamma_\Phi\frac{\partial\Phi}{\partial x_i}\right)=S_\Phi \qquad (4\text{-}65)$$

or

$$\frac{\partial}{\partial t}(\rho\Phi)+\nabla\cdot(\rho U\Phi)-\nabla\cdot(\Gamma_\Phi\nabla\Phi)=S_\Phi \qquad (4\text{-}65)'$$

The contents of Φ, Γ_Φ and S_Φ are listed in Table 4-1.

Table 4-1 The formations of Φ, Γ_Φ and S_Φ in transport equations

Equation	Φ	Γ_Φ	S_Φ
Continuity	1	0	0
Momentum	U V W	μ_{eff} μ_{eff} μ_{eff}	$-\frac{\partial}{\partial x_i}\left(P+\frac{2}{3}\rho k\right)+\frac{\partial}{\partial x_i}\left[\mu_{eff}\left(\frac{\partial U_i}{\partial x_j}+\frac{\partial U_j}{\partial x_i}\right)\right]+B_i$
Energy	H	$\frac{\lambda}{C_p}+\frac{\mu_t}{\sigma_H}$	$\frac{\partial P}{\partial t}$
k	k	$\mu+\frac{\mu_t}{\sigma_k}$	$\mu_t\frac{\partial U_i}{\partial x_j}\left(\frac{\partial U_i}{\partial x_j}+\frac{\partial U_j}{\partial x_i}\right)-C_D\rho\varepsilon+G$
ε	ε	$\mu+\frac{\mu_t}{\sigma_\varepsilon}$	$C_1\mu_t\frac{\varepsilon}{k}\frac{\partial U_i}{\partial x_j}\left(\frac{\partial U_i}{\partial x_j}+\frac{\partial U_j}{\partial x_i}\right)-C_2\rho\frac{\varepsilon^2}{k}+G$

Here G includes buoyancy, rotational and resistive forces wherever applicable. B_i represents all the external forces in the momentum equations wherever applicable.

Equations (4-65) and Table 4-1 describe the fluid flow under transient, turbulent, compressible and non-isothermal conditions. The equations are in general inhomogeneous, highly non-linear and strongly coupled. Further are the flow equations in general too complicated to be dealt with by analytical means so numerical solution techniques are the only way to achieve solutions of these equations. It should be noted that the flow phenomena studied in this research are all steady fluid flows, so we take away all transient terms in governing equations thereafter, and the general governing equation takes the following formation:

$$\frac{\partial}{\partial x_i}(\rho U_i \Phi) - \frac{\partial}{\partial x_i}\left(\Gamma_\Phi \frac{\partial \Phi}{\partial x_i}\right) = S_\Phi \qquad (4\text{-}66)$$

$$\nabla \cdot (\rho U \Phi) - \nabla \cdot (\Gamma_\Phi \nabla \Phi) = S_\Phi \qquad (4\text{-}66)'$$

Before choosing the numerical solution algorithm (CFD algorithm), it is essential to look at the characteristics of the set of partial differential equations (PDEs). The governing equations presented in (4-66) are of elliptic nature, which means that a perturbation in a certain part of the solution domain influences the whole solution domain. This means that in order to have a well posed problem (a well posed problem is, if a solution exists, it is unique and depends continuously on the boundary conditions), one must provide boundary conditions at all boundaries of flow domain for all dependent variables. In contrast to, e.g., the characteristics of parabolic flow, where it is possible to

obtain a local solution in a point immediately adjacent to a boundary by a series expansions, one must , in elliptic flow regime, obtain the solution for all variables in the whole flow domain simultaneously.

The next consideration is to choose the discretisation technique. In the area of CFD, three discretisation techniques, are, currently, widely used: the finite difference method (FD), the finite element method (FEM) and the finite volume method (FV). In this research, the FV approach is applied. This method implies overall integral conservation of all quantities. In fact this feature is, together with its direct physical interpretation, the main reason for its popularity.

Numerical solutions imply that the calculation domain is broken into a finite number of control volumes (cells) where all variables are represented by values located in a grid-point in the mesh of computational cells. A set of algebraic equations containing information of the all discrete values is constructed by integrating the governing equation over a finite three-dimensional space (finite volume). This set of algebraic equations is then solved by applying proper boundary conditions, i.e., the obtained numerical solution of the differential equations is not a general solution but a particular solution involving particular boundary conditions. As the number of grid points in the flow domain becomes larger and larger the solutions of the discretised algebraic equations get closer and closer to the exact solutions of the partial differential equations. The larger the number of grid points, the closer the numerical results to the exact solutions. The trade-off increasing the number of grid points is the larger computer storages and the larger computing demand.

§4.3.1 Integration and discretisation

The general governing equation (4-66) is integrated over a control volume (cell) in the solution domain, for notation see figure 4.2, and can be expressed by

$$\int_v \frac{\partial}{\partial x_i}(\rho U_i \Phi)dV - \int_v \frac{\partial}{\partial x_i}\left[\Gamma_\Phi \frac{\partial \Phi}{\partial x_i}\right]dV = \int_v S_\Phi dV \qquad (4\text{-}67)$$

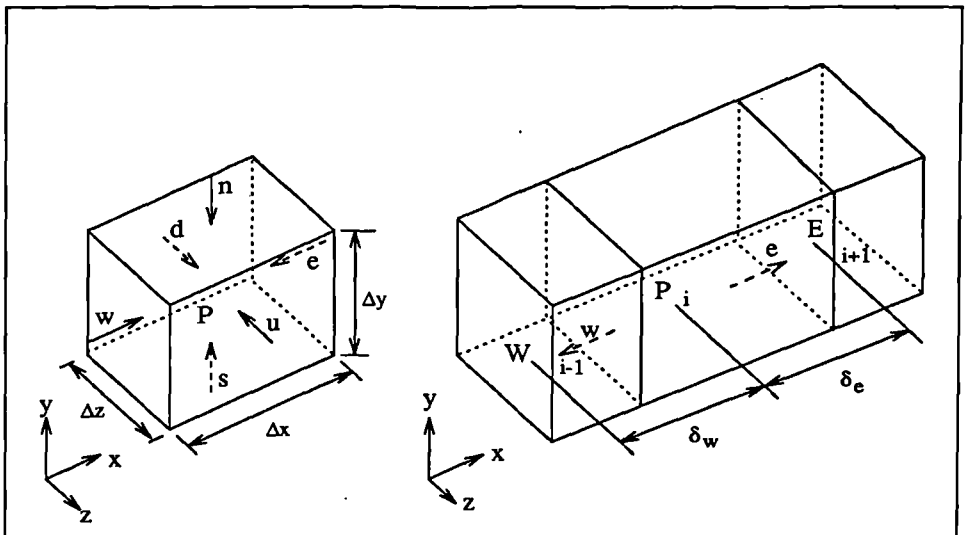

a. A single three-dimensional volume b. An x-array of three-dimensional volume

Figure 4.2 Computational control volume with grid information

In the finite volume technique, it is assumed that the dependent variable Φ is piecewise linear between the grid nodes and that the fluxes across the surfaces

between control volumes are constant over the two successive volumes (one of the four basic rules, see Patankar 1980). If the dependent variable further is treated one-dimensional, it is possible to obtain following coefficient equation (for details, see Appendix C):

$$(a_E + a_W + a_N + a_S + a_D + a_U)\Phi_P =$$

$$a_E\Phi_E + a_W\Phi_W + a_N\Phi_N + a_S\Phi_S + a_D\Phi_D + a_U\Phi_U + (S_P\Phi_P + S_C)\Delta x\Delta y\Delta z$$

$$\Rightarrow \qquad a_P\Phi_P = \sum_K a_K\Phi_K + S_C\Delta x\Delta y\Delta z \qquad (4\text{-}68)$$

where the coefficients are defined as follows:

$$a_E = (\Gamma_\Phi)_e \frac{A_e}{\delta_e} - A_e\frac{(\rho U)_e}{2}, \quad a_W = (\Gamma_\Phi)_w \frac{A_w}{\delta_w} + A_w\frac{(\rho U)_w}{2} \qquad (4\text{-}69)$$

$$a_N = (\Gamma_\Phi)_n \frac{A_n}{\delta_n} - A_n\frac{(\rho U)_n}{2}, \quad a_S = (\Gamma_\Phi)_s \frac{A_s}{\delta_s} + A_s\frac{(\rho U)_s}{2} \qquad (4\text{-}70)$$

$$a_D = (\Gamma_\Phi)_d \frac{A_d}{\delta_d} - A_d\frac{(\rho U)_d}{2}, \quad a_U = (\Gamma_\Phi)_u \frac{A_u}{\delta_u} + A_u\frac{(\rho U)_u}{2} \qquad (4\text{-}71)$$

It is important to notice that the coefficients are equal to the sum of mass flow and the diffusion conductance over a cell face (one of the four basic rules, Patankar 1980).

§4.3.2 Differencing Schemes

The general equation (4-66) can be solved analytically for the one-dimensional convection-diffusion case. This solution is introduced and integrated over a control volume. If the total flux over the cell is modelled by this exact solution, it results in a discretisation equation which describes the behaviour of the one-dimensional convection-diffusion problem (see Appendix D). This scheme, known as exponential scheme, is nevertheless not very widely used. First of all it is only exact for the one-dimensional case and secondly it is rather expansive to compute. But the knowledge from the behaviour of the variable can be used to construct an easier way to use and compare different approximation schemes.

I. Central differencing scheme (CD)

If the coefficients in equation (4-69) ~ (4-71) are examined, it is noticed that the coefficients may become negative if the absolute value of the local Peclet number, defined as

$$P_e = \frac{\delta_e (\rho U)_e}{\Gamma_\Phi} \qquad (4\text{-}72)$$

is greater than 2. This occurrence violates one of the four basic rules in the finite volume technique, namely Scarborough criterion (Patankar 1980) which says that

$$|a_P| \leq \sum_K |a_K| \qquad (4\text{-}73)$$

The criterion is a sufficient condition for convergence of a numerical problem with at least one solution method (the Gauss-Seidel method). Whether or not this method is applied, the fulfilment of the criterion will still be required.

The coefficients in equation (4-69) ~ (4-71) arises from a gradient interpolation over a cell border (see appendix C) of the form

$$\left[\frac{\partial \Phi}{\partial x}\right]_e = \frac{\Phi_E - \Phi_P}{\delta_e} \Rightarrow \Phi_e = \frac{1}{2}(\Phi_E + \Phi_P) \qquad (4\text{-}74)$$

The above approximation of the differential method is known as central differencing scheme (CD). The scheme can be shown to be of second order accurate in terms of truncation errors, but it has big limitations in high Reynolds number flows if one require the criterion in equation (4-73) satisfied.

In order to improve the numerical stability of the differencing procedure, many works have been done to develop more stable methods to approximate the gradient terms. Among the schemes are the upwind scheme, the power-law scheme (PLDS, Patankar 1980), the hybrid scheme (HYB, Patankar 1980) and quadratics QUICK scheme (Leonard 1979).

II. Upwind scheme

The upwind scheme recognises that the weak point in the preliminary formulation is the assumption that the convected property Φ_e at the interface is the average of Φ_E and Φ_P, and it proposes a better prescription as: the value of

at an interface is equal to the value of Φ at the grid point on the upwind side of the face. Thus,

$$\Phi_e = \Phi_P \quad \text{if} \quad (\rho U)_e > 0 \tag{4-75}$$

and

$$\Phi_e = \Phi_E \quad \text{if} \quad (\rho U)_e < 0 \tag{4-76}$$

Let's introduce a symbol $\max[\ ]$, then the upwind scheme implies

$$(\rho U\Phi)_e = \Phi_P \max[(\rho U)_e, 0] - \Phi_E \max[-(\rho U)_e, 0] \tag{4-77}$$

From equation (4-77), we can see that no negative coefficients would arise. Thus, the solutions will always be physically realistic, and the Scarborough criterion will be satisfied. But one thing should be noted that the upwind scheme overestimates the diffusion at large values of $|P_e|$ and leads to inaccurate results.

III. Hybrid differencing scheme (HYB)

The HYB scheme approximates the curve of the exact one-dimensional solution in three different intervals by three straight lines. According to Appendix D, we can deduce that:

$$a_E = \frac{(\Gamma_\Phi)_e}{\delta_e} \frac{(P_e)_e}{\exp[(P_e)_e] - 1} \tag{4-78}$$

let, $D_e = \frac{(\Gamma_\Phi)_e}{\delta_e}$, then the variation of $\frac{a_E}{D_e}$ with P_e is shown in figure 4.3. For positive values of P_e, the grid point E is the downstream neighbour, and its

influence is seen to decrease as P_e increases. When P_e is negative, E is the upstream neighbour and has a large influence. Certain specific properties of the exact variation of $\frac{a_E}{D_e}$ can be seen to be:

For $(P_e)_e \to \infty$, $\frac{a_E}{D_e} \to 0$

For $(P_e)_e \to -\infty$, $\frac{a_E}{D_e} \to -P_e$

For $(P_e)_e = 0$, the tangent is $\frac{a_E}{D_e} = 1 - \frac{P_e}{2}$

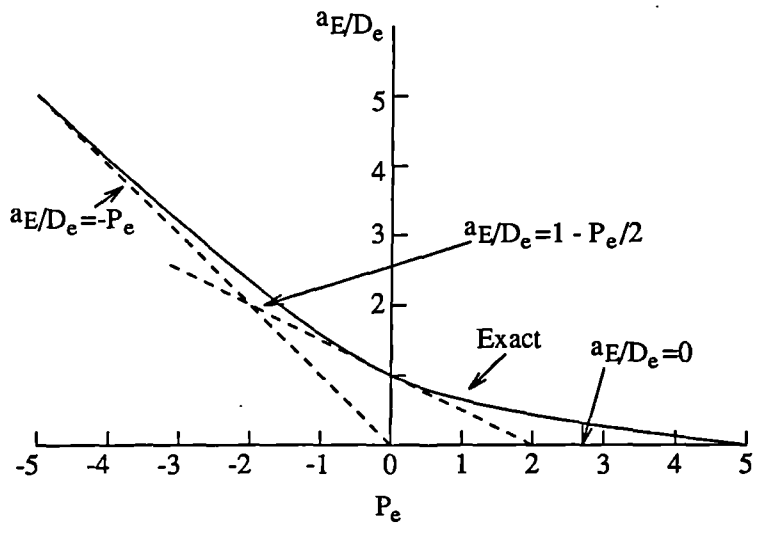

Figure 4.3 Variation of coefficient a_E with Peclet number (Patankar, 1980)

The three straight lines represent the above limiting cases. They can be seen to form an envelope of , and represent a reasonable approximation to, the exact

curve. The HYB scheme is indeed made up of three straight lines, so that in three-dimensional case,

For $(P_e)_e < -2$: $a_E = -A_e \frac{(\Gamma_\Phi)_e}{\delta_e}(P_e)_e$

For $|(P_e)_e| \le 2$: $a_E = A_e \frac{(\Gamma_\Phi)_e}{\delta_e}\left[1 - \frac{(P_e)_e}{2}\right]$

For $(P_e)_e > 2$: $a_E = 0$

These expressions can be expressed in a combination form as below:

$$a_E = A_e \frac{(\Gamma_\Phi)_e}{\delta_e} \max\left[-(P_e)_e,\ 1 - \frac{(P_e)_e}{2},\ 0\right] \qquad (4\text{-}79)$$

The significance of the hybrid scheme can be understood by observing that (1) it is identical with the central-difference scheme for the Peclet-number range $-2 \le (P_e)_e \le 2$, and (2) outside this range it reduces to the upwind scheme in which the diffusion has been set equal to zero. Thus; the shortcomings of the upwind scheme are not shared by the hybrid scheme. The name hybrid is indicative of a combination of the central-difference and upwind-difference schemes, but it is best to consider the hybrid scheme as the three-line approximation to the exact curve.

IV. Power-law difference scheme (PLD)

It can be seen from figure 4-3 that the departure of the hybrid scheme from the exact curve is rather large at $P_e = \pm 2$; also, it seems rather premature to set the

diffusion effects to zero as soon as $|P_e|$ exceeds a. A better approximation to the exact curve is given by power-law scheme, which is expressed as below:

For $(P_e)_e < -10$: $a_E = -A_e \frac{(\Gamma_\Phi)_e}{\delta_e}(P_e)_e$

For $-10 < (P_e)_e < 0$: $a_E = A_e \frac{(\Gamma_\Phi)_e}{\delta_e}\left[(1+0.1(P_e)_e)^5 - (P_e)_e\right]$

For $0 < (P_e)_e < 10$: $a_E = A_e \frac{(\Gamma_\Phi)_e}{\delta_e}(1-0.1(P_e)_e)^5$

For $(P_e)_e > 10$: $a_E = 0$

which in the more compressed form can be expressed as

$$a_E = A_e \frac{(\Gamma_\Phi)_e}{\delta_e}\max\left[0,\ (1-0.1(P_e)_e)^5\right] + A_e \frac{(\Gamma_\Phi)_e}{\delta_e}\max\left[0,\ -(P_e)_e\right] \quad (4\text{-}80)$$

The improvements of introducing the PLD scheme is mainly in the Peclet range around 2 where the HYB scheme has the biggest deviation from the exact solution.

Let's define a function $A(|P_e|)$ representing the formulations in above differencing schemes, then Table 4.2 gives these formulations:

Table 4-2 The function $A(|P_e|)$ for different schemes

Scheme	Formula for $A(\|P_e\|)$
Exponential (exact)	$\|P_e\|/[\exp(\|P_e\|)-1]$
Central	$1-0.5\|P_e\|$
Upwind	1
Hybrid	$\max[0,\ 1-0.5\|P_e\|]$
Power-law	$\max[0,\ (1-0.1\|P_e\|)^5]$

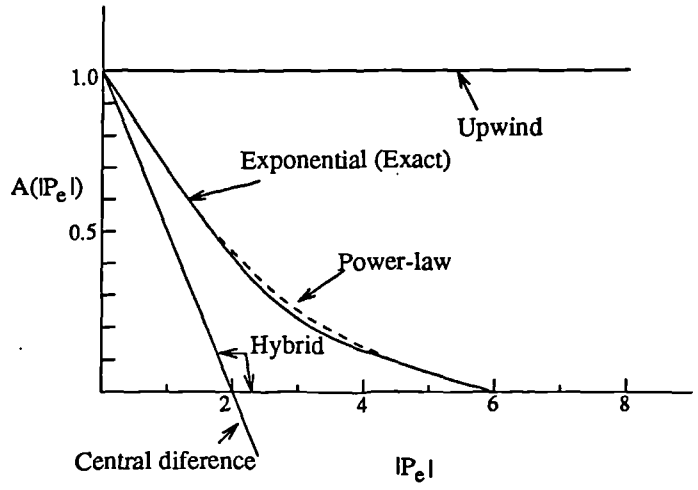

Figure 4.4 The comparisons of different schemes (Patankar, 1980)

Figure 4.4 shows the accuracy of the above differencing schemes. It has proved that the CD scheme has second-order accuracy but less reliable; the upwind scheme is first-order accurate; the HYB scheme is again first-order accurate but better than the upwind scheme and very robust; PLD scheme has the best accuracy among them but more difficult to arrive convergence.

V. QUICK scheme

The latest improved differencing scheme in finite volume technique is the QUICK scheme. The aim with this scheme is to have a scheme which is as accurate as the CD scheme but more stable. The method fits Φ variable on the volume interface by a second order polynomial. The scheme can be interpreted as a central differencing scheme with a stabilising upstream weighted curvature correction arising from the second order polynomial fit.

$$\Phi_e = \frac{1}{2}(\Phi_E + \Phi_P) - \frac{\delta_e^2}{8}\mathrm{CURV}_e \qquad (4\text{-}81)$$

If the grid is uniformly distributed, the above equation can be written:

For $\Phi_e > 0$: $$\Phi_e = \frac{1}{2}(\Phi_E + \Phi_P) - \frac{1}{8}(\Phi_W - 2\Phi_P + \Phi_E) \qquad (4\text{-}82)$$

For $\Phi_e < 0$: $$\Phi_e = \frac{1}{2}(\Phi_E + \Phi_P) - \frac{1}{8}(\Phi_P - 2\Phi_E + \Phi_{EE}) \qquad (4\text{-}83)$$

If the grid, on the other hand, isn't uniformly distributed, the calculation is more tiresome and costly. For a non-uniform grid (see Figure 4.5), the QUICK scheme is as follows:

For $\Phi_e > 0$: $$\Phi_e = \Delta_3\Phi_W + \Delta_1\Phi_P - \Delta_2\Phi_E \qquad (4\text{-}84)$$

For $\Phi_e < 0$: $$\Phi_e = \Delta_1\Phi_P - \Delta_2\Phi_E + \Delta_3\Phi_{EE} \qquad (4\text{-}85)$$

where $$\Delta_1 = \frac{\delta_1\delta_3(\delta_1 + \delta_2)}{\Delta_4}$$

$$\Delta_2 = \frac{\delta_2\delta_3(\delta_2 - \delta_3)}{\Delta_4}$$

$$\Delta_3 = \frac{\delta_1\delta_2(\delta_1 + \delta_2)}{\Delta_4}$$

$$\Delta_4 = \delta_1\delta_2(\delta_1+\delta_2)+\delta_2\delta_3(\delta_2-\delta_3)-\delta_1\delta_3(\delta_1+\delta_3)$$

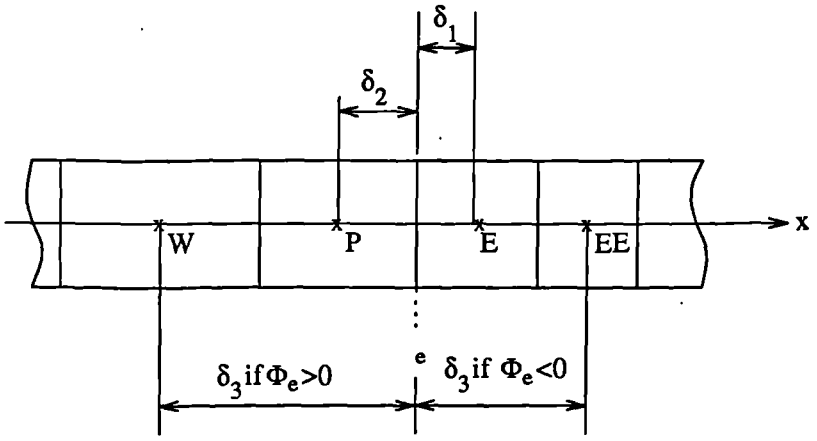

Figure 4.5 One-dimensional non-uniform grid information

In this section, several differencing schemes which are available for the numerical solutions have been introduced. Among them, HYB, PLD and QUICK schemes are widely used. If a comparison between these three schemes is made, it is notice that the QUICK scheme in most cases will be the most accurate but has the drawback that it is more tiresome to implement and the computation cost is also considerably bigger than the two others because it yields slower convergence of the numerical procedure. The PLD scheme is also rather costly to compute compared to the HYB scheme. The HYB scheme is not as accurate as the PLD and the QUICK schemes but more robust and less computational cost. So the PLD and QUICK schemes are therefore frequently used in the two-dimensional calculations. Considering the three-dimensionality of the problems studied in this research, the HYB scheme is applied for all three-dimensional simulations.

§4.3.3 Treatment of the Source Terms

As described in equation (4-68), it is necessary to linearize the source terms, i.e., S_Φ in Table 4-1.

$$S_\Phi = S_C + S_P\Phi_P \tag{4-86}$$

This linearization may be done in several ways and this section is devoted to a discussion of such problem and recommend how to linearize the source terms in the model. If we consider the coefficient definitions in equations (4-69) ~ (4-71), it appears that, even if the neighbour coefficients are positive, the centre-point coefficient a_P still can become negative via the S_P term. Of course, the danger can be completely avoided by requiring the S_P will not be positive. Thus, the following principle (one of the four basic rules) is formulated as below:

When the source term is linearized as $S_\Phi = S_C + S_P\Phi_P$, *the coefficient* S_P *must always be less than or equal to zero.*

This rule is not as arbitrary as it sounds. Most physical processes do have a negative-slope relationship between the source term and the dependent variable. Indeed, if S_P were positive, the physical situation could become unstable. Computationally, it is vital to keep S_P negative so that instabilities and physically unrealistic solutions do not arise. In many of the governing equations the source terms are always positive, but with both negative and

positive parts, i.e., destruction and generation terms. Further are the source terms often large compared to the other terms in the equations. It is therefore crucial to model the source terms in a right way. It is sufficient to note here that, for computational success, the principle of negative S_P is essential. The following method of linearization is recommended:

Momentum equations: $S_P = 0, \quad S_C = S_\Phi$ (4-87)

Energy equation: $S_P = 0, \quad S_C = S_\Phi$ (4-88)

k-equation: $$S_P = -C_\mu C_D \rho^2 \frac{k^*}{\mu_t} \tag{4-89}$$

$$S_C = \mu_t \frac{\partial U_i}{\partial x_j}\left(\frac{\partial U_i}{\partial x_j} + \frac{\partial U_j}{\partial x_i}\right) + G_i \tag{4-90}$$

ε-equation: $$S_P = -C_2 \rho \frac{\varepsilon^*}{k^*} \tag{4-91}$$

$$S_C = C_1 \mu_t \frac{\varepsilon^*}{k^*} \frac{\partial U_i}{\partial x_j}\left(\frac{\partial U_i}{\partial x_j} + \frac{\partial U_j}{\partial x_i}\right) + G_i \tag{4-92}$$

* correspond to the values from the previous iteration.

§4.3.4 The Non-Staggered Grid (Co-located Grid) and The Pressure-Correction Equation

In the source terms of the momentum equation one of the involving terms is the pressure gradient. This means that in order to be able to calculate the velocity field, the pressure field must be known. An assumption of how to approximate the pressure gradient must be made and an additional expression of how to resolve the pressure field from the velocity field has to be established.

The pressure gradient term is integrated over a finite volume

$$-\int_V \frac{\partial P}{\partial x_i} dV = (P_w - P_e)\Delta y \Delta z = \frac{1}{2}(P_W - P_E)\Delta y \Delta z \qquad (4\text{-}93)$$

This approximation of the pressure gradient term may result in a ' wavy ' pressure field which is felt like a uniform pressure field by the momentum equations because the pressure difference is taken between two alternate grid points and not between two adjacent points. This phenomenon is called the chequerboard phenomenon. A similar effect is occurring in the continuity equation if the velocity gradients are approximated in a similar manner. The method to overcome this phenomenon is, normally, to use the staggered grid to relocate the velocity variables and the corresponding grid and computational volume (Patankar 1980). The benefits of doing this is that it eliminates the risk of ' wavy ' velocity and pressure fields but the cost is that it

requires extra computer storage, an additional interpolation effort and it makes the Navier-Stokes equations difficult to solve. The method used to solve such chequerboard oscillation in this study is the Rhie-Chow interpolation algorithm (which produces a non-staggered grid or co-located grid).

I. Rhie-Chow interpolation algorithm

In this research we introduce Rhie-Chow (Rhie, et al. 1983; FLOW3D Menu, 1993) interpolation method to solve such chequerboard oscillation problem. Let's assume a concessive control cell which is described in figure 4.6.

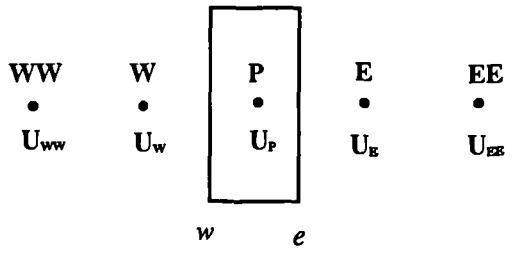

Figure 4.6 Control cells

It is necessary to address the question of how to obtain the velocity components on control volume faces from those on control volume centres. The naive prescription for this would be to use weighted linear interpolation in physical space, i.e.,

$$U_e^i = \overline{U_e^i} = (1 - W_e)U_P + W_e U_E, \quad W_e \text{ is a weighted factor}$$

However, this method is known to lead chequerboard oscillations in pressure and velocity. The Rhie-Chow interpolation algorithm is based on an interpolation of the momentum equations. Consider the interpolation to the east face of a control volume centred at P, note that the velocity components U_P^i at control volume centres obey the discretised momentum equation given in short-hand forms as follows:

$$U_P + (B\nabla P)_P = (AU)_P + S_P \qquad (4\text{-}94)$$

$$U_E + (B\nabla P)_E = (AU)_E + S_E \qquad (4\text{-}95)$$

The traditional method for avoiding pressure oscillation is to use velocity components U_e etc., obtained by discretising the momentum equations on the staggered grids whose centres are the faces of the control volumes. In this case, U_e also obey a discretised momentum equation of the form:

$$U_e + (B\nabla P)_e = (AU)_e + S_e \qquad (4\text{-}96)$$

where pressure gradients are calculated using centred differences. The description of Rhie-Chow method is simply a method of approximating solutions of equation (4-96) from the solutions of equations (4-94) and (4-95). If it is assumed that the terms on the right hand side of equation (4-96) may be approximated by weighted linear interpolations of the corresponding terms in equations (4-94) and (4-95), then:

$$U_e + (B\nabla P)_e = \overline{(AU)_e} + \overline{S_e} = \overline{U_e} + \overline{(B\nabla P)_e}$$

$$\Rightarrow \qquad U_e = \overline{U_e} + \overline{(B\nabla P)_e} - B_e(\nabla P)_e$$

Also assuming $B_e \approx \overline{B_e}$, and $\overline{(B\nabla P)_e} \approx \overline{B_e \nabla P_e}$, the Rhie-Chow interpolation formula is obtained:

$$U_e = \overline{U_e} + \overline{B_e}\left[\overline{\nabla P_e} - (\nabla P)_e\right] \tag{4-97}$$

This is given in component form by:

$$U_e^i = \overline{U_e^i} + \overline{B_{ie}^k}\left[\overline{\left(\frac{\partial P}{\partial x^k}\right)_e} - \left(\frac{\partial P}{\partial x^k}\right)_e\right] \tag{4-98}$$

The Rhie-Chow interpolation algorithm enables us to obtain the velocity components (further the convection coefficients) on the control volume faces without causing chequerboard effects and with no extra computing storages. It greatly simplifies the transformed equations and reduces the storage required (as only one grid is used).

II. Pressure-correction equation

The velocity-pressure coupling is based on the SIMPLE algorithm proposed by Patankar & Spalding (1972) and improved SIMPLEC algorithm proposed by Van Doormal & Raithby (1984) respectively. The aim of the SIMPLE algorithm is to force the relevant dependent variables, i.e., U_i and P, to satisfy the conservation law of mass, i.e., satisfaction of continuity equation.

As described in Table 4.1, the Cartesian form of the momentum equation is given by,

$$\frac{\partial(\rho U_i U_k)}{\partial x_i} - \frac{\partial}{\partial x_i}\left(\mu_{eff}\frac{\partial U_k}{\partial x_i}\right) = -\frac{\partial P}{\partial x_k} + \frac{\partial}{\partial x_i}\left(\mu_{eff}\frac{\partial U_i}{\partial x_k}\right) + B_i = S_{U_k} \quad (4\text{-}99)$$

The corresponding discretised equation for non-staggered grid is

$$a_P^k U_P^k - \sum_{n,K} a_n^k U_K^k = S_C \Delta V_k \quad (4\text{-}100)$$

where

$$a_P^k = \sum_n a_n^k - S_P \quad (4\text{-}101)$$

$$S_C = S_{U_k} \quad (4\text{-}102)$$

The first term in S_{U_k} is called the pressure gradient source term, the others are called non-pressure gradient source terms, denoted as S'_C, so equation (4-100) can be written as

$$a_P^k U_P^k = \sum_{n,K} a_n^k U_K^k + S'_C \Delta V_k - \frac{\partial P}{\partial x_k}\Delta V_k$$

$$\Rightarrow \quad a_P^k U_P^k = \sum_{n,K} a_n^k U_K^k + S'_C \Delta V_k - (P_P - P_K)\Delta A_k \quad (4\text{-}103)$$

Let U_P^{k*}, P_P^* denote the most recently updated velocity and pressure fields after the linearised momentum equations have been solved, so equation (4-103) can be written in the form:

$$a_P^k U_P^{k*} = \sum_{n,K} a_n^k U_K^{k*} + S'_C \Delta V_k - (P_P^* - P_K^*)\Delta A_k \quad (4\text{-}104)$$

Now, the solution U_P^{k*} of equation (4-104) does not yet, in general, satisfy the continuity equation, it has a residual mass source:

$$m_P = [\rho U_P^{1*}]_w^e + [\rho U_P^{2*}]_s^n + [\rho U_P^{3*}]_d^u \quad (4\text{-}105)$$

The terms in equation (4-105) involve the values of the normal velocity components on mass control volume faces, and these must be approximated somehow from the velocity components U_P^{k*} at mass control volume centres.

The main idea of the SIMPLE and SIMPLEC algorithms and their variants is to find updated velocity and pressure fields U_P^{k**}, P_P^{**} obeying the discrete momentum equations and the discrete continuity equation:

$$a_P^k U_P^{k**} = \sum_{n,K} a_n^k U_K^{k**} + S_C' \Delta V_k - \left(P_P^{**} - P_K^{**}\right)\Delta A_k \qquad (4\text{-}106)$$

and

$$\left[\rho U_P^{1**}\right]_w^e + \left[\rho U_P^{2**}\right]_s^n + \left[\rho U_P^{3**}\right]_d^u = 0 \qquad (4\text{-}107)$$

Assuming that the corrected velocities U_P^{k**} on the r.h.s. of (4-106) can be approximated by $U_N^{k*} + \alpha\left(U_P^{k**} - U_P^{k*}\right)$, where $\alpha = 0$ for SIMPLE and $\alpha = 1$ for SIMPLEC, the following formulae are obtained for the velocity- and pressure-correction:

$$U_P^{k**} = U_P^{k*} - \frac{\Delta A_k}{a_P^k - \alpha \sum_n a_n^k}\left(P_P' - P_K'\right), \qquad P_P^{**} = P_P^{*} + P_P' \qquad (4\text{-}108)$$

The pressure-correction equation is obtained by substituting the approximate equation (4-108) for the normal velocity corrections into the mass conservation equation (4-107), this results in:

$$b_P P_P' = \sum_{n,K} b_n P_K' - m_P, \qquad b_P = \sum_n b_n \qquad (4\text{-}109)$$

$$b_{e,w} = \left[\rho \frac{\Delta A_k}{a_P^k - \alpha \sum_n a_n^k}\right]_w^e, \quad b_{n,s} = \left[\rho \frac{\Delta A_k}{a_P^k - \alpha \sum_n a_n^k}\right]_s^n,$$

$$\text{and} \quad b_{u,d} = \left[\rho \frac{\Delta A_k}{a_P^k - \alpha \sum_n a_n^k}\right]_d^u \qquad (4\text{-}110)$$

§4.3.5 Implementation of Boundary Conditions

As mentioned earlier, boundary conditions are required along all the flow domain boundary, because of the elliptic nature of the governing equations. The boundary conditions are unique to a specific flow and thus decisive to the obtained results. The accuracy of the solution of the discretisation equations presented in the above sections will depend on the accuracy of specifying the physical quantities at the boundary of the flow domain and on the methods of linking these quantities to the bulk of the flow. In this research, three types of boundary conditions for fluid flow are used:

(i) Flow boundary;
(ii) Symmetry plane;
(iii) Wall boundary.

I. Flow boundary

A flow boundary is, by definition, a boundary where fluid can enter or leave the flow domain. These are split into three types:

1. Inlets (Prescribed values)

The physical parameters at the inlets are problem specific and are usually known or may be calculated from other quantities. It is necessary to specify the velocity components, fluid temperature, turbulence quantities and concentration level at the inlet. It is recommended that inlet velocities be

specified in such a way that the flow enters the flow domain. The methods to ensure that a desired value in a computational cell remains unchanged during the process of solving the equations are to set the value of the corresponding dependent variable Φ at the inlet cells to the desired value Φ_0 directly, e.g. $U_{in} = U_0, V_{in} = V_0, W_{in} = W_0$, or to make use of the source term in the discretisation equation for the considered variable,

$$a_P \Phi_P = \sum_K a_K \Phi_K + (S_C + S_P \Phi_P)\Delta V_k$$

If the value in the cell is wanted to be Φ_b then

$$S_C + S_P \Phi_P = \lambda \Phi_b - \lambda \Phi_P \qquad (4\text{-}111)$$

where λ is a large number.

2. Mass flow boundaries.

The total mass flow rate $M = \rho UA$ out of the boundary or the fraction of the total mass flow rate out of the boundary is specified. This may be positive or negative, so that the flow may enter or leave the flow domain. This is implemented as follows:

a) Apply a nominal Neumann boundary condition to the velocity field, $\frac{\partial U_i}{\partial n} = 0$;

b) Compute the discrepancy between the actual mass flow rate out of the flow domain and the desired flow rate M;

c) Add an increment to U_i on the boundary, in the direction of the outward going unit normal n^i, to force the outward mass flow rate to the desired value. This is equivalent to

$$\frac{\partial U_i}{\partial n} = \lambda n^i \qquad (4\text{-}112)$$

where λ is chosen to force the desired mass flow rate.

3. Pressure boundaries.

Pressure is specified and Neumann conditions are applied to the velocities, $\frac{\partial U_i}{\partial n} = 0$. The treatment of other variables depends on whether the flow is coming in or going out, and whether it is subsonic or supersonic (details see CFDS-FLOW3D menu, 1994).

II. Symmetry plane.

The boundary conditions at symmetry planes are quite straight forward. All variables are mathematically symmetric, with thus no diffusion across the boundary. On a symmetry plane all gradients normal to the surface are equal to zero and the velocity normal to the surface is prescribed to zero. If, e.g. the south side of a computational cell is required to be a symmetry plane, the required condition can be fulfilled by setting $a_s = 0$ for normal components and $\Phi_{i,j,k} = \Phi_{i,j+1,k}$ for other components.

III. Wall boundaries.

Wall boundaries can be summarised into following types:

1. Wall boundary conditions for velocity.

The general formula for velocity on wall may be written in the following mixed form:

$$A_i U_i + B_i \tau_i = C_i, \qquad i = 1,2,3 \qquad (4\text{-}113)$$

where $\tau_i = \left(\mu \frac{\partial U_i}{\partial y} \right)_w$ is the wall shear stress.

If the no-slip condition is used, then $A_i = 1$, $B_i = C_i = 0$. If $A_i = 1$, $B_i = 0$, and $C_i \neq 0$, a moving wall is specified, C_i represents the velocity of wall relative to the adjacent fluid. If $A_i = 0$, then the shear stress must be specified (details in CFDS-FLOW3D menu, 1994).

2. Wall boundary conditions for turbulent flow.

Because of the damping effect of the wall, the transport equations for turbulent quantities does not apply close to the wall. Many variables, e.g. k and ε, vary rapidly in the near-wall regions of the flow. A fundamental problem is that the model equations, as defined previously, do not accurately represent the turbulence in the near-wall region. The analytical method of dealing with this problem is to add extra source terms to the transport equations for k and ε and use an extremely fine grid close to the surface so that the first few points are within the laminar sub-layer. Although this

procedure has been successful in describing the damping effect of the wall, a vast number of grid points will be needed (i.e., large computer memory and CPU time demanding) and this is impractical for the three-dimensional airflow in complex geometries. The alternative is to extend the Couette flow analysis and apply algebraic relations, the so-called logarithmic laws or wall function concepts, close to the wall.

The main idea of the wall function approximation is based on this: the flow in near wall region can be divided into three sublayers, i.e., laminar sub-layer, buffer zone, fully turbulent layer, see figure 4.7. In the laminar sub-layer, laminar viscosity becomes more important than turbulent viscosity and plays a dominant role in that region due to the damping effect of the wall. The buffer zone is the region of transition from laminar to turbulent. At a point outside the buffer zone, turbulent shear stress becomes significant and overwhelms that area. Although the flow in a near wall region comprises three zones, the wall function approach is to assume that the flow can be represented by a laminar region and a turbulent region. Three scalar variables, i.e., scalar velocity u^+, scalar co-ordinate y^+ and scalar temperature T^+, have been defined in wall function approach:

$$y^+ = \frac{y\left(C_\mu^{1/4} k^{1/2}\right)}{\nu} \qquad (4\text{-}114)$$

$$u^+ = \frac{u\left(C_\mu^{1/4} k^{1/2}\right)}{\tau_w/\rho} \qquad (4\text{-}115)$$

and

$$T^+ = \frac{(T - T_w)\left(C_\mu^{1/4} k^{1/2}\right)}{\left(q_w/\rho C_p\right)} \qquad (4\text{-}116)$$

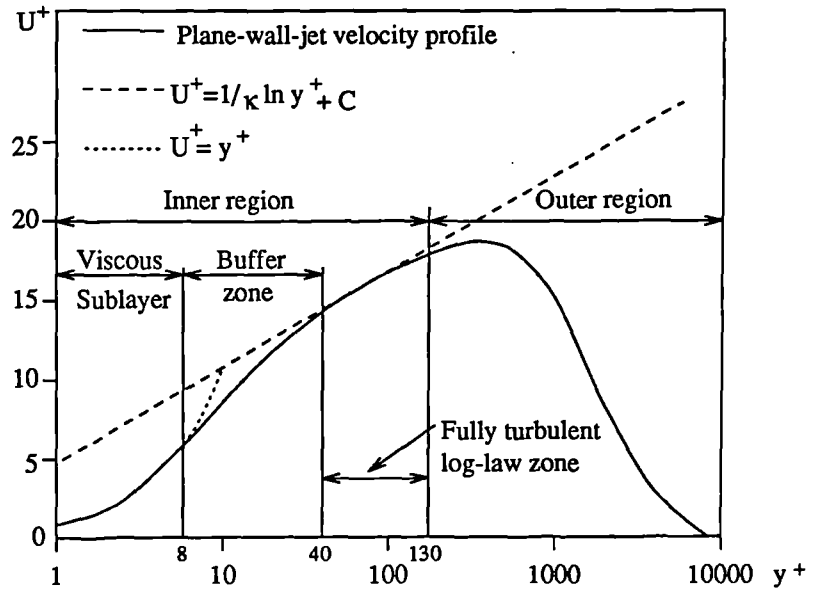

Figure 4.7 Near-wall regions in turbulent flow regime (Launder, et al 1989)

Within the laminar region, viscous effects dominate and the wall shear stress τ_w is described by the usual Couette flow expression ($\tau_w = \mu\frac{u}{y}$, u denotes the parallel velocity relative to the wall), i.e., $u^+ = y^+$ and $T^+ = \sigma_l y^+ (\sigma_l = 0.71)$. At the point outside the laminar region turbulent shear becomes significant and it can be shown that when the generation and dissipation of energy is in balance then $\tau = \rho C_\mu^{1/2} k$ and the corresponding expressions will have to be deduced. Here, y_0^+ denotes the junction point of the laminar region and

turbulent region (for smooth wall surface, y_0^+=11.6), then the wall function can be expressed as below(see Launder & Spalding 1974):

$$u^+ = \begin{cases} y^+ & y^+ < y_0^+ \\ \frac{1}{\kappa}\ln(Ey^+) & y^+ > y_0^+ \end{cases} \tag{4-117}$$

$$T^+ = \begin{cases} \sigma_1 y^+ & y^+ < y_0^+ \\ \sigma_T\left[u^+ + f\left(\frac{\sigma_L}{\sigma_T}\right)\right] & y^+ > y_0^+ \end{cases} \tag{4-118}$$

$$\varepsilon = \frac{C_\mu^{3/4} k^{3/2}}{\kappa y} \tag{4-119}$$

Here $f\left(\frac{\sigma_L}{\sigma_T}\right)$ is a function of the ratio σ_L/σ_T, called Jayatilleke formula, defined by:

$$f\left(\frac{\sigma_L}{\sigma_T}\right) = 9.24\left[\left(\frac{\sigma_L}{\sigma_T}\right)^{0.75} - 1\right] \times \left\{1 + 0.28\exp\left[-0.007\left(\frac{\sigma_L}{\sigma_T}\right)\right]\right\} \tag{4-120}$$

The junction point $(y^+ = y_0^+)$ of these layer is where the linear velocity profile in the laminar sub-layer, meets the logarithmic velocity profile in the turbulent region, see figure 4.8. Wall function approach, which is a special method for local treatment of the flow characteristics, is necessary for the turbulent flow because of the steep variation in fluid properties adjacent to a wall and the limitations in the general turbulence model.

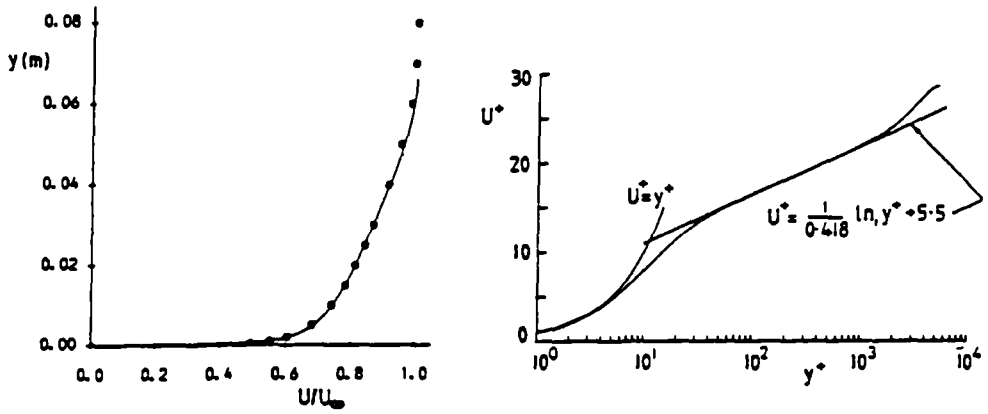

a) Linear plot b) Log-law plot

Figure 4.8 Velocity profile in flat-plate boundary layer (Launder, et al. 1989)

3. Wall boundary conditions for scalar variables

The formula for the value of scalar variables at wall surface is expressed in the general mixed form:

$$A\Phi_{iw} + BJ_w = C \qquad (4\text{-}121)$$

Here Φ_{iw} is the value of Φ at the wall surface, $J_w = \left(\Gamma_\Phi \frac{\partial \Phi}{\partial n}\right)_w$ is the flux at the wall surface, e.g., the heat transfer boundary conditions of wall surface are specified in terms of temperature, then:

$$AT_w + BQ_w = C \qquad (4\text{-}122)$$

where $Q_w = \left(\lambda \frac{\partial T}{\partial n}\right)_w$ is the heat flux at the wall surface. If B=0, A=1, C≠0, the wall surface temperature is specified to a desired value. If A=0, B=1, C≠0, the heat flux must be specified at the wall surface. A special treatment is required for equation (4-122) due to the potentially non-linear relationship between enthalpy and temperature (details in Chapter 8).

§4.3.6 Solution of the Algebraic Discretisation Equations

All governing equations have now been integrated over each finite volume (cell), brought onto a linearized form and the proper boundary conditions have been applied. All these actions result in a set of linear algebraic equations on the form of equation (4-68). The equation can be regarded as ' belonging ' to a particular variable and to a particular cell. It is now possible to assemble all the discretised algebraic coefficient equations on a matrix form and solve the system directly using an algorithm called ' SIMPLE ' or ' SIMPLEC '.

I. SIMPLE and SIMPLEC algorithm

This approach is very time consuming and an iterative method is much more comprehensive. One of the easiest and a quite effective methods is the Tridiagonal-Matrix Algorithm (TDMA) extended to three dimensions by iteration. The method works at one plane at the time and in this plane the equations are solved along a chosen line. All values except the value in the actual cell are assumed known. The method is straight forward and is repeated until a converged solution is obtained in all cells.

The most important step in the whole solution procedure is that the special treatment of pressure is slightly different from the others, since it does not obey a transport equation. Instead, simplified versions of the discrete

momentum equations are used to derive a functional relationship components in each cell. Substitution of this expression into the continuity equation leads to an equation linking the pressure-correction with the continuity error in the cell. This set of simultaneous equation is passed to a linear equation solver. The solution is used both to update the pressure and to correct the velocity field through the functional relationship in order to enforce mass conservation. The implementation of this pressure-correction step can give rise to several different velocity-pressure coupling algorithm, of which the SIMPLE, which stands for Semi-Implicit Method for Pressure-Linked Equations, algorithms the most widely used.

The main solution steps of the SIMPLE algorithm used to solve the set of equations (listed in Table 4-1) can be summarised in the following way:

a) Initialise or guess pressure filed P^*;

b) Assemble coefficients for all momentum equations;

c) Impose boundary conditions for momentum equations;

d) Solve for U^*, V^* and W^* by TDMA technique;

e) Solve the P' equation;

f) Calculate P^{**} by adding P' to P^*;

g) Obtain new U^*, V^* and W^* from pressure-correction formulae;

h) Assemble coefficients for other variables Φ's (such as T, c, k and ε);

i) Impose boundary conditions for those equations;

j) Solve for those Φ's by the TDMA technique;

k) If not converged, P^* is replaced by P^{**}, go to step 2 and repeat the whole procedure until a converged solution is obtained.

In the SIMPLE procedure, the pressure and velocity components can be written as:

$$P^{**} = P^* + P', \qquad U^{k**} = U^{k*} + U^{k\prime} \tag{4-123}$$

Both guess variable and corrected ones have to satisfy the continuity equation, then according to equation (4-106), we have

$$a_P^k U_P^{k**} = \sum_{n,K} a_n^k U_K^{k**} + S_C' \Delta V_k - (P_P^{**} - P_K^{**})\Delta A_k \tag{4-124}$$

and

$$a_P^k U_P^{k*} = \sum_{n,K} a_n^k U_K^{k*} + S_C' \Delta V_k - (P_P^{*} - P_K^{*})\Delta A_k \tag{4-125}$$

Subtracting equation (4-125) from equation (4-124), we obtain:

$$a_P^k U_P^{k\prime} = \sum_{n,K} a_n^k U_K^{k\prime} + (P_P' - P_K')\Delta A_k \tag{4-126}$$

To speed up convergence and improve the stability of the numerical solution, various attempts have been made to modify the SIMPLE algorithm. Because the term $\sum_{n,K} a_n^k U_K^{k\prime}$ has been ignored in SIMPLE method when equation (4-126) is used for correcting the velocity, and exaggerated pressure correction results which must be compensated for by under-relaxation method (details in §4.3.7). A SIMPLEC algorithm proposed by van Doormal and Raithby

(1984) is a modification of the original SIMPLE algorithm which differs in its derivation of a simplified momentum equation. In this method the velocity correction $\sum_{n,K} a_n^k U_K^{k\prime}$ is transferred to the l.h.s. of equation (4-126) and the velocity correction equation becomes:

$$U_P^{k\prime} = \frac{\Delta A_k}{a_P^k - \sum_n a_n^k}\left(P_P' - P_K'\right) \qquad (4\text{-}127)$$

All the other equations in SIMPLEC are identical to those described earlier in SIMPLE with a_P^k replaced by $a_P^k - \sum_n a_n^k$. A trivial amount of work is required for SIMPLEC as compared with SIMPLE, so the cost may be regarded as nearly the same. For a number of model problems, SIMPLEC has proved less sensitive to selection of under-relaxation factors and has required less under-relaxation. Both SIMPLE and SIMPLEC algorithm have been implemented in the CFDS-FLOW3D program.

II. Co-ordinate transformation between physical and computational spaces

It should be noted that all iterations are proceeded in computational space (i.e., single rectangular geometry space) in CFD technique. The transformation between physical and computational space is made by the Jacobian tensor calculus. The procedure may be simplified as follows:

$\left(x^i\right)$ = Cartesian physical space co-ordinates;

$\left(\xi^i\right)$ = General non-orthogonal computational space co-ordinates;

$J^i_j = \dfrac{\partial x^i}{\partial \xi^j}$ = Jacobian matrix;

$\overline{J}^i_j = \dfrac{\partial \xi^j}{\partial x^i} = \left(J^{-1}\right)^i_j$ = Inverse Jacobian matrix;

$|J| = \det\left(J^i_j\right)$ = Jacobian determinant;

$A^i_j = |J|\overline{J}^i_j$ = Adjugate Jacobian matrix.

Throughout, it should be assumed that the co-ordinate transformation is non-singular, i.e., that the functions $x^i\left(\xi^j\right)$ *and* $\xi^i\left(x^j\right)$ are one to one and onto. As a consequence the Jacobian matrix is non-singular, so its inverse always exists, and its determinant is always non-vanishing. Moreover, it is assumed throughout that the co-ordinate transformation is positively oriented, i.e., that a right-hand frame of local basis vectors in computational space is mapped to a right-handed frame in physical space, and vise-versa. This occurs if and only if the Jacobian determinant is everywhere positive. The main importance of the Jacobian matrix and its inverse is that, by the chain rule, they relate derivatives in physical space to derivatives in computational space as follows:

$$\frac{\partial \Phi}{\partial \xi} = \frac{\partial x^j}{\partial \xi^i}\frac{\partial \Phi}{\partial x^j} = J^j_i \frac{\partial \Phi}{\partial x^j} \tag{4-128}$$

$$\frac{\partial \Phi}{\partial x^i} = \frac{\partial \xi^j}{\partial x^i}\frac{\partial \Phi}{\partial \xi^j} = \overline{J}^j_i \frac{\partial \Phi}{\partial \xi^j} \tag{4-129}$$

Of the above two equations, the latter one is the most important, since, in the final analysis, all derivatives must be expressed relative to computational space, where variables are defined on a rectangular grid, so that derivatives may be approximated by standard finite difference operators. It is therefore to be able to obtain numerical approximations to the inverse Jacobian matrix. The basic idea to use a curvilinear Jacobian co-ordinate transformation is to map the complex flow domain in physical space to a simple rectangular flow domain in computational space. In other words, the Cartesian co-ordinate system $\left(x^i\right) = (x, y, z)$ in the physical domain is replaced by a curvilinear co-ordinate system $\left(\xi^i\right) = (\xi, \eta, \zeta)$ such that boundaries of the flow domain correspond to surfaces $\xi^i = \text{constant}$. The equations are then discretised with respect to the computational space co-ordinates. Boundary conditions may then be implemented naturally in the rectangular computational domain, at the expense of making the partial differential equations more complicated due to the non-linear co-ordinate transformation. The final converged solutions in physical space can be obtained from the corresponding computational space by the inverse co-ordinate transformation (more details in FLOW3D menu).

§4.3.7 Convergence Criterion and Convergence Control Techniques

I. Convergence criterion

As it has been noted, an iterative process is said to have converged when further iterations will not produce any change in the values of dependent variables. In fact this will never happen (or is independent of the computer and the problem) so it is necessary to establish a sufficient criterion for convergence of the iterative procedure and such termination criterion does not imply excessive computing effort. A trade-off between accuracy and computing time must be made.

An appropriate convergence criterion depends on the nature of the problem and on the objectives of the computation. The convergence criterion may be based on an acceptable value of the largest residual in the discretisation equation or an acceptable difference in the value of Φ between two successive iterations. The former approach is highly recommended because it is a method to examine how perfectly the discretisation equations are satisfied by the current values of the dependent variables. Every iterative solution involves the occurrence of residual sources after each iteration. For each grid point, a residual R_Φ can be defined by:

$$R_\Phi = \sum_{n,K} a_n \Phi_K + S_C \Delta V - a_P \Phi_P \qquad (4\text{-}130)$$

When the iterative process has converged R_Φ will of course be zero. A suitable convergence criterion to terminate the iterative procedure is to require that the largest value of $|R_\Phi|$ be less than a certain small number. But how small? The answer is that it has to be determined in each case because R_Φ is dependent of the problem which again means that a large R_Φ in one problem can cover a nearly converged solution while a small R_Φ in another case does not guarantee a converged solution. A way to overcome this will be to normalise the residual by inlet values of momentum, mass, etc., e.g., for momentum equations, we have

$$\sum R_\Phi = \frac{\sum_{P=1}^{NN}\left(\sum_{n,K} a_n \Phi_K + S_C \Delta V - a_P \Phi_P\right)}{\text{inflow}-\text{momentum}} \qquad (4\text{-}131)$$

Equation (4-131) is now relatively independent of the problem and can be used as a measure of convergence. The stop criterion is around 10^{-4} to 10^{-6}. This normalised residual ensures that the finite difference equations have been solved and arrived converged solutions.

II. Convergence control techniques.

The SIMPLE procedure with its pressure-correction technique is prone to diverge if the change of the variables is not slowed from iteration to iteration. This will lead to an unconverged solution once it happens. To obtain a steady solution, two different approaches have been developed to prevent the iteration from divergence.

a. Under-relaxation factors (URF)

Introducing under-relaxation factors, the change of a variable from the previous (old) to the current (new) iteration cycle is modified as

$$\Phi_P = \Phi_{P,old} + \alpha_\Phi \left(\Phi_{P,new} - \Phi_{P,old} \right) \qquad (4\text{-}132)$$

where α_Φ is the under-relaxation factor, $0 \leq \alpha_\Phi \leq 1$.

Under-relaxation has several interlinked purposes in the solution process. Firstly and principally, the amount by which a variable would change if its discrete transport equation were solved as it stands is reduced. In this way, difficulties caused instability due to non-linearity are overcome. The smaller this factor is chosen, the more under-relaxation is employed. Under-relaxation may also be regarded as a form of pseudo-time evolution with a different effective time step in each cell. A small URF (close to 0) corresponds to a short time step; while a high URF (close to 1) corresponds to a long time step.

A secondary purpose of under-relaxation which is a consequence of modifying the equations in the way described above is that the linear equation solver is presented with an easier problem to solve. A small URF will yield a strongly diagonally dominant matrix, and hence, a more accurate solution of the equations with a fixed amount of work.

It should be noted that the under-relaxation factors must be optimised. In other words, the α_Φ-values are maximised without causing divergence. A smaller URF (close to 0) can greatly slow down the convergence rate. Previous researchers recommended that α_Φ-values should not be less than 0.1. In CFDS-FLOW3D code, the default values of URF for both SIMPLE and SIMPLEC algorithm are listed in Table 4-3.

Table 4-3 The default values of URF in SIMPLE and SIMPLEC

Variable	SIMPLE	SIMPLEC
U	0.6	0.65
V	0.6	0.65
W	0.6	0.65
P	0.4	1.0
T	1.0	1.0
k	0.6	0.7
ε	0.6	0.7

The above default settings are not suitable for all cases studied in the current research. The modifications will have to be made. The α_Φ-values in this research vary in the range of 0.1~0.7.

b. False time step factors (FTS)

The circumstance frequently encountered in CFD applications is that a steady state calculation is neither converging nor diverging. It is possible that a steady state solution does not exist. This is particularly likely for laminar flows at Reynolds numbers where transition to unsteady flow may be expected. The symptoms are possible even for flows which have steady state

solutions. In this situation, a steady state calculation may be considered as a transient calculation with infinite time step. If a time accurate simulation of the flow from its initial quess to its steady state solution in a very complex manner, then it is quite likely that an attempt to reach the steady state solution in a single time step will overshoot the mark and never recover. This is particularly true for high compressible flow and multi-phase flows, where many complex interacting shock waves may have to pass through the system before a steady state is established. It is also true for flows which are strongly buoyancy driven and internal gravity waves have to dissipate through the system before a steady state is reached.

If the above situation is suspected, the single under-relaxation factor can not help achieve the steady state solution. An alternative way to obtain steady state solution is by using the false time stepping as an under-relaxation parameter. If a small time step is used , the transient term in the governing equations become dominant corresponding to heavy under-relaxation and numerical oscillations are suppressed. The main drawback of false time stepping is that a knowledge of time scales is required. No universal value of FTS is available. However, the more physical character of false time stepping may prove beneficial, particularly when several separate influences are driving the flow, e.g., a forced flow with buoyancy. A typical false time-stepping ΔT for a certain fluid flow is defined by:

$$\Delta T = \frac{\Delta l}{V} \qquad (4\text{-}133)$$

where Δl — typical cell size of flow domain;

V — typical fluid velocity of flow domain.

Similar to the under-relaxation factor, false time step factor must be optimised as well. The procedure is first to try a small time-stepping (i.e., $\frac{1}{10}\Delta T$), then increase the time-stepping to a maximum value without causing divergence. It is possible to use false time steps and under-relaxation factors simultaneously. Both under-relaxation factors and false time-stepping factors are used in this research. The details will be seen in next few chapters.

In general, the majority of CFD researchers has experienced divergence or intolerable slow convergence of the iteration. This is because no recommended values of under-relaxation factor and false time-stepping factor are available instantly. The optimum set of these values depends on the flow type being solved and can only be found by trial and error (details see next few chapters).

§4.4 Particle Transport Model

The flow dynamics of single particle settlement within static continuous fluid has been presented in Chapter III. In this section, a particle transport model will given to describe the particles movement through continuous fluid flow field.

§4.4.1 Equation Set of Particle Transport Model

The motion of particles in a fluid flow can be modelled in two ways: either using a multi-fluid (continuum/Eulerian) approach or by using a discrete trajectory (Lagrangian) approach. The Lagrangian particle transport model is employed in this research.

I. Basic assumptions.

The conditions of particles movement in continuous fluid flow, in this research, are in rooms (single- or two-zone areas) under mechanical ventilation. The situations are very complicated. For simplification of the simulations, the following assumptions are introduced:

i. All particles are sperical particles;

ii. Do not consider the particle rebounce once it has adhered to the solid surface;

iii. No heat and mass transfer exist between the continuous fluid and particles;

iv. Do no consider particle coagulation and break-up phenomena in particles movement;

v. All particles being tracked consist of a base substance, particularly in the current research, particles have same density according to assumption iii.

II. Equation set.

Within the particle transport model, the total flow of the particulate phase in modelled by tracking a number of sample particles through the continuum fluid separately. All sample particles share the total mass of the particle phase. Apart from the Eulerian method for solving the continuous fluid, a discrete trajectory approach (Lagrangian method) is employed in the particle tracking model. The equation of the individual sample particle movement comes directly from Newton's second law:

$$m\frac{du}{dt} = F \qquad (4\text{-}134)$$

The formation of the external forces varies according to the flow conditions. The main external forces exerted on the particle are listed below:

a. Drag force.

The drag force exerted on an immersed body by a moving fluid arises from two mechanisms. The first is due to the viscous surface shear stress, and is called skin friction. The second is due to pressure distribution around the body and is called the form drag. The total drag force F_D exerted on a sample particle is then represented as follows:

$$F_D = \frac{1}{8}\pi d_p^2 \rho C_D |V_R| V_R \tag{4-135}$$

where V_R is the relative velocity between the fluid and the particle, and defined as:

$$V_R = U_f^i - u_p^i \tag{4-136}$$

here U_f^i — velocity components of continuous fluid;

u_p^i — velocity components of particle.

C_D is the drag factor and given by:

$$C_D = \frac{24}{R_{e_p}}\left(1 + 0.15 R_{e_p}^{0.687}\right) \tag{4-137}$$

The particle Reynolds number R_{e_p} is defined by

$$R_{e_p} = \frac{\rho |V_R| d_p}{\mu} \tag{4-138}$$

here d_p is the diameter of the particle, ρ and μ are the density and viscosity of the continuum.

Corresponding to the drag force on the particle, there is a same force F_i acting on the continuous fluid being balanced to F_D according to Newton's third law. So the term, F_i, which represents the momentum transfer between the fluid and the particles, is appearing on the right-hand side of momentum equation in Table 4.1 and given by

$$F_i = \frac{3}{4}\frac{C_D}{d_p}\rho|V_R|V_R \qquad (4\text{-}139)$$

In equation (4-139), F_i counts on the action of all sample particles.

b. Gravitational force.

The gravitational force which the particle experiences can be expressed by:

$$F_B = -\frac{1}{6}\pi d_p^3(\rho_p - \rho)g \qquad (4\text{-}140)$$

where ρ_p is the density of particle, g is the gravitational acceleration.

According to equation (4-140), we can see that the lifting force, $\frac{1}{6}\pi d_p^3 \rho g$, exerted on the particle from the surrounding fluid, is taken into account. If the density difference between the particle and the continuum is large enough,

e.g., $\rho_p = 865\,kg/m^3$ (smoke particle) and $\rho = 1.209\,kg/m^3$ (air medium), the term $-\rho g$ in equation (4-140) can be ignored.

c. Rotational terms in a rotating co-ordinate system.

If the system rotates about a certain axis, then the extra centrifugal and Coriolis forces generated due to the rotation should be considered in the particle movement. Corresponding centrifugal and Coriolis forces can be expressed by:

$$F_R = \frac{1}{6}\pi d_p^3 \rho_p (-\omega\times\omega\times\mathbf{x}-2\omega\times\mathbf{u}) \qquad (4\text{-}141)$$

here $\mathbf{u}$ — velocity vector of the particle;

$\mathbf{x}$ — position vector of the particle to the rotational axis;

ω — rotational velocity vector about the rotational axis.

The particle transport equations are a set of ordinary differential equations. This set of equations is also implemented in CFDS-FLOW3D for solving the particle movement.

III. Particle tracking process.

Similar to the calculation of continuous flows in computational space, the particle tracking procedure is also carried out in computational space for ease

of tracking and where it crosses control volume boundaries. In this space, the equations for particle position have the form:

$$\frac{d\xi}{dt} = \mathbf{C} \qquad (4\text{-}142)$$

where ξ is computational co-ordinate, t is time and **C** is computational velocity.

The computational velocity is obtained from the physical velocity of the particles **u** by calculating the Jacobian of the co-ordinate transformation from the vertices of the control volumes and using the equation:

$$\mathbf{C} = \left(\frac{\partial \mathbf{x}}{\partial \xi}\right)^{-1} \qquad (4\text{-}143)$$

where **x** is position in physical space.

In order that this transformation is continuous across control volume boundaries, the Jacobian is calculated continuously from the discrete information available directly on edges of control volumes using Hermits interpolation within each block of the grid. Thus, the physical velocity of the particle is always smooth across such boundaries. The positions of particles in physical space are only calculated for output purposes.

§4.4.2 Boundary Conditions and Solutions of Particle Tracking

The most important information for particle transport is the physical state of the particles and the initial conditions of the particles in the flow domain.

The physical state of the particles includes:

a) Total particle mass flowrate and the mass flowrates carried by sample particles in each size group; these mass flowrates should add up to the total mass flowrate;

b) Number of sample particles required to be tracked;

c) Particle size groups;

d) Number of sample particles in each size group;

e) Particle density.

The initial conditions of the particles include:

a) The starting positions of sample particles. The basic unit in the flow domain is control volume, so the initial positions of sample particles should be specified in terms of the control volume, e.g., the initial positions of particle can be defined at the cell centres or the cell faces as required. All particleswhich have same size and start from the same positions as the sample particle will follow exactly the same track as the sample particle does;

b) The initial velocities of particles should be specified before the tracking starts according to the conditions of the flow.

II. Iterations of fluid flow and particle tracking.

In CFDS-FLOW3D code, both Eulerian and Lagrangian methods are implemented. The partial differential equations (Eulerian approach) are solved for the continuous fluid flow calculation and then the ordinary differential equations are solved for the particles movement. So the particle transport model forms an extra loop in the solution procedure outside the flow iteration. A coupling procedure is needed to balance the interactive source terms between the continuous fluid and the sample particles. For each control volume, these source terms are calculated as a sum of the contributions of each of the representative particles, weighed according to the amount of the particle mass flow assumed to be carried by the particle as it traverses the control volume. So the following iterations are employed for the flow calculation/particle tracking:

1) Carrying out N iterations of the continuous fluid equations;

2) Tracking the sample particles through the continuous phase;

3) Calculating the interactive sources between the continuous fluid and particles;

4) Coupling these sources back to the fluid equations:

5) Repeating until convergence.

Normally, one coupling process is enough for the iteration because the values of the interactive sources are very small and can be ignored to the continuum, but these terms have a significant influence on the particle movement. The above procedure solves the particle equations for position and velocity, as well as obtaining the source terms and coupling both equation sets simultaneously.

§4.5 Conclusions

A detailed mathematical description and numerical solution technique of fluid flow and particle movement have been discussed in this chapter. The general governing equation of fluid flow is non-linear, inhomogeneous and highly coupled partial differential equation. Several turbulence models have been introduced to solve the turbulent characters involved in the general equation for turbulent flow regime. The particle transport equation is an ordinary differential equation which includes a source term for balancing the interactions between fluid and particles. An extra coupling iteration loop is required for tracking the particles through the continuous fluid. The outline of the whole solution procedure can be summarised in following way

General Description	Technique Used
1. Establish the equation set for both fluid and particle, obtain the corresponding PDEs and ODEs and choose the appropriate turbulence model.	Laws of conservation of mass, momentum and energy, etc. k-ε turbulence model is selected in the study.
2. Look into the physical nature of the governing equations (PDEs) and select discretised technique.	Finite volume (FV) technique, implicit method.

3. Perform the numerical discretisation.	Integrate over a finite volume, linearization of the equations and and the source terms and decoupling of the equations.
4. Improve the stability by selecting the proper differencing scheme.	HYBS: robust in convergence, easy to compute; PLDS: good stability, more accurate than HYBS around $P_e = 2$, easy to compute. QUICK: less stable —not bounded (may produce overshoots), best accuracy, more complex to compute, lower rate of convergence.
5. Solve the pressure-velocity coupling by appropriate algorithm.	The improved SIMPLEC method is employed.
6. Impose boundary conditions	Three different types of boundary are presented: Flow boundary (inlet, mass flow and pressure); Symmetry plane; wall boundary (velocity, turbulent characters and scalar variables).

7. Solve the system of equations by iterations.	TDMA method is used to solve the algebraic equations, under-relaxation and false-time step techniques are used to improve the convergence of iterations.
8. Track sample particles through the continuous fluid.	Solve ODEs and calculate the drag force exerted on the particle (i.e., interactive forces).
9. Coupling the interactive forces between fluid and particles.	balancing two equation sets.
10. Repeat until convergence.	Repeat from step 3 as required.

The above procedures will be applied in the CFD modelling of airflow patterns and aerosol particle movement in ventilated multi-zone systems.

CHAPTER V

FLOW CHARACTERISTICS IN VENTILATED SPACE

Abstract

A numerical simulation of turbulent flow in a room ventilated by an air jet has been set out in this chapter. A set of equations based on momentum and mass conservation has been solved by using a commercial CFD code, CFDS-FLOW3D. The numerical solutions show good agreements with the relevant experimental data (i.e., Nielson's measurement). The discussions of the relevant convergence difficulties and control methods have also been presented in the chapter. The validation of the numerical simulations proves that CFD method is a useful tool to predict and supply detailed information of the flow phenomena in ventilated space. The work presented here also helps establish confidence and carry on more complicated CFD modelling in later chapters.

§5.1 Introduction

Mechanical ventilation of enclosures has been used widely in many modern buildings. Much effort has been done to develop new and better ways to ensure the comfortable indoor environment for the occupants in the ventilated spaces with a minimum of energy consumption.

In order to fulfil these goals in the design of an air conditioning system, it is important to be able to predict the indoor air quality in the ventilated room. The indoor air quality includes two aspects: thermal comfort and pollutant distribution. Both are governed by several parameters, e.g., heat production and loss, room geometry, velocity distribution, turbulence level, temperature distribution, etc.

As mentioned above, one of the main purposes of a ventilation system is to ensure uniform and acceptable conditions in the occupied zone. To design such a system is often a difficult task because the prediction of the flow pattern in such a system is complicated. In a ventilation system, the fresh air is normally led into an enclosure through one or several inlets from plant located outside the occupied zone, e.g., see figure 5.1. The flow of a jet differs from other kinds of flow because a jet is surrounded on one or more sides by a free boundary of the same fluid. These jets have significant impact on the flow field in the entire enclosure as well as in the occupied zone. Under such situations, either a free air jet flow or a wall jet flow is produced as a result. In ventilated

space, the air jet is the main distribution medium of thermal energy, moisture, and fresh air into a room and even the contaminant particles distribution in that space. It is therefore vitally important that the jet is sufficiently mixed with the room air before the air extraction point in the room is reached. Failure to satisfy the mixing purpose may cause some regions of the room improperly ventilated and result in unacceptable indoor air quality.

The work reported in this chapter deals with the prediction of isothermal airflow patterns in ventilated enclosure.

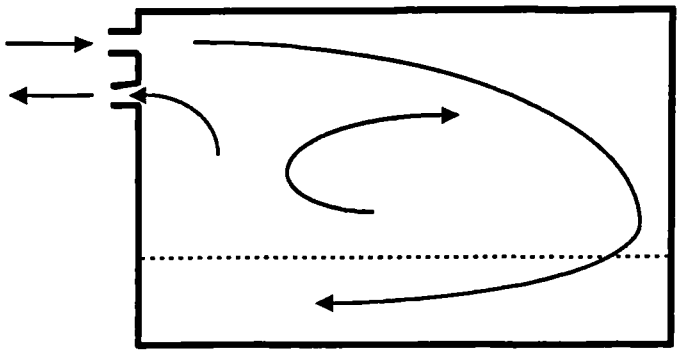

Figure 5.1 Schematic flow pattern in a ventilated room

§5.2 Free Air Jet Flow

§5.2.1 The Sketch of Free Air Jet

A free air jet is encountered when air flows from an opening or a nozzle into a space which includes some fluid medium and no solid boundaries. In the flow pattern, the static pressure within the jet is the same as the static pressure of the surrounding fluid. Under these conditions, a free turbulent shear flow is formed where a shear layer develops around the jet boundary as a result of the velocity discontinuity at this boundary. This is also referred to as the ' free shear layer flow '. Figure 5.2 describes the outline of a free jet. In ventilation systems, such jet flow is normally turbulent and three-dimensional. The important characteristics of a free jet flow is that: a. the velocity in the main flow direction is substantially greater than any others; b. changes of quantities in the direction of the main flow are correspondingly slow with respect to those in the transverse direction.

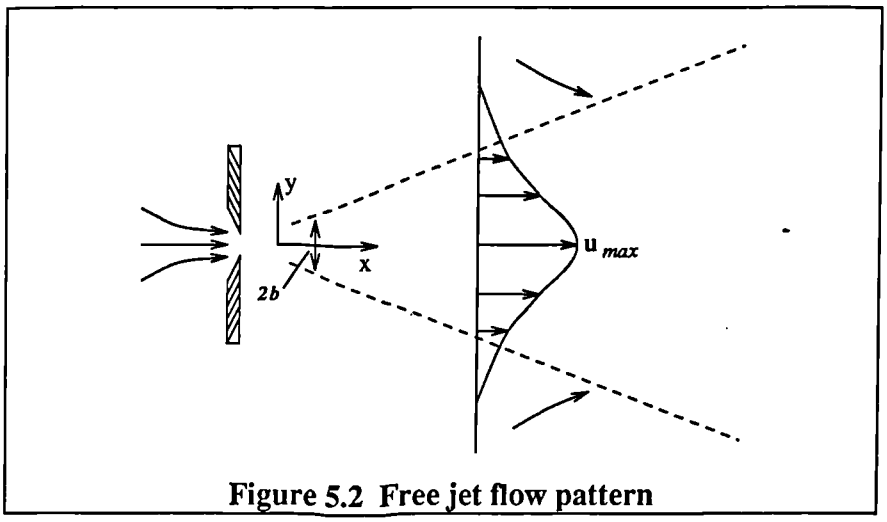

Figure 5.2 Free jet flow pattern

§5.2.2 Characteristics of Free Air Jet

A free jet may be produced by a circular, cylindrical or rectangular opening discharging air into a large enclosure containing a stagnant mass of air. Figure 5.3 presents a typical free jet plot. Four zones may be identified for a free jet according to how the centreline velocity of the jet varies with distance from the opening.

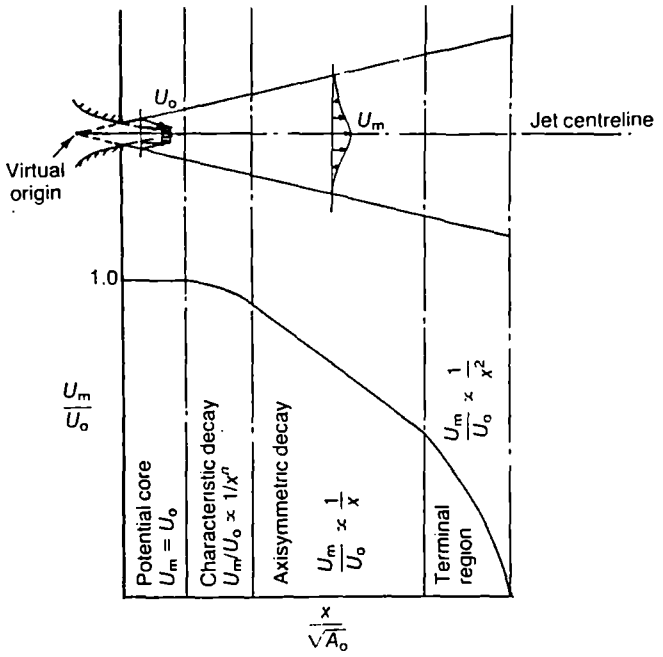

Figure 5.3 A typical free jet plot (Awbi, 1992)

a. Potential core region: This is the region immediately downstream of the supply opening where mixing of the jet fluid with the surrounding fluid is not complete. The length of the core depends on the type of opening and the turbulence of the air supply but usually it extends to 5~10 equivalent opening

diameters. In this region the centreline velocity, U_m, is constant and equal to the supply velocity U_o;

b. Characteristic decay region: After the consumption of the potential core by the free shear layer the centreline velocity begins to gradually decrease as follows:

$$\frac{U_m}{U_o} \propto \frac{1}{x^n} \qquad (5\text{-}1)$$

The extent of this region depends on the shape of the supply opening. The value of n is usually associated with aspect ratio (defined as ratio of length to height) of the opening;

c. Axisymmetric decay region: In this region, the jet is dominated by a highly turbulent flow generated by viscous shear at the edge of the shear layer. For three-dimensional jets it is usually referred to as the ' fully developed flow region ' and normally extends to about 100 equivalent diameters of opening. The centreline velocity decreases inversely with the distance from the opening, i.e.:

$$\frac{U_m}{U_o} \propto \frac{1}{x} \qquad (5\text{-}2)$$

d. Terminal region: This is a region where diffusion grows rapidly and the jet becomes indistinguishable from the surrounding air. The centreline velocity decays with the square of the distance from the opening, i.e.;

$$\frac{U_m}{U_o} \propto \frac{1}{x^2} \qquad (5\text{-}3)$$

In practice, the potential core and the characteristic decay regions are the dominant regions for a two-dimensional free jet (plane jet); while the potential core and the axisymmetric decay regions are the main regions in a three-dimensional free jet (axisymmetric jet). Previous studies have shown that the following principles can be applied to the free jet flow:

i) The total momentum across any section of the jet, M_x, remains constant and it is equal to the initial momentum at the supply opening, M_o, thus:

$$M_x = M_o = \int_o^A \rho u^2 dA = \rho U_o^2 A_o \qquad (5\text{-}4)$$

where A_o — the effective area of the supply opening;

u — the velocity component in the x direction of the area dA;

ρ — the density of fluid.

ii) The profile of the u component of velocity across the jet has the same shape at different axial distances from the supply opening;

iii) The static pressure across the jet is constant and equal to the surrounding pressure.

The above assumptions are helpful in obtaining the solutions to the flow in the intermediate regions of a free jet, including the velocity profiles, the decay of centreline velocity, flow entrainment, etc. The typical free air jets include: circular jet, plane jet, radial jet, etc.

§5.3 Turbulent Wall Jet Flow

In practice, free air jet flow rarely happens in room air flow due to the restriction of boundary surface on one side of the air supply opening. In most cases the air is injected through an opening which is bound by a flat surface on one side (e.g., the ceiling surface for high level supply or the floor surface for low level openings) and the inlet velocity at the exit of the opening is often parallel to such surfaces. A wall jet flow is produced under such conditions. It is common practice in room ventilation to use a wall jet discharging at ceiling level so that the high-velocity region is restricted to the ceiling thus freeing the occupied zone from draught. Under normal design conditions and due to the Coanda effect, the jet remains attached to the ceiling until the opposite wall is reached or until the jet decays where it is then deflected downwards into the occupied zone.

§5.3.1 Plane Wall Jet

A plane wall jet is produced when the flow issues from a slot opening with a large aspect ratio (i.e. b/h>40) where any lateral changes in flow properties happen in a plane normal to the slot length only. Figure 5.4 shows the schematic of a plane wall jet.

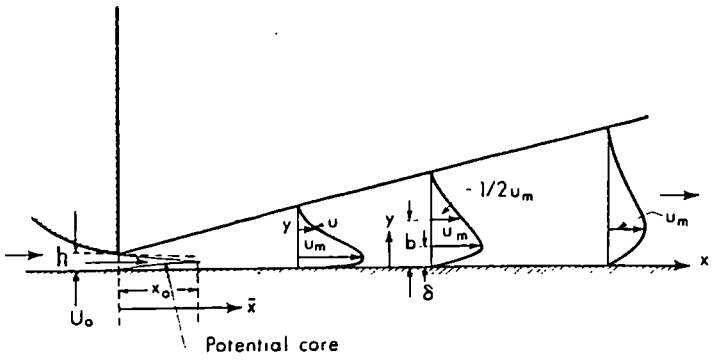

Figure 5.4 Schematic of a plane wall jet plot (Awbi, 1992)

Only potential core and characteristic decay regions are present in a plane wall jet. The region from the wall to δ is known as the boundary layer and above that is the free mixing region. The maximum velocity in the jet occurs at the point where the two regions meet. Rajaratnam (1976) proposed that the decay of the maximum velocity is proportional to the $\left(\frac{x}{h}\right)^{-\frac{1}{2}}$ and the entrainment flowrate is proportional to the $Q_o\left(\frac{x}{h}\right)^{\frac{1}{2}}$.

§5.3.2 Three-dimensional Wall Jet

A typical three-dimensional wall jet and its development along a plane surface are presented by figure 5.5.

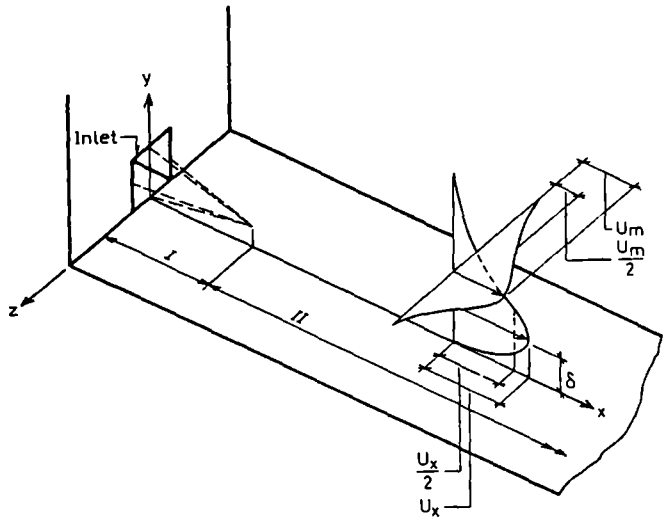

Figure 5.5 Three-dimensional wall jet plot (Rajaratnam, 1976)

The flow is produced by a rectangular opening of aspect ratio $b/h < 40$ with one large side on a flat surface. It can be generally divided into two main regions, see figure 5.5. Region I is the potential core of the jet. This core is affected by the boundary layer on the surface and the shear layer of the free boundary. The potential core is consumed at the point when these two layers

meet and the next region (II), known as the fully developed region, begins. Previous experiments have shown that region II can be subdivided into two regions. According to Viets & Sforsa (1966), from the end of region I there is a region where U_m decays roughly with $\left(x/h\right)^{-1/2}$ (same as in a two-dimensional wall jet). This region is termed the characteristic decay region and reaches up to where the shear layers from the two sides meet (Rajaratnam, 1976). In the next sub-region the velocity U_m decays approximately as $\left(x/h\right)^{-1}$ similar to the results presented by Sforza & Herbst (1967), they found a decay rate proportional to $\left(x/h\right)^{-1.14}$.

§5.4 Numerical Solutions of Wall Jet Flows

The previous section has given a brief discussion of the jet flow in ventilated space. The complexities of the involving flow phenomena turn the design of a ventilation system into a difficult task.

As previously shown, the studies of jet flow in ventilated spaces by both experiments and computations have been reported by Tollmien, Görtler, Sforza et al., Rajaratnam, Nielson et al., etc. Previous experimental investigations mainly used probes, laser-Doppler anemometry and flow visualisation techniques, etc. Some of them were proceeded in full-scale rooms, some were carried out on scaled models. These studies have provided qualitative results of the effects of air jet on the ventilated spaces. These studies were mainly intended to supply assistance for simple design procedures based on correction equations. The drawbacks of the above experimental techniques can be concluded as: a. experimental study is normally expensive and time-consuming, especially for laser-Doppler anemometry and flow visualisation; b. the accuracy of measurement is subject to unknown uncertainty in regions of high turbulence intensity and flow recirculation.

To avoid extensive experimentation, Nielson (1974) first applied CFD methods to model the airflow pattern in ventilated space. The CFD simulation results he obtained presented good agreements with the measured data. Nielson's work provided quantitative results and presented a useful method for the study of the air flow in the ventilated spaces.

The contents presented in this section include some numerical results of wall jet flow in a space by using CFD which are compared with the measured data described in Nielson's work. The simulations are meant to be an introductory study to later and more complicated CFD analyses in ventilation system (Chapter 6, 7, and 8).

§5.4.1 Test Cases

I. Geometrical configuration

The problems presented herein are based on the wall jet flow within a space investigated by Nielson, et al. (1978). The room dimensions are chosen to be the same as the test chamber used in the experiments. Figure 5.6a and b show the geometrical configurations. Table 5.1 lists all relevant geometrical information.

Table 5.1 The geometrical parameters of cases

Case No	H (mm)	L (mm)	W (mm)	h (mm)	w (mm)	t (mm)	l (mm)	w/W	Re_o
Case 1	89.3	267.9	89.3	5.0008	89.3	14.288	15.0	1.0	$5x10^3$
Case 2	89.3	267.9	89.3	5.0008	44.65	14.288	15.0	0.5	$5x10^3$

Case 1 is a jet supplied through a high level side-wall slot with the aspect ratio w/h is about 18. It can be simplified as a two-dimensional flow. Here, both two- and three-dimensional simulations are carried out for that case. The results will show the differences between these two computations. In case 2, the air enters from a long-square section at high level. The flow in the space is three-dimensional. A three-dimensional partial differential equation set is solved for this case. All cases are simulated by both coarse and refined mesh schemes.

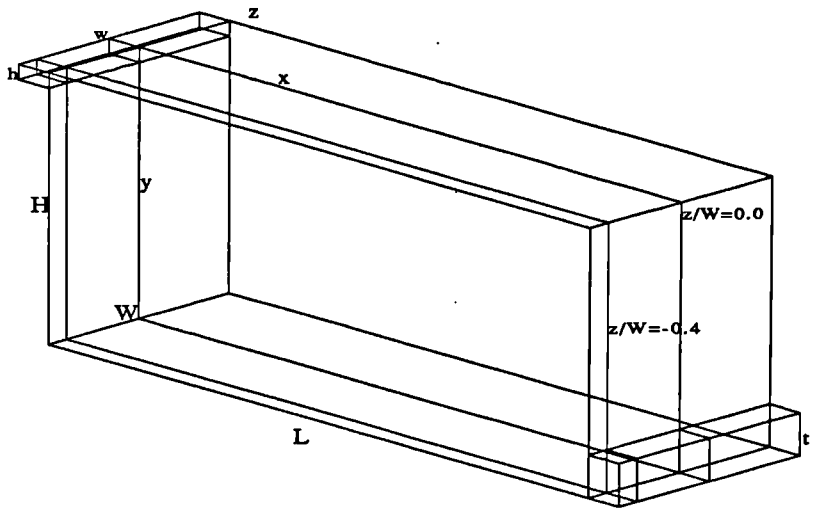

a) Plane wall jet

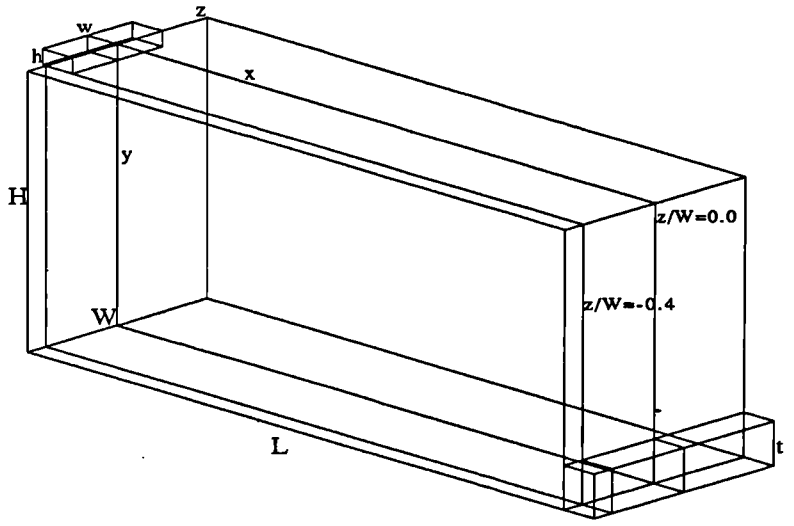

b) Three-dimensional wall jet

Figure 5.6 Geometrical configurations

II. Defining the flow phenomenon

Once the geometry of the problem is confirmed one must think about the flow itself and try to visualise what is happening to the fluid within the bounding surfaces of the flow domain. The initial step in defining the flow is to know which fluid is to be studied, i.e., the flow medium, in this study, is air at the constant temperature 20°C. The density and viscosity are known to be ρ=1.209 kg/m^3 and μ=1.812x10^{-5} kg/ms. Once the density and viscosity are known a calculation can be made of a parameter known as the Reynolds number, R_e, in here, which is defined by

$$R_{e_0} = \frac{\rho U_o h}{\mu} \qquad (5\text{-}5)$$

This parameter is useful in determining whether a flow will be laminar or turbulent. For the cases in Table 5.1, $R_{e_0} = 5\text{x}10^3$, so all the flows belong to turbulent regime. A standard k-ε model is applied in the computation.

The boundary conditions are specified as follows:

a. Inlet: A constant, uniformly distributed U-velocity distribution is specified at the inlet surface; V and W are prescribed to zero for all cases. The following empirical relations are used for describing the turbulence quantities at the inlet surface:

$$k_{in} = C_{p1}\left(U_{in}^2 + V_{in}^2 + W_{in}^2\right) \qquad (5\text{-}6)$$

$$\varepsilon_{in} = k_{in}^{1.5} \Big/ \left(C_{p2} D\right) \qquad (5\text{-}7)$$

here C_{p1} and C_{p2} are constants and take the values of 0.002 and 0.3 respectively. D is the hydraulic diameter of inlet section (defined by $D = 4A/P$, A is the area of supply cross section and P is its perimeter).

b. Wall boundary: The no-slip condition on all walls are introduced by wall functions which either can be of the logarithmic or of the linear (Couette) type depending on the value of y^+ at the first grid node (§4.3.5).

c. Outlet: The outlet conditions are set up according to mass conservation(§4.3.5).

III. Mesh schemes and computational details

For the plane wall jet (case 1) with two-dimensional simulation, the computational domain is divided into non-uniform mesh with two set of grid nodes, see figure 5.7a and b; figure 5.8a and b show the two mesh schemes used for the three-dimensional plane wall jet simulations.

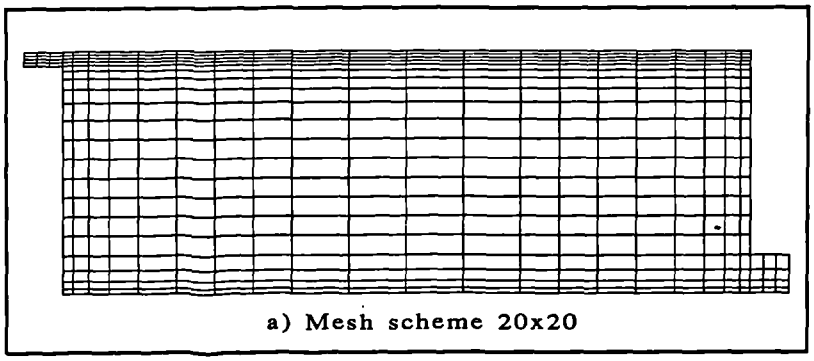

Figure 5.7a Grid nodes of two-dimensional plane jet simulation

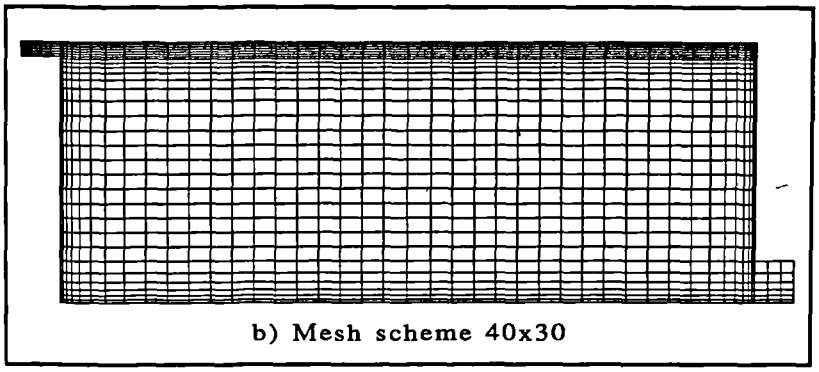

Figure 5.7b Grid nodes of two-dimensional plane jet simulation

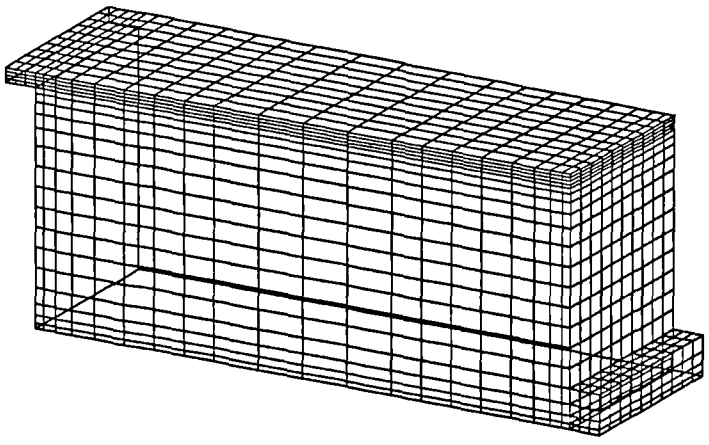

a) Mesh scheme 20x20x10

Figure 5.8a Grid nodes of three-dimensional plane wall jet simulation

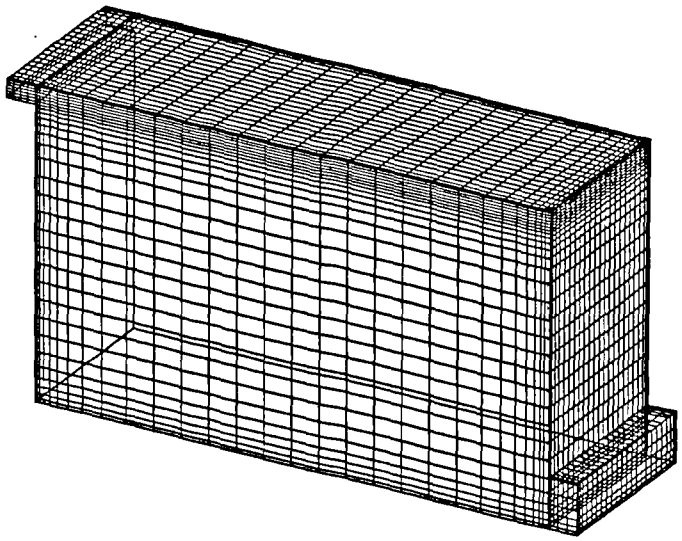

b) Mesh scheme 30x30x24

Figure 5.8b Grid nodes of three-dimensional plane wall jet simulation

For the three-dimensional wall jet flow (Case 2), two mesh schemes are applied to the computations (see figure 5.9a and b). The influence of the number of grid nodes on the final solutions can be tested according to these mesh schemes. Table 5.2 lists the details of all mesh schemes used in the simulations.

Table 5.2 Mesh schemes

Case No	Two-dimensional simulations		Three-dimensional simulations	
Case 1	20x20	40x30	20x20x10	20x20x20
Case 2	—	—	30x30x24	30x30x24

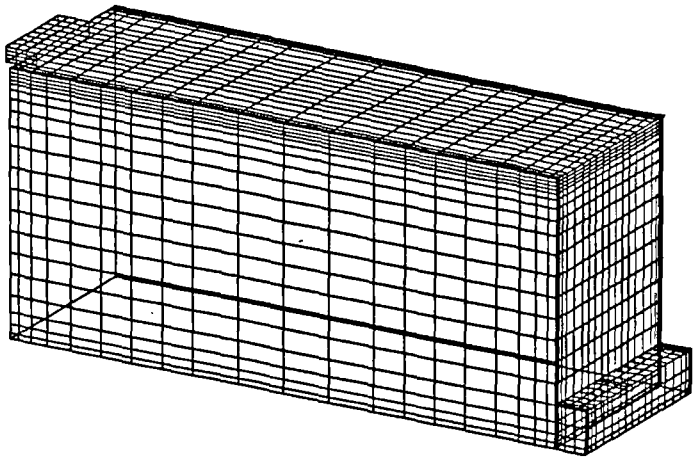

a) Mesh scheme 20x20x20

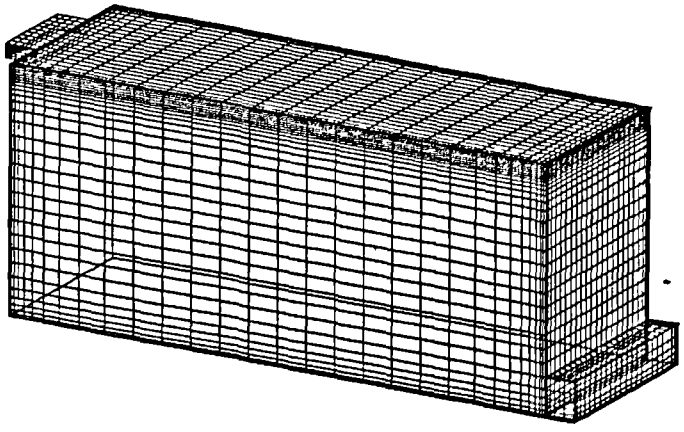

b) Mesh scheme 30x30x24

Figure 5.9 Grid nodes of three-dimensional wall jet simulation

The simulation procedures carried out by CFDS-FLOW3D code have been presented in Chapter IV. Approximately 2500 iterations are required for the two-dimensional computations and at least 5000 iterations are required for the three-dimensional simulations to obtain fully converged results. The convergence criterion is specified as the normalised mass residual falls in the range of 10^{-6} ~ 10^{-4}. Convergence difficulties maybe encountered in the above simulations. The relevant convergence control techniques are used in these simulations (detailed in next section). All simulations are carried out on a Sun SPARC2 workstation.

§5.4.2 Results and Discussions

I. Airflow patterns and comparisons of computations with measurements

a. Two-dimensional simulations of plane wall jet flow.

One of the major strengths of CFD is that it can provide detailed information of the velocity field in the space interested. The following figures present the airflow patterns in the space simulated:

a) Figure 5.10a and b describe the predicted flow patterns of two-dimensional plane wall-jet flow. The air circulation is produced by the wall jet effect.

b) The development of wall jet along the ceiling surface is shown in figure 5.11. It is interesting to notice that the maximum velocity in the ' return flow ' is not located in the centre of the room but instead closer to the side wall, see figure 5.10.

c) It is also seen that the location of the outlet creates a stagnation point near the floor. The comparisons of computational results with experimental data are shown in figure 5.12. It can be seen that the simulation with grid nodes 40x30 produces better results than that with grid nodes 20x20.

d) Figure 5.13 presents the U-velocity distribution across the space height and along the space length. Two mesh schemes produce different results. It shows that mesh scheme does affect the final computational results.

e) Figure 5.14 represents the shaded contour of U-velocity in the plane of z/W=0.0. It shows the wall jet region and decay diagram along the roof surface.

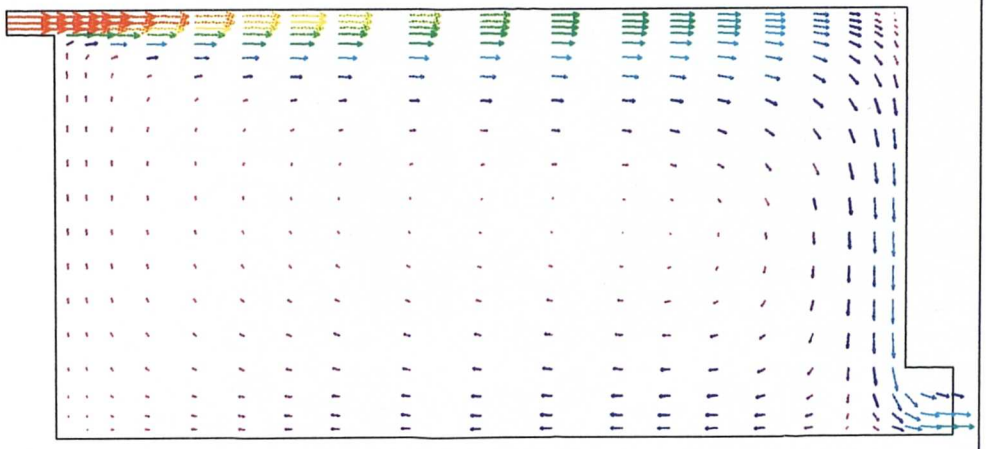

a. Vectors in centreline plane (Grid 20x20)

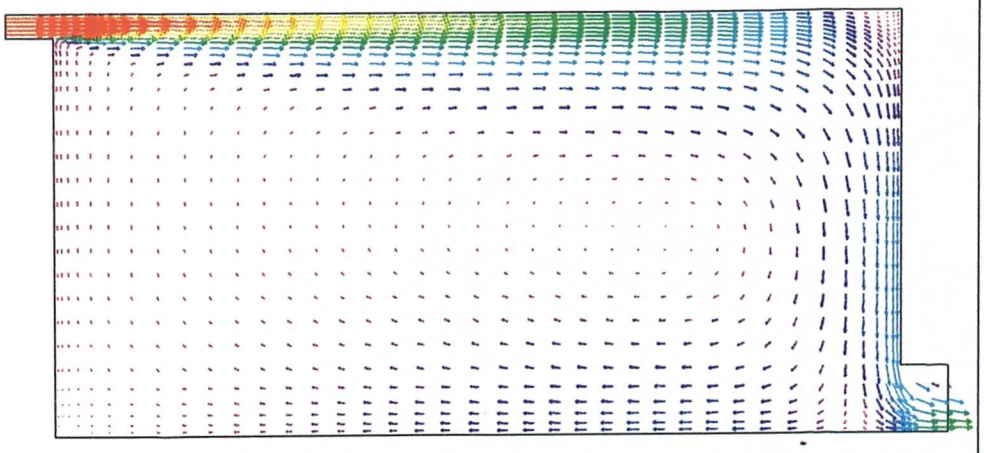

b. Vectors in centreline plane (Grid 40x30)

Figure 5.10 Velocity vectors in two-dimensional simulations of plane wall jet flow (Vector scale: ⟶ 15 m/s)

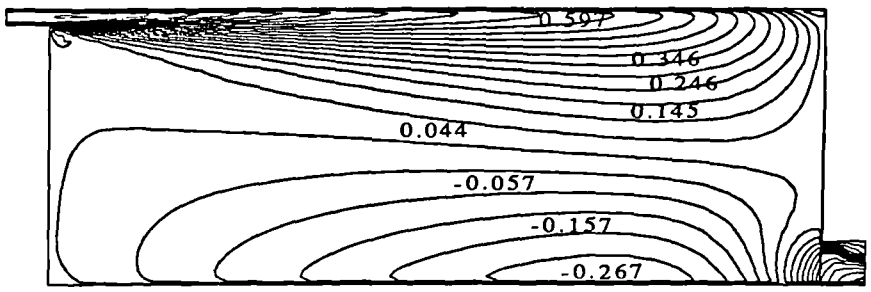

Figure 5.11 Normalised U-velocity contours in centreline plane (Grid 40x30)

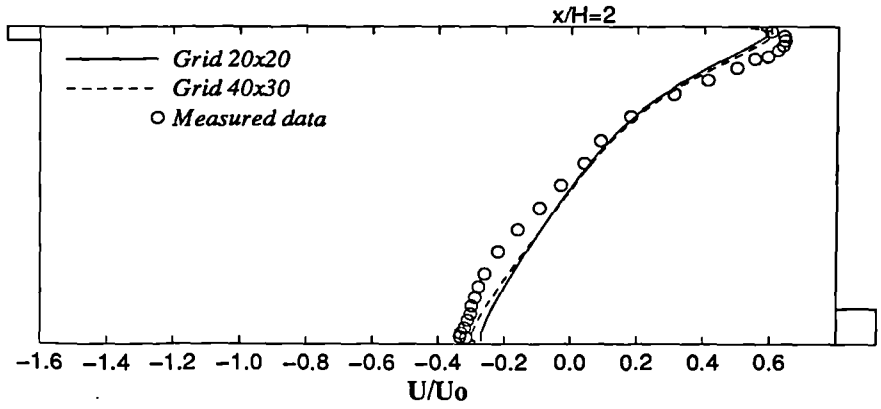

Figure 5.12 Comparisons between computed U-velocity and measured data across the chamber height (2-D simulations)

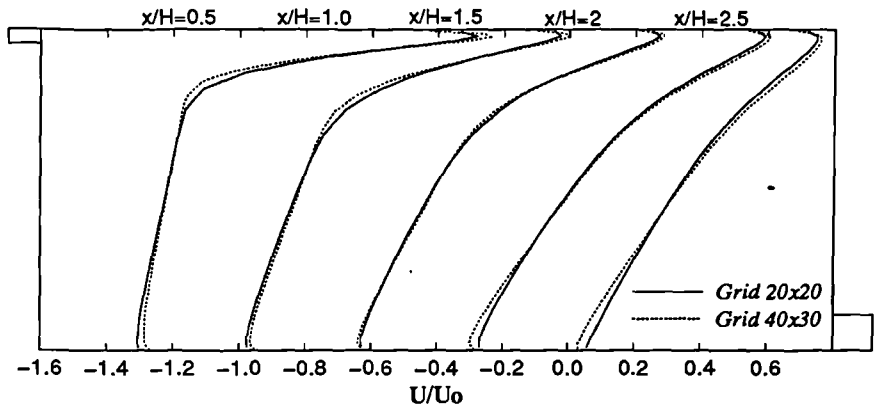

Figure 5.13 U-velocity profiles along the chamber length (2-D simulations)

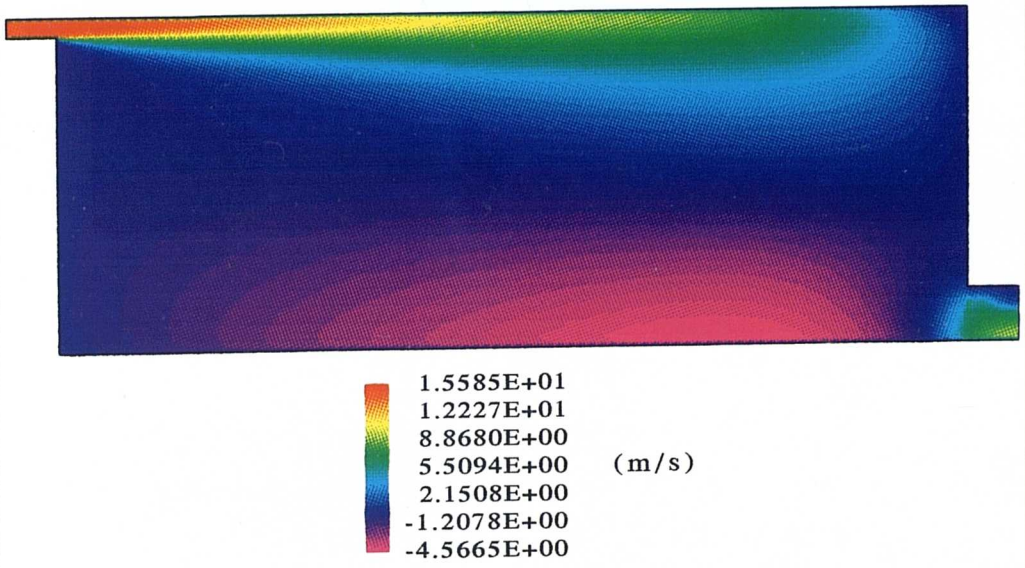

Figure 5.14 Shaded contour of U-velocity at plane of z/W=0 (Grid 40x30)

b. Three-dimensional simulations of plane wall jet flow

The three-dimensional calculations have also been proceeded on the plane wall jet flow with the same parameters as in two-dimensional simulations. The two mesh schemes used are shown in figure 5.8a and 5.8b. The results are as follows:

- Figure 5.15 presents the comparisons between computations and measurements. It can also be seen that the fine mesh produces slightly better results than the coarse mesh does;
- The flow patterns in different planes are described in figure 5.16a, 5.16b, 5.17a and 5.17 b;
- Comparing figure 5.16a with 5.16b and figure 5.17a with 5.17b, it can be seen that the flow patterns are similar at planes of z/W=0.0 and z/W=-0.4. That means the two-dimensional simplification of plane wall jet flow is reasonable and acceptable.

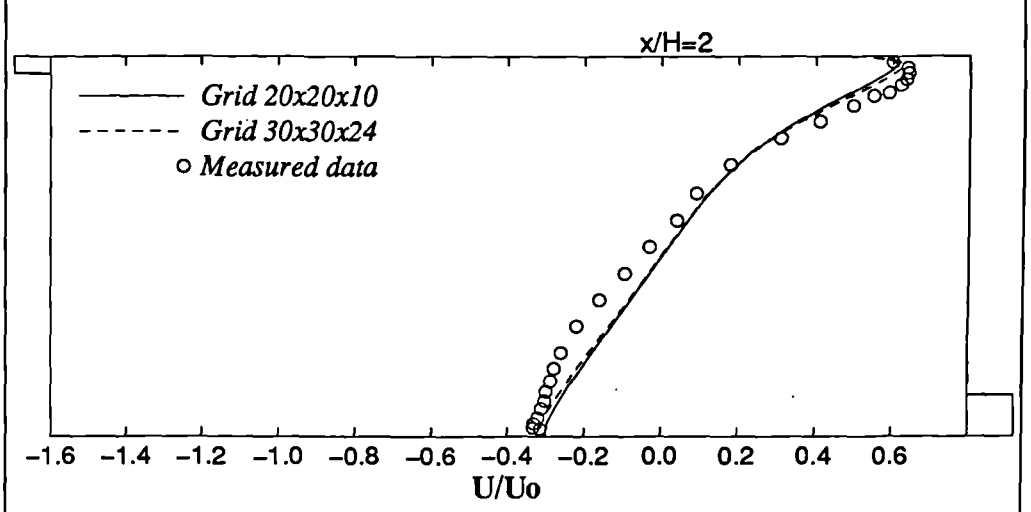

a. U-velocity profiles in centreline plane (z/W=0.0)

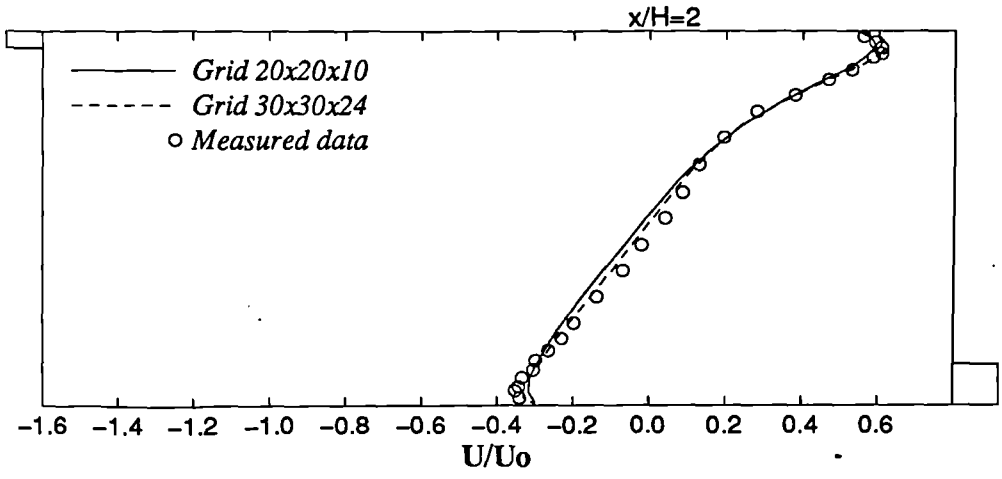

b. U-velocity profiles in side plane (z/W=-0.4)

Figure 5.15 Comparisons of numerical solutions with experimental data at different planes (three-dimensional simulations of plane wall jet flow)

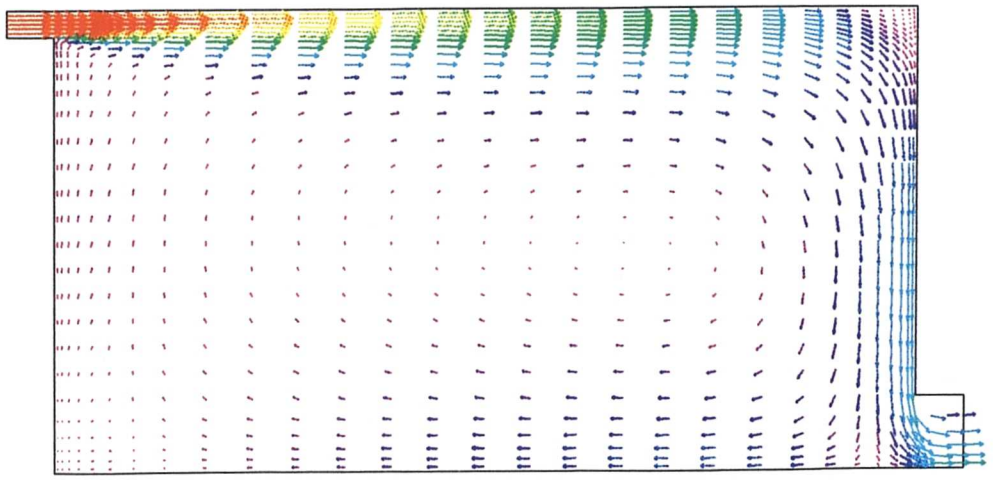

a. Vectors in centreline plane (Grid 30x30x24)

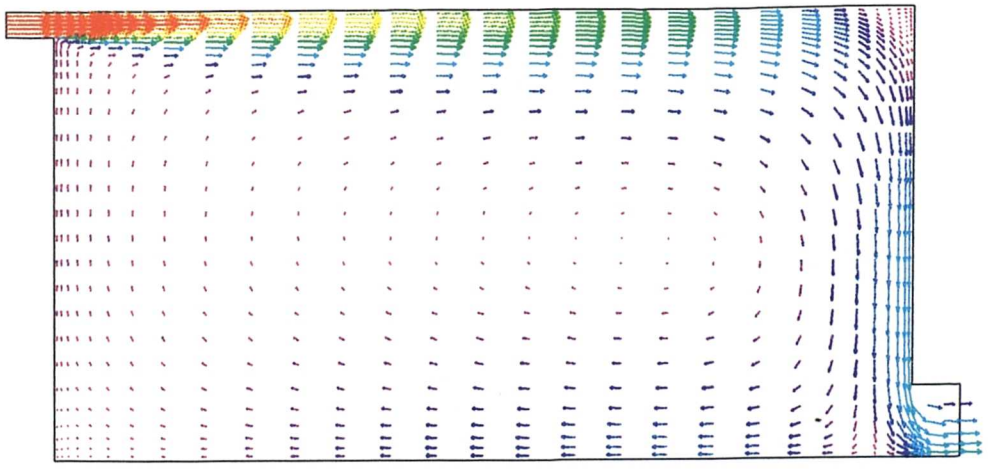

b. Vectors in plane of z/W=-0.4 (Grid 30x30x24)

Figure 5.16 Flow patterns in different planes (3-D simulation of plane wall jet flow, Vector scale: ⟶ 15 m/s)

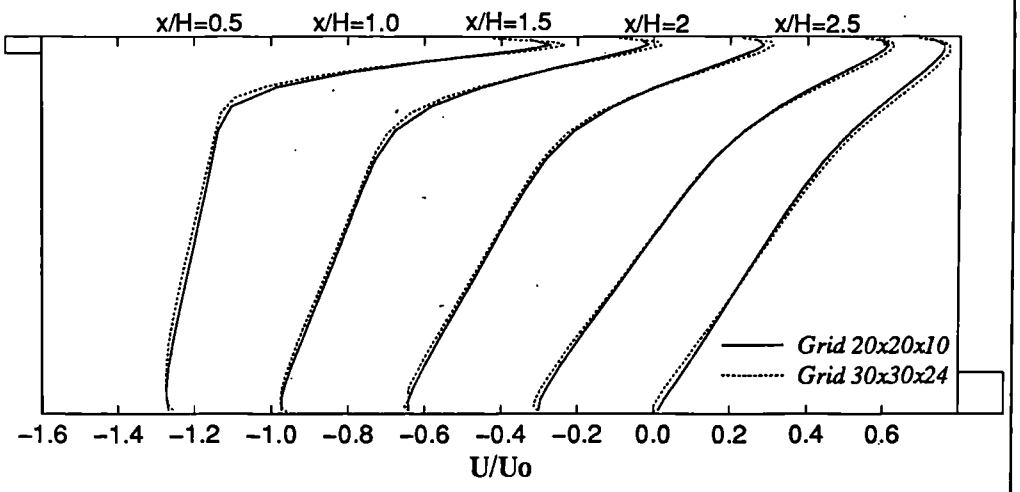

a. U-velocity distribution along the chamber length (z/W=0.0)

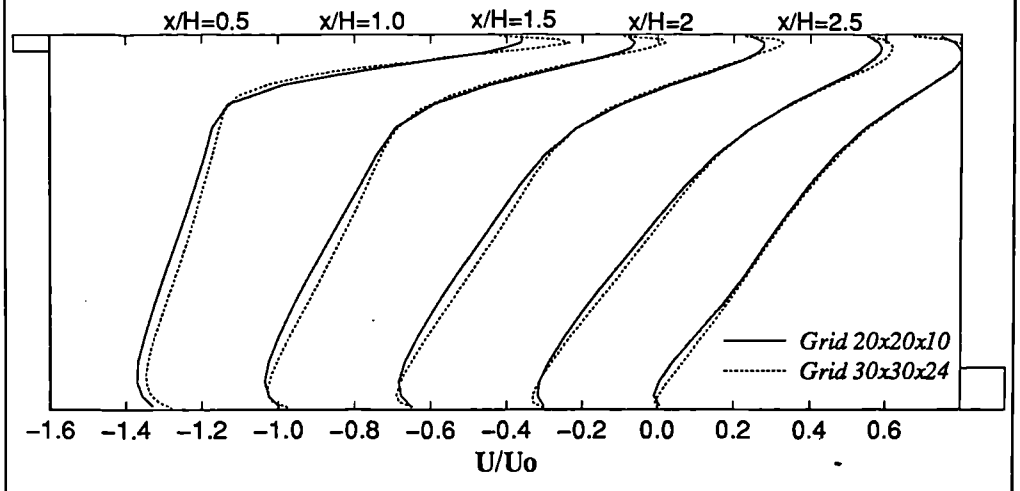

b. U-velocity distribution along the chamber length (z/W=-0.4)

Figure 5.17 U-velocity profiles in different planes (three-dimensional simulations of plane wall jet flow)

c. Simulations of three-dimensional wall jet flow.

For the geometrical configuration shown in figure 5.6b, the three-dimensional simulations are carried out with two mesh schemes (see figure 5.9a and 5.9b). The validation of computational results to the available experimental data is also done here.

The results are presented as below:

- The flow patterns at the planes of z/W=0.0 and z/W=-0.4 are presented in figure 5.18 and figure 5.19. The three-dimensional nature of the wall jet is evident.
- Comparing figure 5.18b with figure 5.16b, it is interesting to observe that the air circulation centre at plane of z/W=-0.4 in three-dimensional wall flow is located nearer to the centre of the room instead of closer to the side wall in plane wall jet situation.
- Figure 5.20 shows the comparisons of U-velocity distributions between the numerical results and the relevant measured data which tell the more satisfied calculations resulting from the mesh scheme with grid nodes 30x30x24. Both simulations produce satisfied results and good agreements with the measured data.

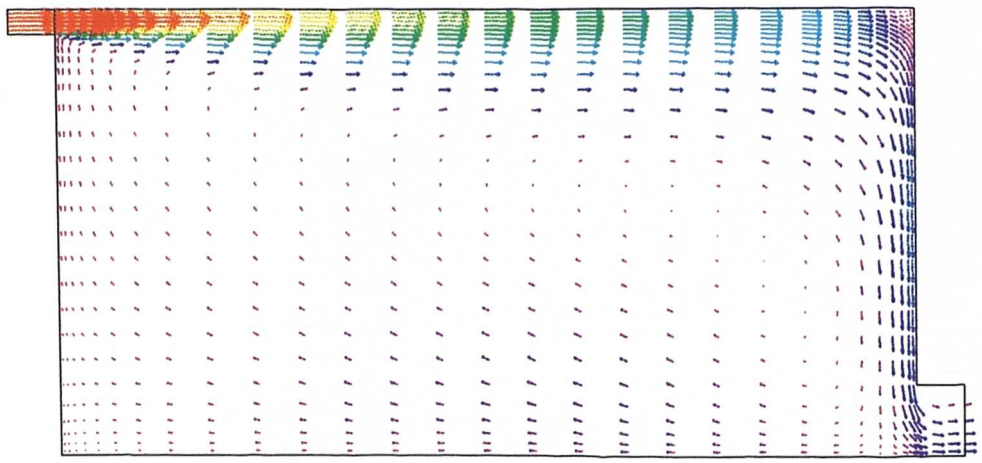

a. Vectors in centreline plane (Grid 30x30x24)

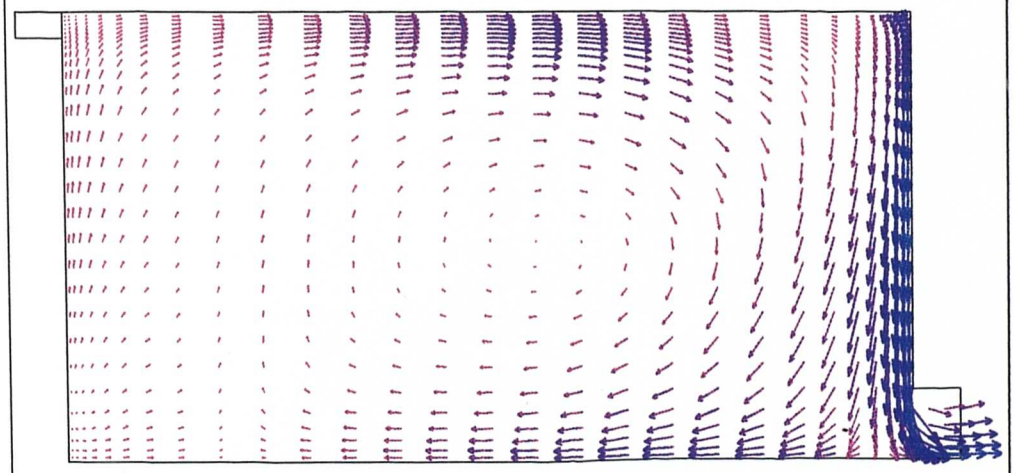

b. Vectors in plane of z/W=-0.4 (Grid 30x30x24)

Figure 5.18 Flow patterns of three-dimensional wall jet flow
(Vector scale: ⟶ 15 m/s)

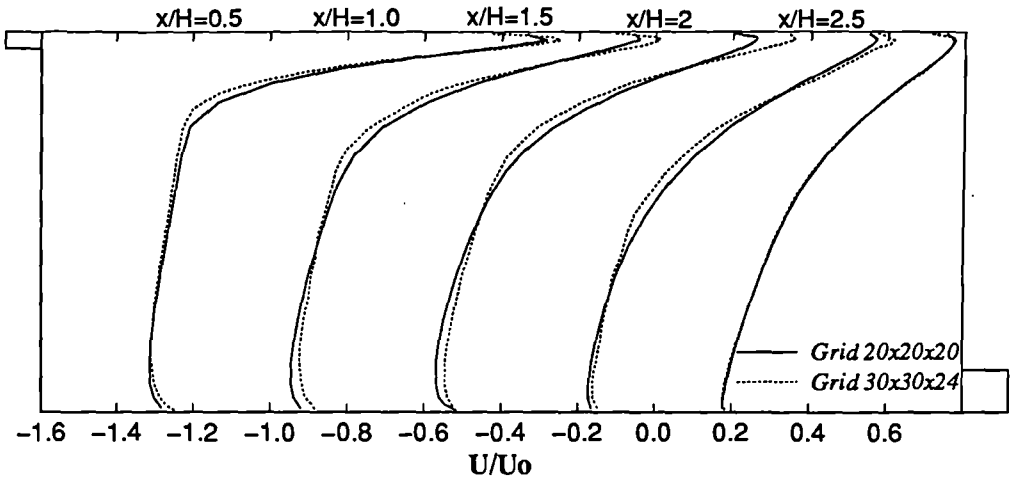

a. U-velocity profiles at plane of z/W=0.0

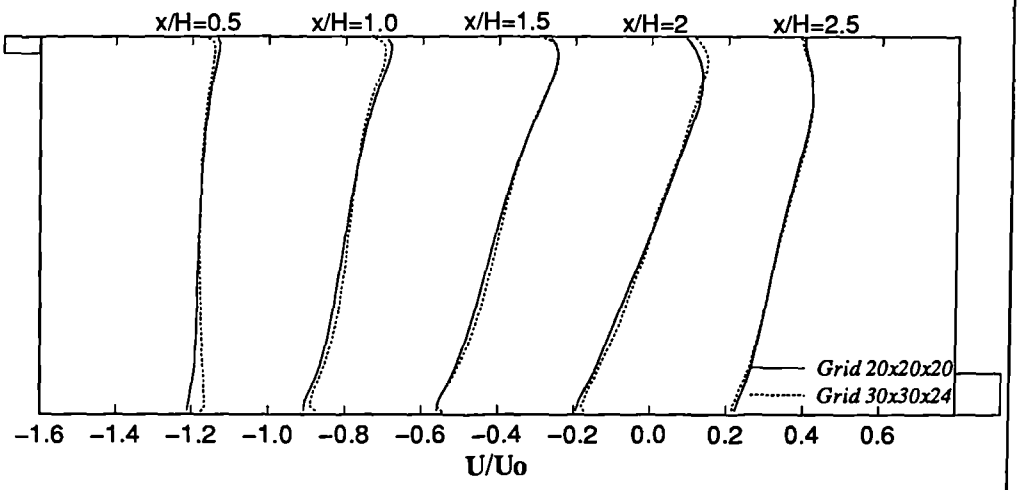

b. U-velocity profile at plane of z/W=-0.4

Figure 5.19 U-velocity distributions in different planes (three-dimensional wall jet flow simulations)

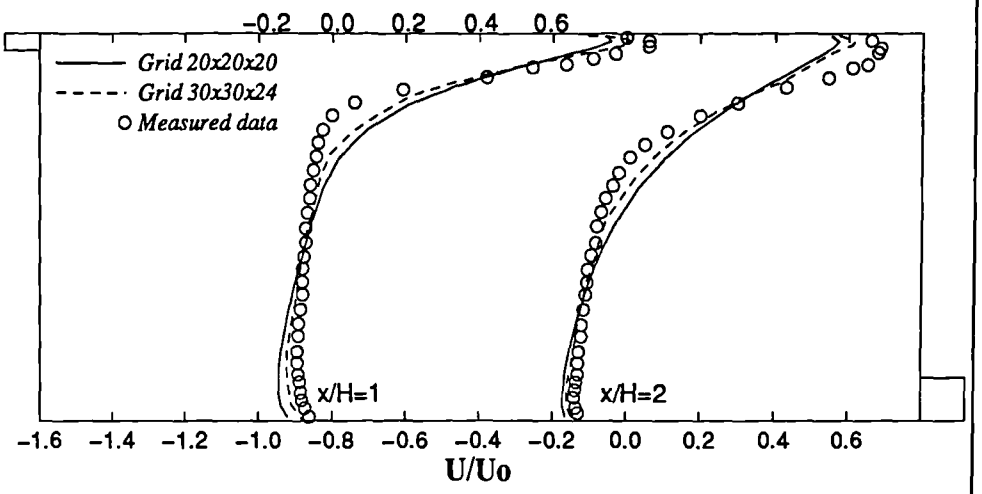

a. U-velocity profiles along the chamber height (z/W=0.0)

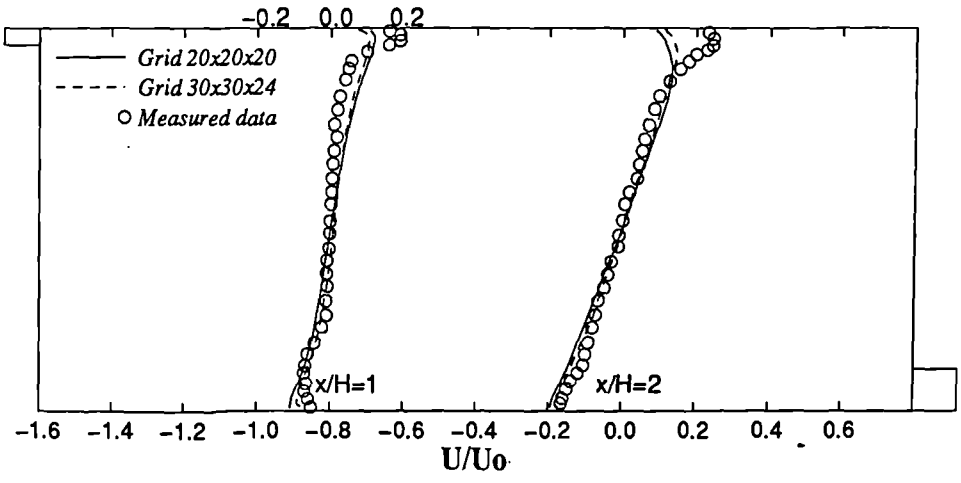

b. U-velocity profiles along the chamber height (z/W=-0.4)

Figure 5.20 Comparisons of computational U-velocity values with relevant experimental data (3-D wall jet flow simulations)

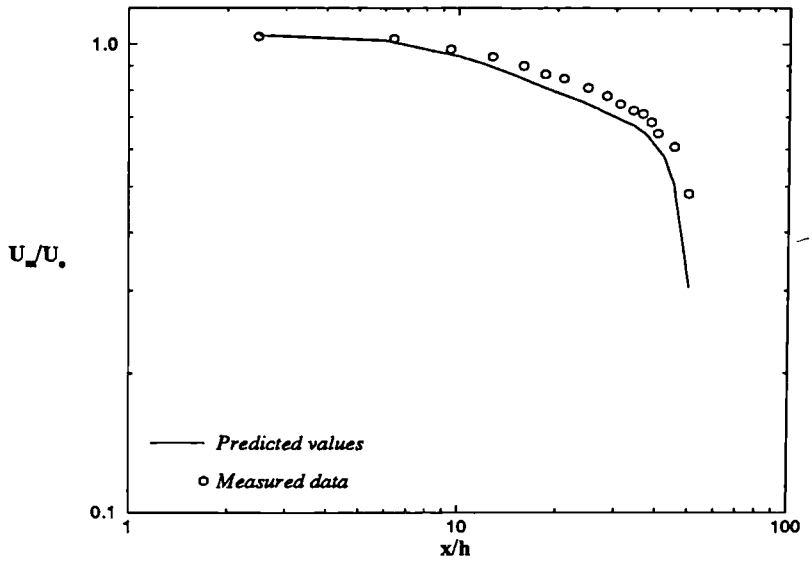

a. Three-dimensional simulation of plane wall jet case (Grid 30x30x24)

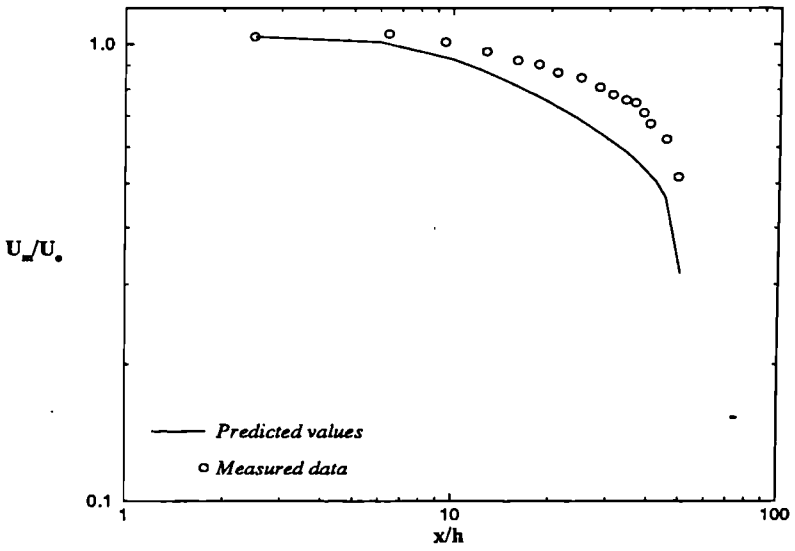

b. Three-dimensional wall jet flow case (Grid 30x30x24)

Figure 5.21 The decay of centreline velocity along the chamber length

- Figure 5.21 represents the decay of centreline velocity along the room length of both jet flows.
- From that figure, an acceptable accordance between the simulations and the experiments can also be seen for the plane wall jet case, but the comparison between computation and measurement of the three-dimensional wall jet flow shows less satisfactory. The further refinement of mesh and maybe some improvements of turbulence model are required for three-dimensional wall jet flow.
- Generally speaking, figure 5.12, 5.15 and 5.20 present good agreements between computational results and experimental data.

II. Convergence control methods.

When using CFD tools that have been written for commercial purposes, it would be ideal if reliable means of producing a converged solution were written in. However, CFD programs are so general that the user must intervene in the solution process for each particular case to assure the satisfied converged results. As mentioned in §4.3.7, convergence difficulties are encountered in the above simulations. The SIMPLEC algorithm is used in these simulations. The FLOW3D code has been devised to have the values of under-relaxation factors (URF) listed in Table 4.3 (said to be default URF values) and with no false time step specifications. At first, all simulations are carried out with those default settings which are applied to all dependent variables. The relevant pressure values of monitor point (see figure 5.22) and the normalised mass residual plots are shown in figure 5.23, 5.24 and 5.25.

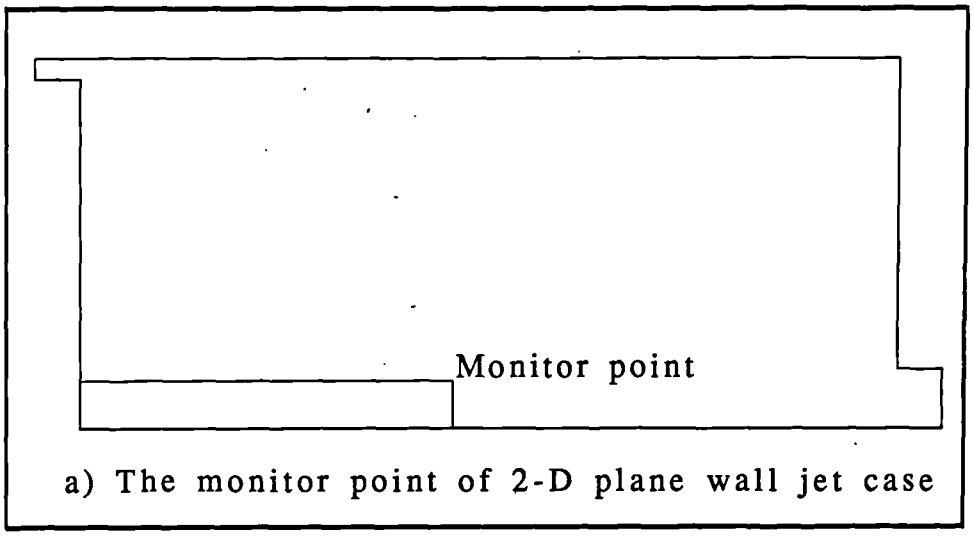

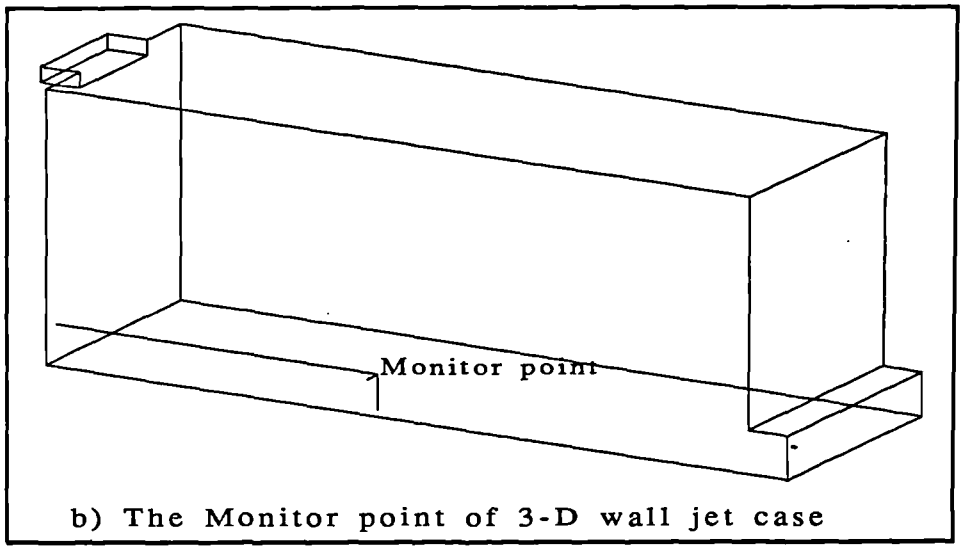

Figure 5.22 Monitor points of simulations

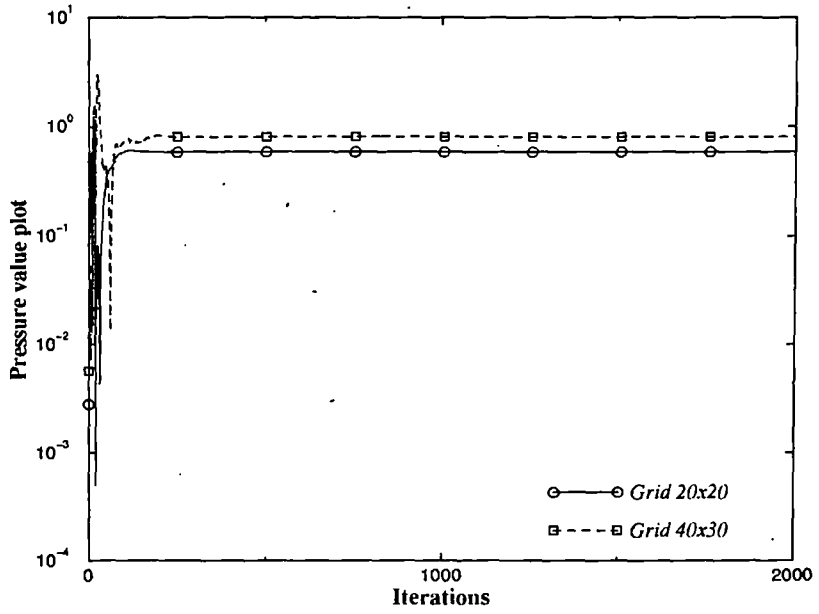

a. Pressure value of monitor point varying with iterations

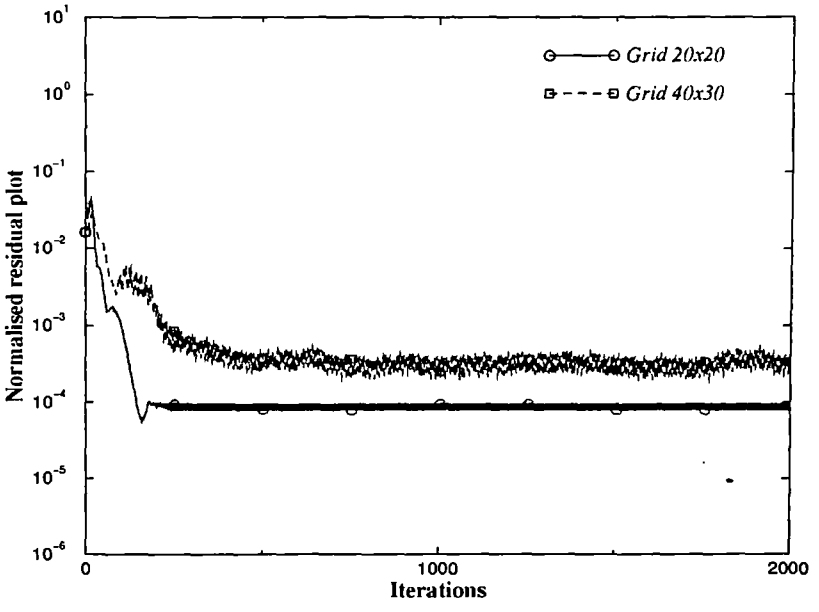

b. Normalised mass residual varying with iterations

Figure 5.23 Convergence history of 2-d plane jet simulations (default settings)

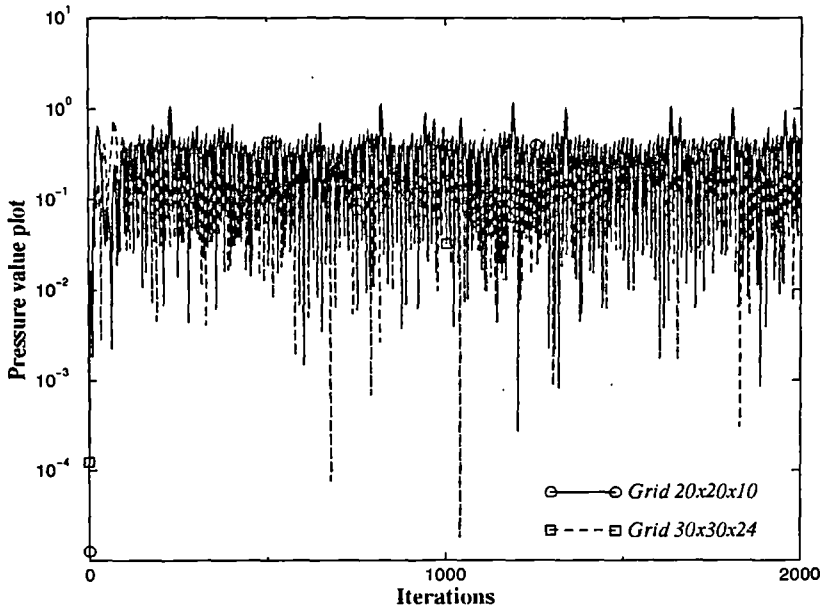

a. Pressure value of monitor point varying with iterations

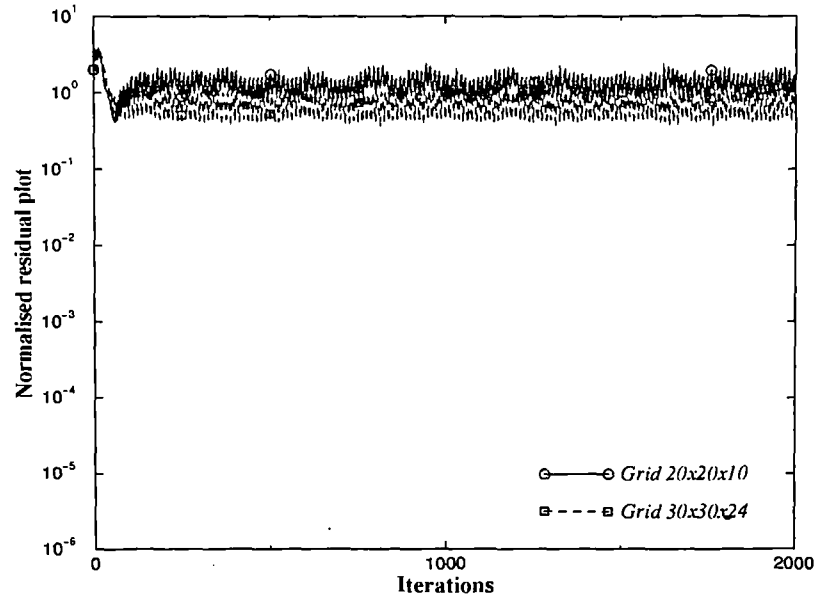

b. Normalised mass residual varying with iterations

Figure 5.24 Convergence history of 3-d plane jet simulations (default settings)

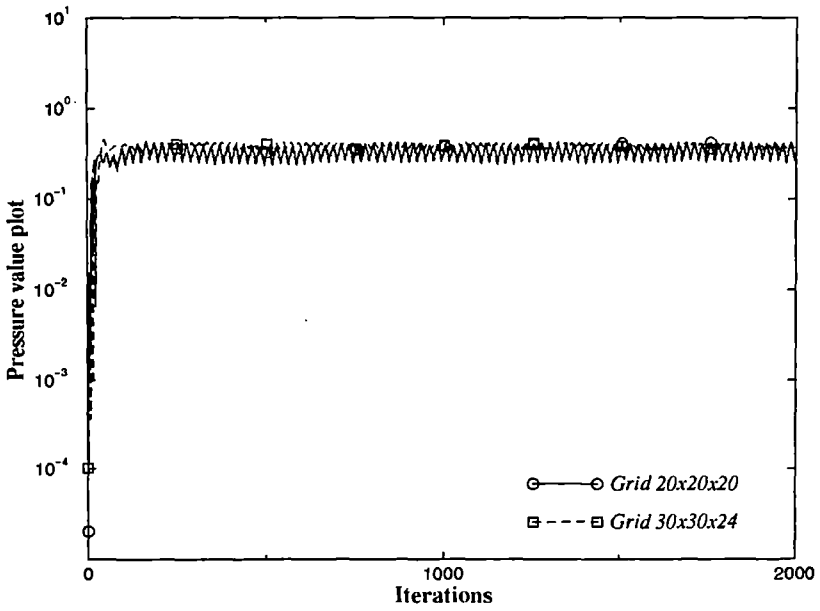

a. Pressure value of monitor point varying with iterations

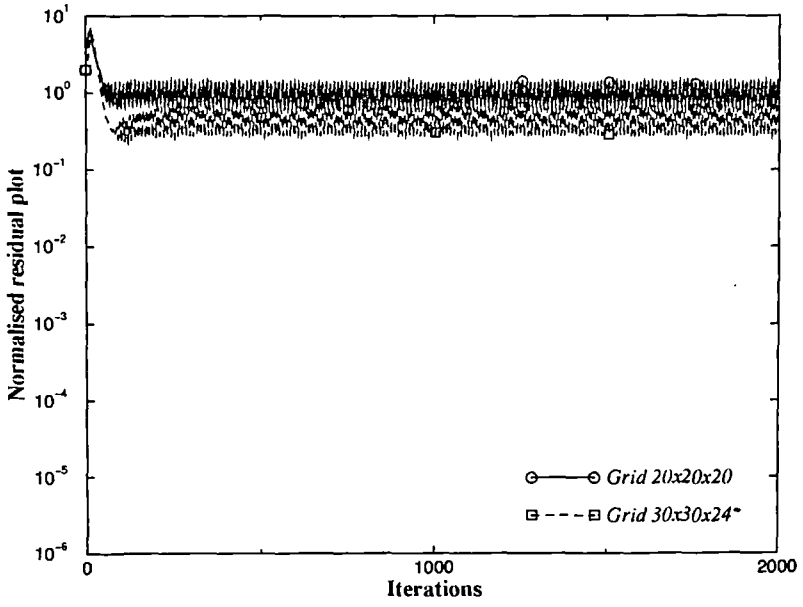

b. Normalised mass residual varying with iterations

Figure 5.25 Convergence history of 3-d wall jet simulations (default settings)

It can be seen that the two-dimensional simulations tend towards the converged status but do not arrive the required values (according to normalised mass residual plots); while the three-dimensional computations oscillate with the iterations, i.e., the pressure values vibrate within a band of values and obviously do not converge with the default setting of under-relaxation factors. It is necessary to apply some convergence control methods to assure the smooth convergence for all simulations, i.e., choosing appropriate values for under-relaxation factors (URF) and false time-steps (FTS) if necessary. As it has been said, there is no general method to select URF and FTS to solve the convergence difficulty; one should select the proper URF or FTS for every single case by trial and error. The recommended range of under-relaxation factors is 0.1<URF<1.0. The typical false time-step factors can be calculated according to equation (4-133), i.e., $\Delta T=\Delta l/V$, here V is chosen as the average supply velocity, Δl is specified as:

Two-dimensional: $$\Delta l = \left(\frac{\text{Area of whole flow domain } (m^2)}{\text{No. of control volumes}} \right)^{1/2} \quad (5\text{-}8)$$

Three-dimensional:

$$\Delta l = \left(\frac{\text{Volume of whole flow domain } (m^3)}{\text{No. of control volumes}} \right)^{1/3} \quad (5\text{-}9)$$

It is recommended to start with a small values of URF and FTS, i.e., deep under-relaxation and a short time-step for the solutions. The smaller the values of URF and FTS, the slower the convergence rate. Obtaining the optimal values of both URF and FTS is a tuff and time-consuming job. The appropriate

values of URF and FTS used for the above simulations, after a number of running by trial and error, are listed in table 5.3.

Table 5.3 Values of URF and FTS for cases

Cases	Default URF	Proper URF	Default FTS	Typical FTS	Proper FTS	No. of cells	No. of Iterations	CPU (h)
Grid 20x20	Table 4.3	0.4	—	5.038E-4	—	424	2500	0.723
Grid 40x30	Table 4.3	0.4	—	2.943E-4	—	1242	2500	1.356
Grid 20x20x10	Table 4.3	0.5	—	5.326E-4	1E-3	4240	5000	6.88
Grid 30x30x24	Table 4.3	0.4	—	3.049E-4	5E-4	22608	5000	40.89
Grid 20x20x20	Table 4.3	0.4	—	4.252E-4	1E-3	8336	5000	13.61
Grid 30x30x24	Table 4.3	0.5	—	3.064E-4	5E-4	22272	6000	44.12

The converged results of the above cases are shown in figures 5.26, 5.27 and 5.28. For two-dimensional simulations, modification of under-relaxation factors to 0.4 can assure the iterations to arrive satisfied convergence range. For three-dimensional cases, just reducing under-relaxation factors is not enough to guarantee the convergence. A combination of under-relaxation and false time-stepping factors must be applied to those three-dimensional simulations to help reach the satisfied convergence status. It is interesting to notice that the dense mesh takes more iterations and is more difficult to arrive convergence than the coarse mesh does (i.e., smaller values of URF and FTS and more CPU time demanded for fine mesh). The proper value of false time-step reduces as the grid nodes increases. All normalised mass residuals of the above cases presented in figure 5.26, 5.27 and 5.28 fall in the specified range of convergence criterion with respective convergence control techniques.

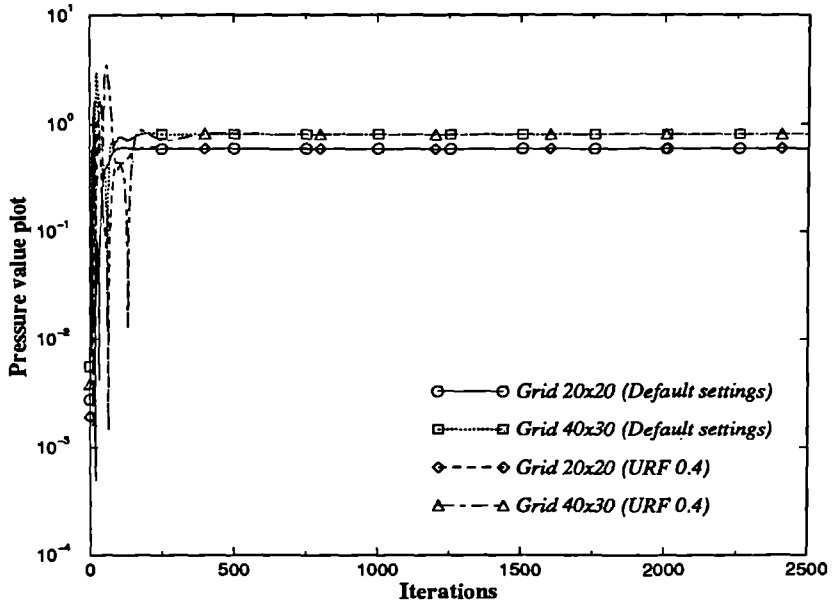

a. Comparisons of pressure values of monitor point with different settings

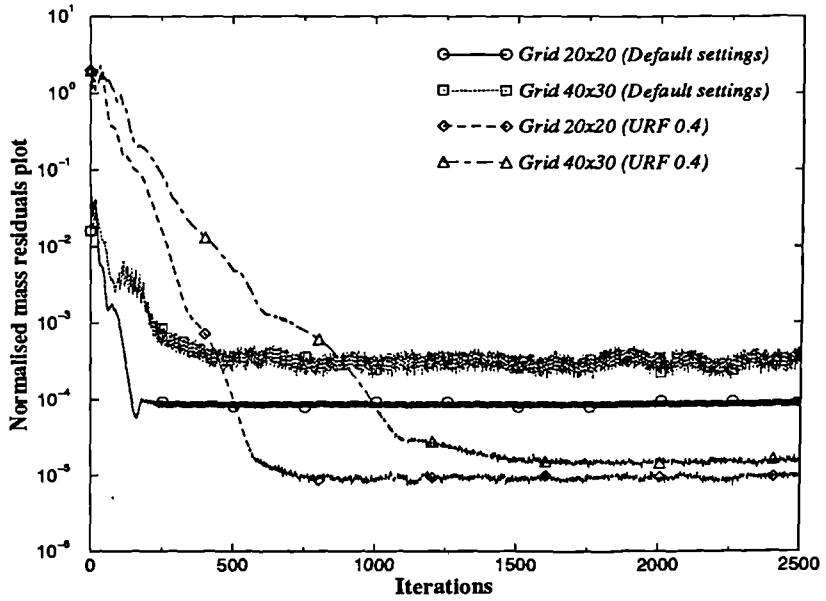

b. Comparisons of normalised mass residuals with different settings

Figure 5.26 Comparisons of convergence history of 2-d plane wall jet simulations

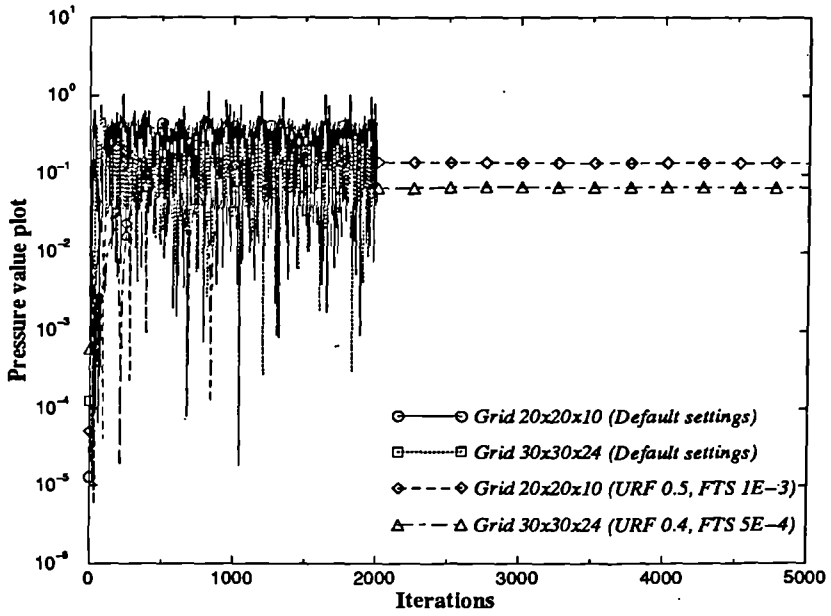

a. Comparisons of pressure values of monitor point with different settings

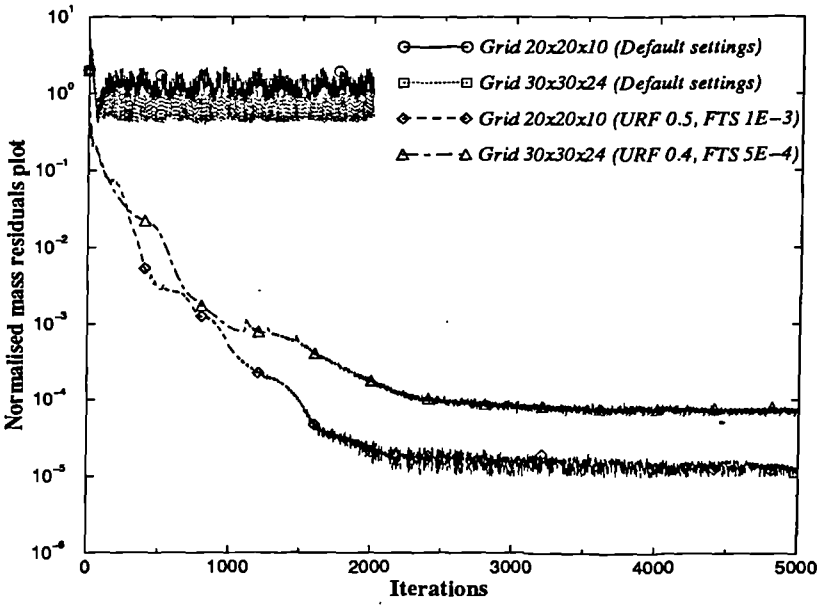

b. Comparisons of normalised mass residuals with different settings

Figure 5.27 Comparisons of convergence history of 3-d plane wall jet simulations

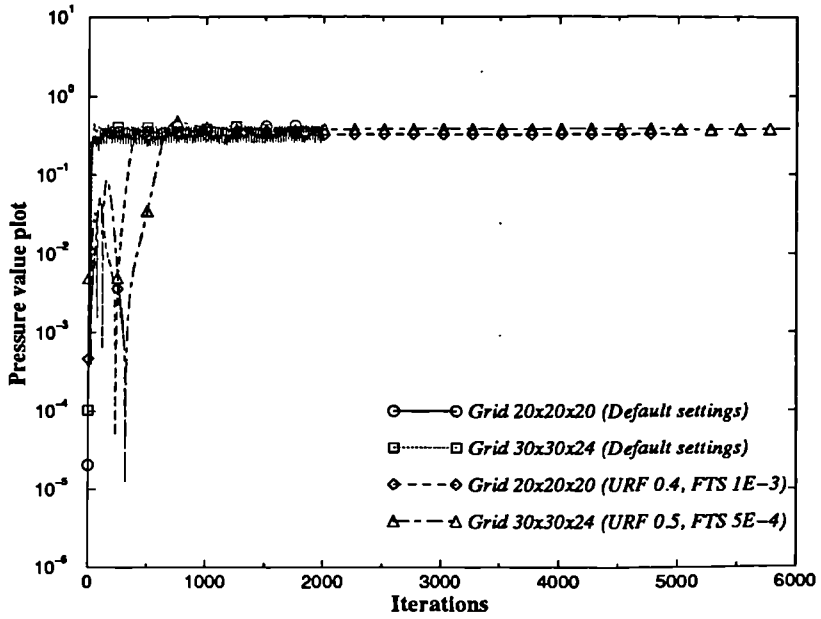

a. Comparisons of pressure values of monitor point with different settings

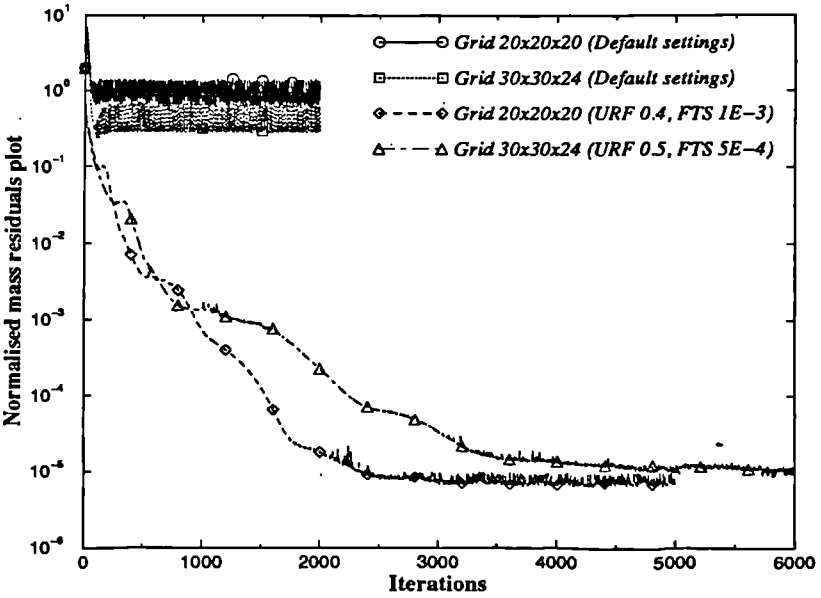

b. Comparisons of normalised mass residuals with different settings

Figure 5.28 Comparisons of convergence history of 3-d wall jet simulations

§5.5 Conclusions

This chapter has dealt with the flow characters in a room ventilated by the mixing principle. An evaluation of CFD techniques used to predict the wall jet flow has also been outlined in this chapter. The cases include both plane-wall jet flow and three-dimensional wall jet flow. The CFD code used, CFDS-FLOW3D, is based on the time-averaged momentum equations, the continuity equation and the standard k-ε model. The numerical results are compared with the relevant experimental data. The following remarks are concluded:

1. The numerical results show generally good agreement with the relevant measured data.
2. The airflow pattern in room ventilated by mixing principle is deeply influenced by the aspect ratio of the supply opening, i.e., the inlet geometry.
3. The mesh scheme used in CFD modelling does affect the numerical results. The fine scheme is able to produce better solutions with the cost of more CPU demand;
4. Convergence difficulty has been encountered in the simulations. Convergence control methods have been successfully applied to the simulations to obtain satisfactory converged results with reasonable time-consuming.
5. The CFD model is a useful tool for the analyses of flow phenomena in ventilated spaces with different geometrical configurations.

CHAPTER VI

MODELLING OF AIR AND PARTICLE FLOW IN A VENTILATED ROOM

Abstract

This chapter presents a detailed numerical analysis of airflow and aerosol particle motion and distribution in a ventilated single zone. The numerical simulations of aerosol particle distribution, deposition and extraction in the ventilated space have been applied under three different ventilation rates. The results show that the ventilation conditions strongly influence the particle movement and distribution in the ventilated area. Increasing ventilation rate can enhance particle extraction and particle concentration decay in the ventilated room but may increase the perceptible surface soiling because it increases the number of particles deposited on the internal surfaces. It can be also concluded that the particle movement is affected by the particle properties. The gravitational sedimentation dominates the large particle movement; while the motion of the small particles is influenced by both the airflow pattern in the ventilated space and the gravity.

§6.1 Introduction

Following the numerical analysis of airflow in a ventilated space, presented in Chapter V, a CFD analysis of both airflow and aerosol particle movement in a ventilated room is described in this chapter. The mechanisms of aerosol particle movement are also described in this chapter. This chapter can be regarded as a logical continuation and extension of Chapter III.

As the incidence of ' Sick Building Syndrome ' is recognised world-wide, the indoor air quality is now promoting more attention than ever before. One of the indicators of indoor air quality is the concentration level of indoor aerosol particles which is known to have significant influence on the occupants' health. Previous studies (Nazaroff, et al, 1990; Schneider, 1991; Owen, et al, 1994; Emmerich, et al, 1994, etc.) show that the indoor aerosol particles can affect human health through inhalation and then enter and deposit on the nasal passages. The aerosol particles can also be deposited on interior surfaces and may, for example, result in soiling and damaging effects on arts and other treasures.

The removal of aerosol particles from the room air occurs by air filtration, mechanical ventilation and by particle deposition. For the purpose of reducing the effect of aerosol particles on human beings, the main removal processes are particle deposition on surfaces or extraction through the ventilation system. Concerning the prevention of soiling problems, the most appropriate way is to

extract particles through ventilation. There is a need to increase the ventilation rate to improve particle removal, but, sometimes, increasing ventilation rate can cause draughts or redisturb the particles from the deposited surfaces to form a secondary source of airborne contamination. Studies have shown that some of the aerosol particles are neither extracted through ventilation nor deposited on surfaces; they may remain suspended in the room air under the influences of airflow patterns and other factors such as external forces acting on them. It can be seen that the aerosol particle deposition process significantly influences the particle concentration level and hence the indoor air quality. Thus particle deposition rate, extraction rate and concentration level in the ventilated space are important indicators of indoor air quality.

As concern about indoor air quality has grown recently, understanding of aerosol particle properties has become increasingly important so that control techniques may be implemented to reduce damaging health effects and soiling problems. Some researchers have reported the studies of aerosol particle movement, deposition and concentration in ventilated rooms (see §2.2), mainly by experimental study. In spite of those studies, the knowledge of aerosol particle characteristics in the ventilated area is still limited. In other words, the experimental study of aerosol particle movement in ventilated spaces is restricted to a limited number of sample test points and those experiments are normally costly. There is a need for fully understanding the characters of aerosol particles within the whole ventilated space. Computational Fluid Dynamics provides a method to analyse both the airflow patterns and aerosol particle movements along with their distribution in the ventilated space. The objectives of the study are as follows:

- To use CFD to simulate the air movement, deposition and concentration of aerosol particles in a full-scale a ventilated room at different ventilation rates;
- To obtain information about those factors which influence aerosol particle distributions within ventilated spaces through a large number of particle tracking analyses.

§6.2 Particle Deposition

§6.2.1 Particle Deposition in Still Air

A study of single particle deposition process in still air was presented in Chapter III. The basic theory of spherical particle deposition by gravitational force is Stokes' law. The mechanical mobility of particles in air determines the basic characters of an aerosol. Particles, suspended in air, after a short time, reach their terminal settling velocities. By calculation of the gravitational settling velocity for a particle with certain size, an indication is obtained about the time during which the particle can be suspended in still air. The sedimentation of a spherical particle in still air may be estimated by equilibrium of gravity and aerodynamic drag forces acting on the particle (see Chapter III). The settling velocity of a spherical particle can be approximated by Stokes' law and is directly proportional to the particle diameter squared (equation (3-11) for $R_{e_p} < 1$; equation (3-30) and (3-31) for $1 < R_{e_p} < 800$ and equation (3-32) for $R_{e_p} > 800$). Settling velocities for spherical particles with different density values at an ambient air temperature of 20°C are calculated and shown in Table 6-1.

Table 6-1 Settling velocities for various particle sizes and density of particles

Particle size (μm)	Settling velocity (m/s) ←Density of particle (kg/m³)→			
	200	500	1000	2000
1	5.9×10^{-6}	1.5×10^{-5}	3.0×10^{-5}	5.9×10^{-5}
2	2.4×10^{-5}	6.0×10^{-5}	1.2×10^{-4}	2.4×10^{-4}
5	1.5×10^{-4}	3.7×10^{-4}	7.4×10^{-4}	1.5×10^{-3}
10	5.9×10^{-4}	1.5×10^{-3}	3.0×10^{-3}	5.9×10^{-3}
20	2.4×10^{-3}	6.0×10^{-3}	1.2×10^{-2}	2.4×10^{-2}
50	1.5×10^{-2}	3.7×10^{-2}	7.4×10^{-2}	1.5×10^{-1}

From Table 6-1, the terminal settling velocity increases rapidly with particle size, since this velocity is proportional to the square of the particle diameter. As the mechanical mobility of aerosol is of fundamental importance, the table gives a useful estimation of the largest particles to be found in still air (here it is assumed the air velocity V<0.1 m/s), i.e., larger particles deposit much faster than smaller particles, and thus smaller particles may stay in the air for longer. In reality, the room air is rarely completely still, i.e., V<0.1 m/s is rare. Clearly, most particles are strongly influenced by the normal air movement patterns. The situations described in Table 6.1 supply a reference for the particle deposition processes.

§6.2.2 The effects of Aerosol Particles in Ventilated Space

As mentioned in §6.2.1, the settling velocities are calculated under the assumption of still air for which reason values, indicated in Table 6-1, should be set in relation to air movement in the indoor environment which is itself under the influence of ventilation. Furthermore, particles are subject to resuspension in response to the human activity within the indoor environment. The knowledge of aerosol particle characters in indoor air is important because of the potential health effects and the problem related to the indoor air quality.

I. Health effects

Previous studies (Emmerich, et al, 1994; Wallin, 1990; Nazaroff, et al, 1989; Casarett, 1975; Lippmam, 1972) show that the health effects that result from inhaling indoor aerosols are directly related to the particle diameters and the total mass of particle inhaled. The most important feature is the size of the particles. Particles larger than 30μm have low probability of entering the nasal passages through inhalation. The distributions of aerosol particle deposition in the nasal passages may be summarised as bellows (see Figure 6.1):

- The depositions of larger particles are mainly found in the passages of nose and pharyngeal regions (i.e., the upper respiratory tract) due to the rapid and sharp changes of direction of air flow. Most of the particles deposited here are found within the range of 5~10μm in diameter;
- In the thoracic region (i.e., the middle respiratory tract), air velocity and directional changes decrease. The aerosol particle size range favoured for deposition in this area is from 1μm to 5μm;

- The smaller particles can be found throughout the bronchioles area (i.e., the lower respiratory tract). Gravity becomes less important as the particles are getting smaller, thus particles, usually smaller than 1μm, are deposited on alveolar walls mostly by diffusion.

In general, the interaction between particles and respiratory cells is largely dependent on where in the respiratory tract the particles deposit. For example, particles deposited in the bronchioles area impose more hazards than particles deposited in the upper respiratory tract. However, the dose received by the occupant is dependent on the solubility of the particles and other aspects, as well as the deposition site. Those particles including bioaerosols deposited in the nasal passages, wherever they are, all present health hazards to human beings due to the risk of infection.

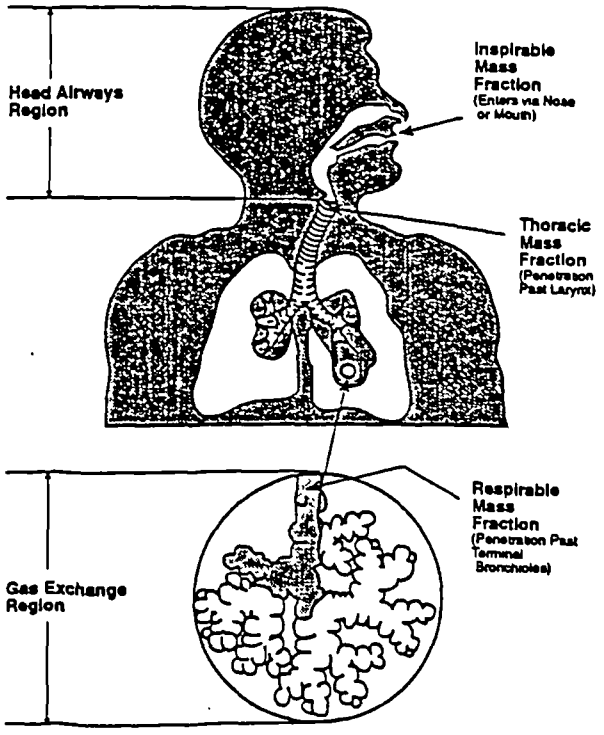

Figure 6.1 The three areas of nasal passages

II. Soiling problem

Besides the imposed health effects resulting from the inhalation and deposition of aerosol particles on nasal passages, aerosol particles that deposit onto indoor surfaces may cause soiling or chemical damage. Contamination of indoor surfaces consists of a mixture of condensed or adsorbed gases and vapours, organic substances, deposited particles, spills, etc. The deposition of aerosol particles onto indoor surfaces may result in dirty floors and windows in the home and office, loss of precision of machinery, soiled and discoloured art work in museums, etc. The indoor surface deposition process is complex and has received recent attention because of the above undesirable effects, especially soiling problem of museum collections. The knowledge of particle deposition onto surfaces is still not well understood. The roles of surface roughness and particle inertia are not well known for indoor conditions. Previous research shows that surface roughness and turbulence intensity (related to the ventilation conditions) as found in the indoor environment appear to affect the particle deposition process. That means both the ventilation and the indoor surface condition have significant influence on the deposition of aerosol particles onto indoor surfaces. Rough surfaces give rise to greater adsorption and therefore clean air, but for a varieties of reasons this would not be a satisfactory strategy for air cleaning. Reducing the risk of soiling has to be achieved using suitable ventilation and cleaning of indoor surfaces.

§6.2.3 Aerosol Particle Removal

I. Factors affecting particle movement

General sources that form aerosols include condensation, combustion, nuclear degradation, resuspension and spraying. The condensation of vapour in gas streams produces small liquid particles. Combustion results in small liquid and solid particles, as well as larger solid particles such as soot. Nuclear degradation forms ultra-small particles of radon progeny. Resuspension that occurs with sweeping or drafts results in large solid particles re-entering the air. Spraying yields medium or small liquid particles. All of these contribute to the mixture of aerosol particles found indoors.

The motion of aerosol particles is determined by the kinetic properties of the air and other external forces that act on the particles. The following physical phenomena can produce forces that result in motion, transport or deposition of aerosol particles in rooms: gravitational(§4.4) and electrical fields, drag forces(§4.4), centrifugal flows(§4.4), interfacial phenomena, inertial forces, Coriolis forces(§4.4), concentration and thermal gradients, and molecular diffusion, etc. Among these, the gravitational sedimentation plays a key role in particle deposition processes. In general, gravity dominates the large particle movement ($d_p > 20\mu m$). For medium particles ($1 < d_p < 20\mu m$), inertial effects (momentum transfer between particle and fluid) in the fluid become important and must be incorporated into the velocity calculation. Gravity becomes less important when the particle size is less than 1μm (see Chapter III and §6.1).

Impaction occurs when a particle collides with an obstacle in the flow field. Smaller particles follow the air flow lines around the obstacle, whereas larger particles, owing to their greater inertia, are unable to change their directions, resulting in impact with the obstacle. Such impaction due to the inertia of particles shifts the particle size distribution in the room toward the smaller particles.

Molecular diffusion of aerosol particles in the air, a microscale mechanism, is the result of their bombardment by molecules of the air (Browning motion). Such diffusion is seldom considered for particles larger than 1μm in diameter. Diffusion can lead to the deposition of particles on surfaces in addition to that caused by gravity and impaction. Special filters based on this principle are used primarily to capture the smaller particles. In practice, the most penetrating size implemented in the filters is in the region between diffusion and impaction.

Interfacial phenomena mainly includes adhesion and coagulation. Adhesion forces arise from particle surface properties and interface geometry. When small aerosol particles deposit on a solid surface, they usually adhere on contact due to such forces. The adhesive force can be increased by particle electrostatic charge, but high humidity can counteract this effect. Most air-cleaning devices apply this principle to collect particles.

It is important to understand these forces in order to predict which particle may remain in the air long enough to be inhaled, imposing potential health problems, and which may deposit onto indoor surfaces, resulting in soiling or damage to the surfaces.

II. Particle extraction through ventilation

Although the above techniques based on particle movement are available to help remove the aerosol particles, however, they are not good enough to rely on. The conventional method of removal of aerosol particles from domestic or working spaces is by ventilation. In addition, removal of aerosol particles is not a sole indicator of indoor air quality; sufficient fresh air supply and maintaining of thermal comfort also help improve the indoor air quality. In detail, the main objectives of a ventilation system used in building can be summarised as follows:

1. Fresh air is needed for removal of carbon dioxide and odours for human comfort and health, especially for well sealed buildings;
2. The supply air acts as a dillutant; the amount of air required depends on the permissible contaminant concentration level for the space;
3. Ventilation promotes and directs air movement in the space, this being one of the comfort factors;
4. Ventilation controls aerosol contamination.

An acceptable indoor air quality is achieved by controlling the contaminant sources within a space and by introducing the amount of ' clean ' air to bring the concentration level of aerosol particles below the recommended values. To date, the information about the distribution of aerosol particles within a ventilated space is limited. The study presented in this chapter is to apply the CFD method to analyse the aerosol particle movement and distribution in ventilated space under different ventilation conditions.

§6.3 Case Studies

The numerical analysis described here is to use both Eulerian and Lagrangian methods to simulate the airflow patterns, and the distribution and concentration of aerosol particles in a mechanically ventilated area.

§6.3.1 Case Descriptions

I. Geometrical configuration.

The physical model represents a three-dimensional full-scale room shown in figure 6.2. The ventilation air enters the room through the supply section at high level of the room. The exit section is located at low level of the room. Both inlet (0.1m from the ceiling) and outlet (0.1m above the floor) are positioned in the middle of the room width. The room air is assumed to be incompressible and iso-thermal. The room temperature is 20°C. The ventilation rates are chosen at three values respectively: a. ACH 0.5 h^{-1} (0.005 m^3/s); b. ACH 1 h^{-1} (0.01 m^3/s); c. ACH 2 h^{-1} (0.02 m^3/s). A mesh scheme is established for the three cases and refined grids are set up near all walls of the enclosure where large gradients of the variables are evident in those areas, see figure 6.3. The relevant parameters are listed in Table 6.2.

Table 6.2 Parameters of cases

Case No.	L (m)	H (m)	W (m)	l (m)	h (m)	b (m)	b/h	R_∞	Ventilation rate (ACH)	Grid nodes
Case 1	5	2.4	3	0.4	0.1	0.2	2	2224.1	0.5	44x34x35
Case 2	5	2.4	3	0.4	0.1	0.2	2	4448.2	1.0	44x34x35
Case 3	5	2.4	3	0.4	0.1	0.2	2	8896.4	2.0	44x34x35

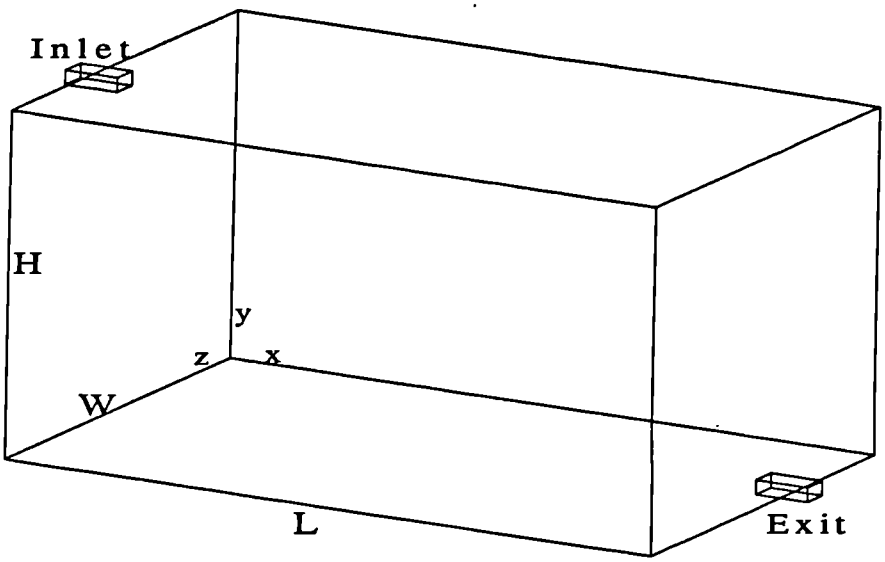

Figure 6.2 The geometrical configuration

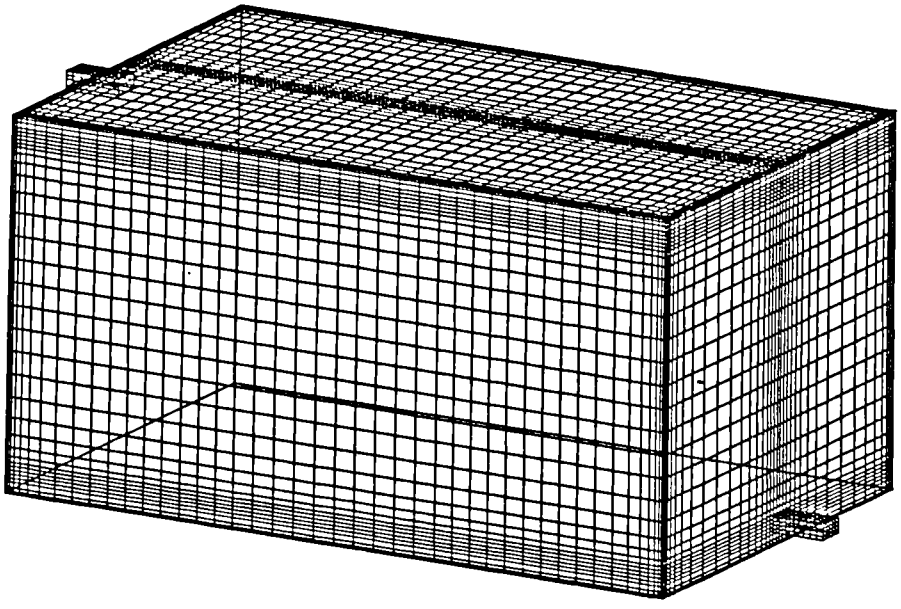

Figure 6.3 The mesh scheme

II. Particle parameters.

As mentioned in Chapter IV, one has to specify all initial information about particles when using particle transport to trace the particles. The information includes: masses, sizes, physical properties, initial conditions, number of sample particles, etc.

Apart from the Eulerian method for solving continuous fluid motion, a discrete trajectory approach (Lagrangian method) is used in the simulation of particle movement. The Lagrangian approach splits the particle phase into a representative set of individual particles and tracks these particles separately through the flow domain by solving the equations of particle movement. For simplifying the simulation, the following assumptions have been introduced:

- No heat and mass transfer exist between the air and the particles;
- All particle are solid spherical particles;
- Particles do not bounce back once settled onto a surface;
- Electrical force, Browning diffusion and coagulation processes are excluded in the current simulations;
- Particle mass is uniformly distributed in each size group.

According to the contents in §6.2 and the limitations of the CFD code, FLOW3D, which is employed in the study, the particle size group, selected in the current simulation, is within the range of 1~10μm. This range covers particle types of smoke, bacteria, mists, pollen, dusts, moulds, asbestos, etc.

The density of particle is chosen within the density range of dust particles, e.g. sawdust, here, it takes ρ_p=1000 kg/m³. As described in Chapter IV each sample particle represents a large mass of particles, the total particle mass is specified at the value of 10% of the mass flow rate of Case 1, i.e., 600 μg. The total particle mass is divided uniformly within the size group. The relevant particle parameters are included in Table 6.3.

Table 6.3 Particle parameters

Particle size d_p (μm)	Particle mass of each size group (μg)	Mass carried by each sample particle (μg)	No. of sample particles	No. of particles represented by each sample particle
1	60	0.9375	64	1.7911813×10^{9}
2	60	0.9375	64	2.2381164×10^{8}
3	60	0.9375	64	6.631456×10^{7}
4	60	0.9375	64	2.7976455×10^{7}
5	60	0.9375	64	1.4323945×10^{7}
6	60	0.9375	64	8.28932×10^{6}
7	60	0.9375	64	5.220096×10^{6}
8	60	0.9375	64	3.497056×10^{6}
9	60	0.9375	64	2.456095×10^{6}
10	60	0.9375	64	1.790494×10^{6}

§6.3.2 Boundary Conditions

I. Boundary conditions for the airflow

The boundary conditions, which are specified for the continuous phase, in this study, are summarised as below:

1. All variables except pressure are specified upstream of the flow domain. Mathematically, this is known as a Dirichlet boundary condition (see §4.3.5). For the cases in Table 6.2, the main flow is defined as entering the

room with a uniform velocity, i.e. a. U_{in}=0.25 m/s, V_{in}=W_{in}=0 m/s(ACH 0.5 h^{-1}); b. U_{in}=0.5 m/s, V_{in}=W_{in}=0 m/s (ACH 1 h^{-1}); c. U_{in}=1 m/s, V_{in}=W_{in}=0 m/s (ACH 2 h^{-1}). The values of k and ε at inlet are normally defined based on the mean flow characteristics at the inlet. Here, the same relations employed in Chapter V are used again for calculating k_{in} and ε_{in}, i.e., equations (5-6) and (5-7).

2. A non-slip condition at the solid walls is applied for velocities, i.e., the velocities at wall surface are set to zero (see §4.3.5, equation (4-113)).

3. The so-called ' wall function ' is applied to describe the turbulent flow properties in near-wall regions where sharp variations of variables in the turbulent regime are expected, detailed in §4.3.5, equations (4-117), (4-119), etc.

4. The Neumann boundary conditions are employed at the outlet to satisfy the mass conservation law, i.e., the mass flow boundaries are specified for the continuous fluid flow at the outlet to ensure the mass flowrate out of the flow domain is set equal to the mass flowrate into the flow domain for the cases in Table 6.2 (see §4.3.5).

II. Boundary condition for particle tracking

The important information for particle tracking is the initial positions and initial velocities of all sample particles. In the present studies, the particles are presumed to be uniformly dispersed in the room space. The starting positions of the sample particles are specified over the whole room, see figure 6.4. The height levels of the initial positions are chosen according to characteristic

height levels above the floor, e.g., the kneel (0.45m), shoulder (0.95m), head (sitting level 1.1~1.3m), and standing (1.7~1.8m) levels. The initial velocities of sample particles are specified as the settling velocities which are calculated from Stokes' law, i.e., equation(3-11).

It should be noted that any momentum transfer from or to the particles must be balanced by a corresponding source or sink of momentum in the continuous phase. For each control volume, these sources are calculated as a sum of the contributions of each of the sample particles, and weighted according to the amount of particle mass assumed to be carried by that sample particle when the particle traverses the control volume. Details can be seen in §4.4.

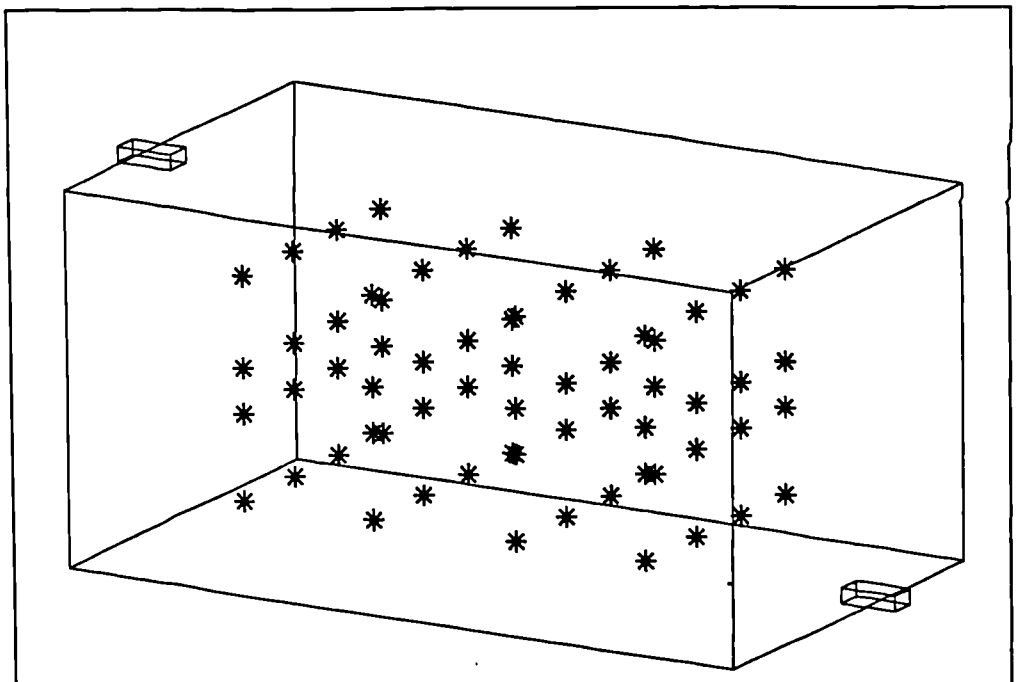

Figure 6.4 The initial positions of the sample particles

§6.3.3 Results and Discussions

I. Convergence control

Convergence difficulties are encountered in the simulations of all cases in Table 6.2. These were overcome by use of the relevant convergence control methods, i.e., under-relaxation factors or false-time steps (Ref. Chapter V). The convergence history of three cases are shown in figure 6.5.

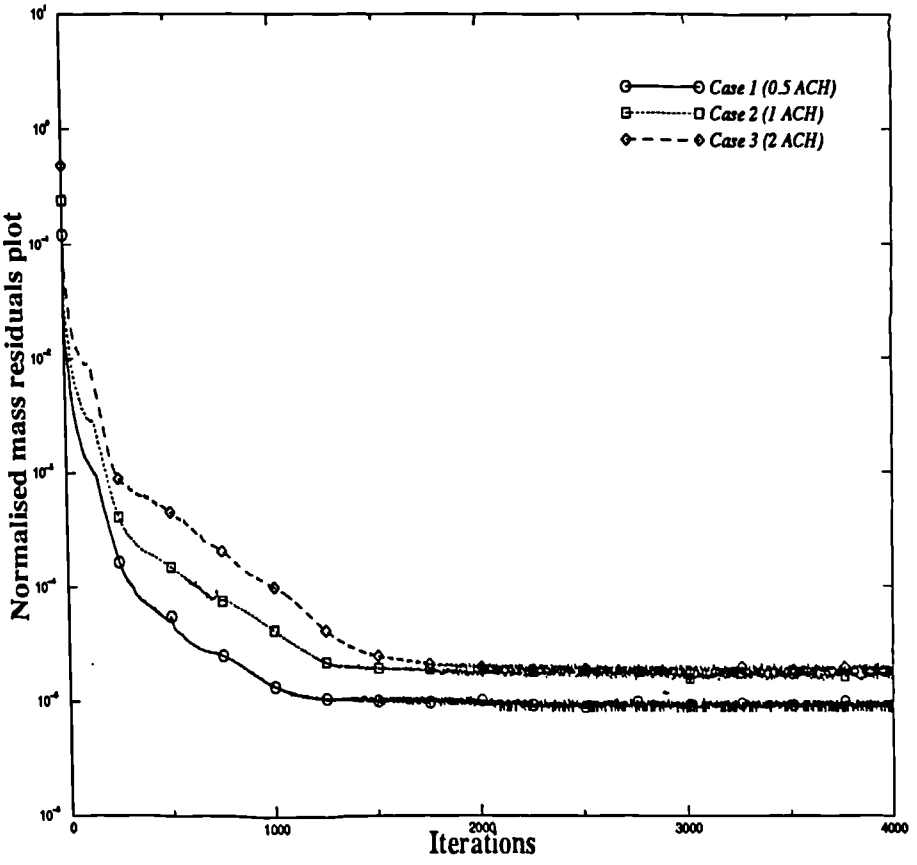

Figure 6.5 The convergence history of cases

II. Air movement in the room

The results of the air movement within the ventilated room are described as follows:

a) Figure 6.6 ~ 6.10 present the airflow patterns in the ventilated space with different ventilation rates.

b) It can be seen that the supply air produces a three-dimensional jet flow. The jets reattach to the roof surface after leaving the supply section due to the Coanda effect*. The jets decay along the ceiling surface.

c) The air circulations are induced in the room space by the jet effect, e.g. one large air circulation is formed in the plane of z=1.5m (see figure 6.6a, 6.6b and 6.6c). There is a stagnation point where the air movement splits and diverges in two directions.

d) The jet also induces the air circulations symmetrically to the jet core in the planes of y=1.2m and 2.25m (see figure 6.7b). Figure 6.7 also shows that the flow field is symmetrical to the centreline plane of the room.

e) The high speed regions are restricted at the ceiling level which is beyond the occupied zone. The velocities in the occupied zone are generally less than 0.3 m/s and do not cause draught problem even in case 3 situation (see figure 6.8 ~ 6.10).

f) The air movement in the plane of y=0.25m is influenced by the exhaust section.

g) Comparing figure 6.8a, 6.9a and 6.10a, it can be noticed that the high ventilation produces stronger non-uniform velocity distribution (i.e., sharp Z-shape profiles) in the occupied area at the planes on both sides of room centreline plane (symmetrical flow).

h) From figure 6.8b, 6.9b and 6.10b, the velocity distributions are quite uniform in the occupied zone at the centreline plane. This is expected in the ventilated spaces for satisfying the required comfort.

* Coanda effect - The jet created from the inlet is entraining air from the surrounding. The ceiling makes it impossible to entrain air from above and this consequently decreases the pressure level compared to the surroundings. This lower pressure is deflecting the jet towards the ceiling where the flow will attach. Further downstream the jet is obtaining the characteristic velocity profile of a wall-jet.

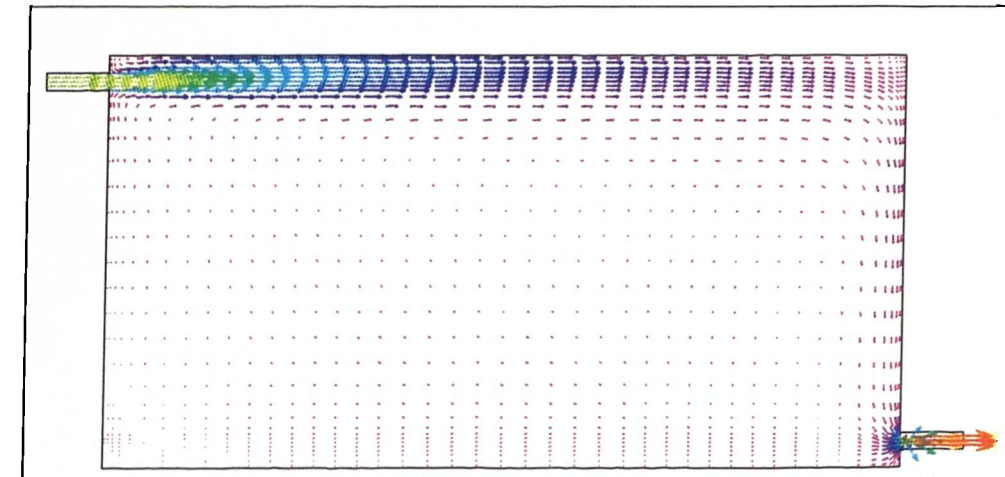

a. Vectors in centreline plane (Case 1, 0.5 ACH; Scale: ⟶ 0.25 m/s)

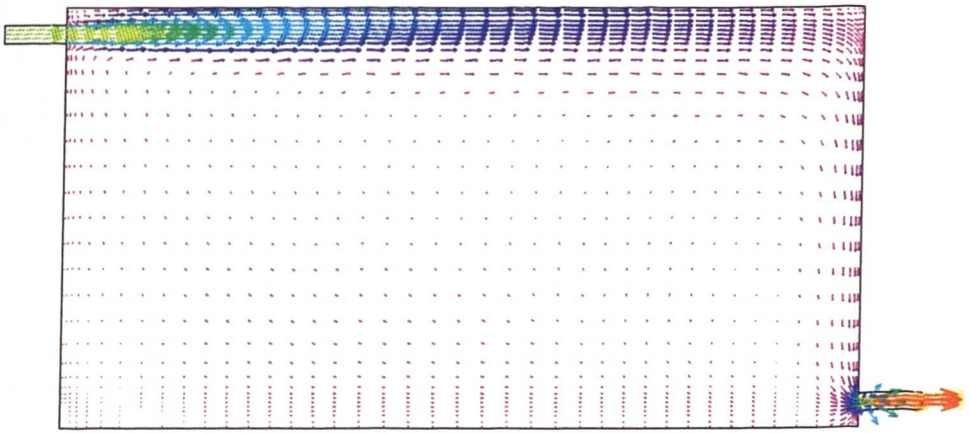

b. Vectors in centreline plane (Case 2, 1 ACH; Scale: ⟶ 0.5 m/s)

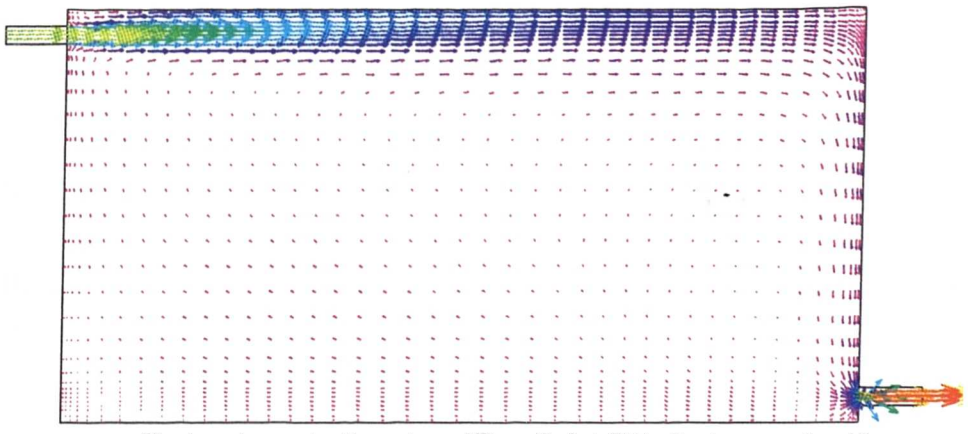

c. Vectors in centreline plane (Case 3, 2 ACH; Scale: ⟶ 1 m/s)

Figure 6.6 Airflow patterns in centreline plane

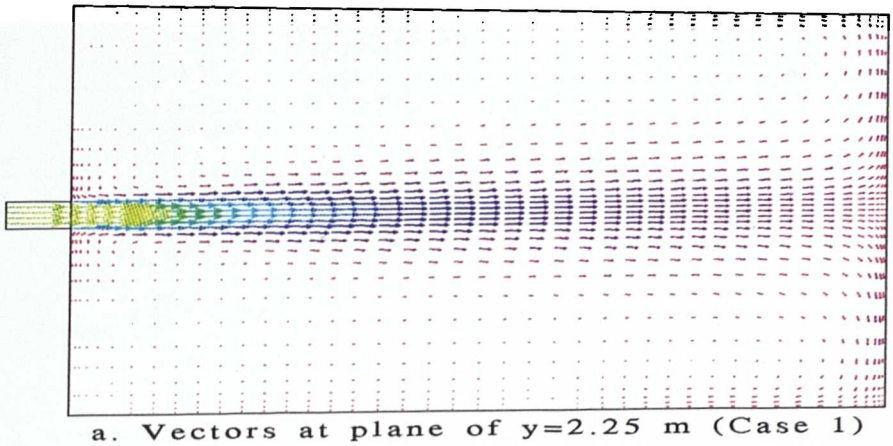

a. Vectors at plane of y=2.25 m (Case 1)

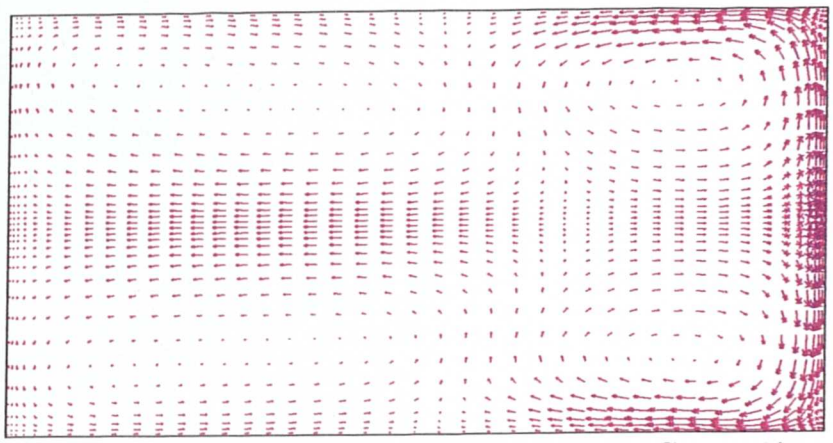

b. Vectors at plane of y=1.2 m (Case 1)

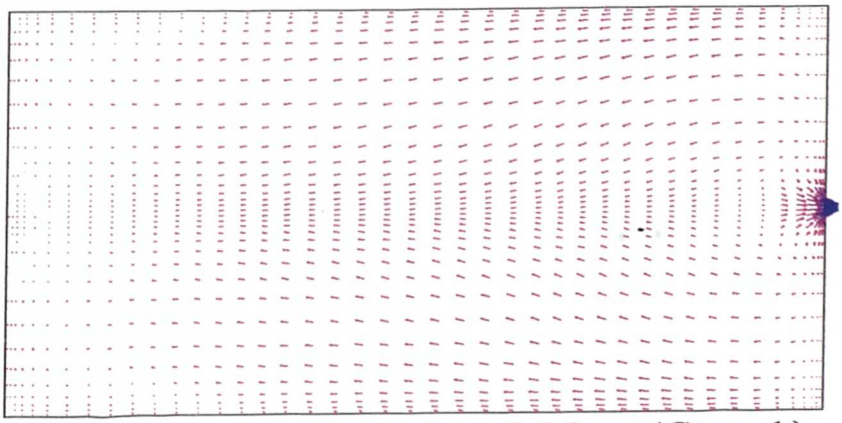

c. Vectors at plane of y=0.25 m (Case 1)

Figure 6.7 Airflow patterns in room height (Vector scale: ⟶ 0.25 m/s)

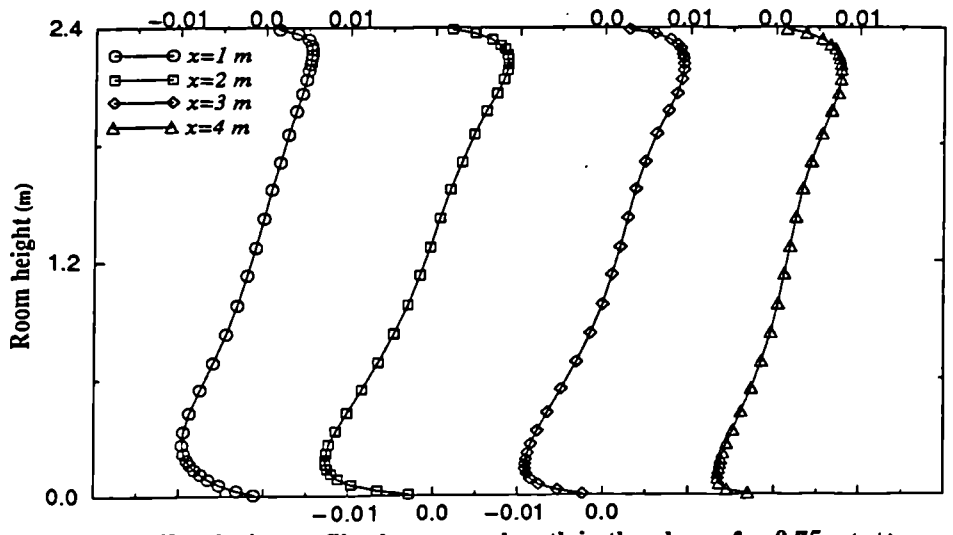

a) U-velocity profile along room length in the plane of z=0.75m (m/s)

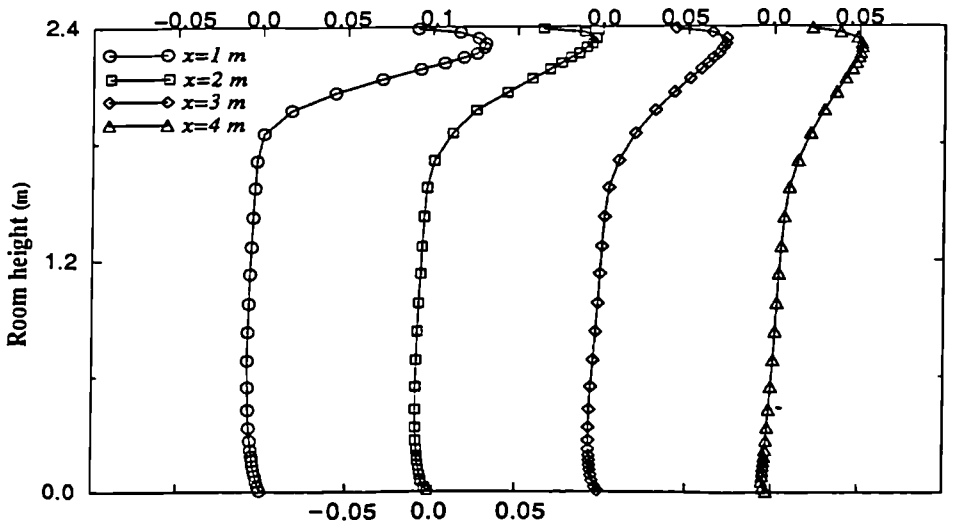

b) U-velocity profile along room length in the plane of z=1.5m (m/s)

Figure 6.8 U-velicty profiles along room length (Case 1)

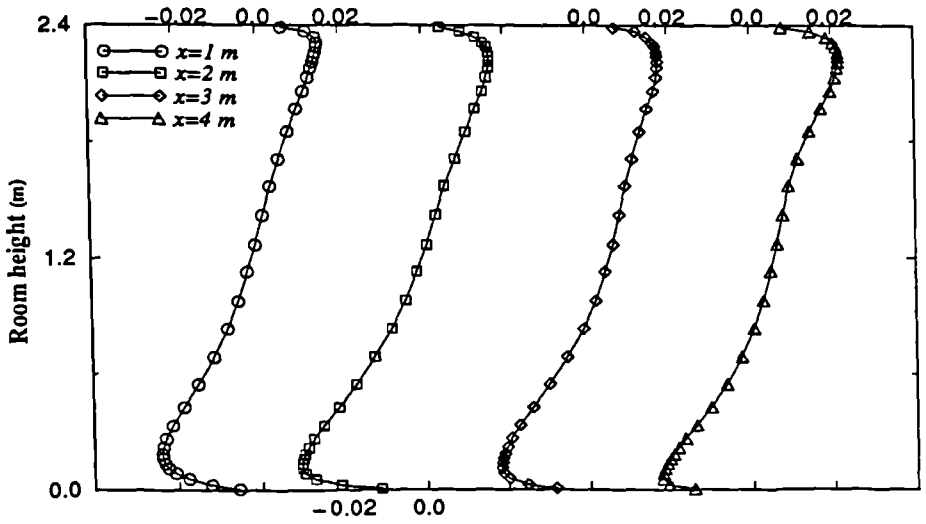

a) U-velocity profile along room length in the plane of z=0.75m (m/s)

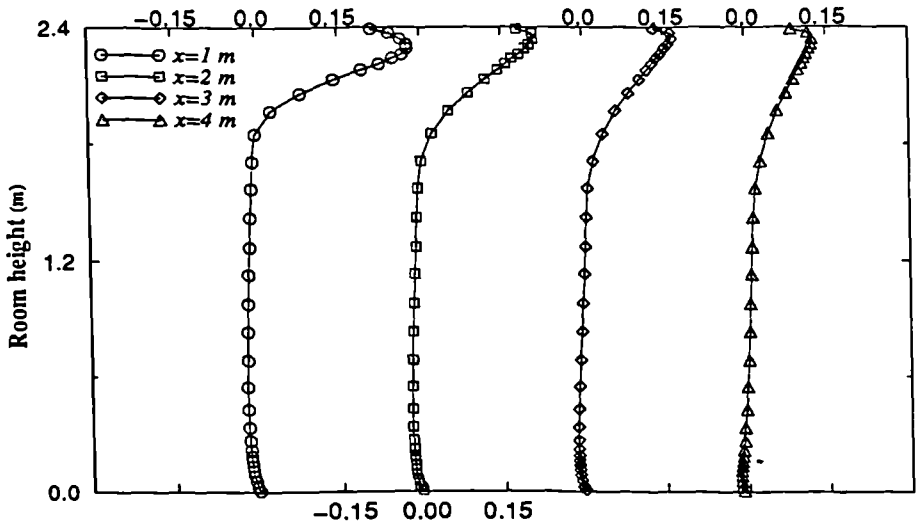

b) U-velocity profile along room length in the plane of z=1.5m (m/s)

Figure 6.9 U-velocity profiles along the room length (Case 2)

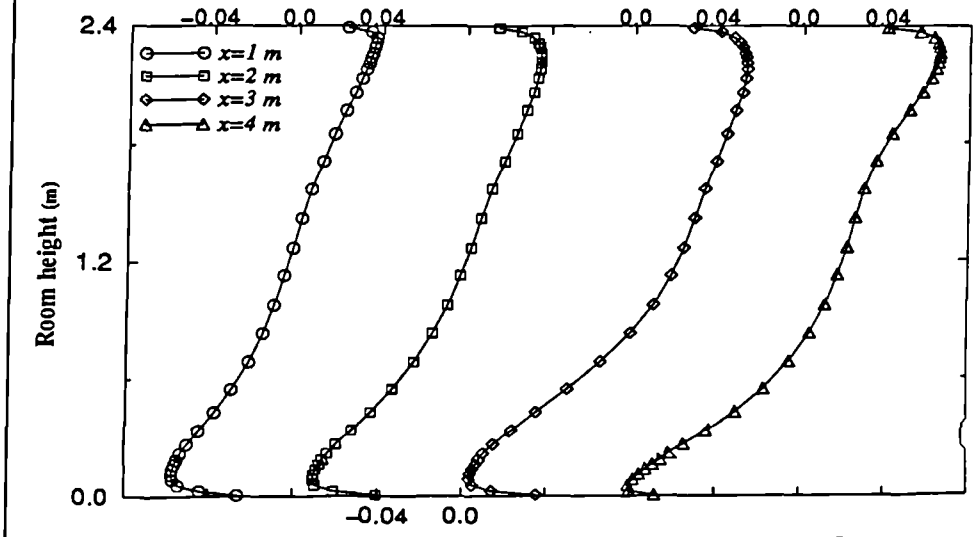

a) U-velocity profile along room length in the plane of z=0.75m (m/s)

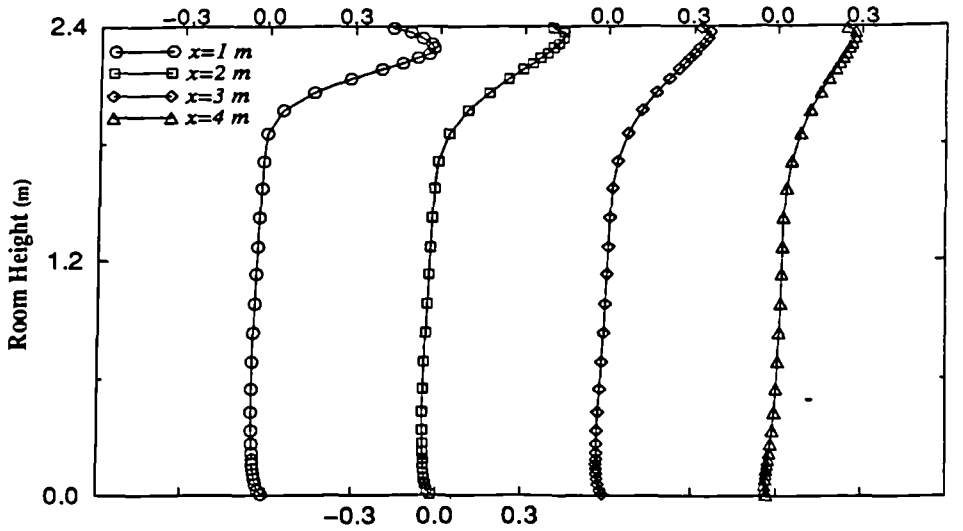

b) U-velocity profile along room length in the plane of z=1.5m (m/s)

Figure 6.10 U-velocity profiles along the room length (Case 3)

III. Aerosol particle movement and distribution in room

As described in §6.3.1, the total number of sample particles in each case is 640 which is uniformly distributed in 10 size groups (i.e., 1~10 μm). The total tracking time is specified as 30 minutes. The particle tracking model can provide details of particle deposition, extraction, and suspension, etc. in the ventilated room.

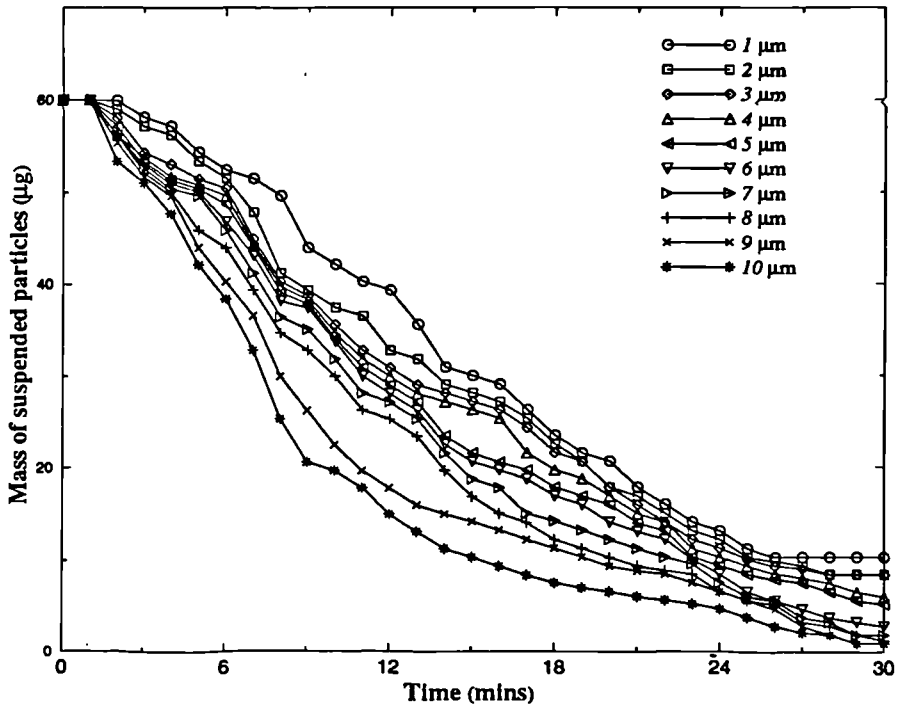

Figure 6.11 Mass of suspended particles varying with time (Case 1, 0.5 ACH)

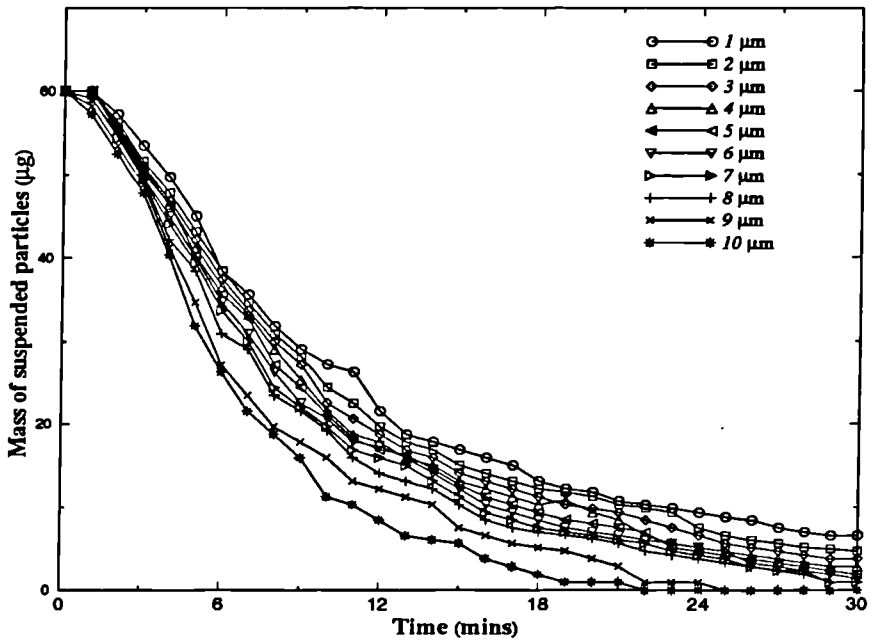

Figure 6.12 Mass of suspended particles varying with time (Case 2, 1 ACH)

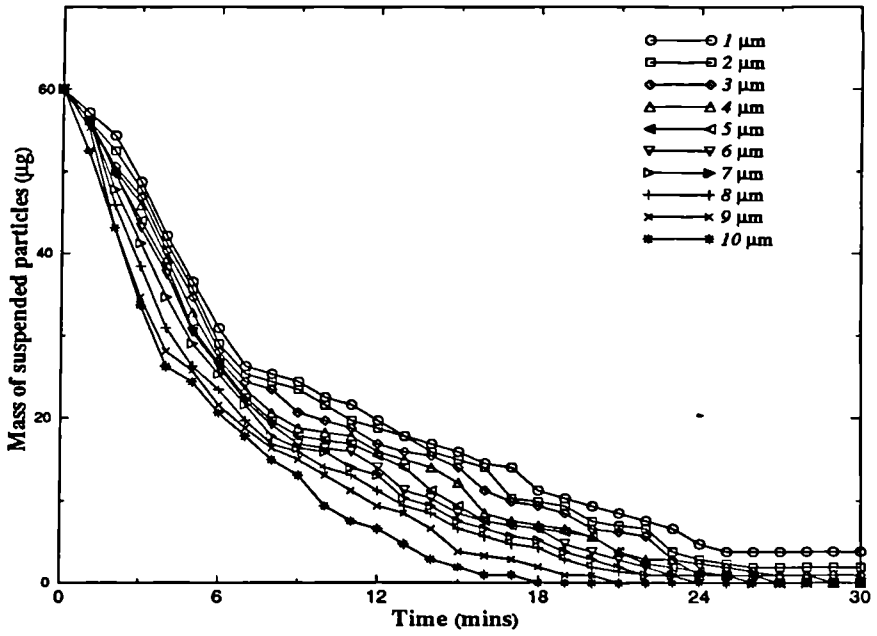

Figure 6.13 Mass of suspended particles varying with time (Case 3, 2 ACH)

- Figure 6.11 ~ 6.13 present the mass of suspended particles varying with the time at different ventilation rates. In general, the masses of suspended particles reduce with time; that means particles deposit on the interior surfaces or extract out of the room continuously with time.
- After a period of tracking time, the majority of particles either deposits onto the internal surfaces or extracts through the exhaust, but some particles still suspend in the room and may remain suspended when the tracking time extends further; these particles comprise the pollutants in the indoor environment.
- From figure 6.11 ~ 6.13, it can be noticed that the masses of large particles decrease faster than those of small particles. The larger the particle, the faster the mass decreases. It can also be seen, from figure 6.11 ~ 6.13, that all particles larger than 7μm are either deposited on the interior surfaces or extracted out of the room.
- Comparing figure 6.11, 6.12 and 6.13, the masses of suspended particles at high ventilation rate decrease faster than those at low ventilation condition. Less particles suspend at high ventilation rate than those at low ventilation rate. It shows that increasing ventilation rate can enhance particle deposition and extraction, and hence reduce particle concentration in the indoor air.
- It is interesting to notice that, at low ventilation rate, some of the large particles, e.g. particles with diameter of 7μm, still keep suspension; while at high ventilation situation, e.g. Case 3, only small particles (e.g. $d_p \leq 3\mu m$ diameter) can remain in suspension.

- The suspended particles are mainly composed of small particles in all three cases. It can be concluded that small particles have greater influence on the pollutant concentration and the indoor air quality in the room.

A detailed analysis of particle removal from the room air is given in figure 6.14 ~ 6.20. The following remarks are concluded:

- From figure 6.14, more than half of the sample particles settle on the floor at low ventilation rate. More particles are deposited on the internal walls instead of on the floor at high ventilation rate (see figure 6.15 and 6.16). In other words, the number of particles sedimented on the floor decreases as the ventilation rate increases, while the number of particles settled on internal walls increases with the ventilation rate (see figure 6.17 and 6.18).
- The results show that gravitational deposition dominates the particle movement at low ventilation rate because the airflow field is close to the static status and the particle is mainly influenced by gravity. The gravitational force becomes less important as the ventilation rate increases. The airflow pattern in the ventilated space plays a key role in the particle movement which means particle movement is more influenced by the flow field rather than the gravity.
- The airflow pattern is influenced by the supply air parameters, turbulence intensity, and geometric parameters, etc.. The velocity values are higher and air circulations are stronger at high ventilation rate than those at low ventilation rate. The drag forces exerted on particles become more important than the gravitational force and dominate the particle movement.

- Some particles follow the air movement, and ultimately either settle on the interior surfaces or extract out of the room. They remain suspension in the room space and comprise the pollutant contaminants in the room which impose the hazards to human being.
- Figure 6.20 describes the number of particles deposited on the floor and the internal walls at different ventilation rates. It can be seen that most large particles ($d_p \geq 5\mu m$) settle on the floor due to the gravity., while particles smaller than 5μm tend to deposit on the interior surfaces rather than floor.
- From figure 6.18 and 6.20b, it is obvious that the number of particles deposited on the internal walls increases with the ventilation rate. This implies that the perceptible soiling phenomena become severe at high ventilation rates.

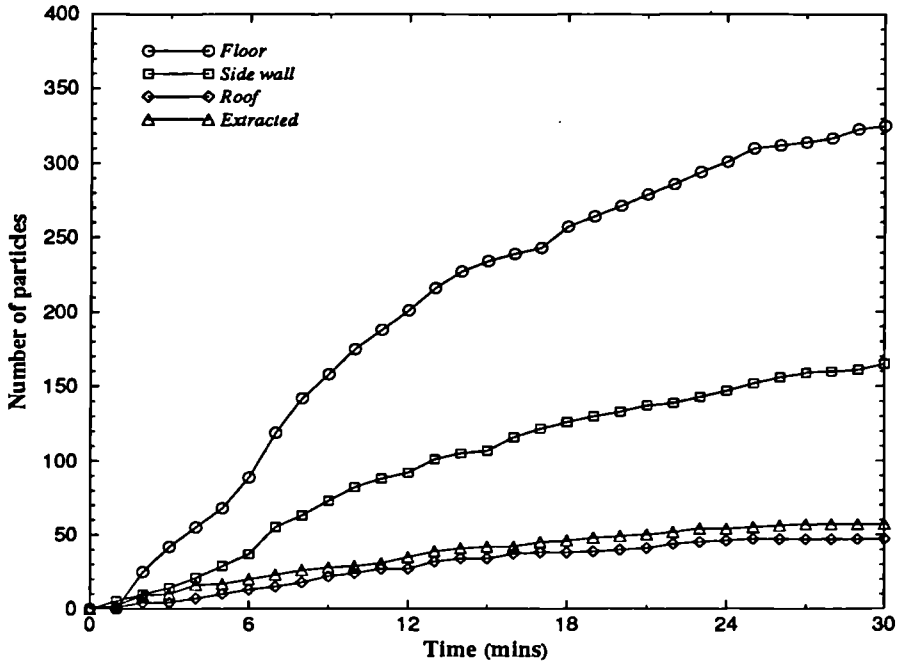

Figure 6.14 Particle removal from the room (Case 1, 0.5 ACH)

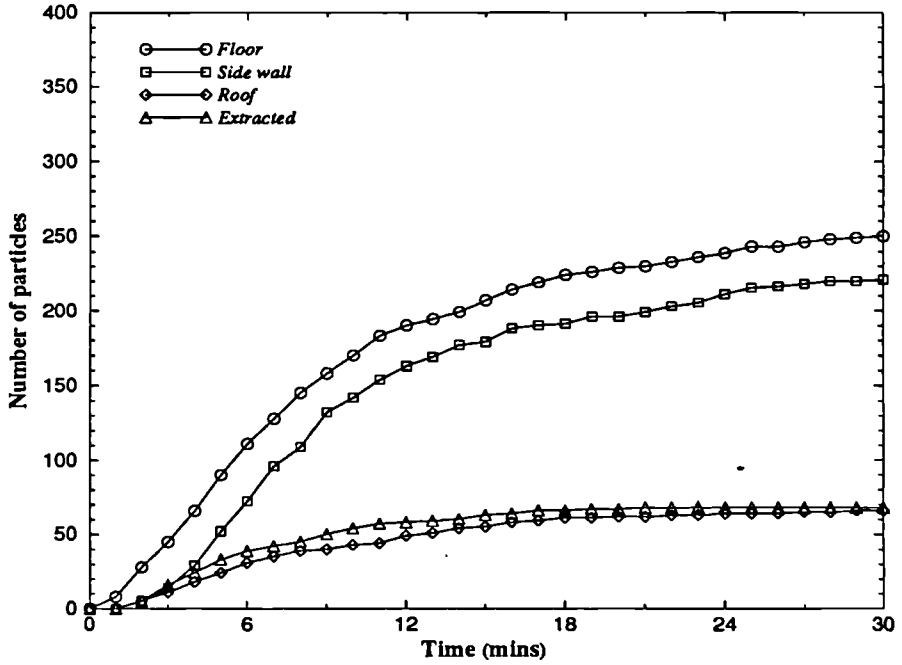

Figure 6.15 Particle removal from the room (Case 2, 1 ACH)

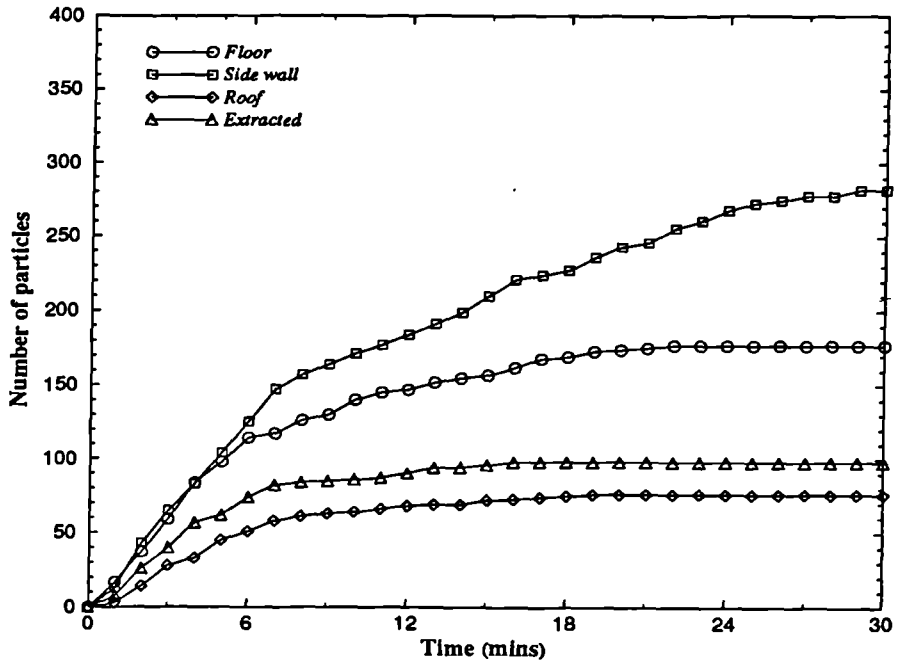

Figure 6.16 Particle removal from the room (Case 3, 2 ACH)

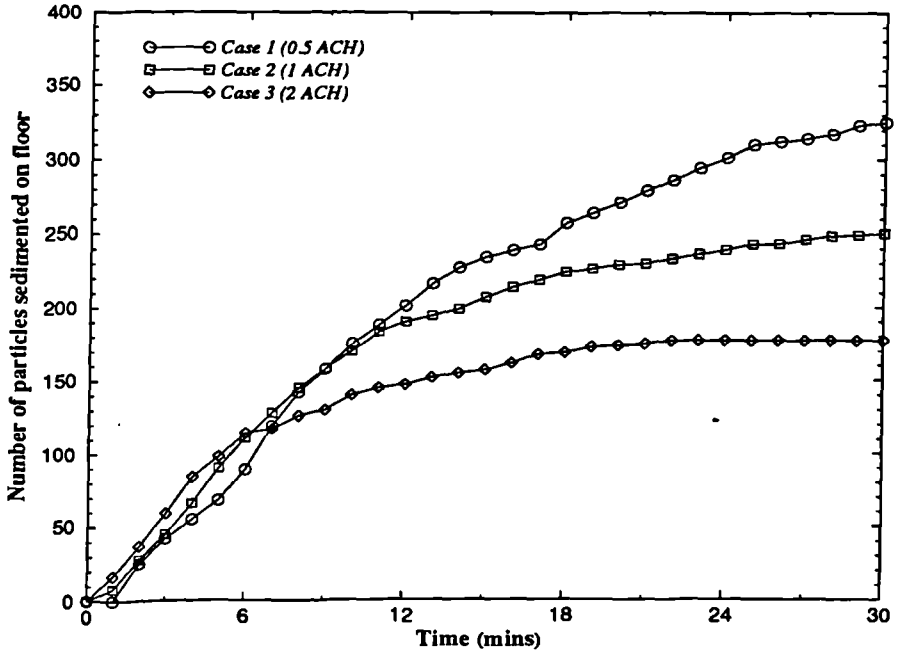

Figure 6.17 Comparison of particles settled on the floor (Case 1, 2 & 3)

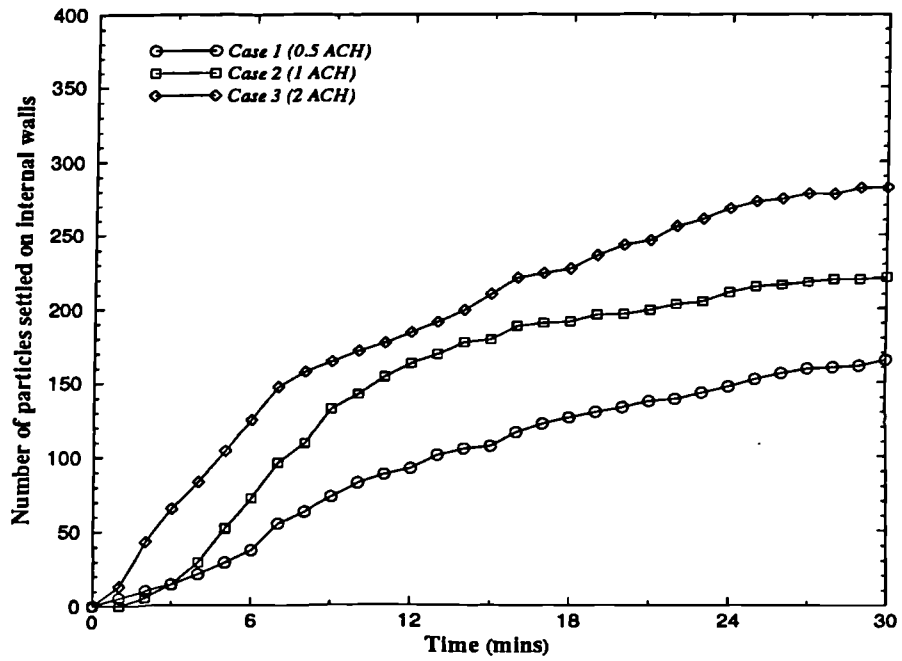

Figure 6.18 Comparison of particles settled on internal walls (Case 1, 2 & 3)

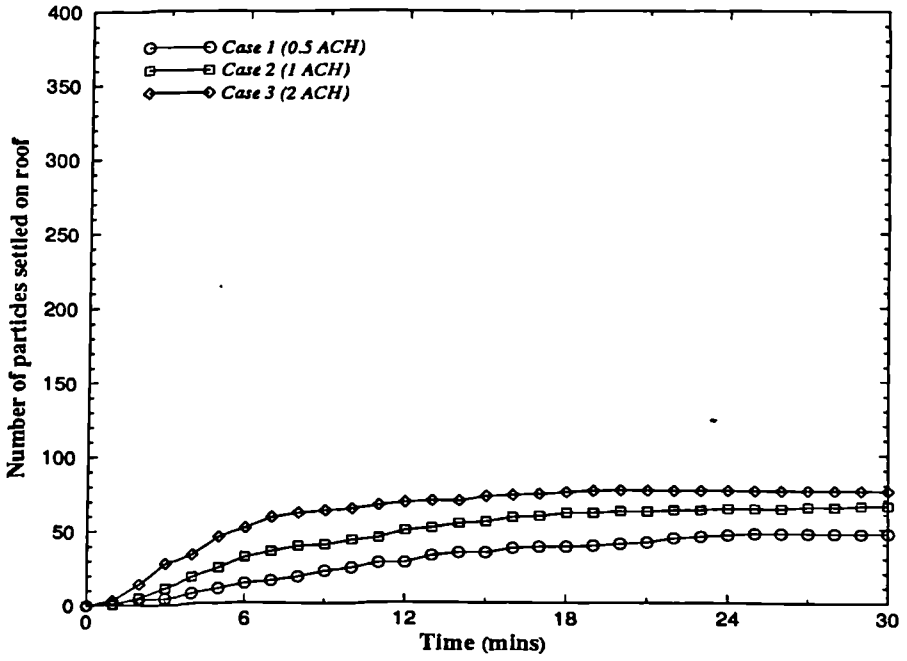

Figure 6.19 Comparison of particles settled on roof (Case 1, 2 & 3)

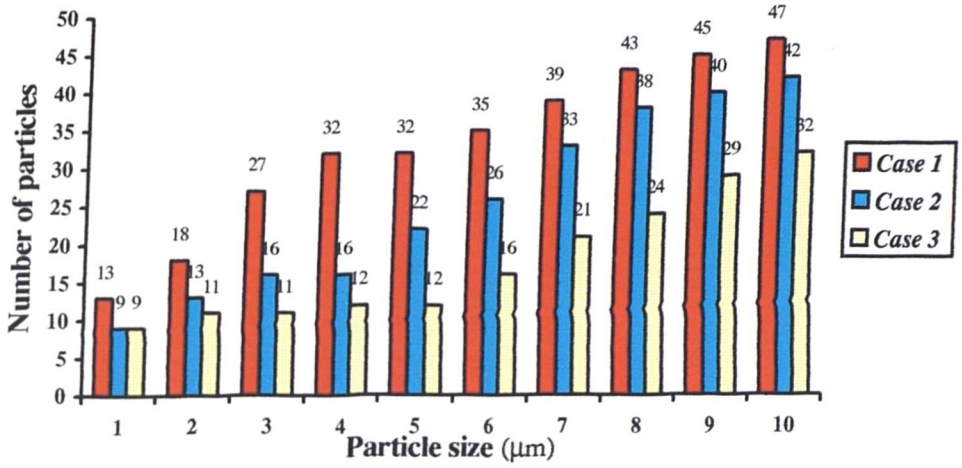

a. Number of particles settled on the floor

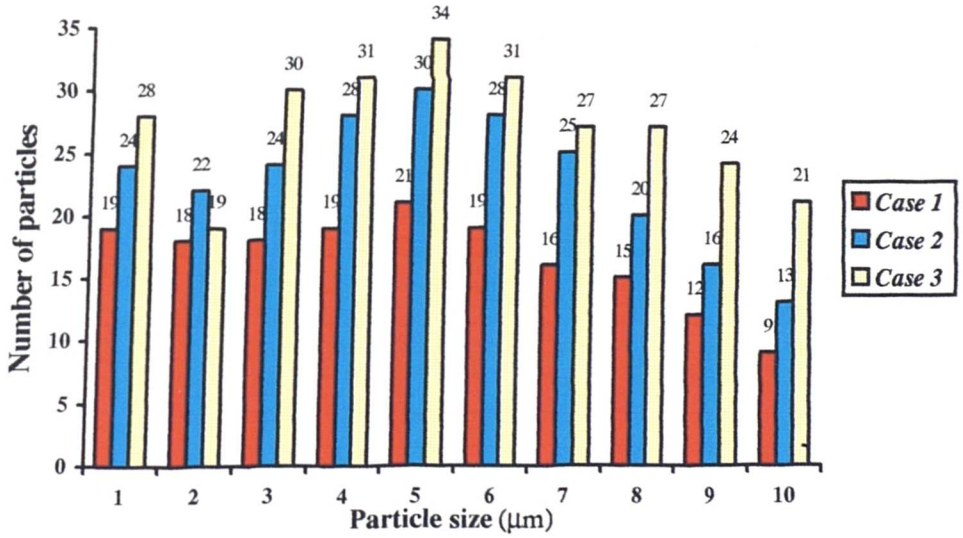

b. Number of particles settled on internal walls

Figure 6.20 Comparison of particle deposition on floor and walls (Case 1 , 2 & 3)

Figure 6.21 presents a comparison of the number of extracted particles at different ventilation conditions. It shows that more particles are removed from the space at high ventilation rates than at low ventilation rates. The results imply that increasing ventilation rate can help extract more particles and reduce the pollutant concentration in the ventilated space.

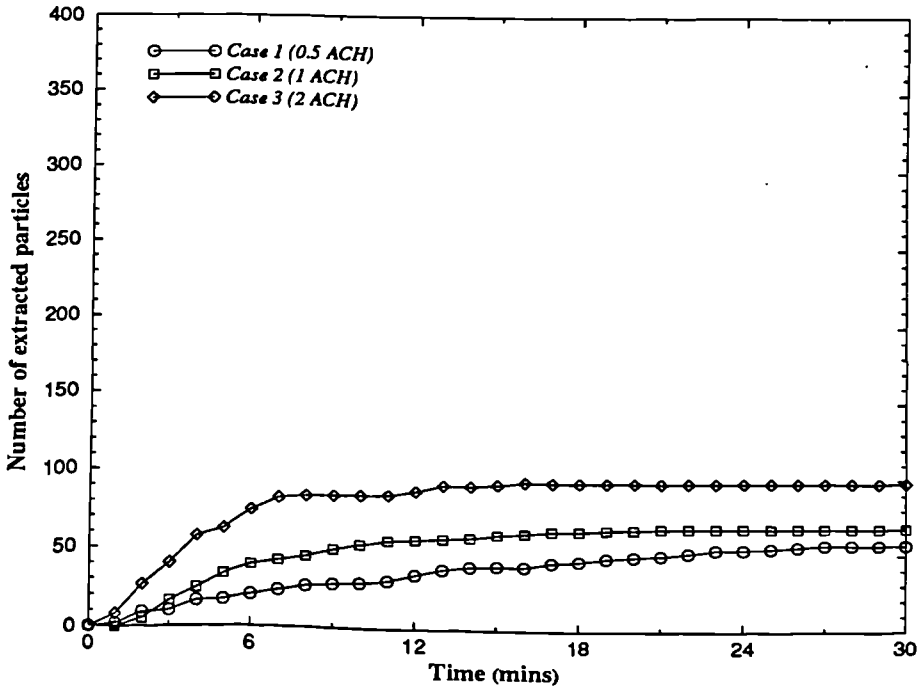

Figure 6.21 Comparison of extracted particles with ventilation rates (Case 1, 2 & 3)

In order to describe the average particle deposition and extraction rates, the following definitions are introduced:

$$R_d = \frac{m_p N_{pd}}{\rho_p T_{trk} V} \tag{6-1}$$

$$R_{ext} = \frac{m_p N_{pe}}{\rho_p T_{trk} V} \tag{6-2}$$

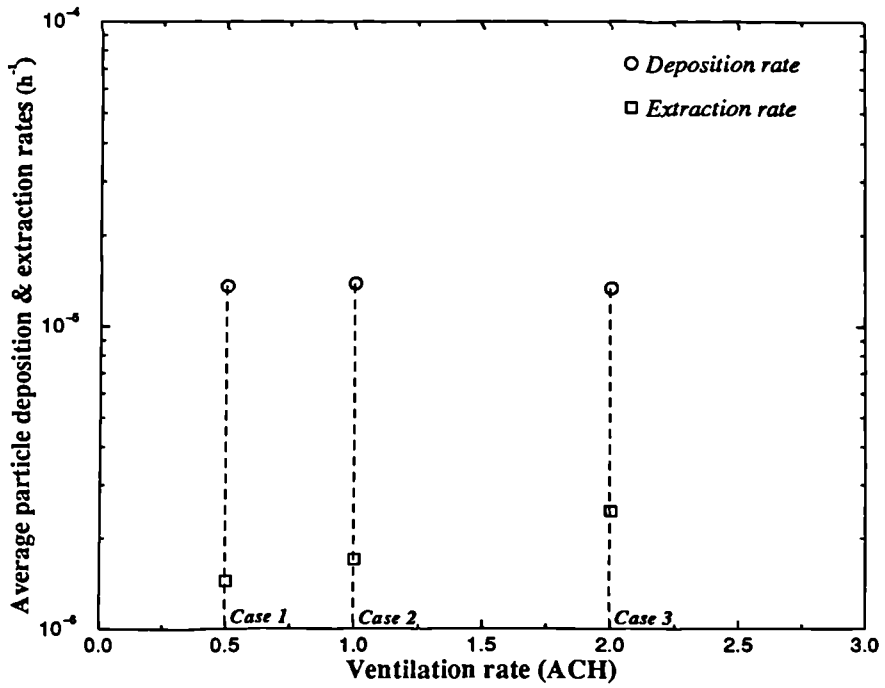

Figure 6.22 Average particle deposition and extraction rates (Case 1, 2 & 3)

The values of average particle deposition and extraction rates at different ventilation conditions are shown in figure 6.22. The results show that the extraction rate increases with the ventilation rate, while the average deposition rate slightly reduces as the ventilation rate increases. This is because more

particles are removed from the ventilated space at high ventilation rates than low ventilation condition, while more particles deposit on the interior surface at low ventilation case than at high ventilation situation.

The profiles of average particle concentration decay of all cases are presented in figure 6.23. The average particle concentration is defined, in this study, as below:

$$C = \frac{\text{Total mass of suspended particles } (\mu g)}{\text{Volume of the ventilated space } (m^3)} \qquad (6\text{-}3)$$

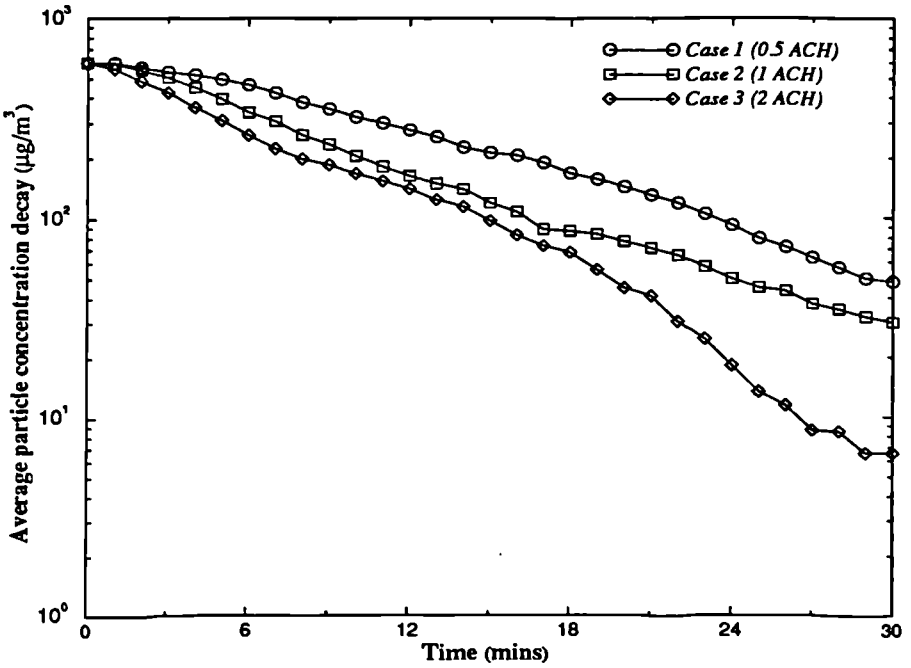

Figure 6.23 Average particle concentration decay with time (Case 1, 2 & 3)

Figure 6.23 shows that the particle concentration decreases with time. The concentration at high ventilation rate decays more rapidly than that at low ventilation rates. This is because more particles are removed from the room at high ventilation rate.

§6.4 Conclusions

This chapter presents a numerical analysis of airflow and aerosol particle movement and distribution in a ventilated one-zone space by using CFD modelling. Both Eulerian and Lagrangian methods are employed to simulate the air movement and particle tracking procedure. A statistical analysis of aerosol particle movement in the ventilated space has proceeded by tracking a large number of sample particles. The conclusions are as follows:

1. The aerosol particle movement is greatly influenced by the ventilation rate and particle properties;
2. The gravitational sedimentation dominates the large particle motion. The majority of large particles ($d_p \geq 5\mu m$) settle on the floor surface. The gravitational sedimentation decreases as the ventilation rate increases;
3. Both airflow pattern and gravitational sedimentation affect the small particle movement. The sedimentation becomes less important as the particle size reduces. Small particles ($d_p \leq 3\mu m$) mainly comprise the suspended particle group and the pollutants in the indoor environment. Small particles greatly influence the indoor air quality and impose the danger to human health;
4. Increasing ventilation rate can enhance the removal of particles but increase the particle deposition on the internal surfaces at the same time. This may worsen the soiling problem of interior surfaces;
5. Aerosol particle concentration in the ventilated space decays more rapidly with increasing ventilation rate.

Generally speaking, increasing ventilation can help reduce the pollutant level and improve the indoor air quality, but it will consume more energy and may increase the internal surface soiling and the risk of draught.

CHAPTER VII

AIRFLOW AND PARTICLE MOVEMENT IN VENTILATED TWO-ZONE ROOM

Abstract

The scope of this chapter is to investigate the influence of the size of interzonal connection and the ventilation condition on the aerosol particle movements and airflow patterns in a ventilated two-zone enclosure. This is done by investigating the air movement, particle deposition, migration, extraction and distribution in both zones by using CFD methods. The simulations are validated by experiment. The conclusions show that the agreements between computations and measurements are generally satisfactory and acceptable; the interzonal opening significantly affects the air movement in the two-zone area and particle migration between zones; particle depositions are mainly influenced by the airflow patterns, particle properties and ventilation conditions; small particles mainly contribute to the pollutant concentration level in the ventilated spaces and greatly affect the indoor air quality. It is shown that the CFD analysis provides valuable detailed information of airflow and aerosol particle movement and distribution in a ventilated two-zone area and therefore can be useful to the evaluation of the indoor air quality and the performance of ventilation system. Furthermore, the research proceeded in this chapter also supply information for the CFD simulation of airflow and aerosol particle movement in more complicated multi-zone ventilated spaces.

§7.1 Introduction

This chapter is devoted to a numerical study of airflow and aerosol particle movement in a ventilated two-zone chamber with different interzonal openings by using CFD modelling. The results will be compared with relevant experimental data.

Today, people spend most of their times in the indoor environment. The indoor air quality has become more important than ever before. Most buildings are divided into multi-zone areas . In large buildings, the air exchanges between the indoor and outdoor of these buildings are often through mechanical ventilation system. In these buildings (e.g., office, museum, etc.), the indoor air quality is greatly influenced by the pollutant particle concentration level and particle movement in the indoor environment.

The aerosol particle is regarded as one of the main pollutant sources in the indoor environment. The indoor aerosol particles are from a combination of indoor sources (e.g. cigarette smoke, building materials, personal products, etc.) and outdoor sources (e.g. car exhaust emissions, coal and oil combustion, pollen, road dust, etc.) which may enter the building through ventilation system. Particle movement in ventilated multi-zone areas is a complicated phenomenon and influenced by many factors, such as airflow pattern, geometrical configurations, particle properties, ventilation conditions, supply and exhaust diffuser locations, internal partitions, thermal buoyancy due to the

heat generated by occupants and/or equipment, etc. Previous studies (as described in Chapter II) show that large particles (particle size d_p>4μm) will be deposited on the internal surfaces (e.g., floor) mainly under the influence of gravity, while particles which are less than 2μm may become aerosol particles and remain suspended in the air and the occupied spaces in which molecular diffusion and air movement dominate the particles' movement while the gravitational force becomes less important. Particles which are between 2 and 4μm may settle on the interior surfaces (e.g., internal walls, floor, etc.) or remain suspended in the air under the influence of both the airflow pattern and gravity. Another important phenomenon of particle movement in multi-zone area is particle migration between zones. In multi-zone area, some particles are neither deposited on the internal surfaces nor extracted through the ventilation system, they may migrate between zones due to the unbalance of momentum and thermal equilibrium between zones. That means that the pollutant source in one zone may be transferred to another one by the particle migration. It has also been shown in the previous studies that particles which suspend in the air or migrate between zones have a significant influence on the human health (i.e., those particles may be inhaled by the occupants and deposit on the nasal passage which may have potential harmful effect on human beings) and the indoor air quality. The indoor air quality in multi-zone buildings has been given much attention in recent years. As mentioned before, particles which deposit on the internal surfaces may cause perceptible soiling problems and further may lead to damage on works of art in museums. The air movement in multi-zone areas is normally promoted by temperature difference between warm and cold zone under natural convection, and/or by pressure difference due to mechanical ventilation. It is known that the airflow pattern plays an important role in the

deposition, migration and distribution of aerosol particles in the ventilated multi-zone area. Previous studies have shown that the knowledge of aerosol particle behaviour in the ventilated multi-zone space is still limited due to the lack of profound understanding of aerosol particles characteristics in such situations.

In most environmental problems encountered today, unacceptable indoor air quality is mainly caused by the high pollutant particle concentrations and the poor ventilation within the space. The removal of contaminant particles is mainly through ventilation and particle deposition processes. Both processes play important roles in improving the indoor air quality.

The study of air movement and aerosol particle distribution in the ventilated area has been carried out both by experimental measurements (see §2.2) and numerical analysis (see §2.3). Generally speaking, experimental study can supply direct knowledge of the movement of air and particle in the ventilated space based on the measurement data. However, it is found that experimental study cannot provide enough information about the air movement and particle deposition and distribution in the whole space due to the limited number of measurement points and some experimental technical difficulties (e.g. measurement difficulty in near-wall regions, etc.). Full-scale experiments can be expensive and time-consuming. The previous studies (as described in Chapter II) also revealed that it is difficult to develop an undistorted test due to the impossibilities of simultaneously satisfying the requirement of similarity of Reynolds number and Archimedes number. Computational Fluid Dynamics (CFD) is a useful and cost-effective method to analyse the airflow patterns and

aerosol particle distribution in full-scale ventilated spaces by solving the appropriate mathematical equations which are suitable for describing the movements of air and particles under certain conditions. The research presented in this chapter uses CFD to predict the airflow and aerosol particle distribution in a full-scale ventilated two-zone chamber and to compare the numerical results with the corresponding experimental data. The purposes of the study are as follows:

1. To simulate the air movement in the ventilated two-zone room under different ventilation rates and interzonal openings;
2. To obtain the information about the aerosol particle deposition, migration and distribution in the above space;
3. To investigate the influence of different ventilation rate and interzonal opening on the particle distribution in the chamber.

§7.2 Numerical Analysis of Airflow and Aerosol Particle Movement in Ventilated Two-Zone Chamber

Similar to the simulations carried out in Chapter VI, a Eulerian continuous mathematical model is employed to simulate three-dimensional air flow; a Lagrangian particle transport model is applied to track sample particles with different particle sizes. Particles' deposition and concentration in the two-zone area are also analysed. The comparisons of particle concentrations between computational results and experimental data are also presented.

§7.2.1 Case Description

I. Geometrical and flow parameters

In a project related to this work, Adam (1995) and Cheong (1994) have conducted experimental investigations in a two-zone chamber with a size of 5m (length) × 2.4m(height) × 3m(width). The room is divided into two zones by a partition with an opening. The partition is in the middle of the room length. The opening is located on the centreline of the chamber. The thickness of the partition can be ignored compared with the room size. Table 7.1 shows the parameters of all cases simulated. The air flow is assumed to be steady, incompressible and iso-thermal. The room temperature is 20°C. The chamber is assumed to be well-sealed and the only way-out for the room air is through the exhaust section. Figure 7.1 shows the geometrical outlines of cases.

Table 7.1 Parameters of cases

Case No.	L (m)	H (m)	W (m)	l (m)	h (m)	w (m)	h_o (m)	w_o (m)	Ventilation rate (h^{-1})	R_∞	No. of iteration	Area ratio of opening to partition
Case 1	5	2.4	3	0.15	0.5	1.0	0.2	0.7	11.484	1277	4000	0.02
Case 2	5	2.4	3	0.15	0.5	1.0	0.2	0.7	14.004	1557	4000	0.02
Case 3	5	2.4	3	0.15	0.5	1.0	0.3	0.7	11.566	1285	4000	0.03
Case 4	5	2.4	3	0.15	0.5	1.0	0.3	0.7	12.708	1413	4000	0.03
Case 5	5	2.4	3	0.15	0.5	1.0	0.95	0.7	9.216	1025	6000	0.092
Case 6	5	2.4	3	0.15	0.5	1.0	0.95	0.7	10.26	1141	6000	0.092

The Eulerian mathematical model for representing the continuous fluid flow and the Lagrangian particle transport model for tracking the particles' movement are described in Chapter IV. Both equation sets are solved by using FLOW3D package. A standard k-ε model is applied to describe the turbulence characters. No heat and mass transfer exist between the air and the particles. All particles are spherical solid particles. Particles do not rebound on making contact with the solid surfaces.

The room is divided into 40×28×30 cells (i.e., control volumes). The supply section is divided in 3×8×14 cells, while 3×4×8 cells are set up for the exhaust section. A refined mesh is established near all walls of the chamber including the partition, see figure 7.2.

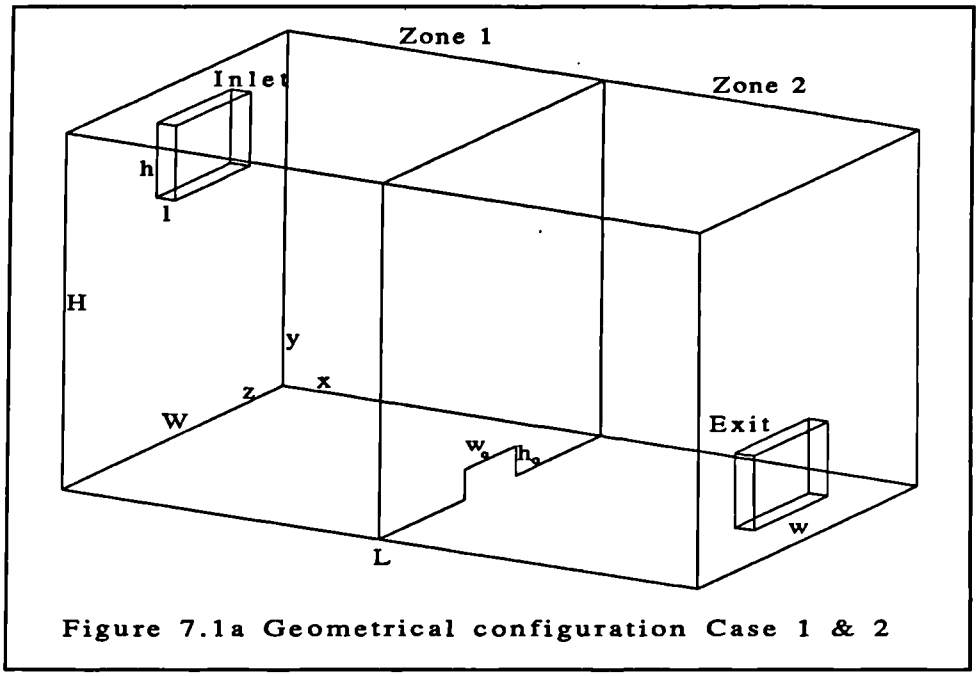

Figure 7.1a Geometrical configuration Case 1 & 2

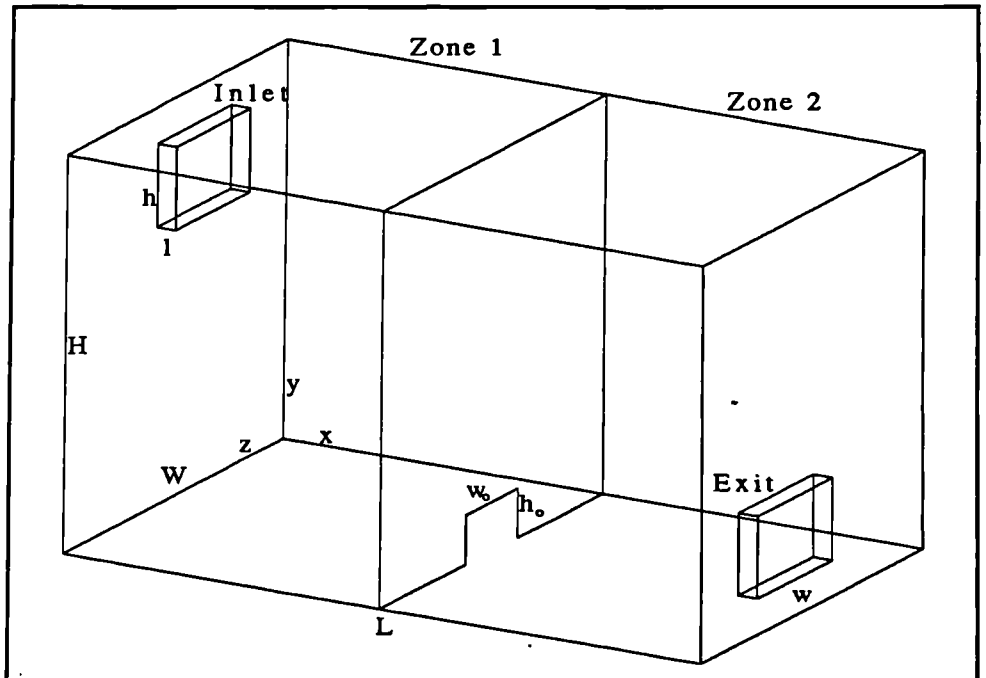

Figure 7.1b Geometrical configuration for Case 3 & 4

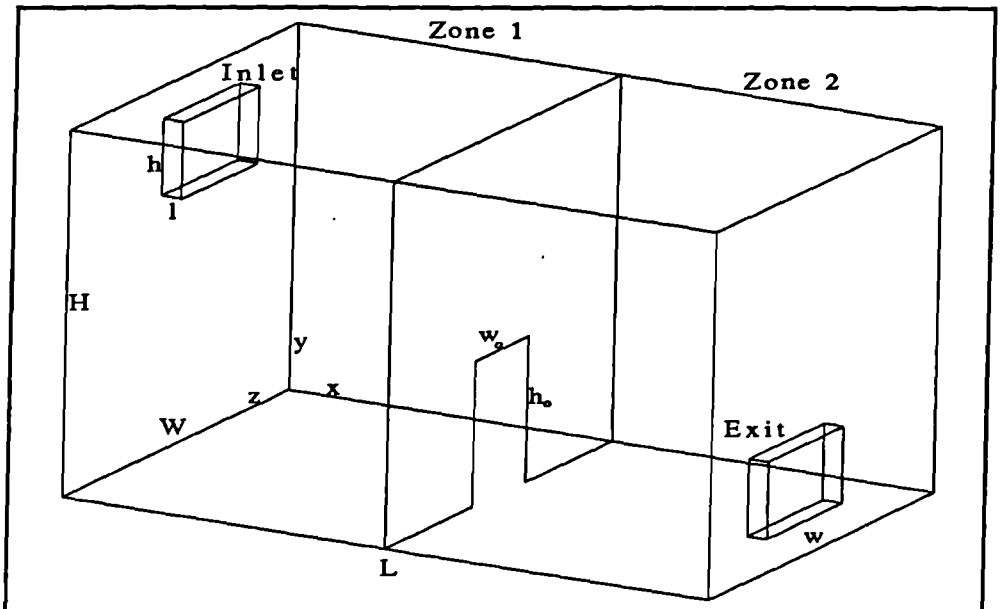

Figure 7.1c Geometrical configuration for Case 5 & 6

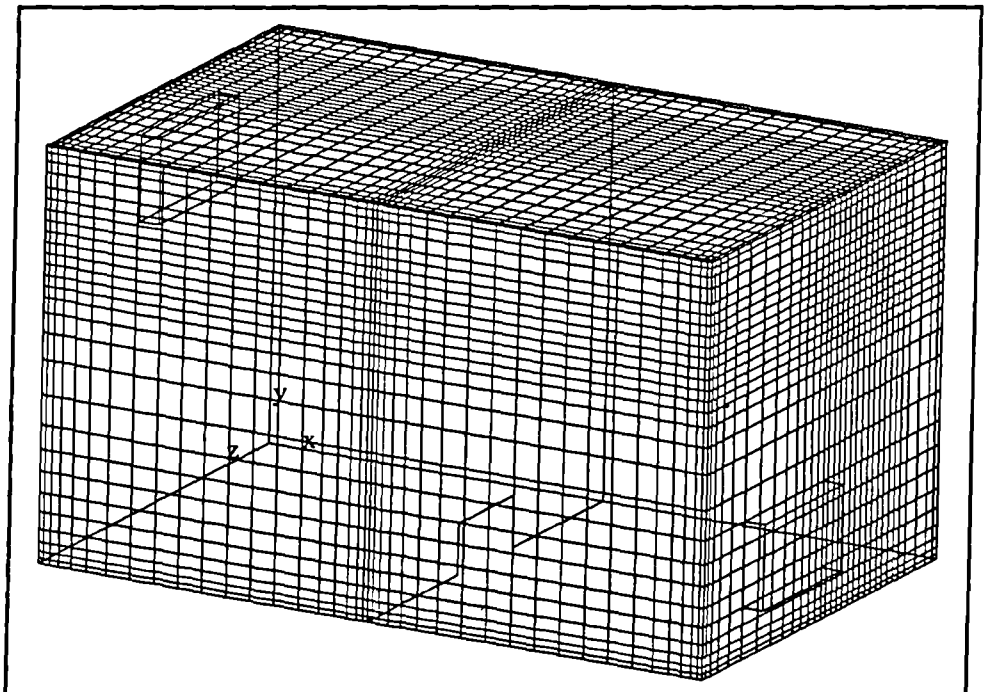

Figure 7.2 The mesh scheme

II. Experimental procedures

The experimental work was carried out in an environmental chamber as described above. The chamber consisted of two tightly-sealed zones. The two zones were connected by an opening with a sliding door (vertical direction). The height of the opening could be adjusted by a pulley arrangement (Table 7.1). A variable-speed fan supplies fresh air into the chamber via the inlet diffuser. The air is removed from the chamber via the exit diffuser.

The experimental procedure involves injecting SF_6 tracer gas and oil-smoke into the chamber with all the dampers, interzonal opening and fan shut. A period of 10 minutes is allowed for the tracer gas and oil-smoke to mix with the air in the chamber. Once a uniform concentration of tracer gas and smoke particles is achieved in the chamber, dampers at the respective diffusers and interzonal opening are opened and the fan is switched on. At the same time, monitoring of the concentration of tracer gas and smoke particles commenced at the centre of each zone using infra-red gas analyser type and an infra-red particle monitor respectively. The measured data represent the corresponding average particle concentrations in each zone.

III. Initial and boundary conditions

1. Boundary conditions for the air

The boundary conditions which are specified for the continuous phase, in this study, are defined as follows:

- All variables at the upstream of the flow domain are set up according to the principal of Dirichlet boundary condition. The main flow is specified as entering the chamber with a uniform velocity which is calculated according to the ventilation rate of each case respectively. The quantities k and ε at the inlet are normally based on the mean flow characteristics at the inlet, here, both are defined by the same method used in Chapter VI. Table 7.2 shows the inlet flow parameters of each case.

- A non-slip condition at the solid wall is applied to the velocities. The wall functions are employed to describe the turbulent properties in near wall regions (see §4.3).

- Neumann boundary conditions are applied at the outlet to satisfy the mass conservation law (see §4.3).

Table 7.2 The inlet flow parameters of cases

Case No.	U	V	W	k	ε
Case 1	1.1484E-1	0.0	0.0	2.638E-5	2.714E-6
Case 2	1.4004E-1	0.0	0.0	3.922E-5	4.913E-6
Case 3	1.156E-1	0.0	0.0	2.675E-5	2.768E-6
Case 4	1.271E-1	0.0	0.0	3.229E-5	3.671E-6
Case 5	9.216E-2	0.0	0.0	1.699E-5	1.402E-6
Case 6	1.026E-1	0.0	0.0	2.105E-5	1.932E-6

2. Initial conditions for particle tracking

The initial conditions for particle tracking include the starting positions and initial velocities of the particles. The particles have the density of oil smoke particles, i.e., ρ_p=865.0 kg/m^3 and are equally divided into five size groups from 1μm to 5μm. Those particles which are less than 1μm are included into 1μm size group. In the experimental work, smoke particles are initially injected into zone 1 and well mixed. They are assumed to be uniformly distributed in that area when the measurement started. So the initial positions of particles are set up within the whole volume of zone 1 as shown in figure 7.3. The total particle mass injected into zone 1 in each case is specified based on the experimental data. The particle mass is uniformly carried by each size group. The initial particle velocities are defined according to the equation (3-11) or (3-30). Table 7.3~7.8 list the relevant particle parameters of each case.

Table 7.3 Particle parameters of Case 1 (11.484 h^{-1})

Size d_p (μm)	Particle mass represented by each sample particle (μg)	No. of sample particles	No. of particles carried	Tracking periods (mins)	Initial velocities U (m/s)	V	W
1	191.07	160	7.5935123E12	40	0	2.65E-5	0
2	191.07	160	9.4918904E11	40	0	1.04E-4	0
3	191.07	160	2.812412E11	40	0	2.34E-4	0
4	191.07	160	1.1864863E11	40	0	4.16E-4	0
5	191.07	160	6.0748099E10	40	0	6.50E-4	0

Table 7.4 Particle parameters of Case 2 (14.004 h^{-1})

Size d_p (μm)	Particle mass carried by each sample particle (μg)	No. of sample particles	No. of real particles carried	Tracking periods (mins)	Initial velocities U (m/s)	V	W
1	130.79	160	5.1979084E12	20	0	2.65E-5	0
2	130.79	160	6.4973856E11	20	0	1.04E-4	0
3	130.79	160	1.9251513E11	20	0	2.34E-4	0
4	130.79	160	8.1217319E11	20	0	4.16E-4	0
5	130.79	160	4.1583268E10	20	0	6.50E-4	0

Table 7.5 Particle parameters of Case 3 (11.566 h^{-1})

Size d_p (μm)	Particle mass represented by each sample particle (μg)	No. of sample particles	No. of particles carried	Tracking periods (mins)	Initial velocities (m/s) U	V	W
1	149.4	160	3.2986472E11	35	0	2.65E-5	0
2	149.4	160	4.123309E10	35	0	1.04E-4	0
3	149.4	160	1.2217212E10	35	0	2.34E-4	0
4	149.4	160	5.1541362E09	35	0	4.16E-4	0
5	149.4	160	2.6389178E09	35	0	6.50E-4	0

Table 7.6 Particle parameters of Case 4 (12.708 h^{-1})

Size d_p (μm)	Particle mass represented by each sample particle (μg)	No. of sample particles	No. of particles carried	Tracking periods (mins)	Initial velocities (m/s) U	V	W
1	118.17	160	2.609055E11	24	0	2.65E-5	0
2	118.17	160	3.259027E10	24	0	1.04E-4	0
3	118.17	160	9.663168E09	24	0	2.34E-4	0
4	118.17	160	4.076649E09	24	0	4.16E-4	0
5	118.17	160	2.087249E09	24	0	6.50E-4	0

Table 7.7 Particle parameters of Case 5 (9.216 h^{-1})

Size d_p (μm)	Particle mass represented by each sample particle (μg)	No. of sample particles	No. of particles carried	Tracking periods (mins)	Initial velocities (m/s) U	V	W
1	147.35	160	3.2533018E11	29	0	2.65E-5	0
2	147.35	160	4.0666273E10	29	0	1.04E-4	0
3	147.35	160	1.2049266E10	29	0	2.34E-4	0
4	147.35	160	5.0832841E09	29	0	4.16E-4	0
5	147.35	160	2.6026415E09	29	0	6.50E-4	0

Table 7.8 Particle parameters of Case 6 (10.26 h^{-1})

Size d_p (μm)	Particle mass represented by each sample particle (μg)	No. of sample particles	No. of particles carried	Tracking periods (mins)	Initial velocities (m/s) U	V	W
1	184.58	160	4.0753693E11	26	0	2.65E-5	0
2	184.58	160	5.0942116E10	26	0	1.04E-4	0
3	184.58	160	1.509396E10	26	0	2.34E-4	0
4	184.58	160	6.3677645E09	26	0	4.16E-4	0
5	184.58	160	3.2602954E09	26	0	6.50E-4	0

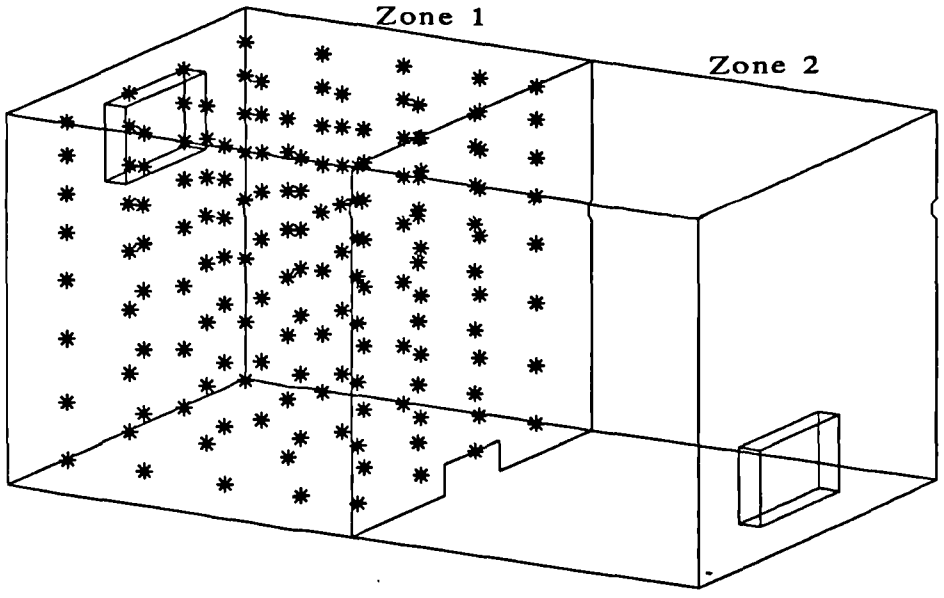

Figure 7.3 The initial positions of sample particles

It should be noted that any momentum transfer from or to the particle must be balanced by a corresponding source or sink of momentum in the continuous phase. For each control volume, these sources are calculated as a sum of the contributions of each of the sample particles, weighted according to the amount of the particle mass of the same size group assumed to be carried by that particle, as it traverses the control volume. So the momentum transfer terms play a key role in coupling both equation sets. It also greatly influences the particle movement.

§7.2.2 Results and Analysis

CFD simulations of the cases described in §7.2.1 are carried out and presented in this section. The analysis of the numerical results and validations with the available experimental data are presented as follows.

I. The convergence history of cases

The convergence criterion here is defined as the values of the normalised mass residuals are reduced to the range of 1×10^{-6} ~ 1×10^{-4} and not increased as the iterations carry on after falling into the defined range. Figure 7.4 ~ 7.6 show the convergence histories of all cases.

a) The relevant convergence control methods (§4.3.7) are employed in the simulations. The values of the under-relaxation factors (URF) have been decreased to 0.4 for Case 1 & 2, see figure 7.4;

b) The URF values of Case 3 & 4 are specified as 0.4 and 0.3 respectively. From figure 7.5, it can be seen that the convergence of high ventilation rate (Case 4) is more difficult than that of low ventilation rate (Case 3) with the same interzonal opening. The high ventilation rate requires deeper under-relaxation than the low ventilation rate does.

c) For Case 5 & 6, the sole under-relaxation method can not assure the converged simulations. The false time-step (FTS) is applied for the iterations of Case 5 & 6. The relevant FTS values of 0.86 and 0.78 are

specified for the momentum equations of Case 5 & 6 respectively. At least 6000 iterations are required to obtain reductions of the mass-residuals to the range of 1×10^{-6} ~1×10^{-4}, see figure 7.6. It can be seen that the FTS method requires more iterations than the URF method.

d) Figure 7.4 ~ 7.6 show that the convergence of the numerical simulations are influenced by the geometrical configurations. The larger the interzonal opening, the more difficult the arrival of convergence and also the more computational time.

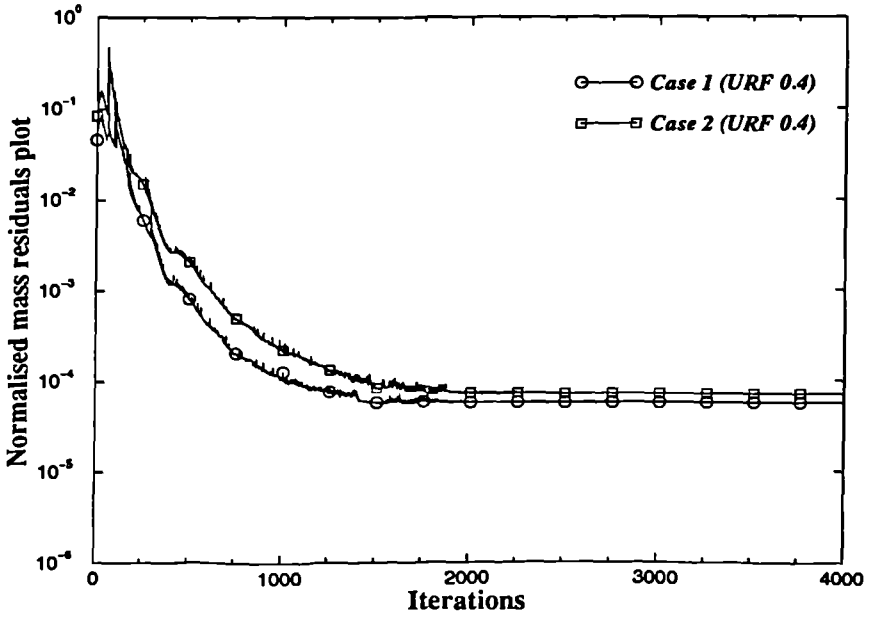

Figure 7.4 The convergence history of Case 1 & 2

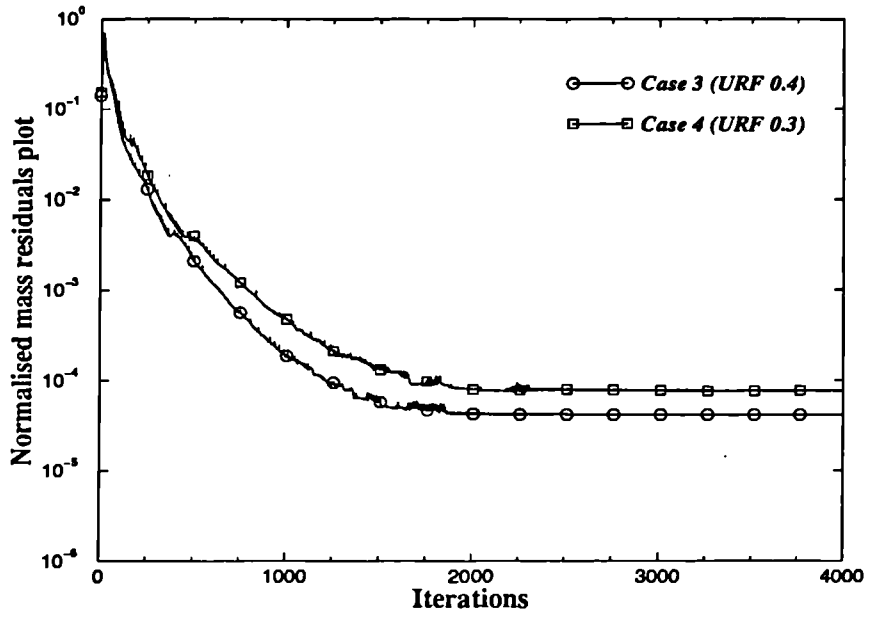

Figure 7.5 The convergence histroy of Case 3 & 4

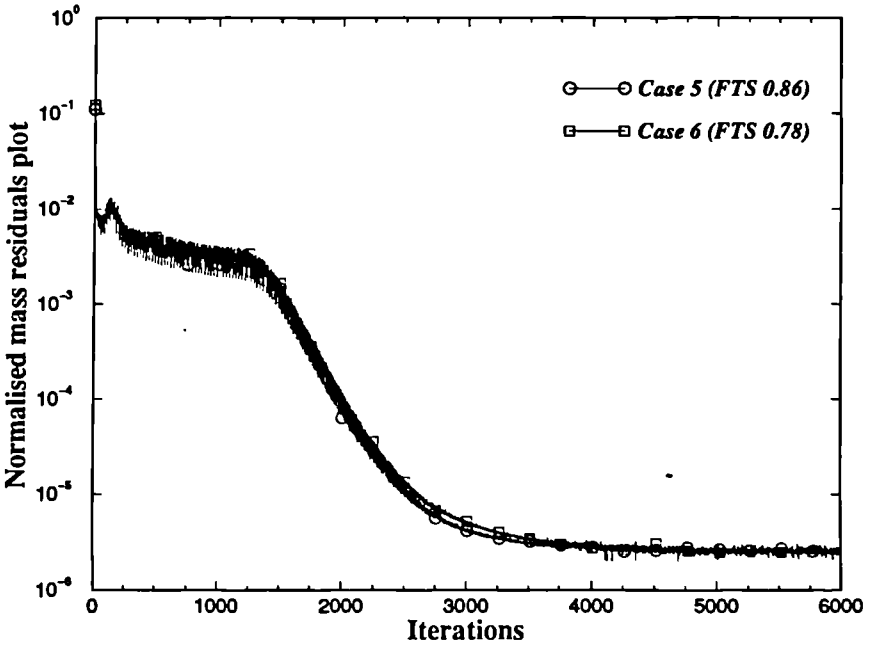

Figure 7.6 The convergence history of Case 5 & 6

II. The airflow patterns in the two-zone area

The airflow patterns in the different planes of Case 1, 3 & 5 are presented in figure 7.7 ~ 7.10. From these figures, the three-dimensional nature of the flow is evident.

a) The airflow patterns in the planes of z=0.75m (figure 7.8a, 7.9a and 7.10a) in three cases are similar. The air circulations are induced by the supply air. The high velocity regions in zone 1 area are restricted at high level due to the Coanda effect. The centres of the air circulation in zone 1 are skewed to the left side wall due to the influence of partition, while the air circulation centres in zone 2 are located close to the exhaust section.

b) In the planes of z=1.5m (figure 7.8b, 7.9b and 7.10b), the airflow patterns are greatly affected by the sizes of the interzonal openings. For the cases with small interzonal openings (e.g., Case 1 and 3), the wall-jet effect can be observed at the floor level in zone 2, i.e., the small interzonal openings act as an air-jet discharger to the space of zone 2 which may cause draught in that area (figure 7.8b and 7.9b). For the cases with large interzonal openings (e.g., Case 5), the air movement in zone 2 is quite different from those with small interzonal openings. The velocity distributions at low level are relatively uniform with large interzonal opening. The size of interzonal opening might influence the particle movement in both zones as well.

c) It is also interesting to notice the differences of the airflow patterns between Case 1, 3 & 5 at the plane of z=2.25m (figure 7.8c, 7.9c and 7.10c). For the cases with small interzonal openings, the air circulations are formed in zone 2 due to the discharge effect of small openings (figure 7.8c and 7.9c). The

centres of air circulation are located at the high level due to the effect of the exhaust locations. For the case with a large interzonal opening, the circulation is not as strong as those in small opening situations (see figure 7.10c). The velocity field is relatively uniform compared with the situations in Case 1 & 3.

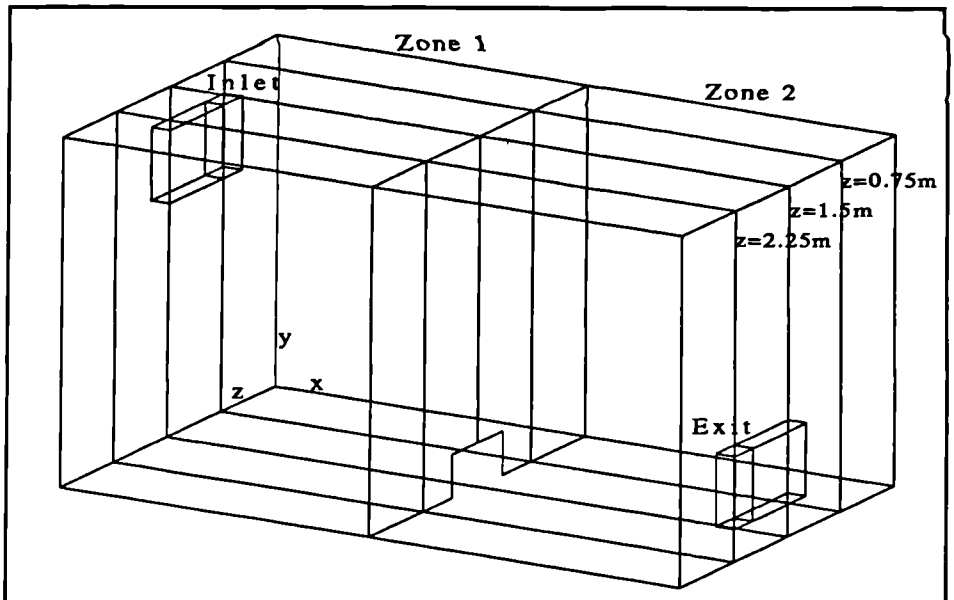

Figure 7.7 Typical planes in the two-zone chamber

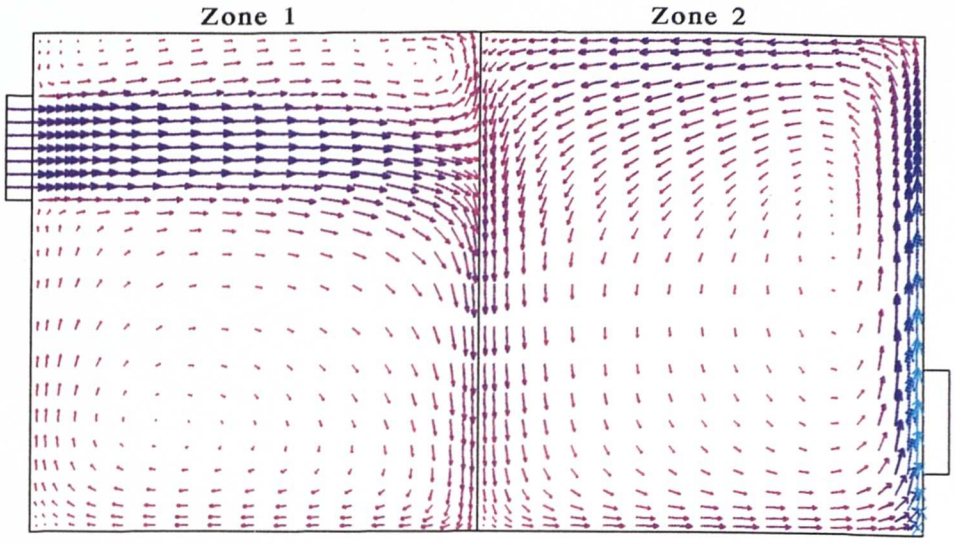

Figure 7.8a Vectors in plane of z=0.75 m (Case 1; Scale: ⟶ 0.115 m/s)

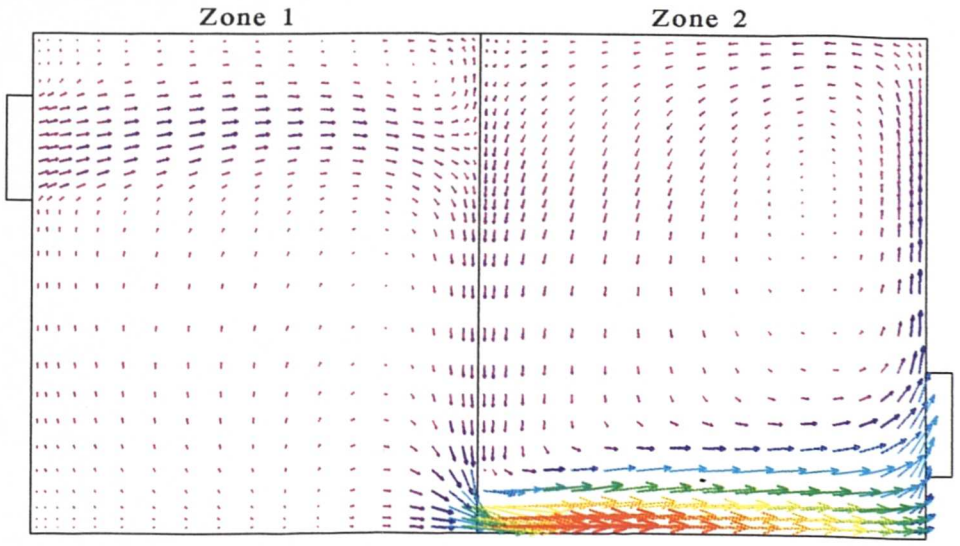

Figure 7.8b Vectors in plane of z=1.5 m (Case 1; Scale: ⟶ 0.115 m/s)

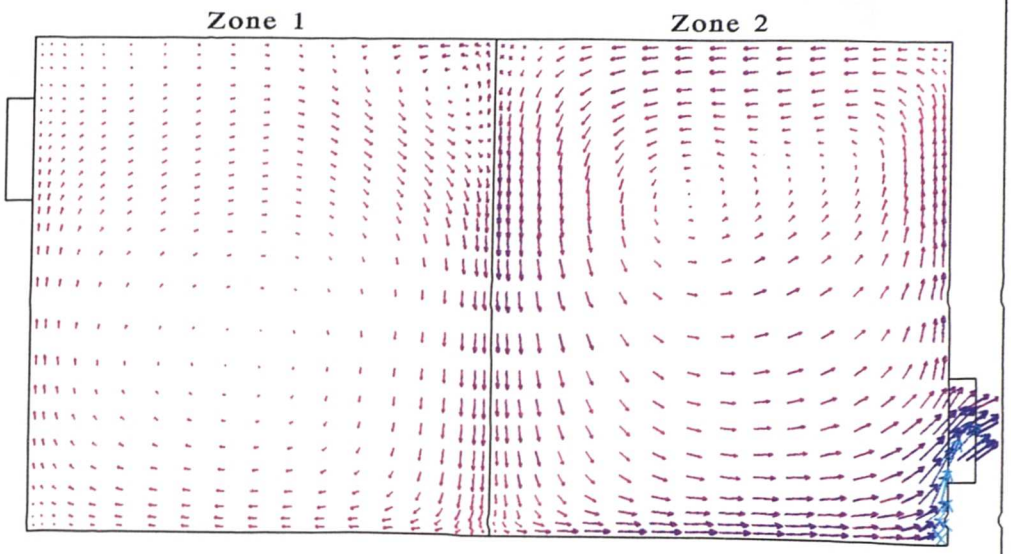

Figure 7.8c Vectors in plane of z=2.25 m (Case 1; Scale: ⟶ 0.115 m/s)

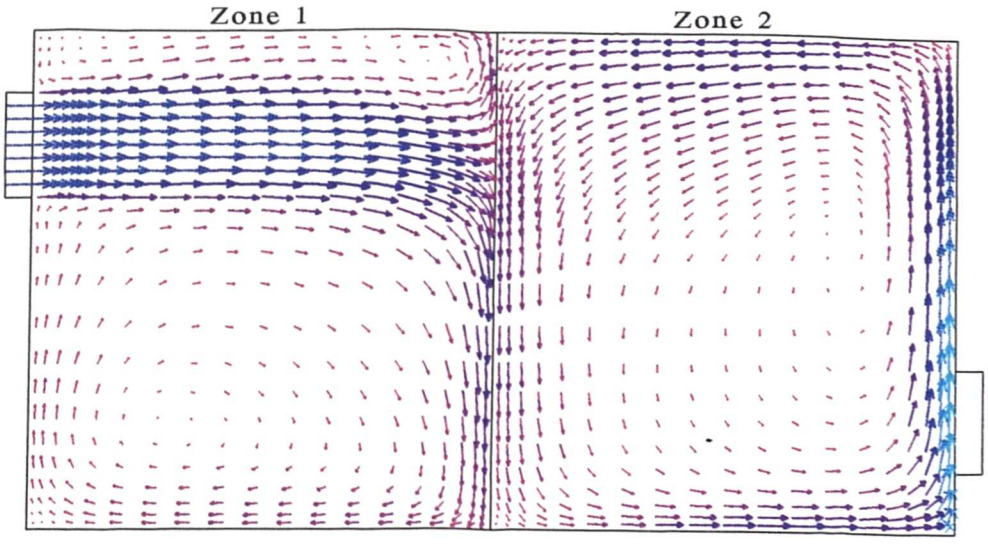

Figure 7.9a Vectors in plane of z=0.75 m (Case 3; Scale: ⟶ 0.116 m/s)

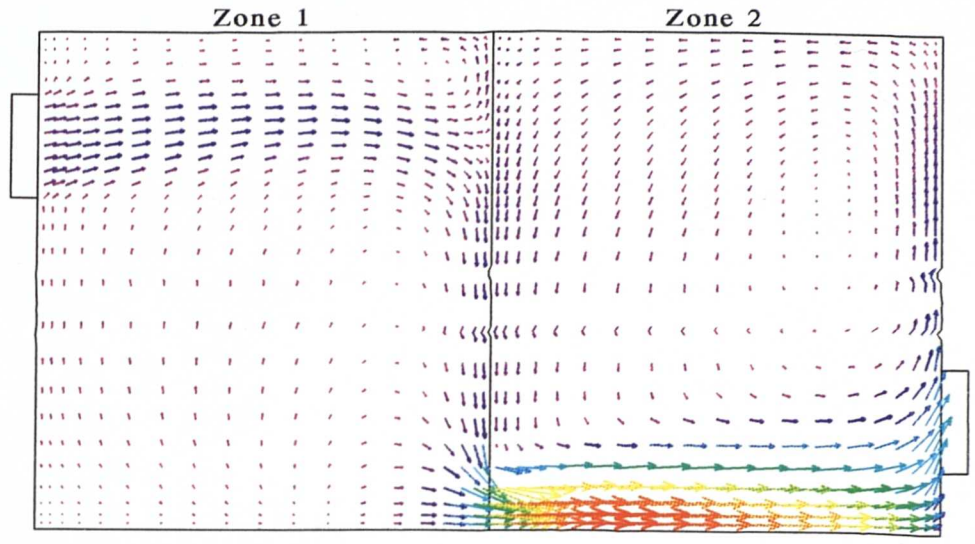

Figure 7.9b Vectors in plane of z=1.5 m (Case 3; Scale: ⟶ 0.116 m/s)

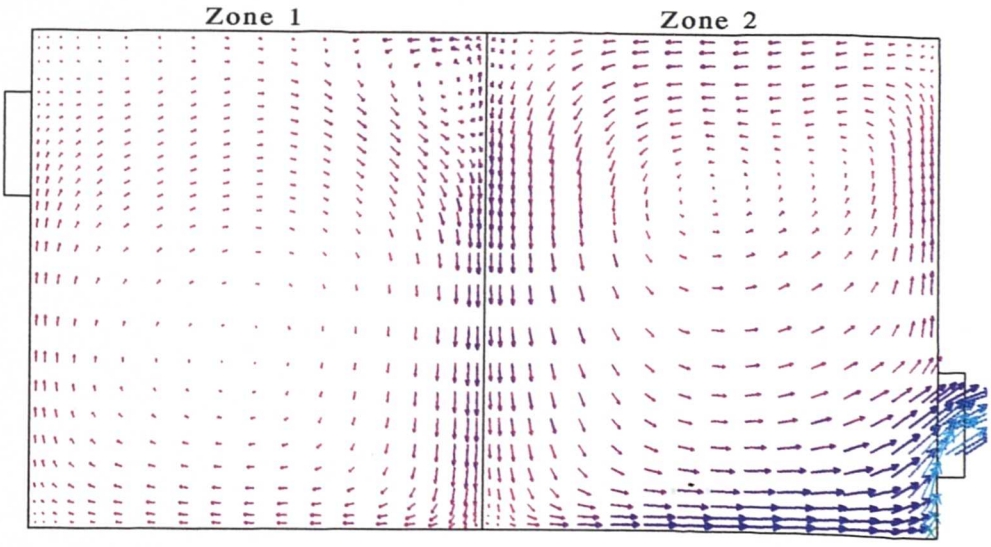

Figure 7.9c Vectors in plane of z=2.25 m (Case 3; Scale: ⟶ 0.116 m/s)

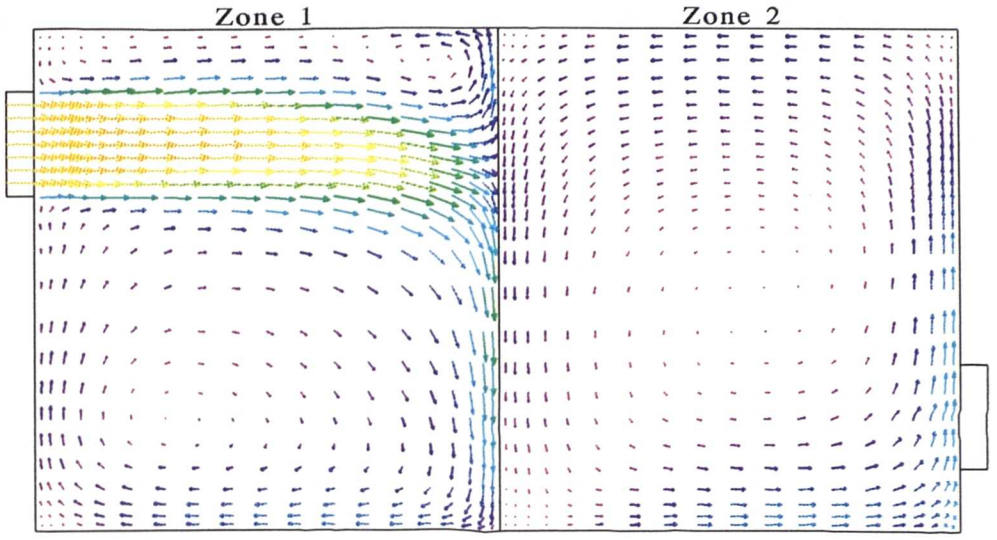

Figure 7.10a Vectors in plane of z=0.75 m (Case 5; Scale: ⟶ 0.1 m/s)

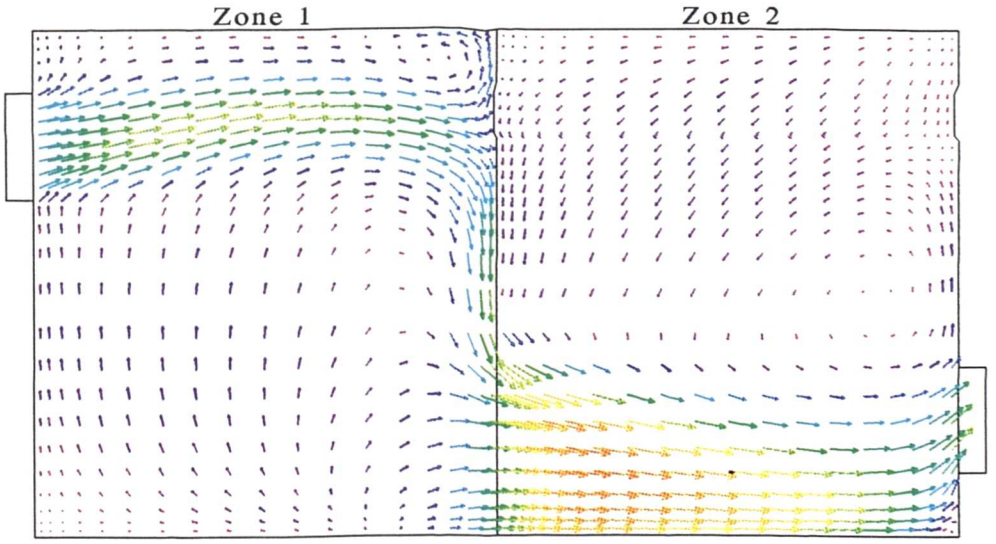

Figure 7.10b Vectors in plane of z=0.75 m (Case 5; Scale: ⟶ 0.1 m/s)

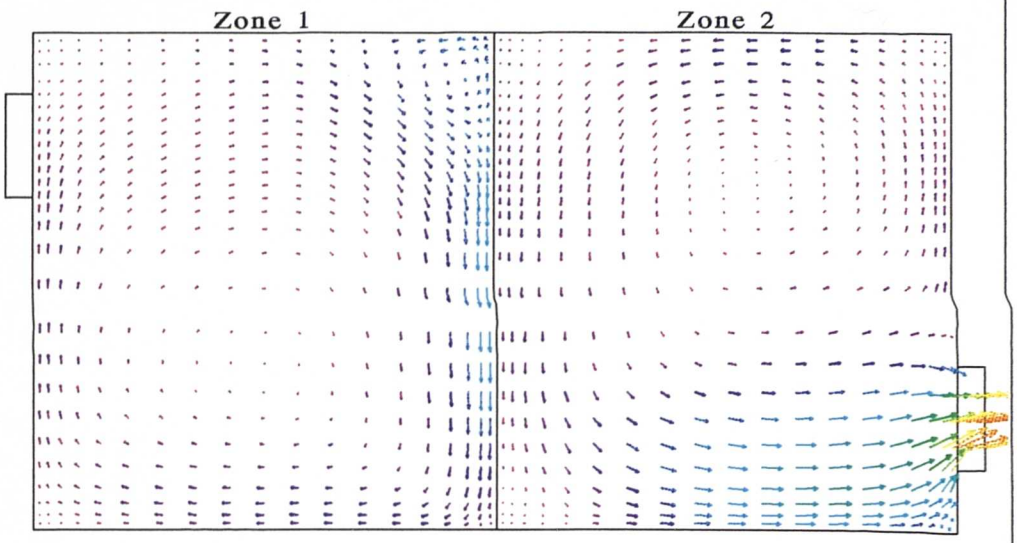

Figure 7.10c Vectors in plane of z=2.25 (Case 5; Scale: ⟶ 0.1 m/s)

III. The particle deposition, migration & distribution in two zone chamber

The numerical analysis of particle movement in the two-zone room with the experimental validation are given in this section. The average particle concentration of numerical analysis in each zone is defined as follows:

$$C_p = \frac{\text{Mass of suspended particles in each zone}}{\text{Volume of zone}} \qquad (7\text{-}1)$$

The comparisons of the average particle concentration decay with the time between computations and experiments in each zone of all cases are demonstrated in figures 7.11 ~ 7.16. The deposition, migration, extraction, and distribution of particles in each zone are presented in figures 7.17 ~ 7.27.

1. Average particle concentration decay in zone 1.

In zone 1 (figures 7.11a ~ 7.16a), the comparisons between computational results and measured data of particle concentration decay with the time show reasonably good agreement, especially within the first 10 minutes. The deviations between predictions and experiments become evident as the time extends. The computations are generally higher than the measurements. That means the deposition and migration of particles are slower than those in experiments. The reasons causing these discrepancies might be explained as below:

a. The particle mass distribution is assumed to be uniformly divided into each size group. This assumption does not reflect the real situation of particle mass distribution within the each size group which is difficult to measure;

b. The number of sample particles defined in the simulations is not enough to specify the initial conditions of particles within the flow domain, i.e., the number of sample particles need to be increased further to make the tracking process more close to the reality. This is restricted by the limited space of the SUN SPARC2 workstation;

c. In the experimental situations, the electrical field generated from the measurement equipment in each zone might enhance the particle deposition which is not considered in the numerical simulations.

2. Average particle concentration decay in zone 2.

In zone 2, the average particle concentrations increase rapidly in the first few minutes and then start to reduce continuously with the time (see figure 7.11b ~ 7.16b). The agreements between computations and measurements are satisfactory and acceptable. The numerical particle concentrations generally decay faster than the experimental ones. The particles either deposit onto the interior surfaces or extract through the exit diffuser. Some discrepancies exist between computations and measurements. The reasons resulting the errors might be explained as follows:

a. In simulations, the particles are assumed equally distributed in each size group due to the lack of information about the particle distributions in

experimental situations. This assumption does not coincide well with the real situation;

b. The particle rebounding processes are not considered in the simulations and so may also contribute to the errors as well;

c. The other factors in experiments, e.g., electrical charges resulting from the measurement equipment, are not included in the particle transport model.

In general, the comparisons of average particle concentration decay between computations and measurements in each zone are satisfactory and reasonable.

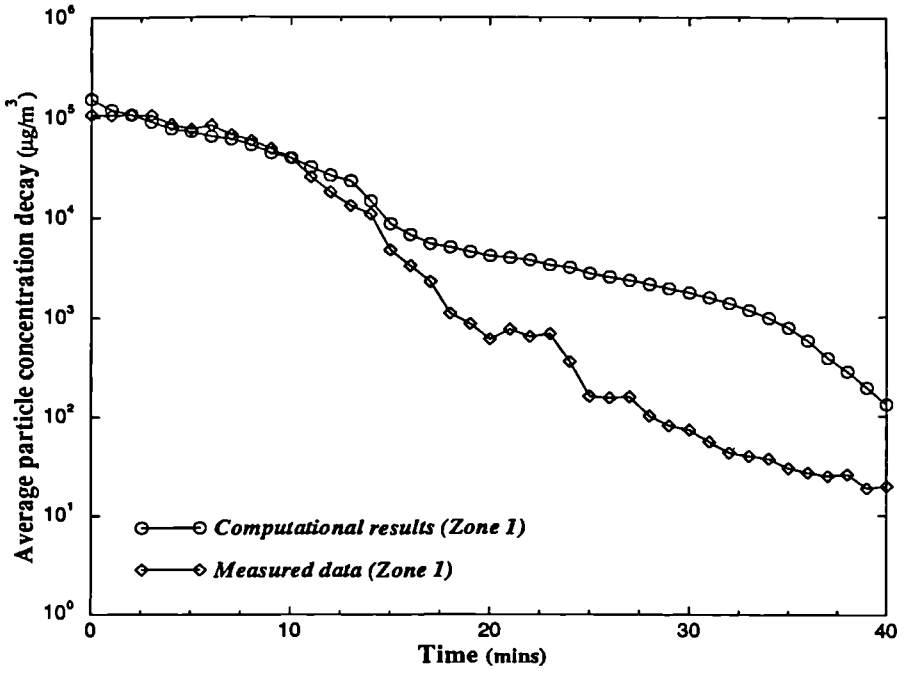

a. Particle concentration decay in zone 1

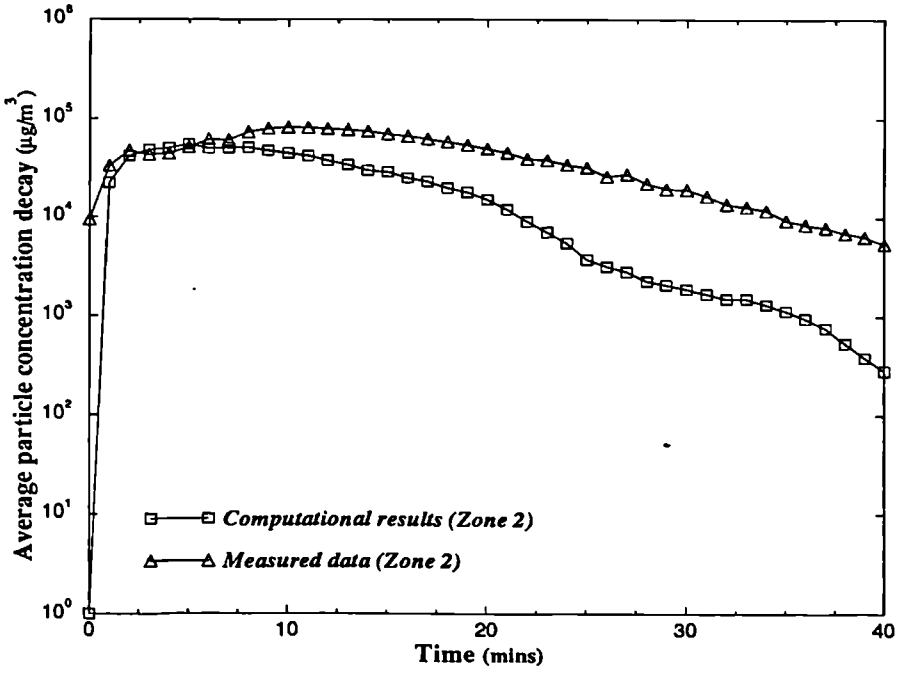

b. Particle concentration decay in zone 2

Figure 7.11 Comparison of average particle concentration decay (Case 1)

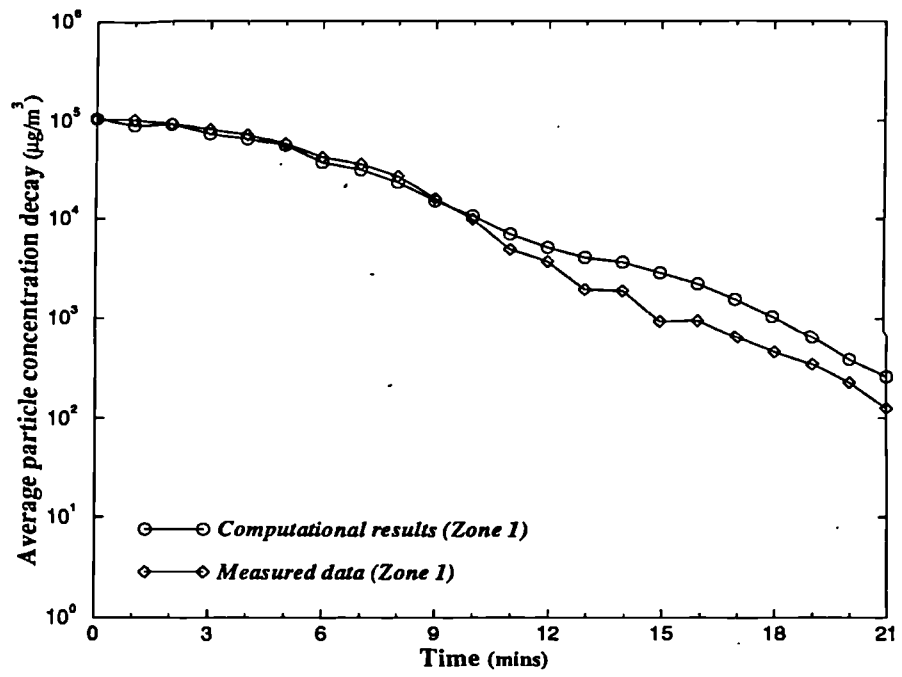

a. Particle concentration decay in zone 1 (Case 2)

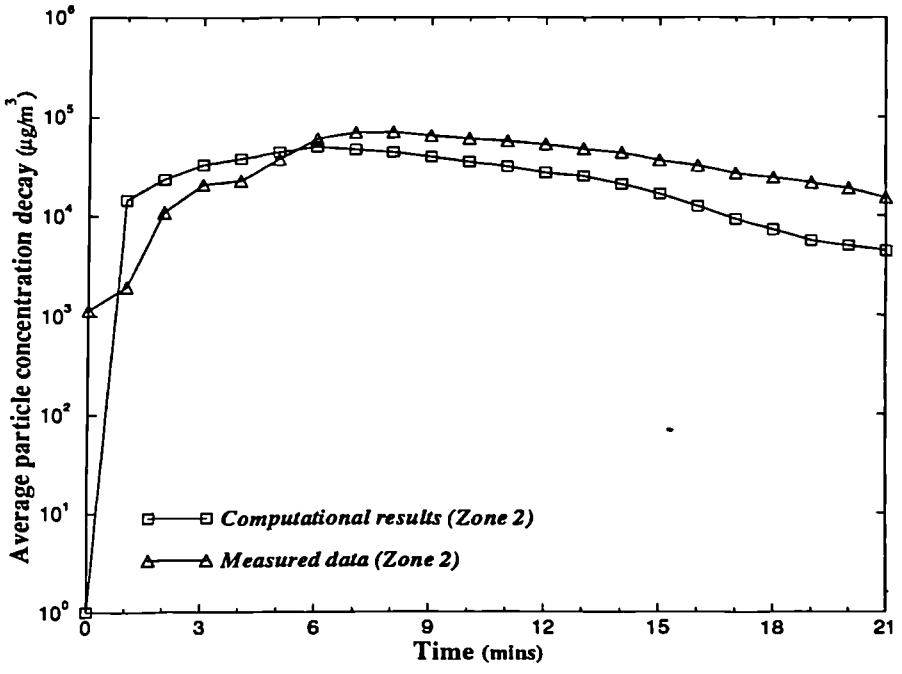

b. Particle concentration decay in zone 2 (Case 2)

Figure 7.12 Comparisons of average particle concentration decay (Case 2)

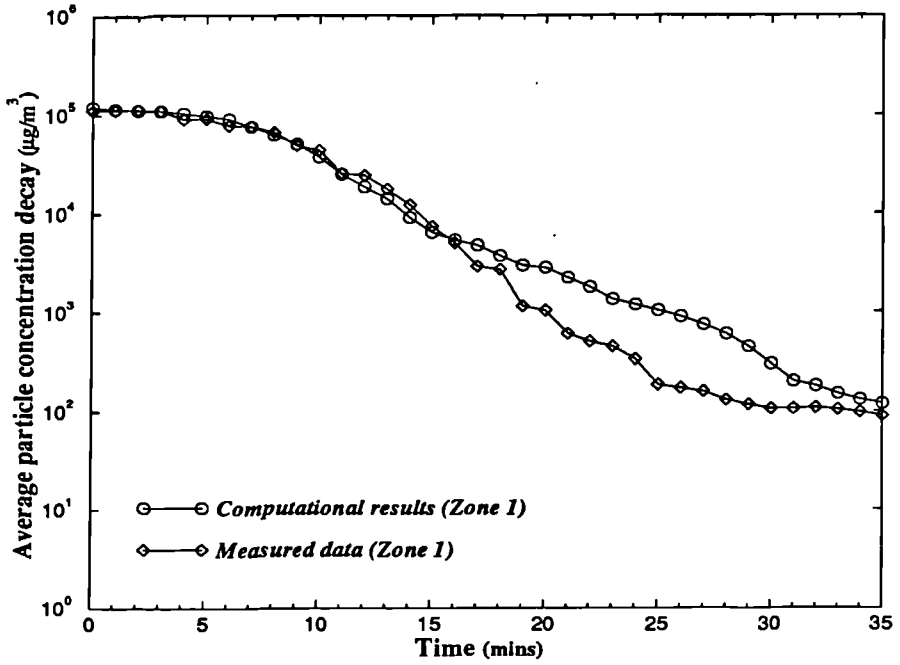

a. Particle concentration decay in zone 1 (Case 3)

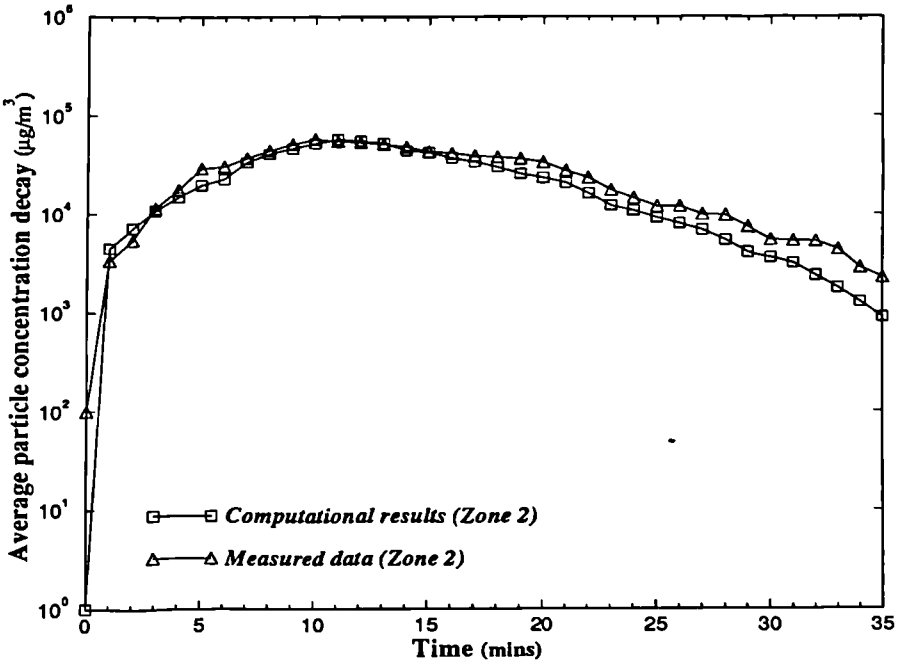

b. Particle concentration decay in zone 2 (Case 3)

Figure 7.13 Comparisons of average particle concentration decay (Case 3)

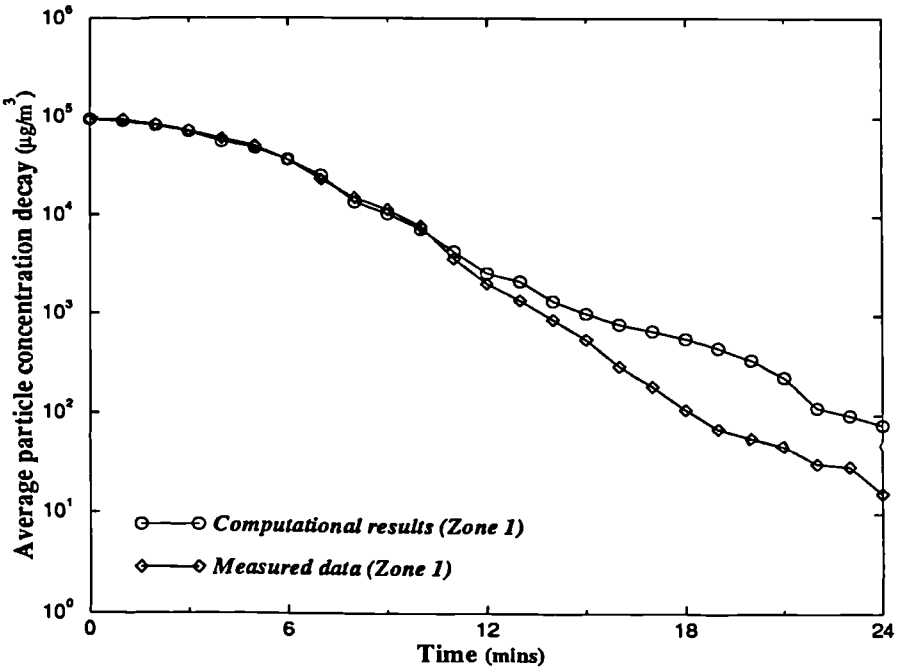

a. Particle concentration in zone 1 (Case 4)

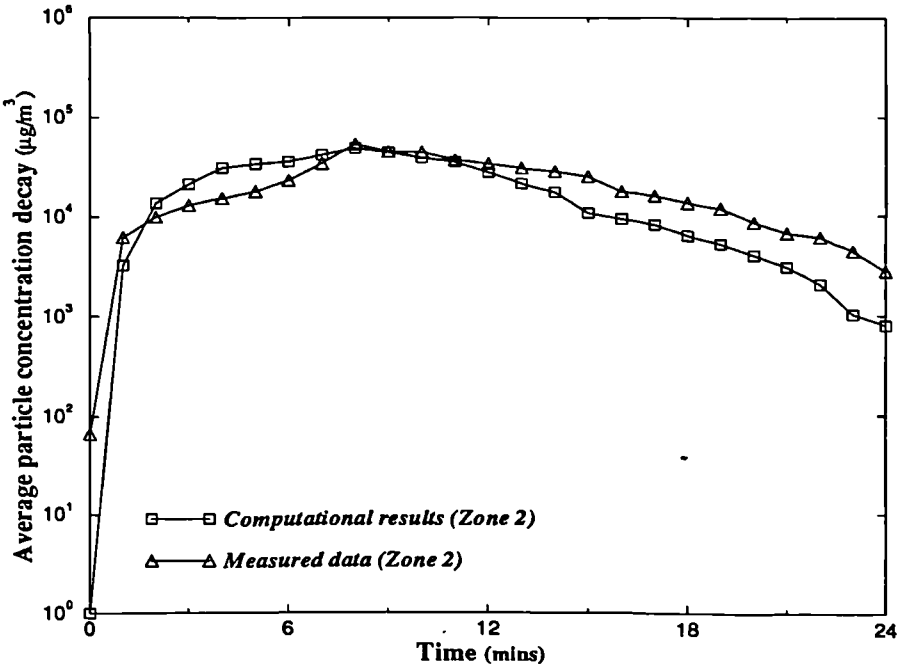

b. Particle concentration decay in zone 2 (Case 4)

Figure 7.14 Comparisons of average particle concentration decay (Case 4)

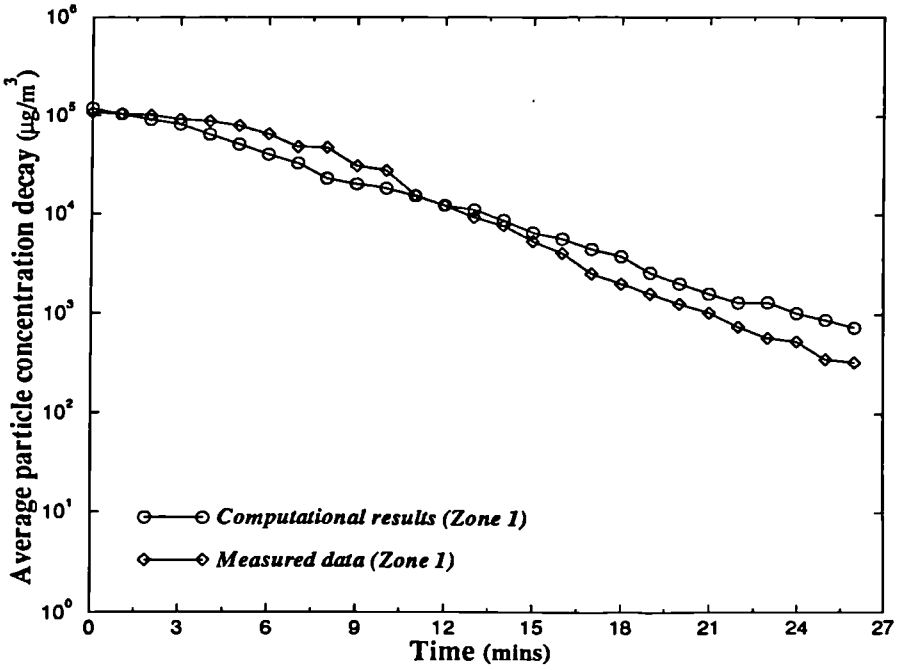

a. Particle concentration decay in zone 1 (Case 5)

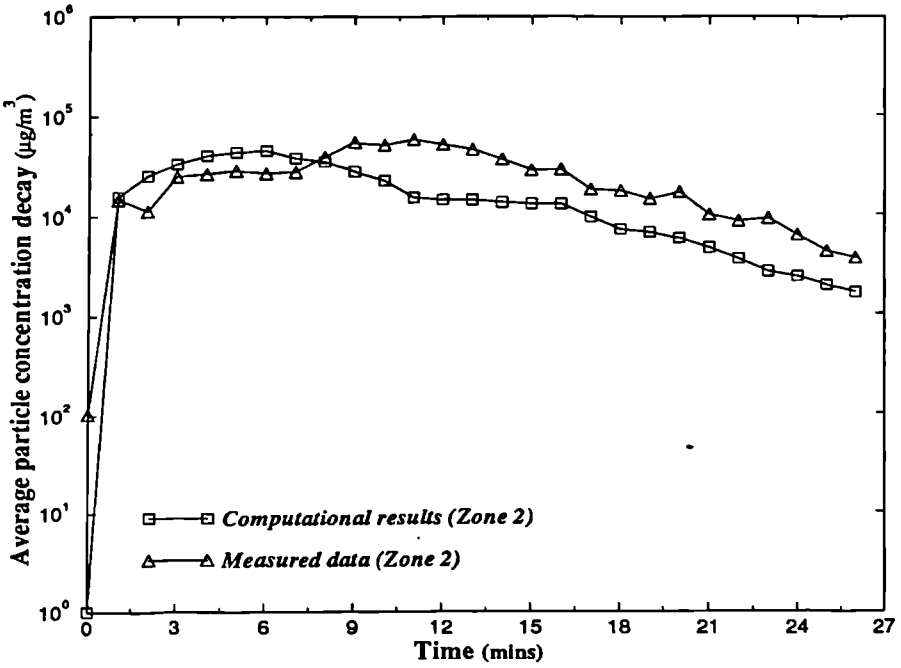

b. Particle concentration decay in zone 2 (Case 5)

Figure 7.15 Comparisons of average particle concentration decay (Case 5)

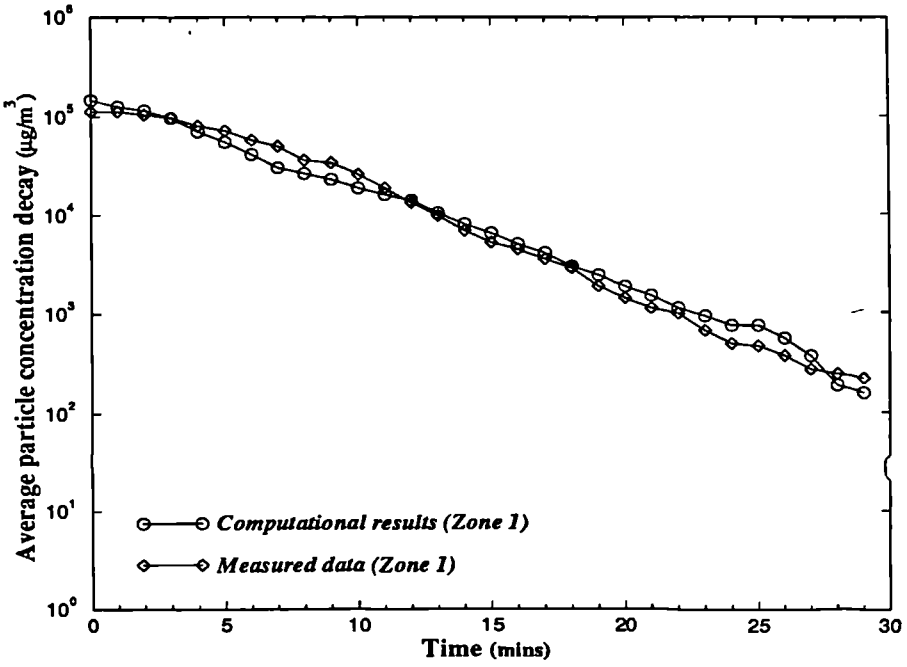

a. Particle concentration decay in zone 1 (Case 6, 10.26 ACH)

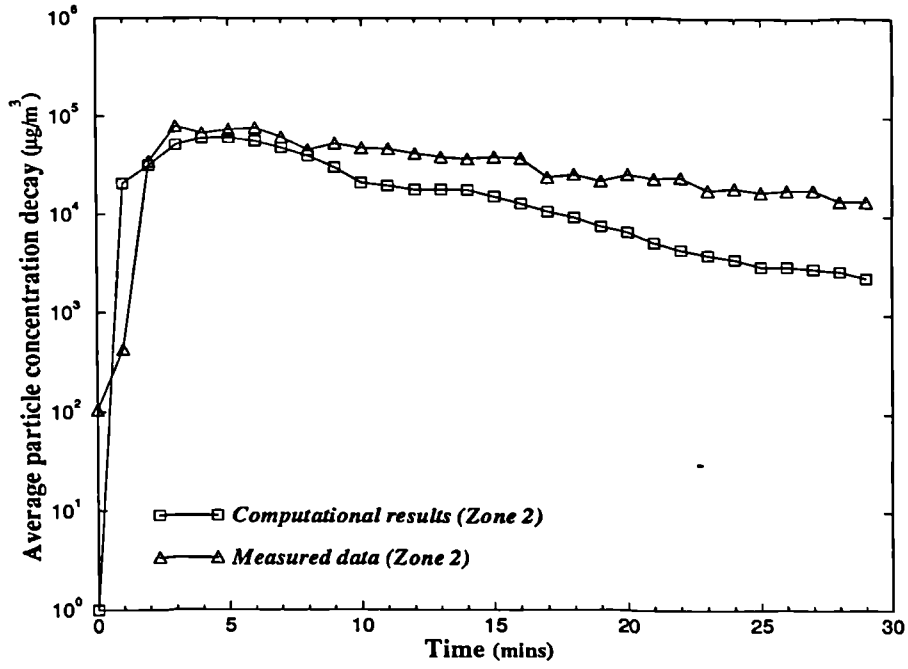

b. Particle concentration decay in zone 2 (Case 6, 10.26 ACH)

Figure 7.16 Comparisons of average particle concentration decay (Case 6)

3. Particle deposition, migration and distribution in two-zone room.

a. Figures 7.17a ~ 7.22a reflect the numerical results of the particle deposition, migration and distribution in zone 1. It can be seen that the masses of suspended particles reduce continuously with the time as described in figures 7.11a ~ 7.16a, while the masses of the migrated particles increase with the time first and change slightly after some periods of time. This means that the particle migration mainly happens within the first few minutes after the interzonal connection opened (e.g., from figures 7.17a ~ 7.22a, 16 minutes and 12 minutes for Case 1 and Case 2; 15 minutes and 10 minutes for Case 3 and Case 4; 8 minutes and 6 minutes for Case 5 and case 6 respectively). Here, the phenomenon is named the massive particle migration and the relative period is called massive migration period. The massive migration period reduces as the interzonal opening increases. After the massive migration period, the migration of particles increases slowly with the time (see figure 7.11a ~ 7.16a). It is also interesting to notice that the migration phenomena are enhanced as the ventilation rate increases with the same geometrical configuration, i.e., the ventilation rate does influence the migration processes of particles;

b. Figures 7.17a ~ 7.22a also show that the mass of the deposited particles on the internal surfaces increases with time first, and after periods of massive particle migration, it increases slowly as the time extends. The figures also show that the majority of particles migrate into zone 2 under the influences of the airflow patterns and some particles suspend in zone 1 area for quite a long time. These suspended particles greatly affect the indoor air environment in that area;

c. The deposition and extraction of particles in the space of zone 2 are described in figures 7.17b ~ 7.22b. As mentioned before, the masses of suspended particles in zone 2 increase rapidly in the first few minutes due to the massive migration of particles from zone 1 to zone 2 and then decrease with the time. The particles are either deposited onto the interior surfaces or extracted via the exhaust. From figures 7.17b ~ 7.22b, it can be seen that the particle extraction rarely happen from 0 to 3 minutes of tracking periods and after that periods increase with the time. The deposition processes of particles in the area of zone 2 are different from those in the space of zone 1. The particle depositions keep happening consistently with the time due to the influence of particle migration and air movement induced by the interzonal openings. Comparing the masses of suspended particles in the area of zone 1 with those in the space of zone 2 respectively, it can be seen that more particles suspended in zone 2 than those in zone 1; and also more particles deposited onto the internal surfaces in zone 2 than those in zone 1. That means the particle concentration level in zone 2 is sensitive to the upstream situations of airflow patterns and particle migrations.

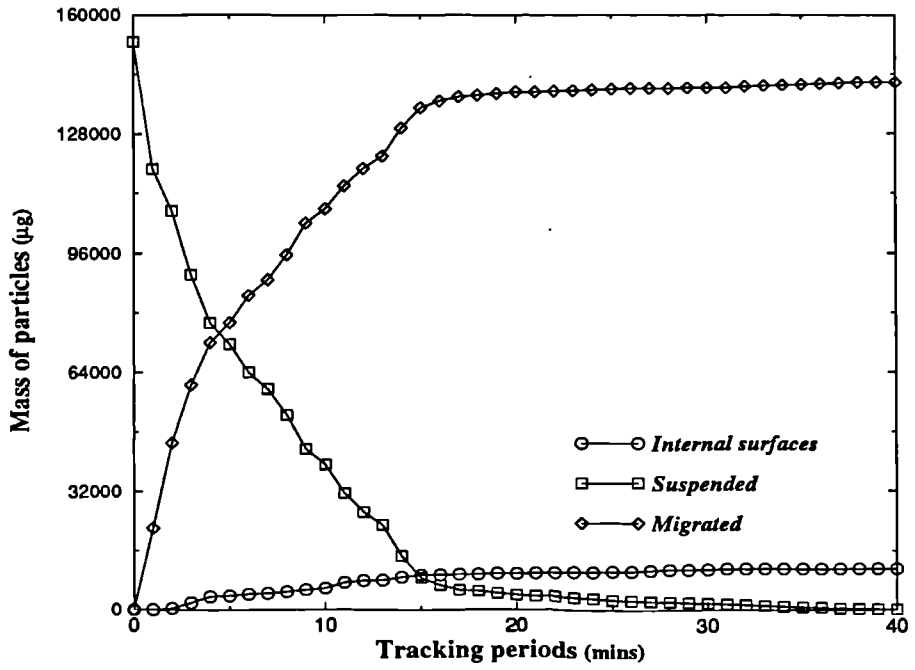

a. Particle distribution in zone 1 (Case 1, 11.484 ACH)

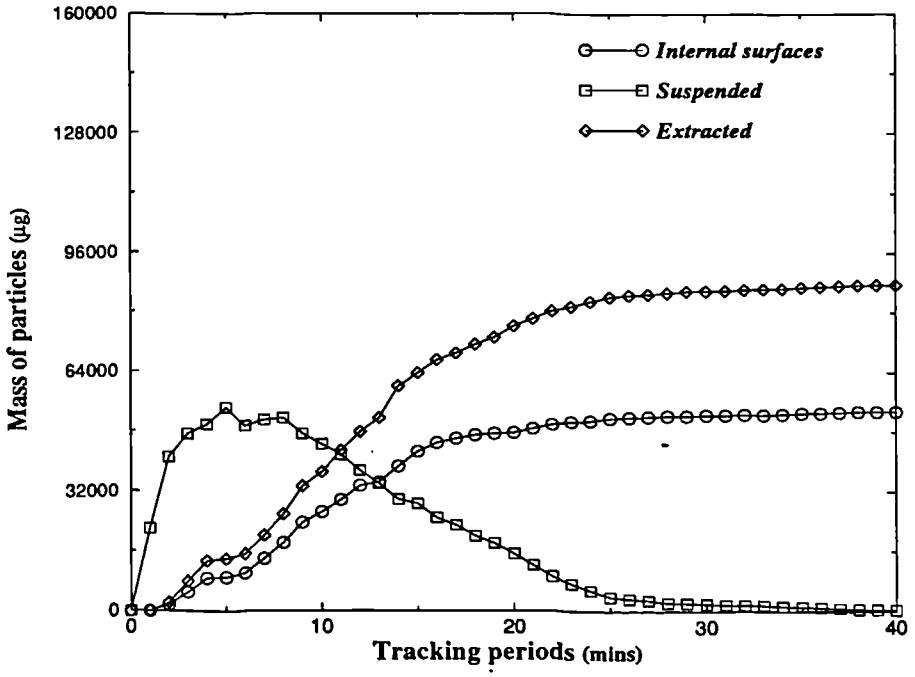

b. Particle distribution in zone 2 (Case 1, 11.484 ACH)

Figure 7.17 Particle distribution in two-zone area (Case 1)

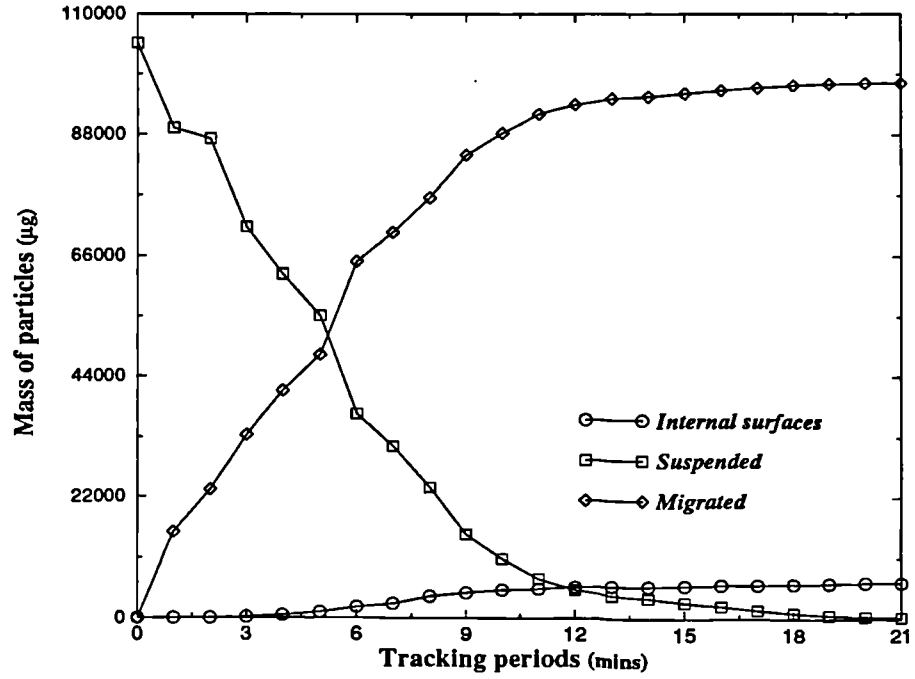

a. Particle distribution in zone 1 (Case 2, 14.004 ACH)

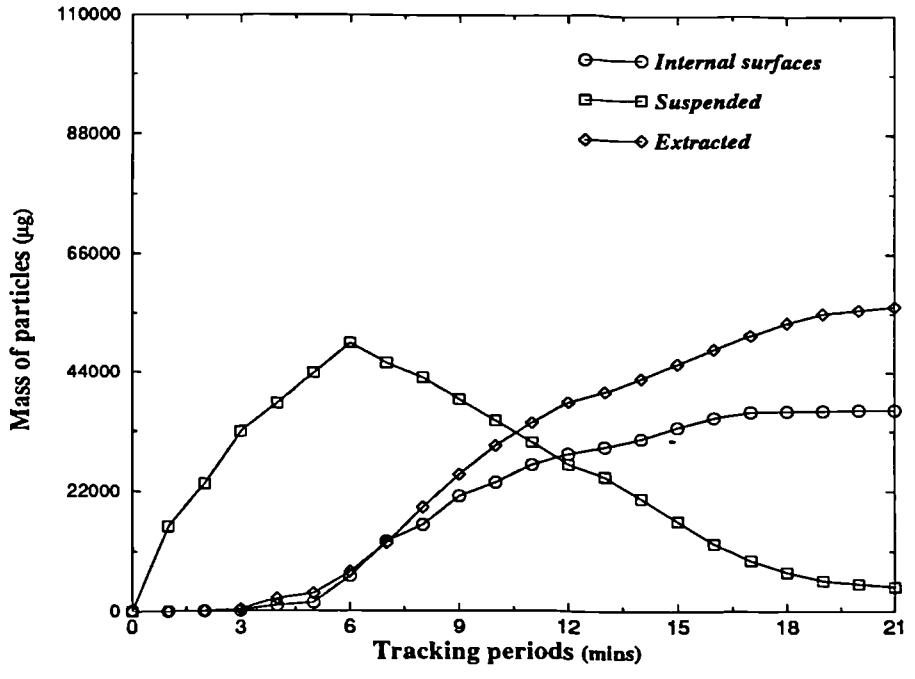

b. Particle distribution in zone 2 (Case 2, 14.004 ACH)

Figure 7.18 Particle distribution in two-zone area (Case 2)

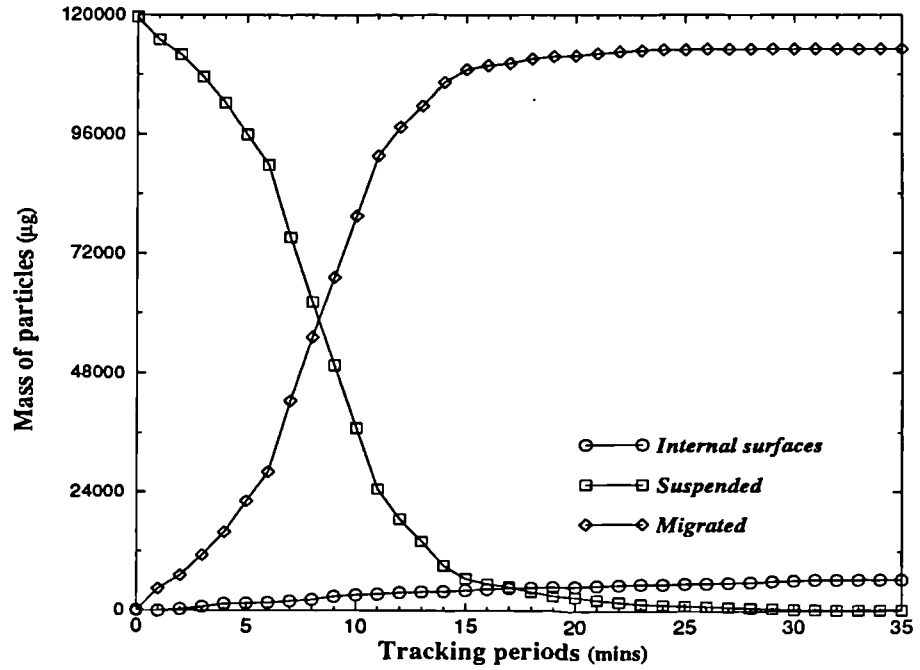

a. Particle distribution in zone 1 (Case 3, 11.566 ACH)

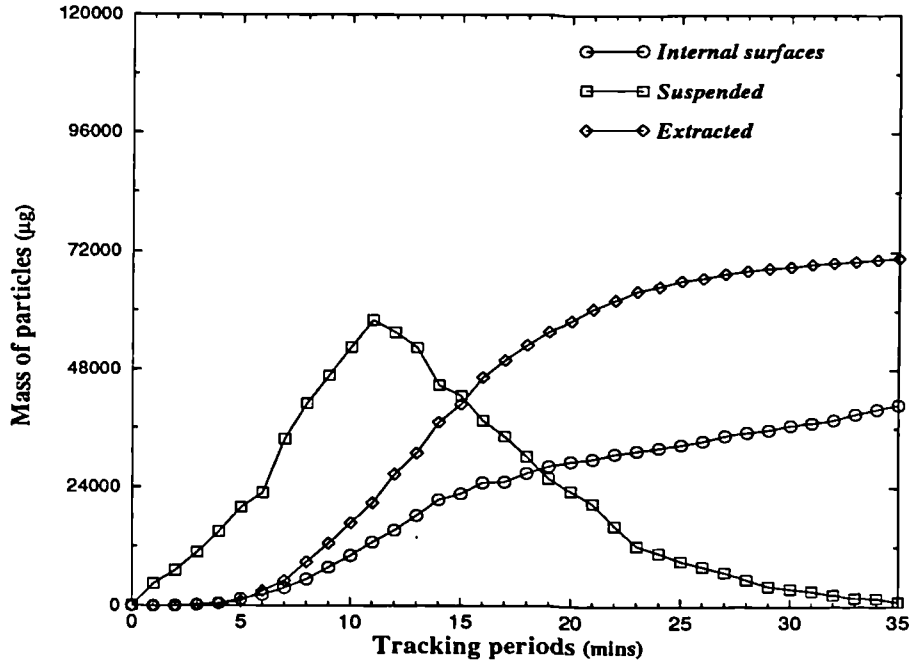

b. Particle distribution in zone 2 (Case 3, 11.566 ACH)

Figure 7.19 Particle distribution in two-zone area (Case 3)

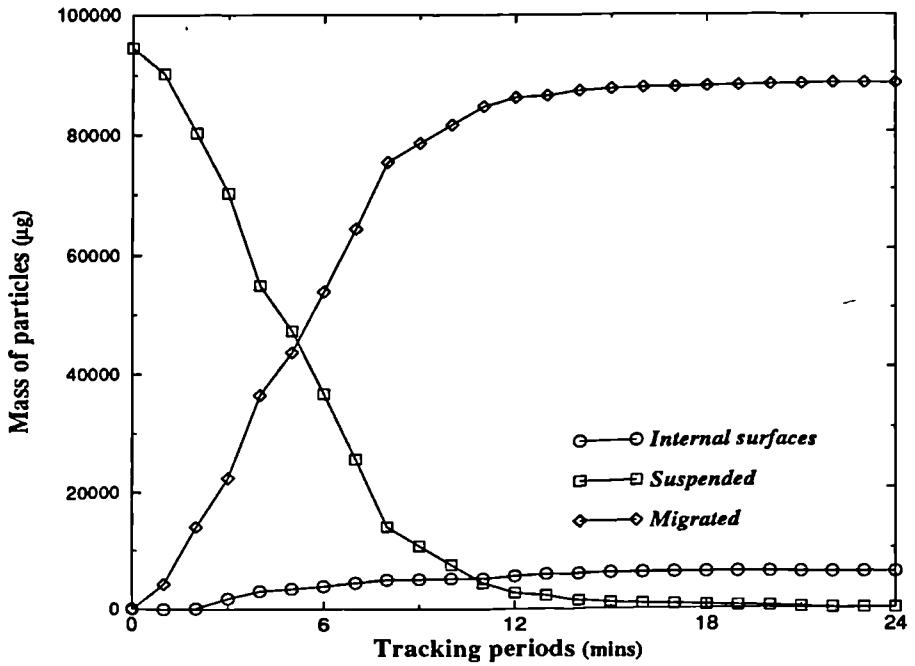

a. Particle distribution in zone 1 (Case 4, 12.708 ACH)

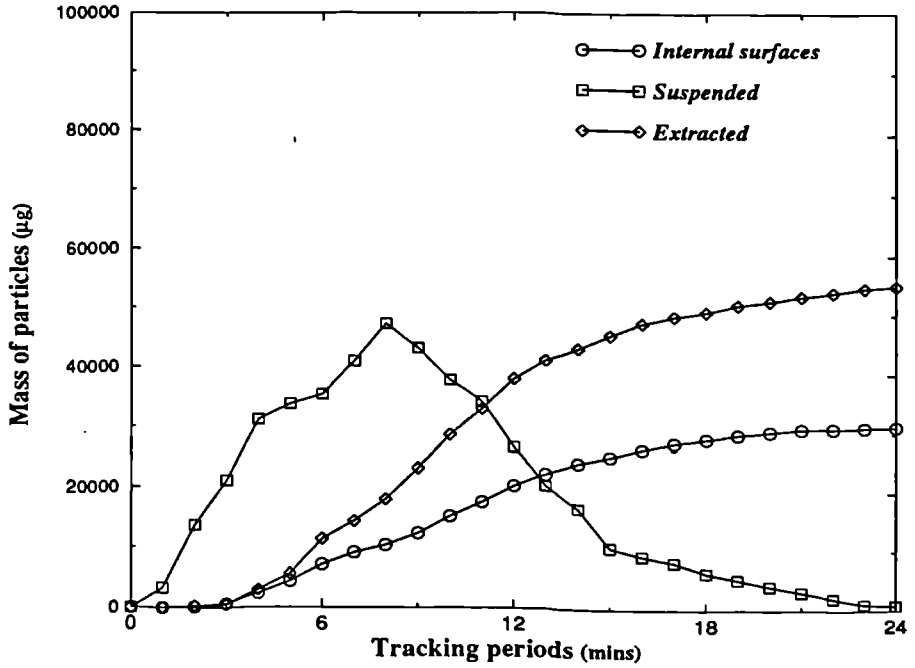

b. Particle distribution in zone 2 (Case 4, 12.708 ACH)

Figure 7.20 Particle distribution in two-zone area (Case 4)

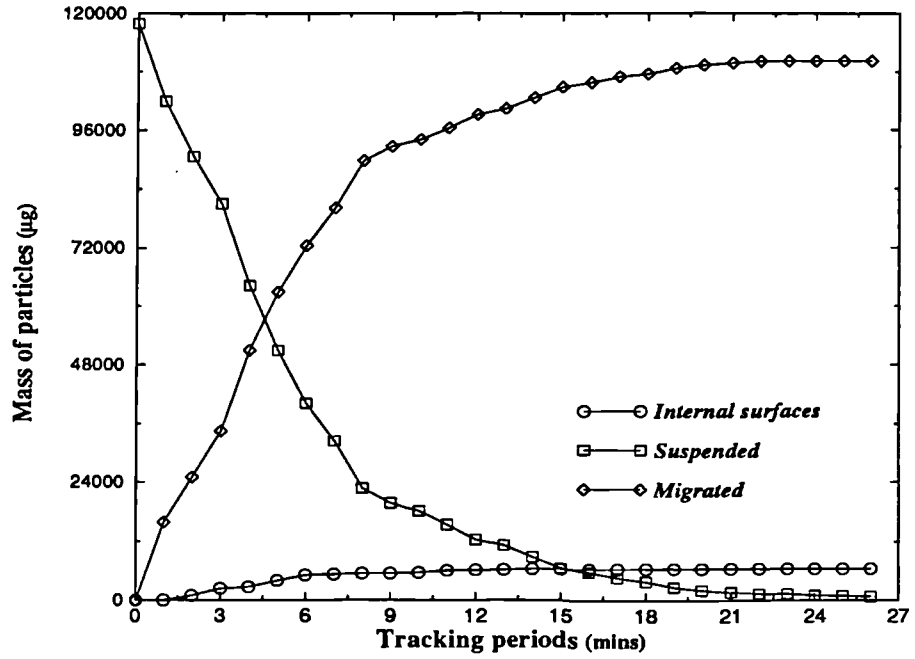

a. Particle distribution in zone 1 (Case 5, 9.216 ACH)

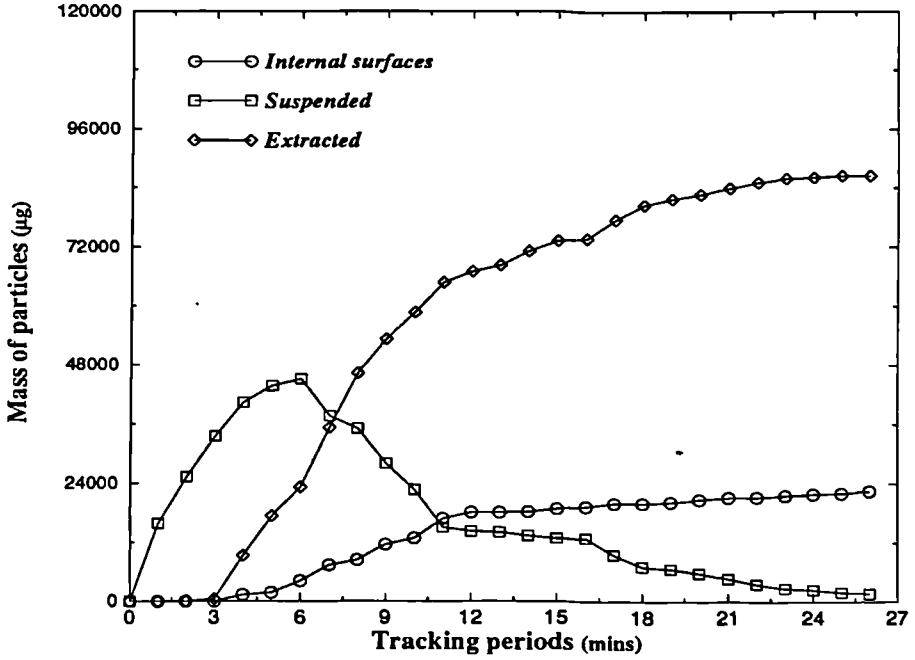

b. Particle distribution in zone 2 (Case 5, 9.216 ACH)

Figure 7.21 Particle distribution in two-zone area (Case 5)

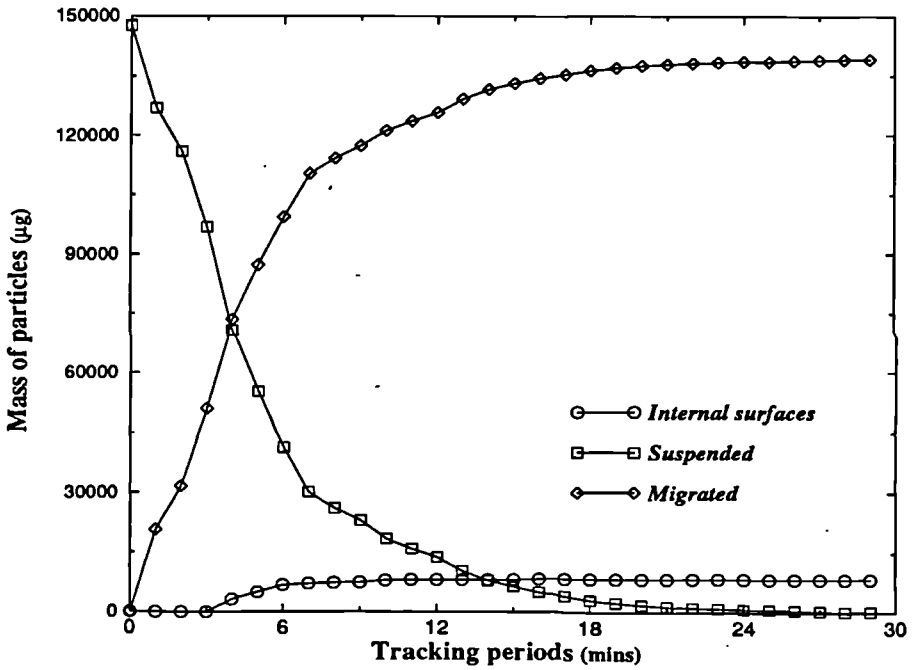

a. Particle distribution in zone 1 (Case 6, 10.26 ACH)

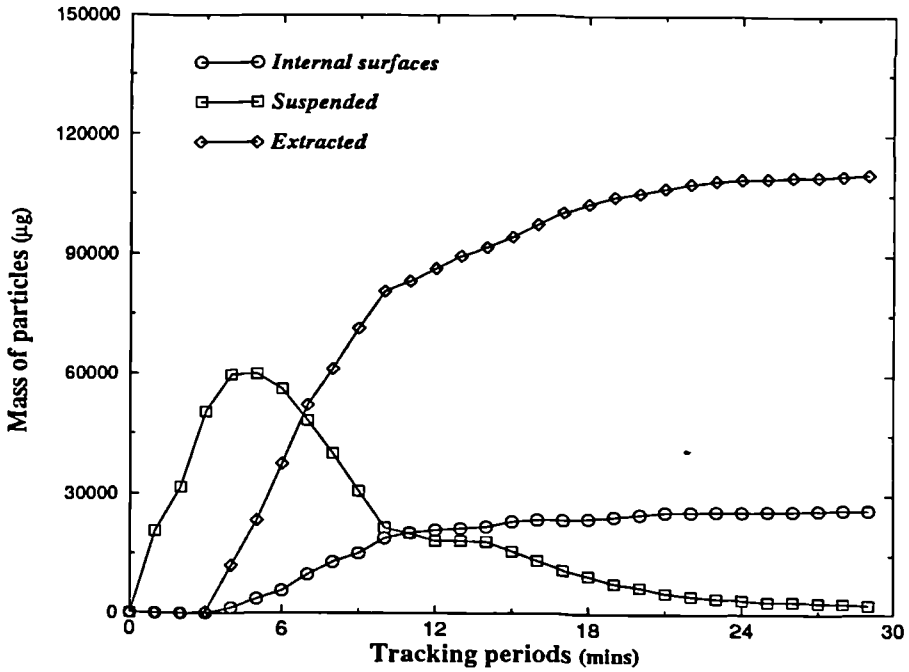

b. Particle distribution in zone 2 (Case 6, 10.26 ACH)

Figure 7.22 Particle distribution in two-zone area (Case 6)

4. The average particle deposition, exchange and extraction rates.

For the purposes of describing the total deposition, migration and extraction of particles in all cases, the following definitions are introduced:

$$R_d = \frac{m_p N_{pd}}{\rho_p T_{trk} V_z} \tag{7-2}$$

$$R_{exc} = \frac{m_p N_{pm}}{\rho_p T_{trk} V} \tag{7-3}$$

$$R_{ext} = \frac{m_p N_{pe}}{\rho_p T_{trk} V} \tag{7-4}$$

Figures 7.23 ~ 7.25 represent the variations of the average particle deposition, exchange and extraction rates with the ventilation rate. These values consistently increase as the ventilation rate increases under the same geometrical configuration. Increasing ventilation rate can help extract particles but may enhance particle migrations between zones.

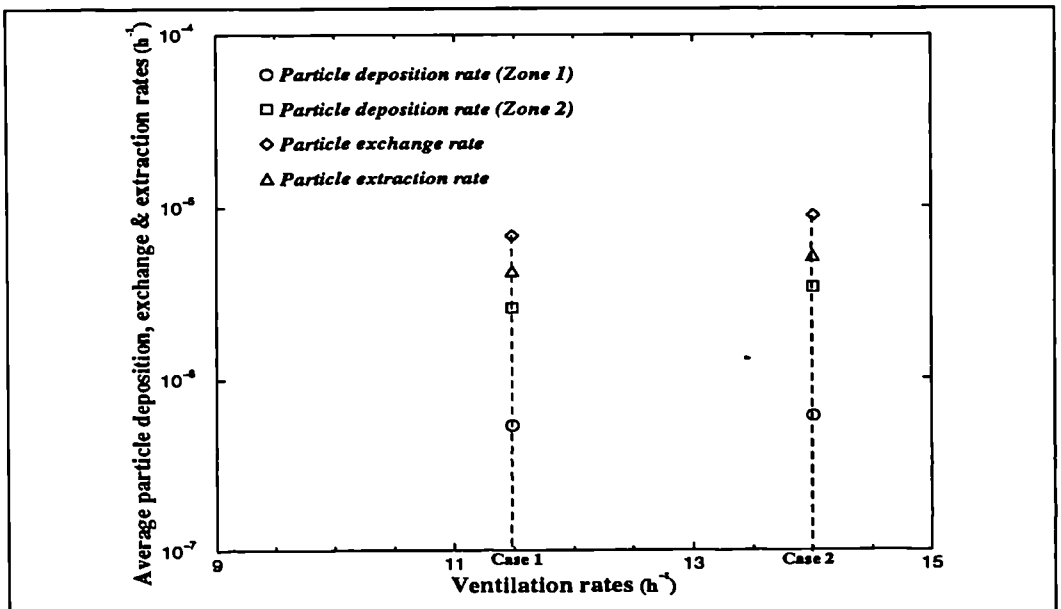

Figure 7.23 Average particle deposition, migration & extraction rates (Case 1 & 2)

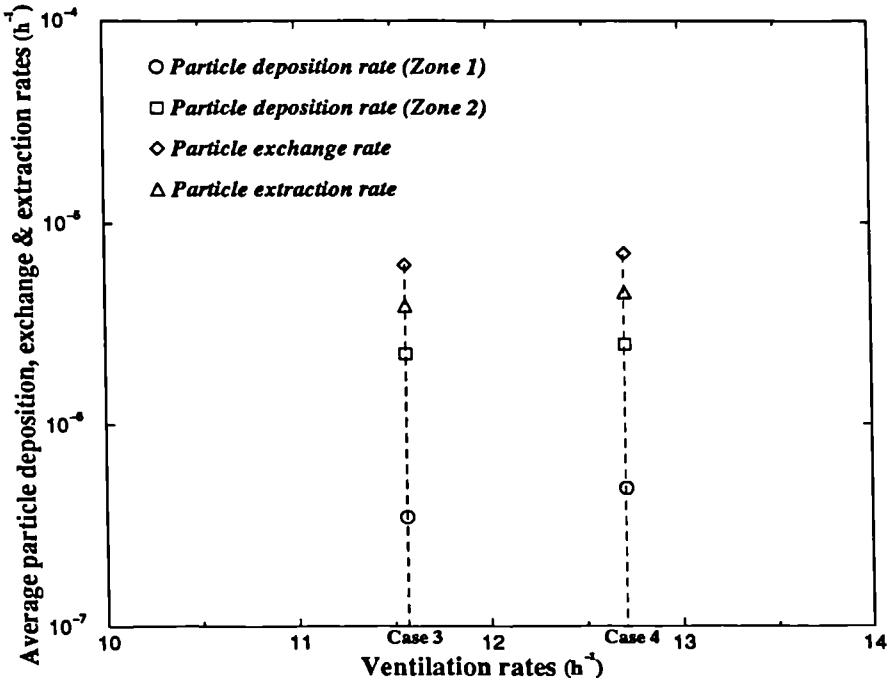

Figure 7.24 Average particle deposition, migration & extraction rates (Case 3 & 4)

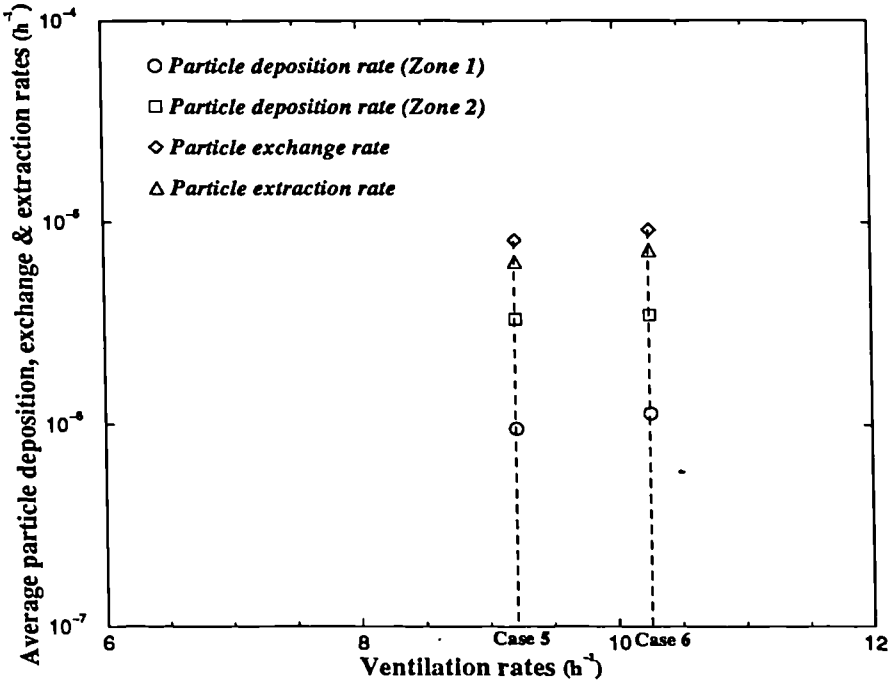

Figure 7.25 Average particle deposition, migration & extraction rates (Case 5 & 6)

5. sample particle tracking routes.

Figures 7.26 and 7.27 demonstrate some sample particles tracking routes with different sizes. the figures show that small particles are greatly influenced by the airflow pattern, remaining in the occupied zone longer than the large particles and thus affecting the indoor air quality. Large particle movements are mainly affected by the gravity deposition. It can also be seen that these is a substantial difference of particle movement between particles with size $d_p \leq 2$ μm and particles with size $d_p \geq 3$μm. Small particles mainly contribute to the pollutant particle concentration and the indoor air quality.

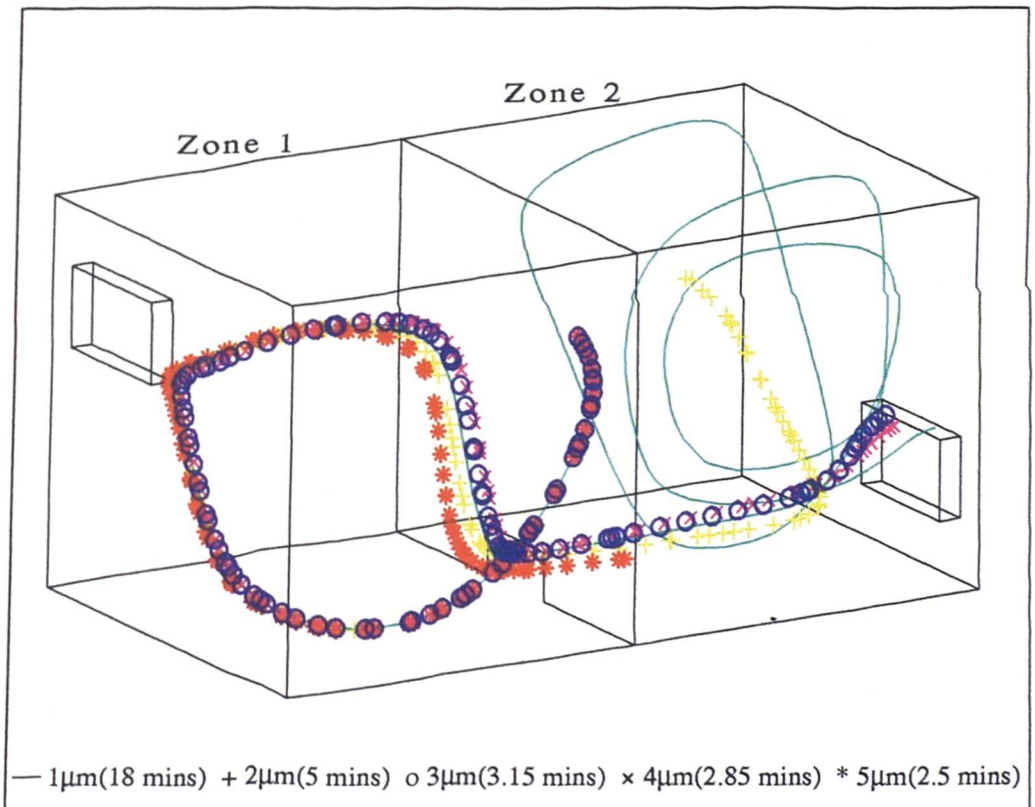

Figure 7.26 Five sample particles tracking routes (Case 2)

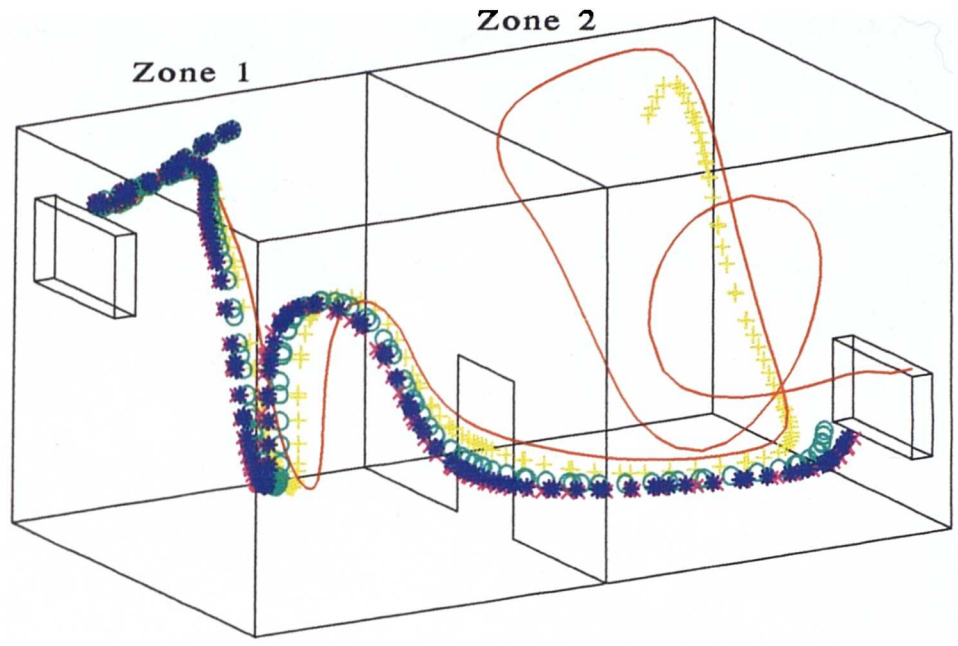

— 1μm(29 mins) + 2μm(18.8 mins) o 3μm(9.6 mins) × 4μm(8.9 mins) * 5μm(8 mins)

Figure 7.27 Five sample particles tracking routes (Case 6)

§7.3 Conclusions

A CFD analysis of aerosol particle distribution, migration, and deposition in a ventilated two-zone chamber has been carried out with different geometrical configurations and ventilation conditions. The airflow patterns of different situations have also been simulated by CFD modelling. The numerical results of particle concentrations in the two-zone area have been validated with the relevant experimental data. The following conclusions emerge:

1. The airflow patterns in a ventilated two-zone enclosure are greatly influenced by the interzonal connection. A small interzonal opening produces a jet-like flow in the low level of zone 2;
2. The particle transport model presented in chapter IV can be used to predict the aerosol particle movement and distribution in the ventilated two-zone area.
3. The comparisons between computations and measurements are generally satisfactory and acceptable;
4. Particle depositions are influenced by the airflow patterns and particle properties. The gravity deposition dominates the large particle movements ($d_p \geq 3\mu m$), while both airflow patterns and gravity deposition influence the small particle movements. Small particles suspend in the occupied zone longer than large particles do and significantly affect the pollutant concentration level and the indoor air quality of ventilated spaces;

5. The results of cases show that the particle migrations between zones are significantly influenced by the interzonal opening and ventilation conditions. The large interzonal opening can increase the particle migration between zones. The particle migration can also be increased by increasing ventilation rate;

6. The results also point out that the indoor environment in the area of zone 2 is more sensitive to the geometrical configuration and ventilation rate than that in the space of zone 1 due to the air movement and particle migration induced by the interzonal openings;

7. The ventilation conditions do affect the average particle deposition, exchange and extraction rates. In this study, these parameters increase with the growth of ventilation rates.

CFD simulations of airflow patterns and particle movement in a ventilated two-zone chamber result in valuable detailed information of particle distribution, migration and deposition in the two-zone area and therefore are very useful as an analysis tool to evaluate the indoor environment and the performance of a ventilation system. CFD results of this research also provide useful information for the prediction of the particle movements and airflow patterns in more complicated multi-zone areas.

CHAPTER VIII

MODELLING OF AIR AND PARTICLE MOVEMENT UNDER BUOYANCY EFFECT

Abstract

A CFD analysis of airflow and particle movement under buoyancy influence has been presented in this chapter. The validation has also been carried out in the study. The comparisons between simulation and measurement are satisfactory. The method of estimating the heat source proposed and used in the chapter is reasonable and acceptable. The room airflow pattern is affected by the thermal wall jet produced by the heat source. The hot wall jet entrains air from the surroundings, induces the air circulation and temperature stratification in the room space, and also entrains the particles from the source. The particle movement depends on the airflow pattern, the buoyancy effect and particle properties.

§8.1 Introduction

CFD analysis of airflow patterns and aerosol particle movement and distribution in mechanically ventilated single- and two-zone spaces have been presented in previous chapters. The content of this chapter focuses on the prediction of the influence of thermal buoyancy on the air movement, the thermal comfort and the pollutant particle distribution in a room with convective heat sources.

Air movement in a building or a room is normally caused by a temperature difference between the warm and cold zones (natural convection), by mechanical ventilation system (forced convection) or by a combination of both. In practice, temperature gradients are usually present as a result of heat transfer through walls and windows, heat generation by the room occupants or heaters, or air at different temperature being blown through the ventilation system. The airflow pattern induced by such thermal differences plays a fundamental role in the distribution of heat within the occupied room and between rooms in a multi-zone building, in the thermal comfort, and in the control of air quality. In the mean time, energy is transported through the room space as a passive property and interacts with the velocity field, causing non-uniform buoyancy forces that affect both the mean flow and the turbulence intensity. This sort of airflow is called buoyancy-affected flow.

The buoyancy effect may not be negligible if the room is not well insulated, or, if there exists a heat source. The heat source is not necessarily a stove or fireplace. Many kinds of heat sources may occur in a room, e.g., occupants

and computers generate heat constantly, and could also be considered as heat sources. The heat sources warm the surrounding air, induce buoyant flows and/or form thermal plumes. The heat sources may also be a source of contamination, and the plume can transfer the contaminants to the whole room space, accompanying the energy transfer procedure. In this circumstance, the ventilation system functions not only to supply fresh air and remove contaminants, but also to maintain a thermal comfort level for the occupants. Some typical buoyant flows are introduced in the following sections.

§8.1.1 Characters of Buoyancy-Affected Flows

I. Thermal plumes in a displacement ventilated room

Displacement ventilation is characterised as a plug or piston flow referring to the air volume being successively and uni-directionally displaced from the inlet towards the outlet. Such ventilation principles have become popular in recent years for ventilating spaces occupied by people with a low activity level, for instance, offices, conference rooms, computer and lecturer rooms, etc. Figure 8.1 shows the sketch of a displacement ventilation system. Air with a temperature lower than the average temperature is supplied through the supply diffuser located near the floor. The supply air enters the room at a rather low velocity and drops to the floor due to the gravity forces. The lower part of the room is gradually filled by the cool air. The heated ascending air above the heat sources constitutes, together with the cool injected air, the driving forces which are decisive for the performance of the displacement ventilation system. The heat sources including occupants, machines, etc., generate thermal plumes

which transport warm air to the upper parts of the room. Due to the entrainment of surrounding room air the volume flow in the plumes increases with the height above the heat source. At a certain level the convective flows induced by the heat sources equal the supply air flowrate and a more or less distinctly separated upper zone may appear from which the excess heat and contaminants are removed effectively. The vertical temperature gradients which cause a stratified flow and the mixing between horizontal layers in the occupied zone are larger than those in rooms with traditional mixing ventilation whilst relatively high velocities and low temperature could also be observed near the floor.

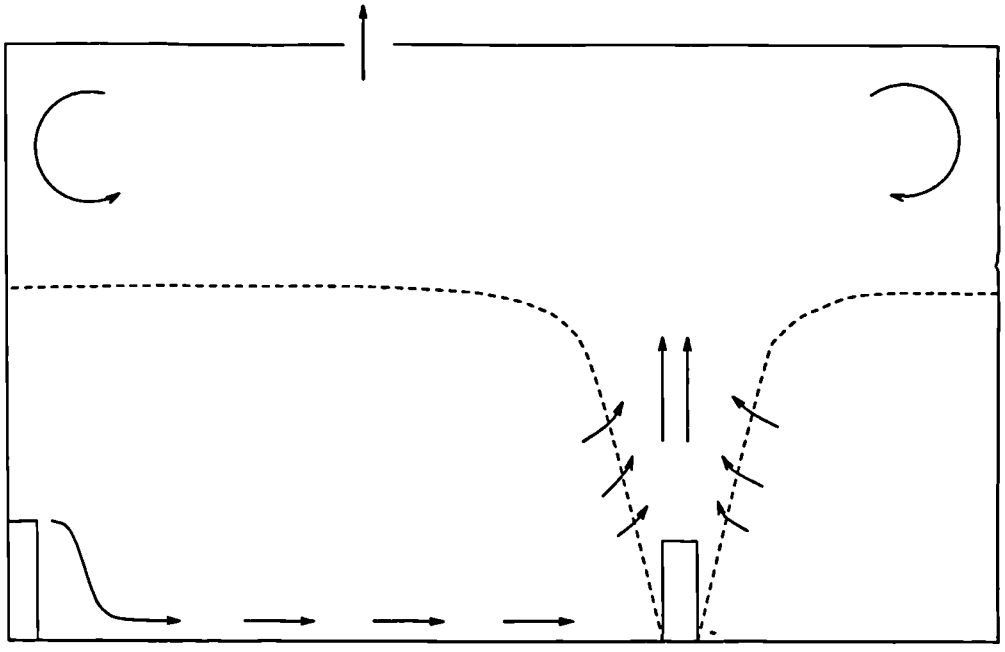

Figure 8.1 The sketch of displacement ventilation system

Figure 8.1 The sketch of displacement ventilation system

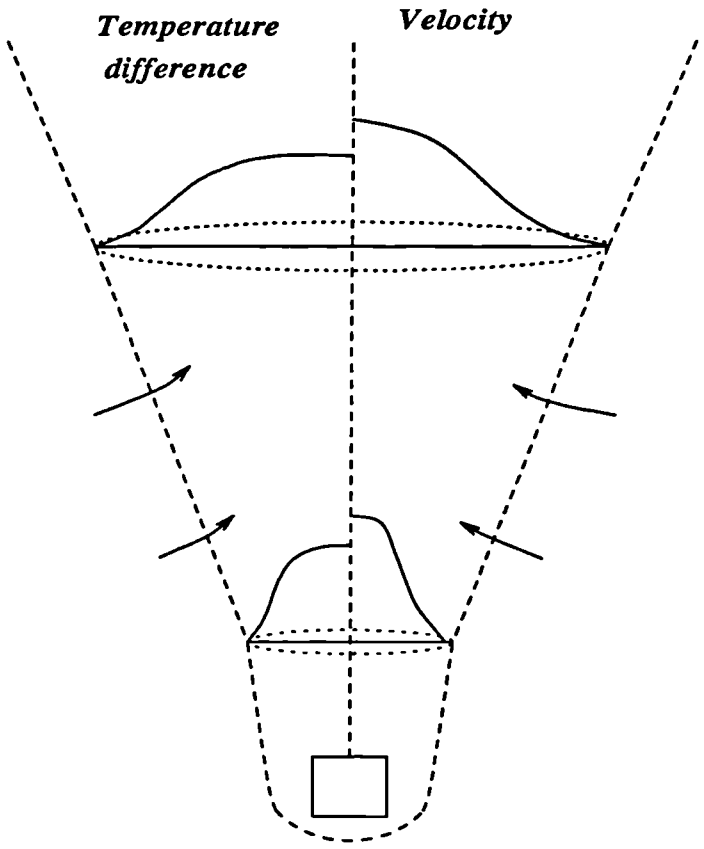

Figure 8.2 Emergence and development of a thermal plume

Figure 8.2 describes a sketch of the thermal plume from the boundary layer close to the heat source. Heat is transferred from the surface of the heat source to the adjacent air and gives rise to density differences and the propagation of a boundary layer flow driven by natural convection. In the above vicinity of the heat source the flow converges and merges into the thermal plume. At this intermediate stage a transition takes place and the turbulent plume is established. At the shear layer between the rising plume and the surrounding air entrainment occurs. This causes a reduction in the temperature difference

between the plume and the surrounding air and subsequently increasing the plume. The actual shape of the plume and its maximum height of elevation depends not only on the temperature difference to the ambient air but is affected to a large extent by the geometry of the heat source. It can be seen that the thermal plume is the sole driving force which not only transports excess heat towards the outlet in the ceiling but also ensures the supply of fresh air through openings near the floor by creating a negative pressure in the lower regions - known as the stack effect.

It is obvious that the over all flow pattern in the displacement ventilated space is affected by the heat source, the boundaries and the exits. Temperature differences between the inner and outer wall-surface induce an ascending and a descending boundary layer flow. The effect of buoyancy is commonly expressed by a global Archimedes number as below:

$$A_r = \frac{\beta g h \Delta T_o}{U_o^2} \qquad (8\text{-}1)$$

with ΔT_o the temperature difference between outlet and inlet, and h and U_o a characteristic length and velocity of the diffuser employed. It can be regarded as the ratio between buoyancy and momentum forces and it is of crucial importance to the air motion under buoyancy influence.

II. Buoyancy influence of non-isothermal wall jet flow.

1. The isothermal jet flow.

As mentioned in chapter V, the wall-jet flow is normally encountered in ventilated space resulting from the effect of wall mounted grilles. Figure 8.3

shows an example of this type of flow in a room with side-wall mounted grille. The flow below the ceiling is an isothermal wall jet flow which is independent of the downstream room geometry and hence independent of the room height and the room length. The jet reattaches to the ceiling surface due to the Coanda effect and keeps moving along that surface until the opposite wall is reached. The surrounding air is entrained during the jet development and the air recirculation is induced in the room.

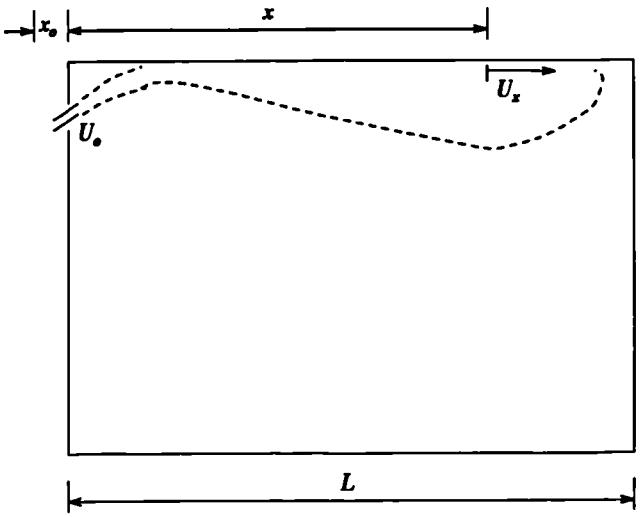

Figure 8.3 An iso-thermal wall jet in a ventilated room

The velocity decay in an iso-thermal three-dimensional wall jet below the ceiling can be described by a simple relation as:

$$\frac{U_x}{U_o} = K_1 \frac{\sqrt{a_o}}{x + x_o} \qquad (8\text{-}2)$$

where U_o and U_o are supply velocity and maximum velocity in the wall jet in the distance x from the opening, respectively. a_o is the supply area of the diffuser and x_o is the distance to the virtual origin of the wall jet. K_a is a constant. Another important parameter is the throw l_{Th} which is defined as distance from the opening to a location where the maximum velocity U_x is equal to a given reference value U_{Th}, the expression is as below:

$$l_{Th} = \frac{U_o K_a \sqrt{a_o}}{U_{Th}} - x_o \qquad (8\text{-}3)$$

The purpose of the design procedure of ventilation is to control the air distribution in the room in such a way that the maximum velocity in the occupied zone U_m is up to 0.15 m/s. General experience shows that this can be achieved when the l_{Th} is equal to room length L and reference velocity U_{Th} is in the range of 0.2 ~ 0.25 m/s according to CIBSE Guide.

2. The non-isothermal jet flow.

An undistorted wall jet will penetrate the ventilated space in case of isothermal flow, and it will entrain air from the occupied zone to induce recirculating air movement in the room. This picture will change when a thermal loaded air is supplied to the room. The supply temperature is reduced to a certain level lower than the average room temperature such that the wall jet will separate from the ceiling at a distance x_s from the diffuser and flow down into the occupied zone as shown in figure 8.4. Situations with such a short penetration depth are undesirable because the jet may have high velocity and low temperature when it flows into the occupied zone. This phenomenon will cause draught and thermal discomfort in the occupied zone. A calculation of

the penetration depth is thus a part of design procedure of such ventilation system.

Previous studies (Nielson, 1988, Lemaire, 1989, Nielson, et. al., 1987, Awbi, 1992) have shown that the penetration depth for a cold three-dimensional wall jet is proportional to $1/\sqrt{A_r}$. The following simplified equation is proposed by analysing the forces acting on a non-isothermal wall jet

$$\frac{x_s}{\sqrt{a_o}} = 0.19 K_{ss} K_s \left(\frac{1}{A_r}\right)^{0.5} \qquad (8\text{-}3)$$

where K_{ss} is a constant dependent on parameters such as room dimensions, location of diffusers, etc.

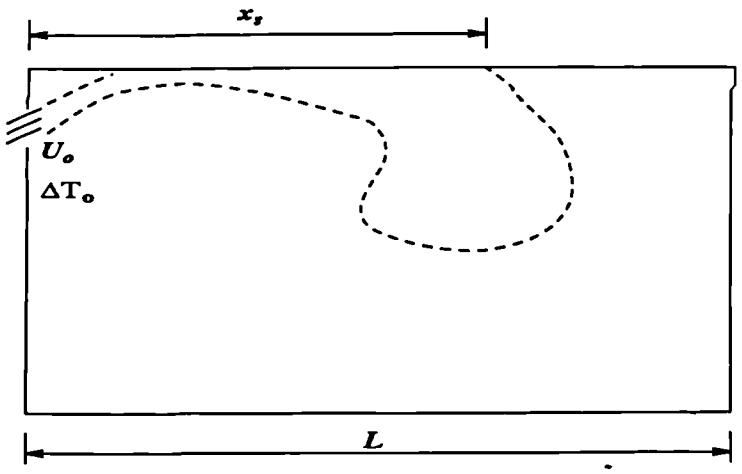

Figure 8.4 Penetration depth of a thermal wall jet

It is evident that the buoyancy effect does have a significant influence on the air distribution in the ventilated space with a non-isothermal supply air.

§8.1.2 The Objectives of Study

The influence of buoyancy effect on the air movement in rooms has been described in §8.1.1. It can be seen that the buoyancy effect plays a key role in the air distribution, the thermal comfort and further the pollutant concentration in the space where certain heat sources exist.

The investigations on the heat and mass transfer in ventilation systems have been carried out by both experimental measurement, e.g., Brown, et. al., 1972; Shaw, 1972; Scott, et. al., 1972; Nielson, et. al, 1979; Weber, et. al., 1980; Gadgil, et. al., 1982; Mahajan, 1987, etc., and numerical analysis (see §2.2). Generally speaking, experimental investigations may not provide enough information about the flow patterns which are directly related to the heat and mass transfer and the contaminant distribution. This is due to the fact that the air movement in an enclosure is affected by many parameters, such as the dimensions of the space, the size and location of supply, exhaust section and internal partitions, the conditions of the walls, ceiling and floor, and the strength and size of heat and/or contaminant sources. If tests are to be carried out in a model, these should be made with both dynamic and thermal similarity. This normally requires the equality of the Reynolds number, R_e, and the Archimedes number, A_r, which is not possible to achieve in the model concurrently. It is rarely to deal with the variations of each of the above parameters in an experimental study concurrently.

Computational Fluid Dynamics provides a cost effective method of predicting the whole flow field in the ventilation system. Previous studies (see §2.2) have

been carried out with different geometric configurations and ventilation conditions. Some of them presented promising results and captured the main flow features of phenomena studied. The use of CFD-models to simulate the flow field in ventilation system has contributed to the understanding of flow features in ventilated spaces. Studies have also shown that CFD application in building engineering is associated with certain shortcomings, e.g., modelling of turbulence, limited knowledge of heat and mass transfer through the building materials as influenced by the temperature difference between indoor and outdoor, prediction of pollutant particle distribution under buoyancy effect, etc. The work reported here is: a. To use CFD to predict the airflow pattern and temperature distribution in an enclosure with convective heat source. The predicted temperature field will be validated by the measured data carried out by Lebrun & Marret (1976); furthermore, b. To use CFD (particle transport model) to predict the pollutant particle distribution in the enclosure.

§8.2 Modelling of Airflow and Aerosol Particle Movement in Buoyancy Effected Flow

A CFD simulation of a three-dimensional airflow, temperature distribution and aerosol particle movement in an enclosure with a convective heat source (i.e., a radiator) is carried out in this study. The purpose is partly to obtain the information of the overall airflow pattern in the room and partly to obtain the distribution of aerosol particles within the space. The validation of temperature distribution with the relevant measurements is also presented here. The following sections describe the physical phenomenon, the specification of the simulation and the results of the calculation.

§8.2.1 Description of Physical Problem

The physical phenomenon studied by Lebrun & Marret (1976) is a full-scaled laboratory test chamber shown in figure 8.5. One end wall is an external wall with a window. A radiator is located near the external wall below the window. The relevant parameters of the case are listed in Table 8.1.

Table 8.1 Parameters of case

Case	L (m)	H (m)	W (m)	Window h×w (m^2)	Radiator h×w (m^2)	Heat source (W)
No. 1	4.74	2.7	3.45	1.6×2.2	0.6×1.1	780

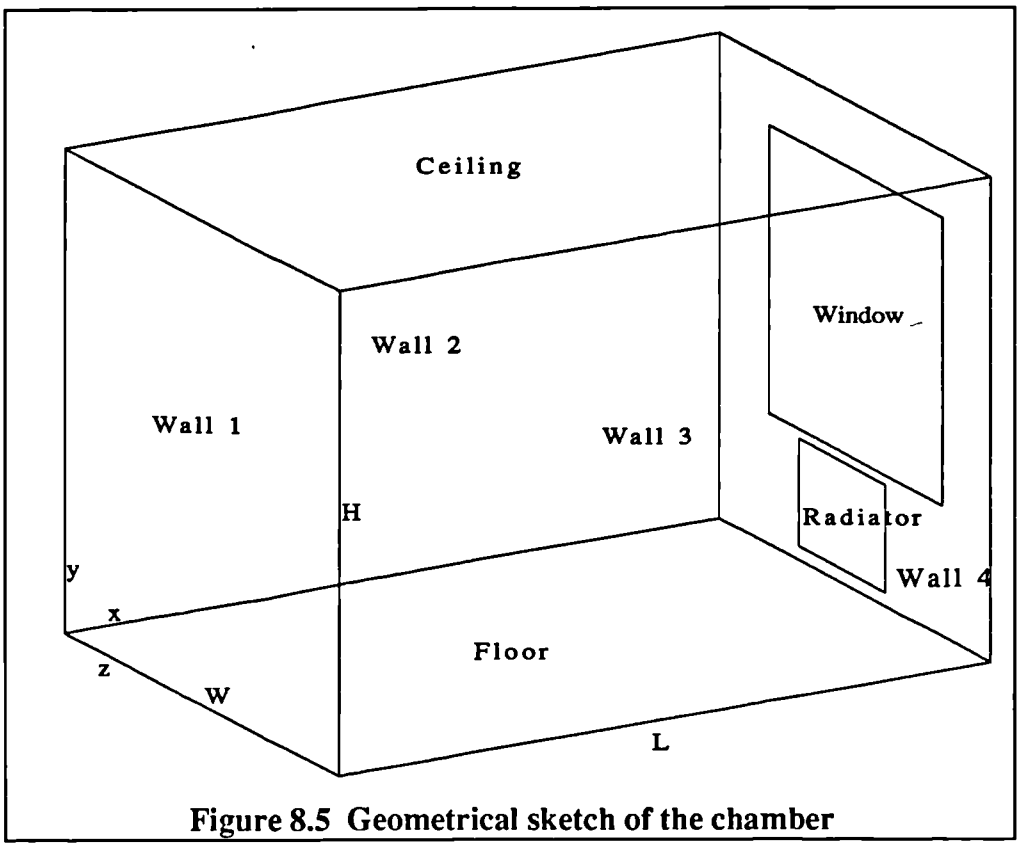

Figure 8.5 Geometrical sketch of the chamber

The experiment was carried out by measuring the temperatures at certain sample points within the room and on the internal surfaces of the room. The outside environment situation considered here is the winter season.

The outside environment temperature: $t_o = -3°C$ $(T_o = 270.15K)$;

The outside temperature of internal wall: $t_{ol} = 9.5°C$ $(T_{ol} = 282.5°C)$;

The bulk temperature of the room air: $t_{ai} = 22°C$ $(T_{ai} = 295°C)$

The temperature difference between inside and outside environment is equal to

$$\Delta t = t_{ai} - t_o = 25°C$$

Based on the bulk room temperature t_{ai}, the relevant physical properties of room air are listed in Table 8.2.

Table 8.2 Physical properties of air

Fluid	Reference temperature T_{ref} (K)	Density ρ ($kg \cdot m^{-3}$)	Laminar viscosity μ ($kg \cdot m^{-1} \cdot s^{-1}$)	Thermal expansion coefficient β (K^{-1})	Thermal conductivity λ ($W \cdot m^{-1} \cdot K^{-1}$)	Specific heat C_p ($J \cdot kg^{-1} \cdot K^{-1}$)
Air	295	1.201	1.821e-5	3.382e-3	2.586e-2	1005

The chamber was lined with sort of insulating materials. Table 8.3 lists the properties of chamber materials.

Table 8.3 Properties of the test chamber

Items	Area (m^2)	U-values ($W \cdot m^{-2} \cdot K^{-1}$)	Condition
Ceiling	16.35	0.87	Internal wall
Floor	16.35	0.55	Internal wall
Wall 1	9.32	0.71	Internal wall
Wall 2	12.8	0.35	Internal wall
Wall 3	12.8	0.35	Internal wall
Wall 4	5.8	0.78	External wall
Window	3.52	2.54	Double glazing

§8.2.2 The CFD modelling process

I. The influence of buoyancy effect on the equation set

The mathematical equations of isothermal turbulent fluid flow has been given in chapter IV. As mentioned in §8.1, the attention in this chapter is turned to convective heat transfer flow, in which buoyancy force plays the major role because it is the source of energy for the mean motion itself. Such movement is produced under gravity by a density contrast between the source fluid and its surrounding fluid. Certain expressions of this phenomenon is needed to describe the buoyancy effect. The reflection of buoyancy influence in the mathematical equations can be generally expressed as below:

$$\frac{\partial}{\partial t}(\rho\phi)+\mathrm{div}\left(\rho V_\phi-\Gamma_\phi \mathrm{grad}\phi\right)=S_{\phi i}+S_{\text{Buoyancy}} \qquad (8\text{-}4)$$

where $S_{\phi i}$ represents all source terms except the buoyancy term. It is clear that the buoyancy effect has no direct influence on the transient, convective and diffusion terms of the general equation. It affects the flow field through the formations of source terms in the equation. The detailed information about the equation (8-4) is given in Table 8.4.

Table 8.4 Source terms for conservation equations in buoyant flow

Φ	Γ_Φ	$S_{\phi i}$	S_{Buoyancy}
1	0	0	0
U V W	μ_{eff}	$-\frac{\partial}{\partial x_i}\left(P+\frac{2}{3}\rho k\right)+\frac{\partial}{\partial x_i}\left[\mu_{eff}\left(\frac{\partial U_i}{\partial x_j}+\frac{\partial U_j}{\partial x_i}\right)\right]+B_i$	0 $-\rho\beta g\theta$ 0
H	$\frac{\lambda}{C_p}+\frac{\mu_t}{\sigma_H}$	$\frac{\partial P}{\partial t}$	0
k	$\mu+\frac{\mu_t}{\sigma_k}$	$G_k-\rho\varepsilon$	G_B
ε	$\mu+\frac{\mu_t}{\sigma_\varepsilon}$	$\varepsilon(C_1G_k-C_2\rho\varepsilon)/k$	$C_1C_3\varepsilon G_B/k$

where $\mu_{eff} = \mu + \mu_t$, $\mu_t = C_\mu C_D k^2 / \varepsilon$

$$G_k = \mu_t \frac{\partial U_i}{\partial x_j}\left(\frac{\partial U_i}{\partial x_j} + \frac{\partial U_j}{\partial x_i}\right)$$

The term $-\rho\beta g\theta$ represents the buoyancy term in the momentum equation which has

$$-\rho\beta g\theta = -\rho\beta g(T - T_o) \qquad (8\text{-}5)$$

where T_o is the reference temperature which is normally chosen as a ' mean temperature ' in some sense; here T_o is chosen as the bulk temperature of the room air. The effect of equation (8-5) is to reduce the size of momentum sources due to the buoyancy forces.

In Table 8.4, the source terms of both equations of k and ε include an extra term G_B which is called a generation term due to the buoyancy effect. According to Boussinesq buoyancy approximation, it is defined as

$$G_B = -\beta g \frac{\mu_t}{\sigma_H}\frac{\partial \theta}{\partial y} \qquad (8\text{-}6)$$

This equation indicates the exchange between the kinetic energy of turbulence and the potential energy of the flow. In a stable stratified flow G_B becomes a sink term so that the turbulent mixing is reduced while the potential energy is increased.

The constants appearing in the k-ε two-equation model shown in Table 8.4 are assigned, in this study, the following values recommended by Launder & Spalding (1974).

$$C_1 = 1.44 \quad C_2 = 1.92 \quad C_3 = 1.0 \quad C_\mu = 0.09 \quad C_D = 1.0$$

$$\sigma_k = 1.0 \quad \sigma_\varepsilon = 1.3 \quad \sigma_H = 0.9$$

The above constants are not universally valid but dependent on the flow type. The variation of these constants has been addressed by many researchers. For example, the constant C_3 is an additional buoyancy constant. It is treated as an empirical function of the flow Richardson number(R_f, defined as $R_f = -G_B / G_k$) by Rodi (1980). Its value varies between zero and unity. It takes zero for stable conditions in reacting flow and unity for unstable conditions in general. σ_H is typically assigned a constant value in the range of 0.7~1.0 in heat transfer calculations in room air flow but in reality it also depends on the type of flows. Nielson, et. al. (1979) applied a σ_H depending on a buoyancy parameter in room air flow.

II. Boundary conditions imposed on the flow simulation.

1. Flow boundary.

As described in §4.3.5, boundary conditions have to be implemented in the simulation for specifying the characteristics of the case. In particular, the non-slip condition at the solid surfaces is applied for the velocities, i.e., $u_w = v_w = w_w = 0$. The so-called wall function is imposed for describing the variations of turbulent parameters in near wall regions, see details in §4.3. The flow domain is divided into 33x20x23 cells, shown in figure 8.6.

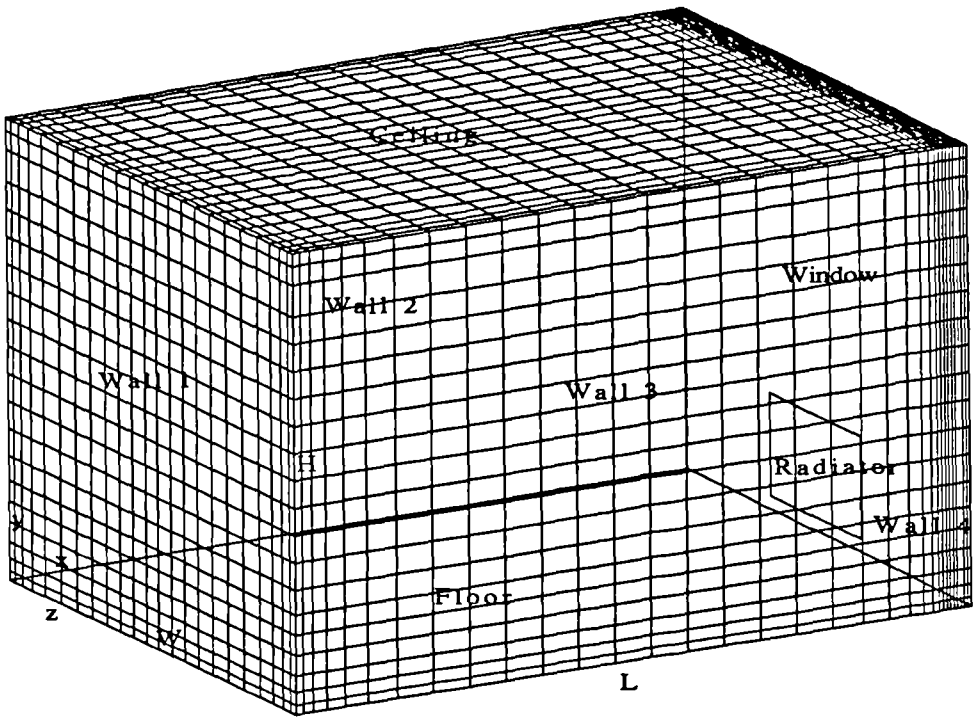

Figure 8.6 The mesh scheme of the simulation

2. Thermal boundary conditions

The wall function is also applied to the temperature boundary layer, i.e., equations (4-116) and (4-118). The temperature of wall surface T_w and the heat flux Q_w (W/m^2) at the wall surface have to be defined for calculating the scalar temperature T^+.

The room studied here is not well insulated and heat losses exist due to the temperature differences between the inside and outside. So the heat flux at the wall surface (mixed thermal boundary condition) has to be specified in the cases.

According to §4.3.5, the formula of the heat transfer boundary conditions at the wall surface can be expressed in a general form as below:

$$AT_w + BQ_w = C \tag{8-7}$$

$$Q_w = \left(\lambda \frac{\partial T}{\partial n}\right)_w \tag{8-8}$$

A special treatment is required for defining the T_w and Q_w in the simulation because the thermal boundary condition is not so simple to specify the wall temperature or its time derivative, Q_w. Here A, B and C are non zero values. The following method is introduced according to CIBSE Guide (1986).

Taking the structure of a typical wall shown in figure 8.7.

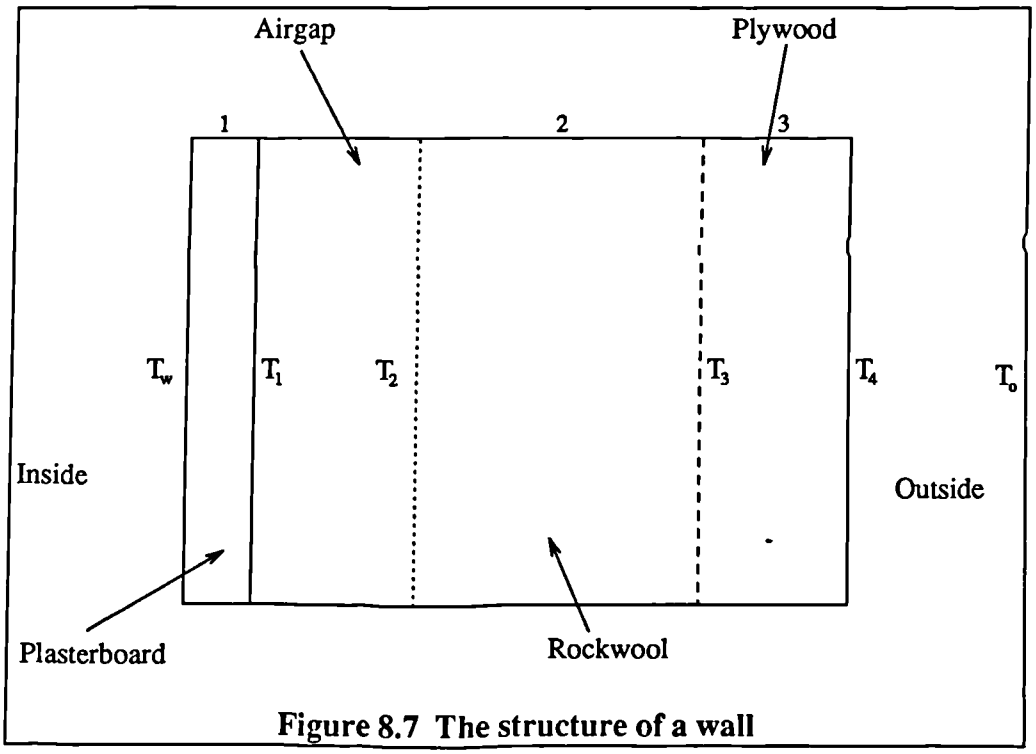

Figure 8.7 The structure of a wall

The method of specifying the thermal wall boundary conditions used in this study is based on the CIBSE Guide (1986), see details in Appendix E. By specifying the values of A, B and C defined in Appendix E, the CFD code can then calculate the internal surface temperature of the wall, the heat flux at the wall, and the amount of heat loss through the wall as follows:

Ceiling:	A=1.0,	B=1.0494,	C=282.5
Floor:	A=1.0,	B=1.7818,	C=282.5
Wall 1:	A=1.0,	B=1.3085,	C=282.5
Wall 2:	A=1.0,	B=2.7571,	C=282.5
Wall 3:	A=1.0,	B=2.7571,	C=282.5
Wall 4:	A=1.0,	B=1.1821,	C=270.15
Window:	A=1.0,	B=0.2937,	C=270.15

3. Heat source

The specification of heat source is the most difficult task in the heat transfer simulation process. The heat source (radiator), in this study, is treated as a ' Thin Surface '. The thickness of the radiator can be ignored compared with the room size. The boundary conditions on the heat surface have the same form as the ' wall function ' boundary and again, the non-slip condition is applied to the velocities.

The method of defining the thermal boundary on the radiator surface is to specify a constant heat flux, i.e., in equation (8-7), set a=0, B=1 and C=the value of the heat flux based on the power of the radiator. For the case listed in §8.2.1, the heater produces 780W uniformly distributed over 0.6×1.1 m^2 from

both sides of the ' Thin Surface ', i.e., Q=590.9 W/m^2, so C=590.9 for each side of ' Thin Surface '.

However, the case is treated as a steady-state problem. If the value of 590.9W/m^2 is used in the simulation, that would bring the room temperature up continuously and the simulation would not arrive at a steady state. According to the experimental results, the bulk temperature of the room air is 22°C. That means a heat balance has to be maintained between the inside and the outside. In reality, the radiator would be turned on at time t=0 at Q=590.9 W/m^2, and switched off at t=t_1 once the required temperature arrived. The real process of heating a room with a radiator is time-dependent. When seeking a steady-state solution, the total heat input through the radiator must be balanced by the total heat loss through the room surfaces based on the required room temperature. Based on heat balance principle, the following routine is applied to define the heat flux of radiator.

Total heat loss through ceiling, floor, walls and window can be calculated as below:

$$Q_{out} = \sum UA\Delta T \quad (J/s) \tag{8-9}$$

In order to maintain the required bulk room temperature, such heat loss must be compensated by the heat coming from the radiator, therefore

Heat flux from radiator $$Q_{Rad} = \frac{\sum UA\Delta T}{A_{Rad}} \quad (W/m^2) \tag{8-10}$$

where A_{Rad} is total surface area of radiator (both sides).

From the above role, the key problem in the simulation is to estimate value of ΔT. The conventional way is to choose the bulk temperature of the room air to represent the inside temperature based on the assumption of uniform distribution of inside and outside air. Such an assumption is accurate enough to the outside air, but does not reveal the inside situation properly, e.g., a large temperature decrease exists from the radiator to the window surface. The temperature difference between the inside and the outside at the window surface is much different from the assumed value. The more precise calculation of heat losses is required. The following method is applied in this study.

Considering the realistic room surface conditions, engineering knowledge is used in the study. According to CIBSE, the following concepts are introduced:

The mean surface temperature $$t_{ms} = \frac{\sum A t_s}{\sum A} \qquad (8\text{-}11)$$

The inside environmental temperature $$t_{ei} = \frac{1}{3} t_{ai} + \frac{2}{3} t_{ms} \qquad (8\text{-}12)$$

The total heat loss $$Q_{out} = \sum (t_{ei} - t_o) UA \quad (J/s) \qquad (8\text{-}13)$$

The mean radiant energy factor $$F_r = \frac{\sum A - \sum AUR_{ei}}{\sum A} \qquad (8\text{-}14)$$

Then, the effective steady-state heat flux from the radiator is

$$Q_{Rad} = F_r \frac{Q_{out}}{A_{Rad}} \quad (W/m^2) \qquad (8\text{-}15)$$

where t_s is room surface temperature, here it takes the experimental values (Lebrun & Marret, 1976).

From equations (8-11) ~ (8-15), it can be seen that the actual room surface temperatures are taken into account. The main point of these equations is based on the energy input into the whole volume of the room, i.e., the environmental point. Since no radiation is considered in the simulation, i.e., the convection is the sole heat transfer process, the effective input energy should be weighted by the mean radiant energy factor. Table 8.5 gives the estimated data of the heat losses based on the equations (8-11) ~ (8-15), here F_r=0.78.

Table 8.5 The estimated heat losses

Items	t_{ms} (°C)	t_{el} (°C)	t_o (°C)	U-value ($Wm^{-2}K^{-1}$)	Area (m^2)	Heat loss (Js^{-1})
Ceiling	20	20.6	9.5	0.87	16.353	157.9
Floor	20	20.6	9.5	0.55	16.353	99.8
Wall 1	20	20.6	9.5	0.71	9.32	73.4
Wall 2	20	20.6	9.5	0.35	12.8	49.7
Wall 3	20	20.6	9.5	0.35	12.8	49.7
Wall 4	20	20.6	-3	0.78	5.8	106.6
Window	20	20.6	-3	2.54	3.52	211.0

Therefore, the effective heat flux from the radiator can be calculated as below:

$$Q_{Rad} = F_r \frac{Q_{out}}{A_{Rad}} = 0.78 \times \frac{748.1}{0.6 \times 1.1 \times 2} = 442 \ \left(W/m^2\right)$$

The above empirical method will be validated by comparing the numerical results with the available experimental data.

4. Particle boundary conditions

The particle tracking simulation carried out in this case will demonstrate the particles movement and their distribution in the room under buoyancy effect. The particles are coming from a cigarette smoking source. The source is simplified as a point. The heat emitted from the cigarette can be ignored comparing with the heat coming from the radiator. The particles are assumed to be spherical and have density $\rho_p = 865.0\,kg/m^3$. The particles sizes cover the range of 1 ~ 20μm. The initial motion of particles, based on common knowledge, is specified as opposite to the gravity, i.e., $u_p = w_p = 0$, and $v_p = 0.1m/s$. Other conditions are the same as those used in Chapter VI & VII. The tracking period is specified as 30 minutes.

§8.2.3 Results and Analysis

The numerical simulation of a three-dimensional flow in the room with a radiator (shown in figure 8.5) is performed and analysed in this section. The results are presented as follows.

I. The airflow patterns and temperature distributions in the room.

a. Figure 8.9a, b and c describe the airflow patterns in different planes in the room width (see figure 8.8a). A thermal rising wall jet is produced along the window surface above the radiator in the centreline plane (see figure 8.9b). The jet develops into a convective thermal boundary layer along the surface and entrains the cold air from the surroundings. The air in the boundary layer flows upwards along the surface and then deflects when it reaches the ceiling. The air movement under the ceiling surface is rather complex. The airflow develops into a ' buffer zone ' under the ceiling. Some of the hot air flows along the ceiling surface and some disperses downwards. A large air circulation is formed at the high level of the room due to the mixing of hot and cold air. The main flow direction under the 'buffer zone' is towards the hot wall jet due to the entrainment of the jet. A downdraught flow is formed near the side wall opposite to the external wall. The airflow patterns in the planes besides the central plane are shown in figure 8.9a and 8.9c. It can be seen that the flow is axisymmetrical about the centreline plane. The air movement in those planes are separated into two main regions — the upper warm counter clockwise circulation and the lower cool clockwise circulation. The flow between these two regions is

mainly towards the thermal wall jet. The entrainment of cold air from the surrounding and disperse of hot air to the room space complete the air circulation and heat exchange.

b. The development of the wall jet flow is shown in figure 8.10. The high speed region is restricted in a narrow area above the radiator. The air velocity reduces rapidly outside that area. The velocity of bulk room air (i.e., in occupied zone) is generally below 0.15 m/s.

c. Figure 8.11 shows the temperature interface in the room space. It can be seen that the room air is generally divided into two zones: the upper warm zone and the lower cool zone. A temperature interface exists between these two zones. The position of the temperature interface is about at the middle of the room height. The temperature above the interface is over 22°C and its value is lower 22°C below that interface.

d. The temperature distributions in the room space are presented in figure 8.12 and 8.13. The temperature stratification exist along the room height. A steep variation of temperature from the radiator to the window surface can be observed from figure 8.12 and 8.13. The relatively cool areas are located at floor level and all regions near the wall surfaces.

e. The airflow patterns and temperature distributions in different planes along the room height and length are demonstrated in figure 8.14 and 8.15. A symmetrical air movement about the central plane can be seen from these figures. The entrainment of cool air to the hot boundary from the surroundings also induces air circulation in those planes.

f. Figure 8.16a and 8.16b describe the v-velocity and temperature profiles in the jet boundary layer in central plane above the radiator. Both temperature

and velocity change rapidly in the convective boundary layer above the radiator. These variations reduce as the jet rises and travels along the surface.

g. The U-velocity profiles in the centreline plane along the room length are shown in figure 8.17. It shows that the U-velocities vary rapidly in the region close to the ceiling surface due to the convective flow and the damping effect of the wall, while the distributions of U-velocity in the occupied zone are relatively uniform and the absolute values are less than 0.15m/s. Figure 8.16 and 8.17 also show that the grid nodes used in the simulation are not fine enough to reflect the details of the flow in the boundary layers of the walls. If detailed analysis of the near-wall flows is required, the mesh would need to be further refined.

h. The comparisons of temperatures between simulation and measurement are presented in figure 8.18 and 8.19. Generally, the numerical results show good agreement with the relevant measured values. It can be seen that the numerical simulation produces satisfactory results. Some differences exist between the computation and the measurement. The following reasons may cause the errors: a. the mesh used in the simulation is not fine enough and needs to be further refined; b. the turbulence model used may need to be improved, e.g., low-Reynolds number k-ε model may produce better results; c. the measurement may not accurate enough due to the errors of experimental equipment.

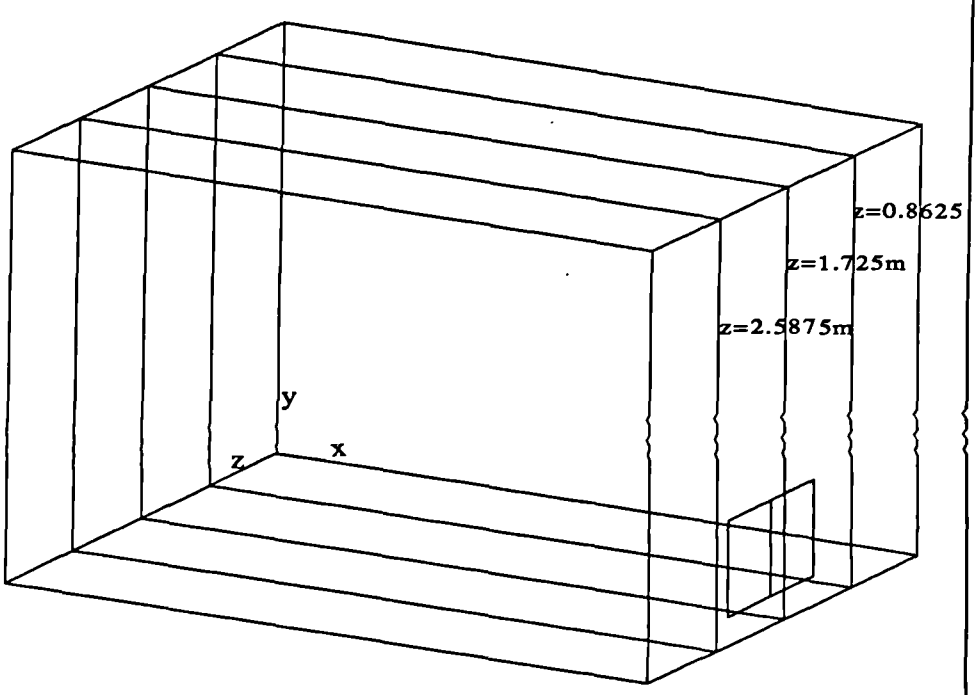

Figure 8.8a Typical planes in the room width

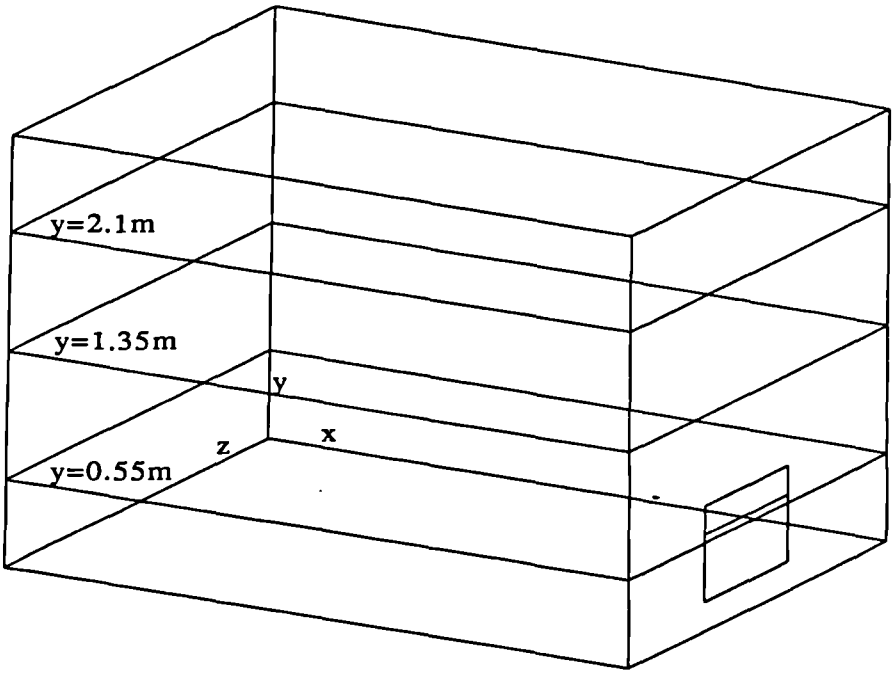

Figure 8.8b Typical planes in the room height

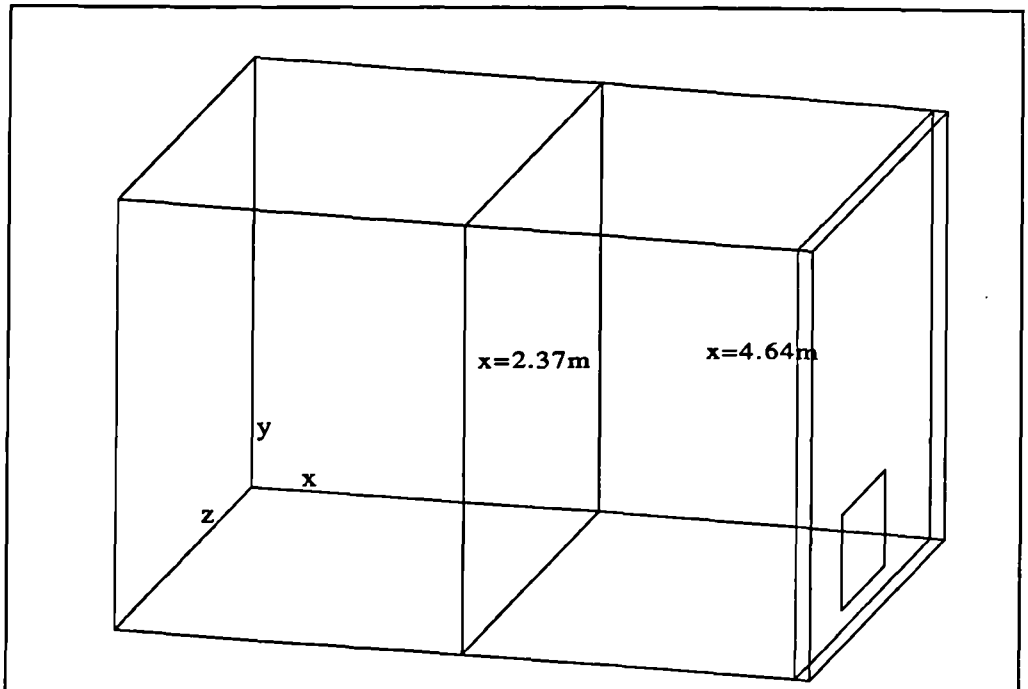

Figure 8.8c Typical planes in the room length

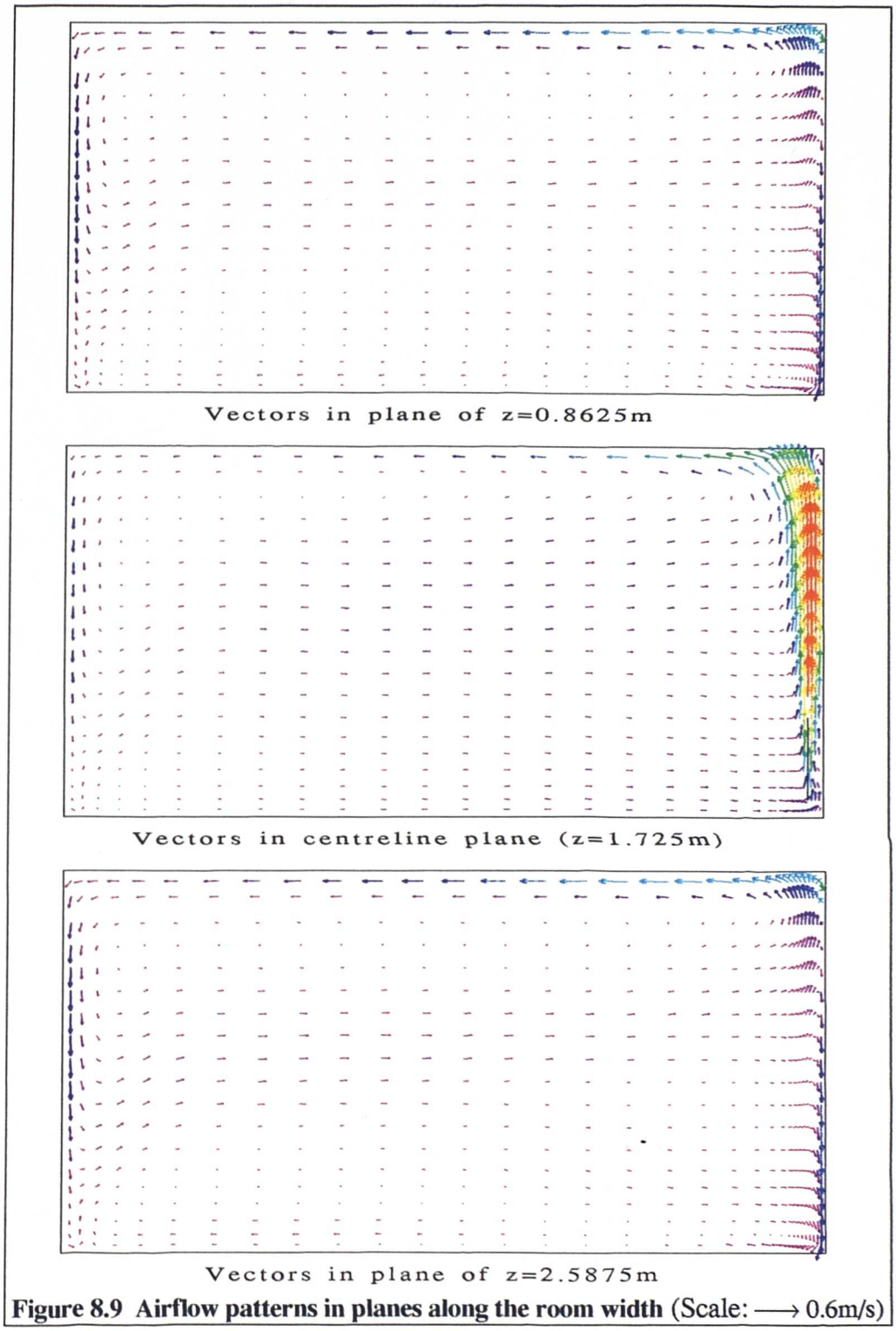

Figure 8.9 Airflow patterns in planes along the room width (Scale: ⟶ 0.6m/s)

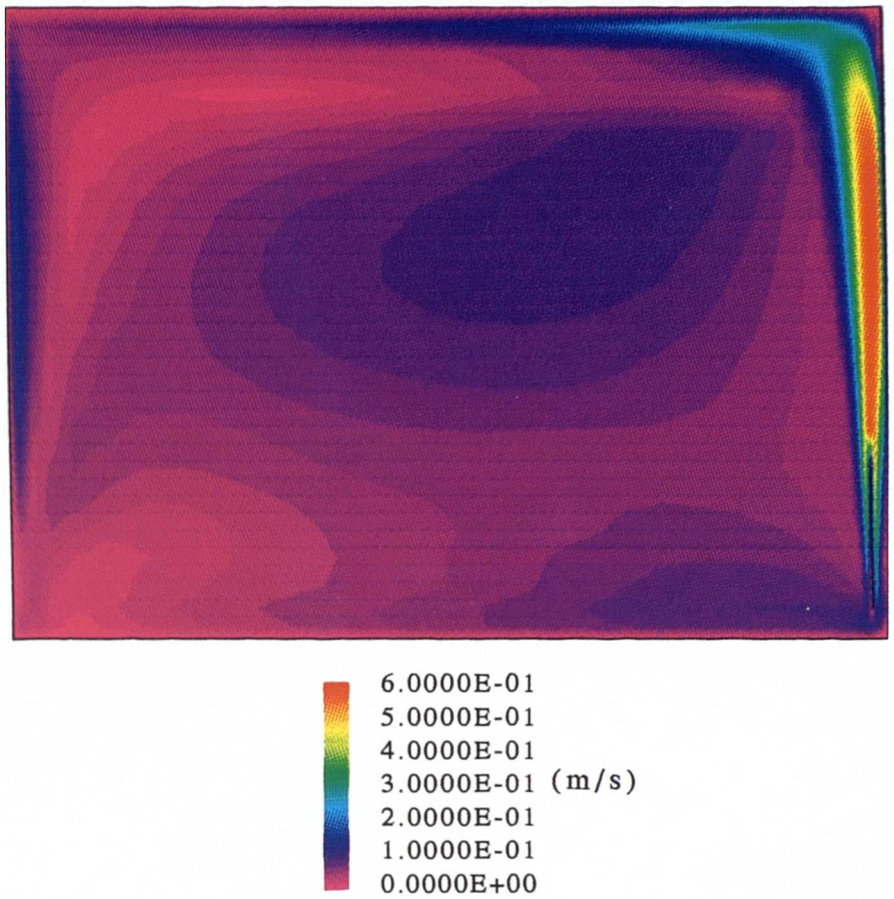

Figure 8.10 The development of the thermal wall jet flow

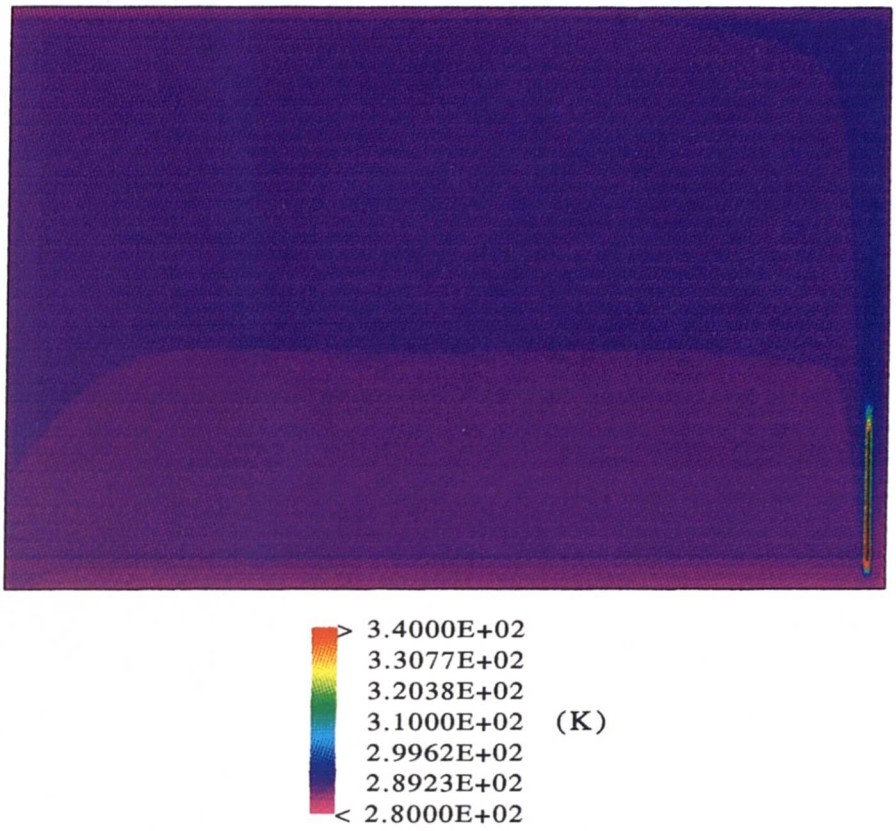

Figure 8.11 Temperature interface in room space

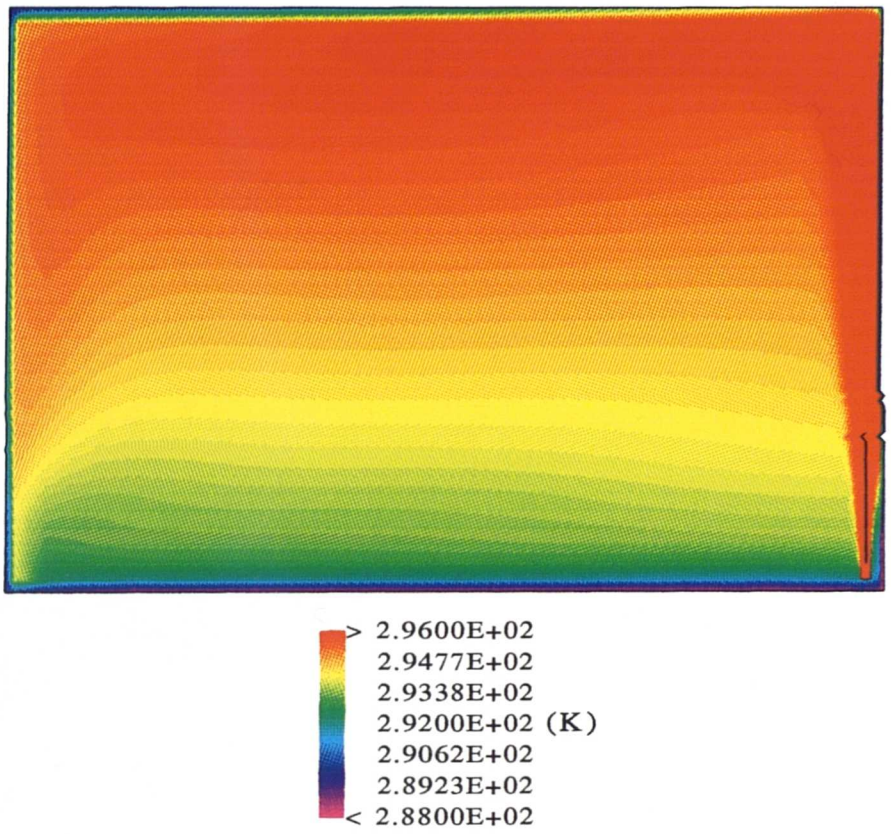

Figure 8.12 Temperature stratification in centreline plane

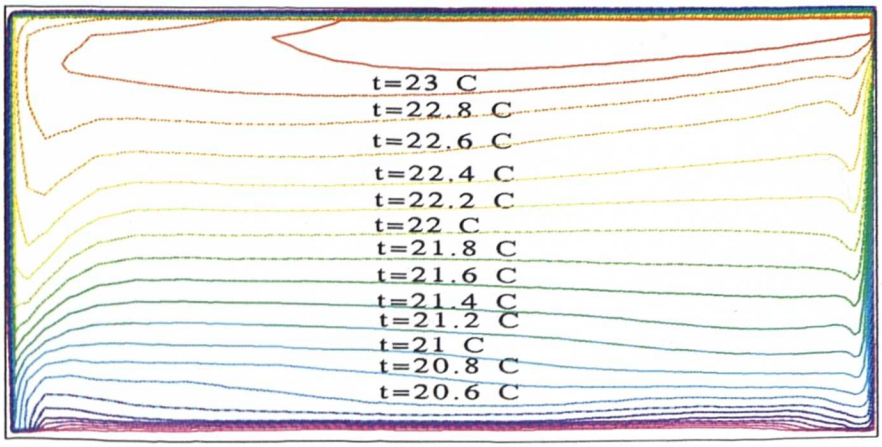

a. Temperature contours in the plane of z=0.8625m

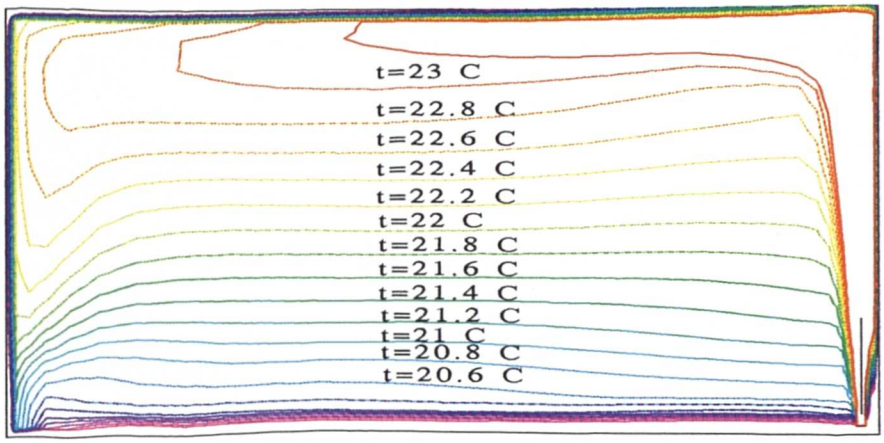

b. Temperature contours in centreline plane (z=1.725m)

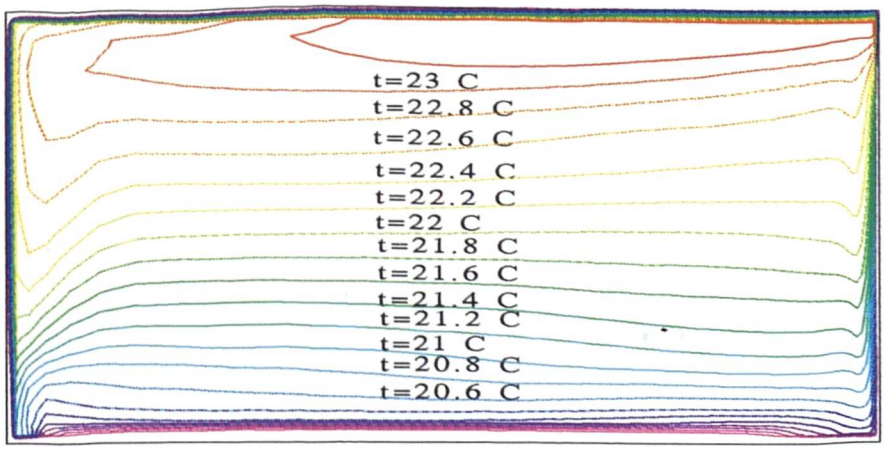

c. Temperature contours in the plane of z=2.5875m

Figure 8.13 Temperature distributions in planes along the room width

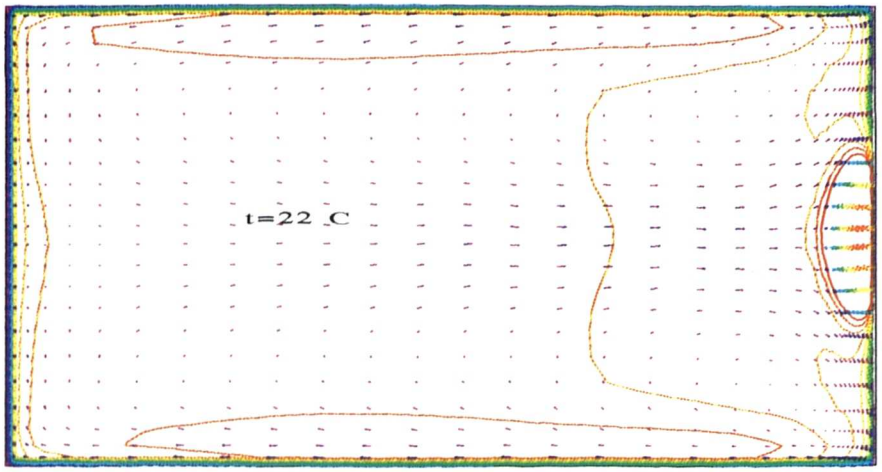

a. Vectors and temperatures in plane of y=2.1m

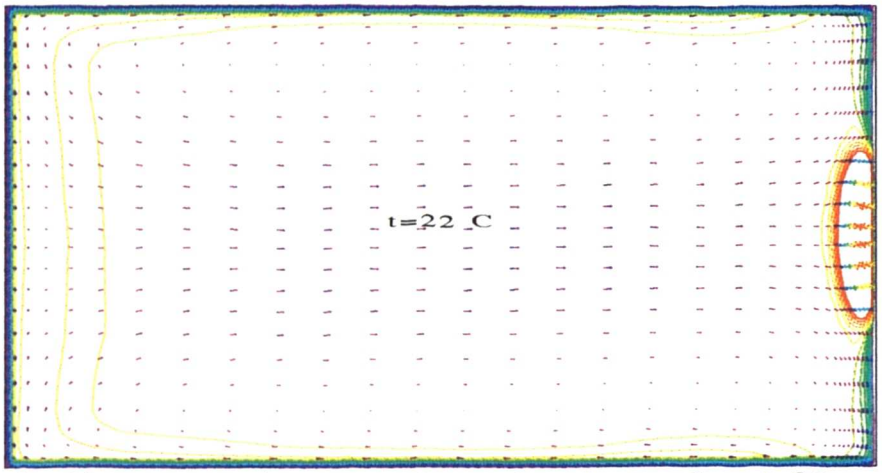

b. Vectors and temperatures in plane of y=1.35m

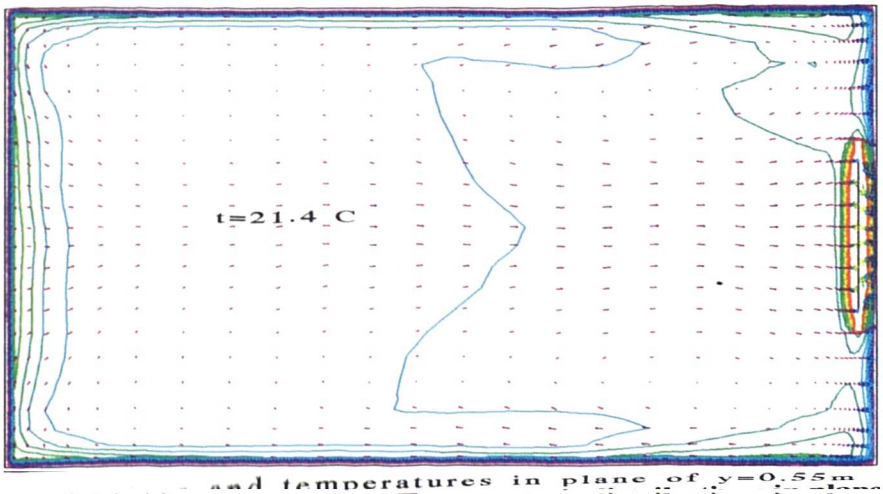

and temperatures in plane of y=0.55m

Figure 8.14 Air movement andTemperature distributions in planes in the room height (Vector scale: ⟶ 0.6 m/s)

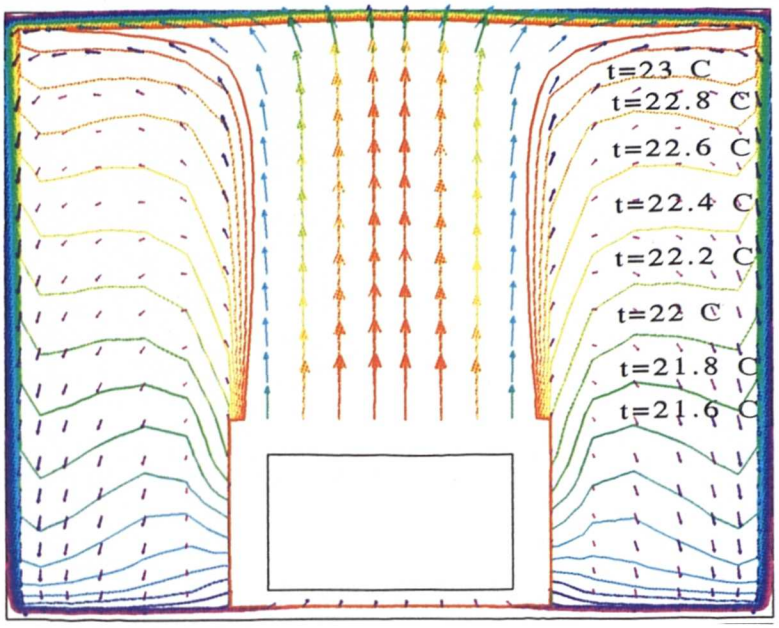

a. Vectors and temperature in plane of x=4.64m

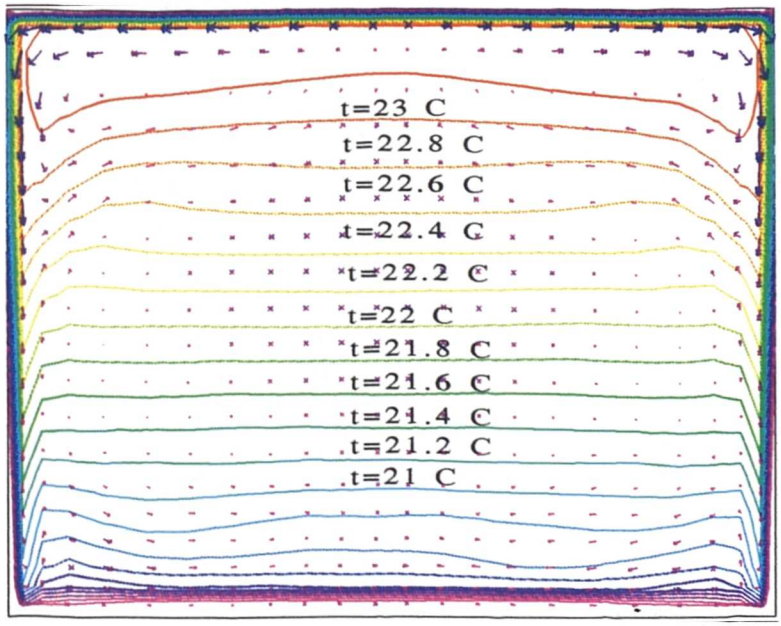

b. Vectors and temperature in plane of x=2.37m

Figure 8.15 Vectors and temperature profiles in planes along the room length
(Vector scale: ⟶ 0.6 m/s)

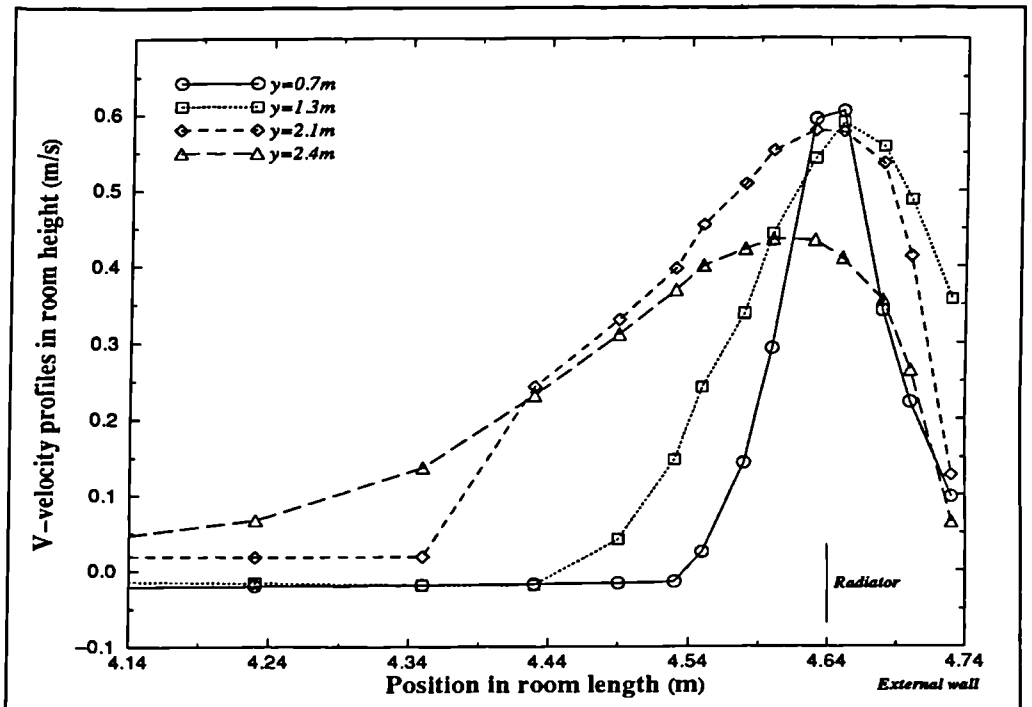

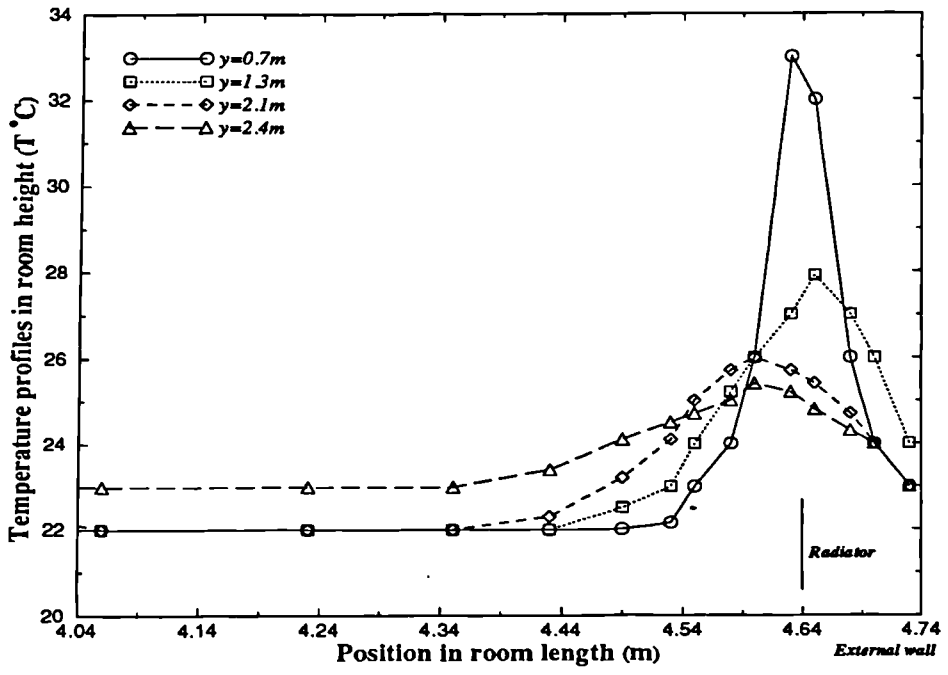

Figure 8.16 V-velocity and temperature profiles in thermal boundary layer

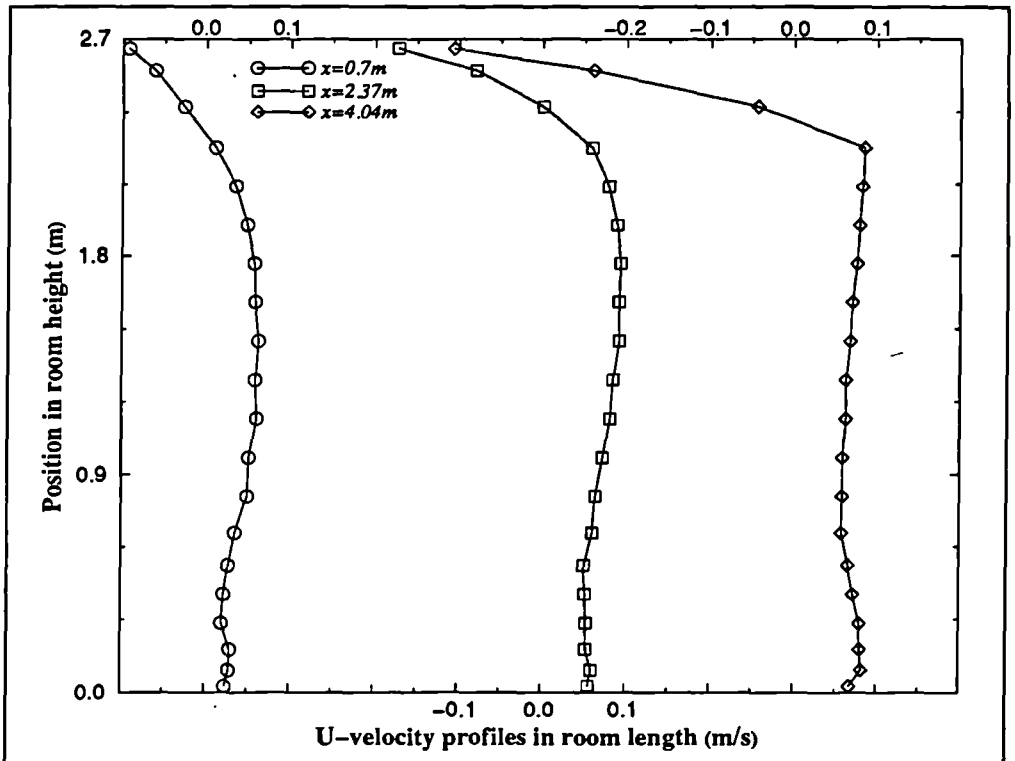

Figure 8.17 U-velocity distributions in centreline plane along the room length

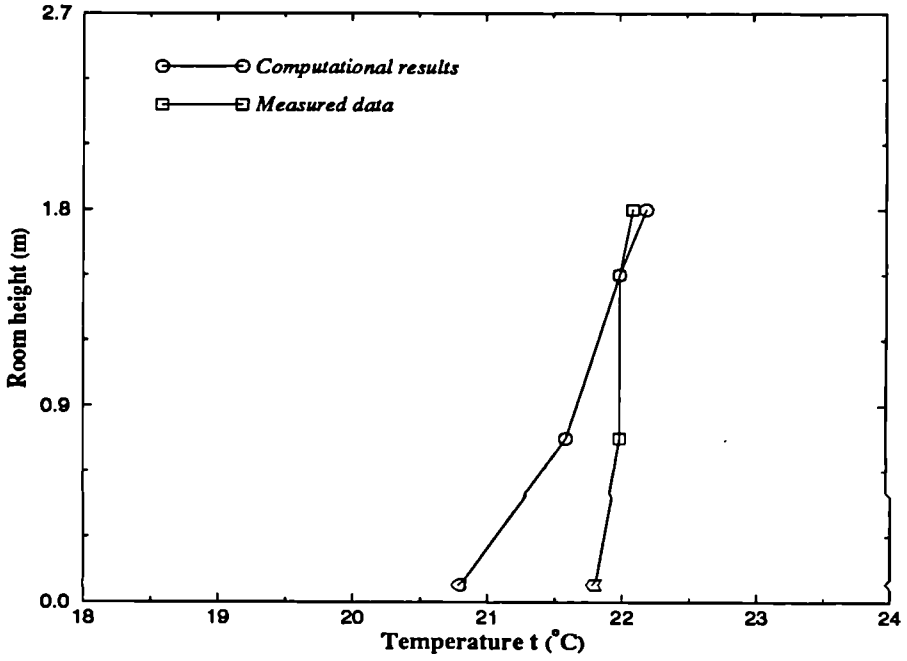

Figure 8.18a Comparison of temperature in centreline plane (x=2.37m)

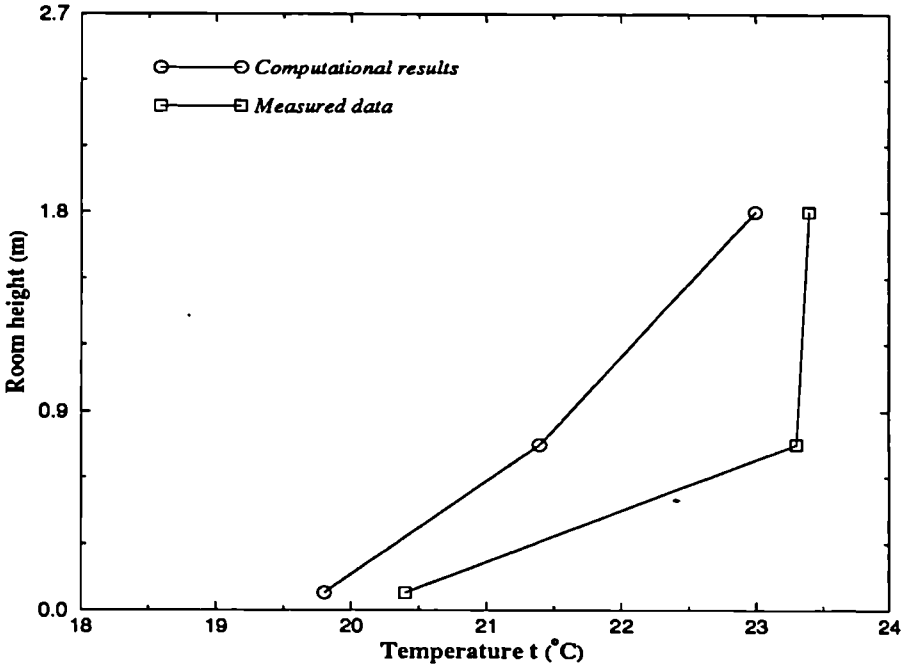

Figure 8.18b Comparison of temperature in centreline plane (x=4.04m)

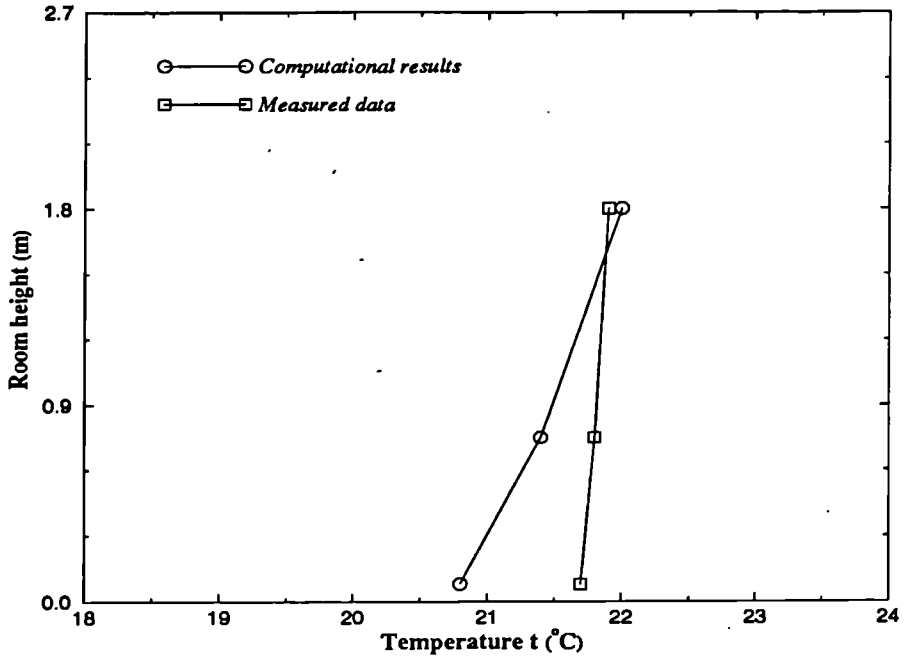

Figure 8.19a Comparison of temperature in side plane (x=0.7m, z=2.75m)

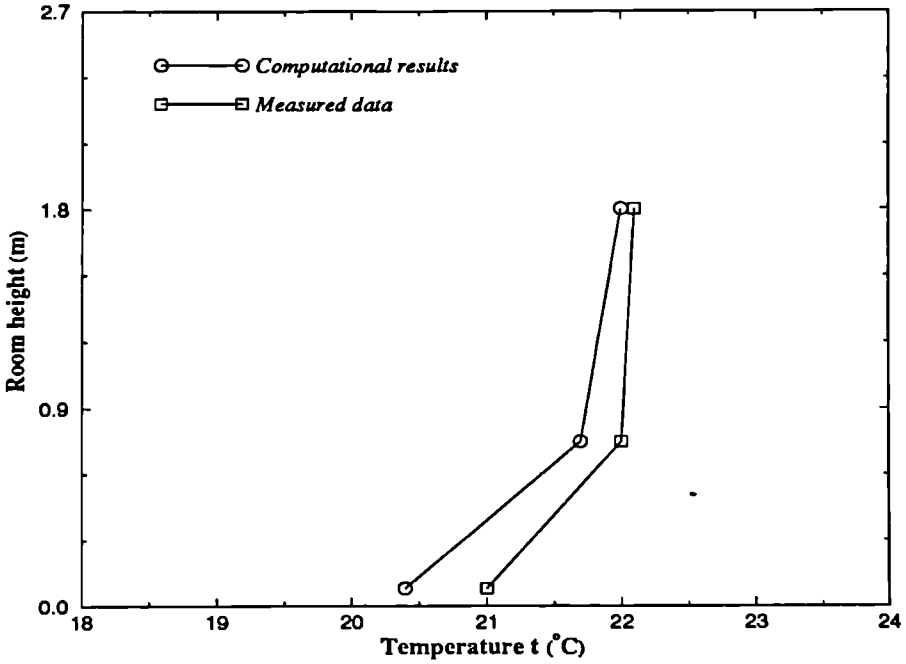

Figure 8.19b Comparison of temperature in side plane (x=4.04m, z=2.75m)

II. Particle movement in the room

Figure 8.20a, b, c and d present the particle tracking routes in the room. From these figures, it can be seen that all particles are moving towards to the hot plume first due to the entrainment of the thermal jet. The particles go up with the hot air once they are entrained into the hot jet and then disperse into the room space. It is interesting to notice that small particles (d_p<10μm) mainly suspend or deposit in upper warm zone (see figure 8.20a and 8.20b) due to the buoyancy effect (i.e., the density difference induced by buoyancy effect), while large particles (d_p>10μm) disperse through the whole room space and finally deposit on the floor or wall surfaces. Those particles deposit on the ceiling or wall surfaces impose the possibility of soiling problem, e.g., the wall surface close to the radiator takes the higher chance to be contaminated by smoking particles than other wall surfaces due to the large amount of particles entrained to the hot plume above the radiator. In practice, this phenomenon can be observed that the internal surface close to the radiator becomes yellow with the time. Figure 8.20 shows that particles are more concentrated in the area close to the heat source than the others. That means the occupants sitting close to the radiator take higher possibility of passive smoking than those sitting at the other side of the pollutant source. Those particles dispersed in the room space significantly influence the indoor air quality. From figure 8.20, it can seen that the thermal wall jet flow produced by the radiator greatly influences the pollutant particle movement and distribution in the room. Figure 8.20 also implies that the method to improve the indoor environment is to install an extracted fan at the ceiling which may remove the smoking particles from the room effectively and maintain the acceptable indoor air quality.

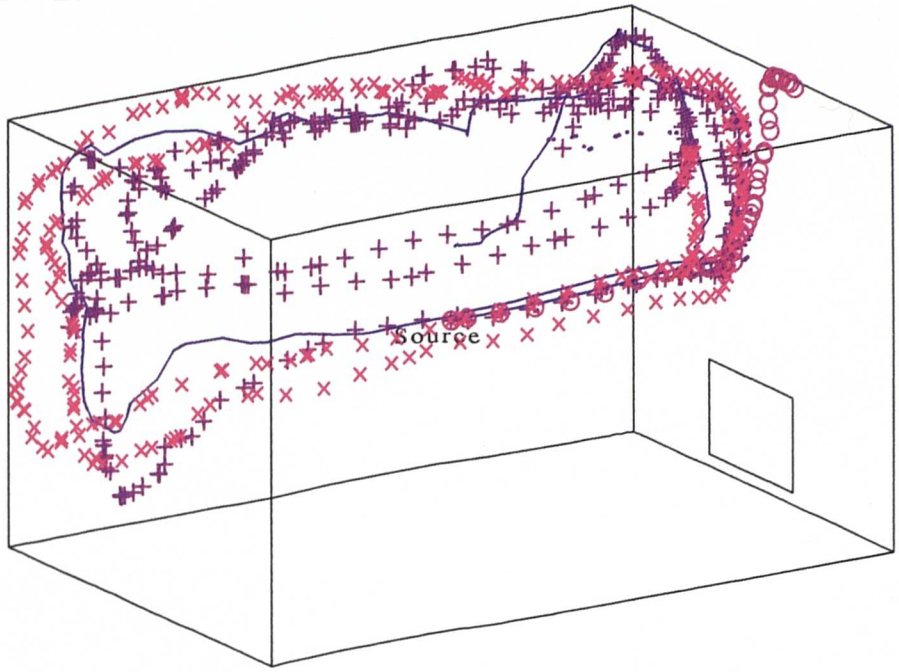

× 1μm o 2μm + 3μm • 4μm – 5μm

Figure 8.20a Five sample particle tracking in the room

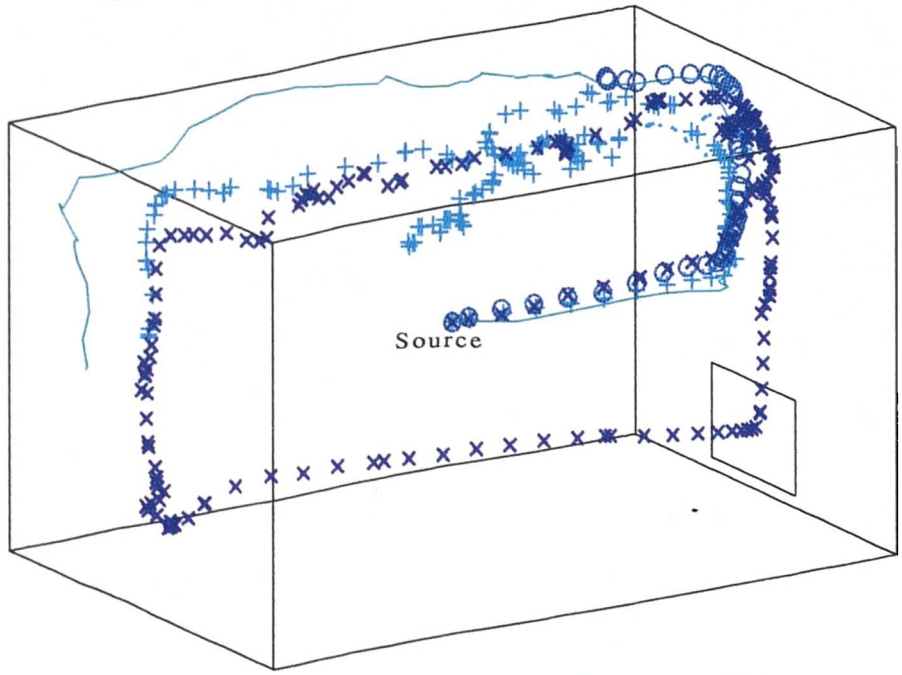

× 6μm o 7μm + 8μm • 9μm – 10μm

Figure 8.20b Five sample particle tracking in the room

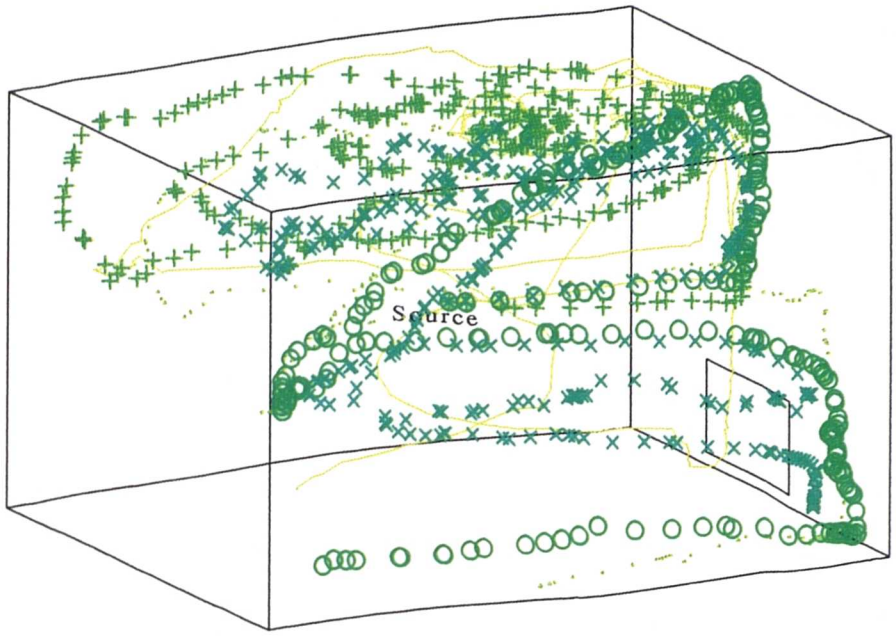

× 11μm o 12μm + 13μm • 14μm - 15μm

Figure 8.20c Five sample particle tracking routes in the room

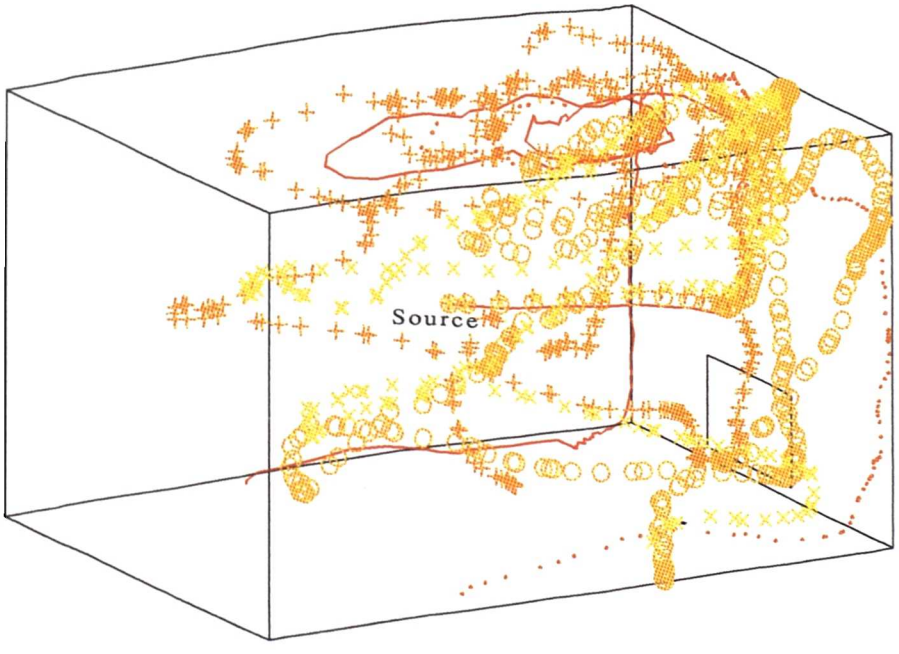

× 16μm o 17μm + 18μm • 19μm - 20μm

Figure 8.20d Five sample particle tracking routes in the room

§8.3 Conclusions

A CFD modelling of air and particle movement in a room heated by a radiator has been presented in this chapter. The following remarks emerge:

1. The predicted temperature results show good agreement with the measured data. The method used to estimate the heat source in the study is reasonable and acceptable.
2. The convective thermal boundary layer above the radiator entrains and heats the air from the surroundings and also induces the air circulation and temperature stratification in the room. Both velocity and temperature vary rapidly in the thermal boundary layer.
3. The thermal wall jet also entrains the particles from the source and then disperse them into the room space. The particle movement depends on the airflow pattern, the buoyancy influence and the particle properties. Small particles are likely to suspend in the upper warm zone or deposit on the high level of internal surfaces; while large particles travel through the room space and deposit on the floor level.
4. The area close to the heat source risks higher possibility of contamination and imposes harmful to the occupants in that area.
5. The numerical results also shows the possible method to improve the indoor air quality.

CHAPTER IX

GENERAL CONCLUSIONS AND SUGGESTIONS FOR FURTHER STUDY

§9.1 General Conclusions

The investigations of airflow patterns and aerosol particle movement and distribution in ventilated spaces (i.e., single- and two-zone room) are carried out using Computational Fluid Dynamics modelling. The studies are covering the significant parameters which indicate the indoor air quality and comfortable environment, e.g., particle concentration decay, mean velocity and temperature distribution. The validations of numerical results with the available experimental data are also presented. The following conclusions can be made:

1. It is concluded that the particle transport model can be used to predict the aerosol particle movement in a ventilated multi-zone area; the results produced captured the main features of particle motion and were satisfactory compared with measurements. This also suggests that certain aspects of the techniques applied in the research are satisfactory, in particular, the k-ε turbulence model, the differencing scheme and the mesh schemes.
2. The discretisation and implementation of the model are discussed and techniques regarding differencing, source term linearisation and the strategy of solution of the equations are described. Difficulties are often encountered concerning convergence of the calculations. Several factors influence the ability of simulations to obtain fully converged results. They are discussed and found to be strongly affected by the specific type of flow phenomenon. The optimisation of these factors can be achieved mainly by trial and error.

3. The first stage of application of a particle transport model is to predict a single particle deposition process within still air under the condition of different particle sizes. The results showed good agreement between the simulations and the theoretical results proposed by Stokes, Allen and Newton (see Chapter III) in three flow regimes. It can be concluded that the particle gravitational deposition is strongly influenced by the properties of the particle and the surrounding fluid. The terminal settling velocity of a particle is mainly dependent on the particle size. The gravitational force dominates the deposition process, especially in the acceleration periods. The drag force is proportional to the particle velocity and eventually arrives at a balance with the gravitational force when the particle velocity reaches its terminal value. Deposition is a fundamental phenomenon of particle motion.

4. A numerical analysis of airflow pattern, aerosol particle deposition and distribution in a mechanically ventilated one-zone room is performed in this project. The studies were carried out under different ventilation rate and different particle sizes. The results showed that the aerosol particle movement is greatly influenced by the airflow pattern and particle properties. Gravitational sedimentation dominates the large particle motion, i.e., large particles deposit rapidly due to gravity. Both airflow pattern and gravity affect the movement of small particles. Gravity becomes less important as the particle size decreases. Small particles are likely to remain suspended in the indoor air for longer time than large particles and strongly influence the indoor air quality. Increasing ventilation rate can enhance the removal of particles from the ventilated space but may increase the soiling phenomena of internal surfaces.

5. The effect of geometrical configuration and ventilation rates on the distribution deposition, migration and deposition of aerosol particles in a mechanically ventilated two-zone area has been investigated and reported in this thesis. It is concluded that the interzonal opening significantly affects the airflow patterns in the ventilated two-zone enclosure. Small interzonal openings produce a jet-like flow at low level in the downstream area. The agreements between the computational results and the experimental data of particle concentration decay profiles are generally satisfactory and acceptable, both airflow patterns and particle properties affect the particle movements. Their influences mainly related to the particle sizes. As above small particles remain suspended in the occupied zone longer than large particles and significantly affect the pollutant concentration level and the indoor air quality. The interzonal opening plays an important role in the particle migration phenomena, the period of massive particle migration reduces as the interzonal opening increases. The results also pointed out that the ventilation conditions do affect the average particle extraction, migration and deposition rates. In this study, these parameters increase with ventilation rate.

6. A CFD simulation of velocity and temperature fields in a room heated by a radiator is carried out in this study. The predicted temperature results show good agreement with the measured data. The convective thermal wall jet produced by the radiator entrains and heats the air from the surroundings and also induces the air circulation and temperature stratification in the room. A modelling of particle movement and distribution from a pollutant source in the room is also carried out in the simulation. The results show that the thermal wall jet flow also entrains the particles from the contaminant

source and disperse them into the room space. The area close to the heat source exposes occupants to a higher risk of air-borne pollution. The particle movement and distribution are mainly influenced by the airflow pattern, the particle properties and the buoyancy effect.

7. The results of this research provide valuable guidance which could be used in the design of building ventilation systems. For example,

   - high ventilation rates can enhance the particle extraction process;
   - particle removal from the air occurs mainly by deposition at low ventilation rates (< 2 air change per hour).

   Thus high ventilation rates ensure a high rate of particle removal from the air. When ventilation rates are low the majority of particles must be removed by cleaning the surfaces upon which they have been deposited.

§9.2 Suggestions for Further Study

The previous studies have shown that some of the CFD calculations of two- and three-dimensional flows produced reliable and promising results (§2.3). The study made in this thesis shows that it is also possible to obtain acceptable results of flow pattern and pollutant particle concentration and distribution in complicated, full-scale ventilated rooms if the CFD simulation is properly specified. This means that the CFD prediction can model the main features of flow and pollutant movement in ventilated areas. But the work in this thesis shows there are still areas which need further investigation, e.g., the diffusion and coagulation effects in particle motion, the heat and mass transfer between particles and fluids, the modelling of thermal boundary layers and heat source, the influence of low turbulent intensity, etc.

The following points are drawn out for future study:

1. The particle movement is affected by many factors, e.g., diffusion, coagulation, electrostatic force, etc., other than the gravitational and drag forces considered in this study. Little research has been done to quantify these factors in the prediction of particle movement. The situation restricts the capability and versatility of the particle transport model. More study is needed in this area.

2. The study in this thesis demonstrated that the knowledge of heat and mass transfer between particles and surrounding fluids is limited and more attention should be focused on this aspects.

3. The calculations performed in this research emphasised that the difficulty associated with the specification of boundary conditions is a major drawback of applying CFD for predicting both airflow patterns and particle motion in ventilated space, especially in buoyancy-affected flow. Improvements are required in this area to make the numerical model more accurate and reliable.

4. Low Reynolds phenomenon, i.e., low turbulent intensity, that arises from different heat sources, and occurs in ventilated spaces is an established fact. In order to be able to predict this effect some theoretical as well as experimental work is required in this are to provide a better understanding of the phenomenon.

5. Research on the type of particles found in buildings — analysis of their size distribution and other properties would help further research on particle pollution.

6. CFD models should be applied to various environmental control systems to assess their abilities to remove particles.

REFERENCES

Adam, N M, 1995

' Measurement of aerosol particles in buildings ', PhD Thesis, University of Nottingham, Nottingham, UK, 1995.

Adam, N M & Riffat, S B, 1993

' Flow of aerosol particles through large openings ', 14th AIVC Conference, Copenhagen, Denmark, 21~23 September, 1993.

Alamdari, F, Bennett, K M & Rose, P M, 1994

' Airflow and temperature distribution within an open-plan office building space using a displacement ventilation system ', Proc. of Roomvent'94: Air Distribution in Rooms, Fourth International Conference, Poland, Vol. 1, pp481~496, 1994.

Allard, F & Inard, C, 1992

' Natural and mixed convection in rooms. Prediction of thermal stratification and heat transfer by zonal models ', Int. Symppon Room Air Convection and Ventilation Effectiveness, University of Tokyo, July 22-24, 1992.

Armstrong, C W, Sherertz, P C & Liewellyn, G C, 1989

' Sick building syndrome traced to excessive total suspended particulates ', Proceedings IAQ 89 (international Air Quarterly), pp2~7, 1989.

Awbi, H B & Setrak, A A, 1986

' Numerical solution of ventilation air jet ', Pro. of the 5th Int. Symppon the Use of Computers for Environmental Engineering related to Buildings, pp236~246, Bath, UK, 1986.

Awbi, H B, 1989

' Application of Computational Fluid Dynamics in room ventilation ', Building and Environment, Vol. 24, No. 1, pp73~84, 1989.

Awbi, H B, 1992

' Ventilation of buildings ', E&FN SPON Company, 1992.

Baker, A J & Kelso, R M, 1990

' On validation of CFD procedures for room air motion prediction ', ASHRAE paper No. At-90-2-4, Vol. 96, pp760~774, 1990.

Batchelor, G K, 1967

' An Introduction: Fluid Dynamics ', Cambridge University Press, London and New York, 1967.

Béghein, C, Penot, F, Mergui, S & Allard, F, 1993

' Numerical and experimental evaluation of turbulent models for natural convection simulation in a thermally driven square cavity ', ASME paper, Winter Annual Meeting, New Orleans, Louisiana, Nov., 1993.

Brohus, H & Nielson, P V, 1994

' Contaminant distribution around persons in rooms ventilated by displacement venitlaiton ', Proc. of Roomvent'94: Air Distribution in Rooms, Fourth International Conference, Poland, Vol. 1, pp293~312, 1994.

Brown, W G & Solvason, K R, 1962

' Natural convection through rectangular opening in partitions, part 1: vertical partition ', International Journal of Heat & Mass Transfer, Vol. 5, pp859~868, 1962.

Buchmann, P, Ribéron, J, Millet, J R & Lauriat, G, 1994

' Numerical prediction of air flow patterns in large enclosures with supplied air jet system ', Proc. of Roomvent'94: Air Distribution in Rooms, Fourth International Conference, Poland, Vol. 1, pp467~480, 1994.

Byrne, M A, Lange, C, Goddard, A J H & Roed, J, 1993

' Indoor aerosol deposition measurements for exposure assessment calculations ', Proceedings of Indoor Air' 93, Vol. 3, pp415~419, 1993.

Casarett, L J, 1975

' Toxicology of the respiratory system ', In Toxicology: The basic science of poisons, Chap. 9, Macmillan, New York, 1975.

CFDS-FLOW3D Menu, AEA Harwell Laboratory, Didcot, UK, 1993

Chen, Q & J. van der Kooi, 1988

' ACCURACY - A program for combined problems of energy analysis, indoor airflow and air quality ', ASHRAE Trans. No. 94, part 2, 1988.

Chen, Q, Moser, A & Huber, A, 1990

'Prediction of buoyant, turbulent flow by a low-Reynolds-number k-ε model ', ASHRAE, Vol. 96, pt 2, pp564~573, 1990.

Chen, Q, Suter, P & Moser, A, 1991

' Influence of air supply parameters on indoor air diffusion ', Building and Environment, Vol. 26, No. 4, pp417~431, 1991.

Chen, Q, Moser, A & Suter, P, 1991

' Interpolation theory and influence of boundary conditions on room air diffusion ', Building and Environment, Vol. 26, No. 4, pp. 433~445, 1991.

Cheong, K W, Adam, N M & Riffat, S B, 1994

' Interzone particle movement ', CIBSE National Conference, Buxton, UK, Oct. 1994.

CIBSE Guide (1986)

Clift, R, Grace, J R & Weber, M E, 1978

' Bubbles, Drops and Particles ', Academic Press, Inc., London, 1978.

Crump, J G & Seinfeld, J H, 1983

Journal of Aerosol Science, Vol. 12, pp405~415, 1981

Crump, J G, Flagan, R C & Seinfeld, J H, 1983

' Particle wall loss rates in vessels ', Aerosol Science & Technology, Vol. 2, pp303~309, 1983.

Davidson, L, 1989

'Ventilation by displacement in a three-dimensional room - A numerical study', Building and Environment, Vol. 24, No. 4, pp363~372, 1989.

Emmerich, S J & Persily, A K, 1994

' Indoor air quality impacts of residential HVAC systems, Phase I report: computer simulation plan ', NISTIR 5346, Building & Fire Research Laboratory, Gaithersburg, MD 20899, 1994.

Fanger, P O, 1972

' Thermal comfort ', McGraw-Hill, New York, 1972.

Fanger, P O, Melikov, A K Hanzawa, H & Ring, J, 1988

' Air turbulence and sensation of draught ', Energy & Buildings, Vol. 12, pp21~39, 1988.

Fanger, P O, 1990

' New principles for a future ventilation standard ', Proc. 5th International Conference on Indoor Air Quality and Climate: Indoor Air'90, Vol. 5, pp353~363, Toronto: Indoor Air Technologies, D.S. Walkinshaw, ed., 1990.

Faulkner, D, Fish, W J & Sullivan, D, 1995

' Indoor airflow and pollutant removal in a room with floor-based task ventilation: results of additional experiments ', Building & Environment, Vol. 30, No. 3, pp303~332, 1995.

Fontaine, J R & Rapp, R, 1994

' Design of air supplt systems of workshops equipped with pollutant removal devices. A CFD approach ', Proc. of Roomvent'94: Air Distribution in Rooms, Fourth International Conference, Poland, Vol. 1, pp513~530, 1994.

Gosman, A D, Pun, W K, Runchal, A K, Spalding, D B & Wolfshtem M, 1969

' Heat and mass transfer in recirculating flow ', Academic Press, London, 1969.

Gosman, A D, Nielson, P V, Restivo, A, & Whitelaw, J H, 1980

' The flow properties of rooms with small ventilation openings ', J. Fluids Engineering, Vol. 102, pp316~323, 1980.

Haghighat, F, Jiang, Z & Wang, J, 1990

' Three-dimensional analysis of air flow pattern and contaminant dispersion in a ventilated two-zone enclosure ', ASHRAE Vol. 96, AT-90-5-1, 1990.

Haghighat, F, Jiang, Z & Wang, J, 1991

' A CFD analysis of ventilation effectiveness in a partitioned room ', Indoor Air, Vol. 4, pp606~615, 1991.

Hanzawa, H, Melikov, A K, & Fanger, P O, 1987

' Airflow characteristics in the occupied zone of ventilated spaces ', ASHRAE, Trans. Vol. 93, part 1, pp524~539, 1987.

Harlow, F H & Welch, J E, 1965

' Numerical calculation of time-dependent viscous incompressible flow of fluid with free surface ', Phys. Fluids, Vol. 8, pp2182, 1965.

Hinze, J O, 1975

' Turbulence ', Mcgrill-Hill Book Company, 1975.

Holmes, M J, 1982

' The application of fluid mechanics simulation program PHOENICS to a few typical HAVC problems ', Ove Arup Partnership, London, 1982.

Howarth, A T, 1980

' Temperature distribution and air movement in rooms heated with a convective heat source ', PhD. Thesis, UMIST, Manchester, 1980.

Howarth, A T, 1985

' The prediction of air temperature variations in naturally ventilated rooms with convective heating ', BSERT, Vol. 6, No. 4, pp169~175, 1985.

Ideriah, F J K, 1980

' Prediction of turbulent cavity flow driven by buoyancy and shear ', J. Mech. Engng. Sci., Vol. 22, pp287~295, 1980.

Ishizu, Y & Kaneki, K, 1984

' Evaluation of ventilation systems through numerical computation and presentation of a new ventilation model ', Trans. SHASE. No. 24, pp47, 1984.

J von der Kooi, Wan J W & Saurwalt, F W, 1993

' Prediction of airflow pattern and air quality in am operating room ', AIVC Paper No. 7225, CLIMA 2000 Conference, 1993.

Jacobsen, T V & Nielson, P V, 1994

' Investigation of airflow in a room with displacement ventilation by means of a CFD-model ', AIVC Paper No. 7486, 1994.

Jiang, Z, Haghighat, F & Wang, J C Y, 1992

' Thermal comfort and indoor air quality in a partitioned enclosure under mixed convection ', Building and Environment, Vol. 27, No. 1, pp77~84, 1992.

Jiang, Z, Haghighat, F & Chen, Q, 1995

' Buoyancy effects on air quality in a partitioned office with displacement ventilation ', Proc. " Indoor Air Quality, Ventilation and Energy Conservation in Buildings ", Second International Conference, Montreal, Vol. I, pp435~447, 1995.

Jones, P J & Reed, N, *1988*

' Air flow in large spaces ', PHOENICS Newsletter, No. 13, CHAM Ltd, April, 1988.

Jones, P J, 1990

'Room air distribution and ventilation effectiveness in air conditioned offices', Proc. 5th International Conference on Indoor Air Quality and Chinnock ToroTo Canada, Part 4, pp133~138, 1990.

Jones, P J & Whittle, G E, 1992

' Computational Fluid Dynamics for building air flow prediction — current ststus and capabilities ', Building and Environment, Vol. 27, No. 3, pp321~338, 1992.

Launder, B E & Spalding, D B, 1974

' The numerical computation of turbulent flows 'comput. Meth. Appl. Mech. Engng., Vol. 3, pp269~289, 1974.

Launder, B E & Shima, N, 1989

' Second-moment closure for the near-wall sublayer: development and application ', AIAA Vol. 27, No. 10, pp 1319~1325, 1989.

Lebrun, J & Marret, D, 1976

' Convection exchanges inside a dwelling room in winter ', International Seminar of ICHMT, Dubrovnik, Yugoslavia, September, 1976.

Li, Y, Holmberg, S, Paprocki, A & Tang, Y Q, 1993

' Simulation of room flows with small ventilation openings by a local grid-refinement technique ', BSER&T, Vol. 15, No. 1, pp1~10, 1993.

Lindvall, T, 1994

' The sick building syndrome — overview and frontiers ', AIVC paper, No. 7325, 1994.

Lippmann, M, 1972

' Respirable dust sampling in air sampling instruments for evaluation of atmospheric contaminants ', 4th edition. American Conference of Governmental Industrial Hygienists, 1972.

Mahajan, B M, 1987

' Measurement of interzonal heat and mass transfer by natural convection ', Solar Energy, Vol. 38, No. 6, pp437~446, 1987.

Markatos, N C, Malin, M R & Cox, G, 1982

' Mathematical modelling of buoyancy-induced smoke flow in enclosure ', Int. J. Heat & Mass Transfer, Vol. 25, pp63~75, 1982.

Markatos, N C & Pericleous, A K, 1984

' Laminar and turbulent natural convection in an enclosed cavity ', Int. J. Heat & Mass Transfer, Vol. 27, pp755~772, 1984.

McLaughlin, A, MacKnight,S, 1994

' Study of indoor air particulates, Grace Maternity Hospital, Canada ', AIVC Paper No. 8765, 1994

Moser, A, 1992

' Numerical simulation of room thermal convection , - Review of IEA Annex-20 results ', Int. Symppon Room Air Convection and Ventilation Effectiveness University of Tokyo, July 22-24, 1992.

Mulholland, G & Ohlemiller, T J, 1982

' Aerosol characterisation of a smouldering source ', Aerosol Science & Technology, Vol. 1, pp59~71, 1982.

Murakami, S, 1992

' New scales for ventilation efficiency and their application based on numerical simulation of room airflow ', International Symposium on Room Air Convection and Ventilation Effectiveness ' University of Tokyo, July 22-24, 1992.

Nazaroff, W W& Cass, G R, 1989

' Mathematical modelling of indoor aerosol dynamics', Environmental Science & Technology, Vol. 23, No. 2, pp157~166, 1989.

Nazaroff, W W, Ligocki, M P, Ma, T & Cass, G R, 1990

' Particle deposition in museums: comparison of modelling and measurement results ', Aerosol Science & Technology, Vol. 13, pp332~348, 1990.

Nielson, P V, 1974

' Moisture transfer in air conditioned rooms and cold stores ', Paper 1.2.1, Pro. 2nd Int. CIB/RILEM Symppon moisture problems in buildings, Rotterdam, 1974.

Nielson, P V, Restivo, A, & Whitelaw, J H, 1978

' The velocity characteristics of ventilated room ', Trans. ASME. J. of Fluids Engineering, Vol. 100, pp291~298, 1978.

Nielson P V, Restivo, A, & Whitelaw, J H, 1979

' Buoyancy affected flows in ventilated rooms ', Num. Heat Transfer, Vol. 2, pp115, 1979.

Nielson, P V & Möller, A T A, 1985

' Measurement of the three-dimensional wall jet from different types of air diffuser ', Porc. CLIMA 2000, p383, 1985.

Nielson, P V, & Möller, A T A, 1987

' Measurements on buoyant wall jet flows in air-conditioned rooms ', Roomvent'87, International Conference on Air Distribution in Ventilated Spaces, Stockholm, 1987.

Nielson, P V, 1988

' Selection of air terminal device ', IEA annex 20, ISSN 0902-7515 R8838, 1988.

Owen, M K, Ensor, D S & Sparks, L E, 1992

' Airborne particle sizes and sources found in indoor air ', Atmospheric Environment, Vol. 26, No. 12, pp2149~2162, 1992.

Patankar, S V & Spalding, D B, 1972

' A calculation procedure for heat, mass and momentum transfer in three-dimensional parabolic flows ', Int. J. Heat & mass transfer, Vol. 15, pp1787, 1972.

Patankar, S V, 1980

' Numerical heat transfer and fluid flow ', MaGraw-Hill Publisher, 1980.

Rajaratnam, N, 1976

' Turbulent jets ', Elsevier Scientific Publishing Company, Amsterdam, 1976.

Raw, G J, 1994

' The importance of indoor surface pollution in sick building syndrome ', AIVC Paper No. 8750, 1994.

Reinartz, A & Renz, U, 1984

' Calculation of the temperature and flow field in a room ventilation by a radial air distribution ', Int. J. Refrigeration Vol. 7, pp308~312, 1984.

Riffat, S B, Cheong, K W & Adam, N, 1994

' Evaluation of aerosol-particle flow in a two-zone environmental chamber ', Proceedings of the 4th International Symposium on Ventilation for Contaminant Control, Ventilation' 94, Stockholm, September, 1994.

Rodi, W, 1980

' Turbulence models and their applications in Hydraulics — a state of the art review ', Inst. für Hydromechanik, Univ. of Karlsruhe, Germany, 1980.

Schneider, T, 1991

' Indoor aerosols: measurement and analysis ', J. of Aerosol Science, Vol. 22, Suppl.1, pp5817~5822, 1991.

Schneider, T, 1994

' Particulates in indoor air ', AIVC paper No. 7309, 1994.

Scott, D, Anderson, R & Figliola, R, 1988

' Blockage of natural convection boundary layer flow in a multizone enclosure ', Int. J. Heat & Fluid Flow, Vol. 9, No. 2, June, 1988.

Sforza, P M & Herbst, G A, 1970

' A study of three-dimensional, incompressible, turbulent wall jets ', AIAA Journal, Vol. 8, p276~283, 1970.

Shaw, B H, 1972

' Heat and mass transfer by natural convection and combined natural and forced air flow through large rectangular openings in vertical partition ', Proc. Int. Mech. Eng. Conf. on Heat & Mass Transfer by combined forced & natural convection, Manchester, Vol. 1, pp819, 1972.

Spalding, D B, 1982

' Mathematical modelling of fluid mechanics, heat transfer and chemical reaction processes ', CFDU Report No. HTS/80/1, Imperial College, London, 1982.

Svidt, K, 1993

' Numerical prediction of buoyant air flow in livestock buildings ', AIVC paper No. 7487, 1993.

Thorshauge, T, 1982

' Air velocity fluctuations in the occupied zone of ventilated space ', AHSRAE Trans. Vol. 88, part 2, pp753~764, 1982.

Timmons, M B, Albright, L D, Furry, R B & Torrance, K E, 1980

'Experimental and numerical study of air movement in slot ventilation enclosures', ASHRAE Trans. pp221~240, 1980.

Turner, J S, 1973

' Buoyancy effects in fluids ', Cambridge University Press, 1973.

Wallin, O, 1994

' Computer simulation of particle deposition in ventilating duct systems ', Final report for BFR project, Building Services Engineering, Royal Institute of Techonology, Stockholm, Sweden, 1994.

Walkinshaw, D S, 1994

' Designing buildings for improved indoor air quality: ventilation system and contaminant migration ', AIVC paper No. 7291, 1994.

Walsh, P J, Dudney, C S & Copenhaver, E D, 1984

' Indoor air quality ', CRC Press, Boca Raton, FL, 1984.

Warsi, Z U A, 1993

' Fluid Dynamics — Theoretical and computational approaches ', CRC Press, Inc., 1993.

Webber, D D & Kearney, R J, 1980

' Natural convection heat transfer through an aperture in passive solar heated building ', Proc. 5th Nat. Passive Solar Conf., Amherst, MA, October, pp19~26, 1980.

Whittle, G E, 1987

' Numerical air flow modelling ', BSRIA Tech. Note TN 2/8, UK, 1987.

Van Doormal, J P & Raithby, G D, 1984

' Enhancements of the SIMPLE method for predicting incompressible fluid flows ', J. of Numerical Heat Transfer, Vol. 7, pp147~163, 1984.

Vazquea, B, Samano, D & Yianneskis, M, 1993

' Ventilation of an auditorium and its effect on wall heat transfer ', AIVC Paper No. 7224, CLIMA Conference, 1993.

Xu, M, Nematollahi, M, Sextro, R G, Gadgil, A J & Nazaroff, W W, 1994

' Deposition of tobacco smoke particles in a low ventilation room ', Aerosol Science & Technology, Vol. 20, pp194~206, 1994.

PUBLICATIONS BY AUTHOR

Lu, W & Howarth, A T

' Indoor aerosol particle deposition and distribution: Numerical analysis for a one-zone ventilation system ', BSER & T, Vol. 16, No. 3, 1995.

Lu, W & Howarth, A T

' Numerical analysis of indoor aerosol particle deposition and distribution in two-zone ventilation system ', To be published on Building & Environment, Vol. 31, No. 1, 1996.

Lu, W, Howarth, A T, Adam, N & Riffat, S B

' CFD analysis of aerosol particle distribution and air movement in ventilated two-zone room and comparison with experimental results ', Submitted to ASHRAE Journal.

Lu, W, Howarth, A T, Adam, N & Riffat, S B

' Modelling and measurement of airflow and aerosol particle distribution in a ventilated two-zone chamber ', Accepted by Building & Environment Journal.

Howarth, A T & Lu, W

' Modelling of aerosol particle distribution in ventilated room ', to be presented at Aerosol Society Conference, Imperial College, November, 1995.

APPENDIX A NUMERICAL RESULTS OF SINGLE PARTICLE SETTLING PROCESSES

One lead particle falling in stagnant air, particle tracking data

Particle No.1 Diameter=1.000E-06 m Mass=5.236E-15 kg

T(s)	X(m)	Y(m)	Z(m)	U(m/s)	V(m/s)	W(m/s)
0.00E+00	2.00E+00	2.75E+00	1.50E+00	0.00E+00	0.00E+00	0.00E+00
1.10E+02	2.00E+00	2.72E+00	1.50E+00	5.22E-08	-3.01E-04	-1.12E-07
1.66E+02	2.00E+00	2.70E+00	1.50E+00	6.27E-08	-3.01E-04	-1.34E-07
4.98E+02	2.00E+00	2.60E+00	1.50E+00	1.02E-07	-3.01E-04	-2.64E-07
8.30E+02	2.00E+00	2.50E+00	1.50E+00	8.91E-08	-3.01E-04	-2.61E-07
1.16E+03	2.00E+00	2.40E+00	1.50E+00	6.57E-08	-3.01E-04	-2.06E-07
1.49E+03	2.00E+00	2.30E+00	1.50E+00	4.38E-08	-3.01E-04	-1.56E-07
1.82E+03	2.00E+00	2.20E+00	1.50E+00	2.41E-08	-3.01E-04	-1.17E-07
2.16E+03	2.00E+00	2.10E+00	1.50E+00	5.93E-09	-3.01E-04	-8.54E-08
2.49E+03	2.00E+00	2.00E+00	1.50E+00	-1.25E-08	-3.01E-04	-5.99E-08
2.82E+03	2.00E+00	1.90E+00	1.50E+00	-3.36E-08	-3.01E-04	-3.71E-08
3.15E+03	2.00E+00	1.80E+00	1.50E+00	-6.11E-08	-3.01E-04	-1.46E-08
3.48E+03	2.00E+00	1.70E+00	1.50E+00	-1.00E-07	-3.01E-04	1.07E-08
3.81E+03	2.00E+00	1.60E+00	1.50E+00	-1.56E-07	-3.01E-04	4.12E-08
4.00E+03	2.00E+00	1.54E+00	1.50E+00	-1.86E-07	-3.01E-04	5.83E-08
4.14E+03	2.00E+00	1.50E+00	1.50E+00	-2.08E-07	-3.01E-04	7.11E-08
4.47E+03	2.00E+00	1.40E+00	1.50E+00	-2.27E-07	-3.01E-04	9.33E-08
4.80E+03	2.00E+00	1.30E+00	1.50E+00	-1.46E-07	-3.01E-04	6.46E-08
5.13E+03	2.00E+00	1.20E+00	1.50E+00	-1.90E-08	-3.01E-04	-1.50E-09
5.46E+03	2.00E+00	1.10E+00	1.50E+00	2.33E-08	-3.01E-04	-1.96E-08
5.80E+03	2.00E+00	1.00E+00	1.50E+00	1.51E-08	-3.01E-04	5.02E-10
6.13E+03	2.00E+00	9.00E-01	1.50E+00	1.10E-08	-3.01E-04	1.77E-08
6.46E+03	2.00E+00	8.00E-01	1.50E+00	1.28E-08	-3.01E-04	3.09E-08
6.79E+03	2.00E+00	7.00E-01	1.50E+00	1.75E-08	-3.01E-04	4.36E-08
7.12E+03	2.00E+00	6.00E-01	1.50E+00	2.42E-08	-3.01E-04	5.76E-08
7.45E+03	2.00E+00	5.00E-01	1.50E+00	3.29E-08	-3.01E-04	7.45E-08
7.78E+03	2.00E+00	4.00E-01	1.50E+00	4.44E-08	-3.01E-04	9.62E-08
8.11E+03	2.00E+00	3.00E-01	1.50E+00	5.93E-08	-3.01E-04	1.24E-07
8.44E+03	2.00E+00	2.00E-01	1.50E+00	7.80E-08	-3.01E-04	1.59E-07
8.78E+03	2.00E+00	1.00E-01	1.50E+00	9.78E-08	-3.01E-04	1.96E-07
9.11E+03	2.00E+00	0.00E+00	1.50E+00	8.97E-12	-3.01E-04	1.80E-11
9.11E+03	2.00E+00	0.00E+00	1.50E+00	2.99E-12	-1.40E-05	6.01E-12
9.11E+03	2.00E+00	0.00E+00	1.50E+00	1.85E-15	-2.01E-07	3.43E-15

One lead particle falling in stagnant air, particle tacking data

Particle No.1 Diameter=5.000E-06 m Mass=6.545E-13 kg

T(s)	X(m)	Y(m)	Z(m)	U(m/s)	V(m/s)	W(m/s)
0.00E+00	2.00E+00	2.75E+00	1.50E+00	0.00E+00	0.00E+00	0.00E+00
6.67E+00	2.00E+00	2.70E+00	1.50E+00	4.10E-07	-7.51E-03	-5.06E-07
1.60E+01	2.00E+00	2.63E+00	1.50E+00	5.77E-07	-7.51E-03	-9.25E-07
2.00E+01	2.00E+00	2.60E+00	1.50E+00	6.46E-07	-7.51E-03	-1.10E-06
3.33E+01	2.00E+00	2.50E+00	1.50E+00	5.14E-07	-7.51E-03	-1.25E-06
4.66E+01	2.00E+00	2.40E+00	1.50E+00	3.65E-07	-7.51E-03	-1.13E-06
6.00E+01	2.00E+00	2.30E+00	1.50E+00	2.89E-07	-7.51E-03	-9.29E-07
7.33E+01	2.00E+00	2.20E+00	1.50E+00	2.50E-07	-7.51E-03	-7.25E-07
8.66E+01	2.00E+00	2.10E+00	1.50E+00	2.18E-07	-7.51E-03	-5.58E-07
9.99E+01	2.00E+00	2.00E+00	1.50E+00	1.85E-07	-7.51E-03	-4.32E-07
1.13E+02	2.00E+00	1.90E+00	1.50E+00	1.55E-07	-7.51E-03	-3.37E-07
1.27E+02	2.00E+00	1.80E+00	1.50E+00	1.29E-07	-7.51E-03	-2.62E-07
1.40E+02	2.00E+00	1.70E+00	1.50E+00	1.06E-07	-7.51E-03	-2.03E-07
1.53E+02	2.00E+00	1.60E+00	1.50E+00	8.68E-08	-7.51E-03	-1.53E-07
1.66E+02	2.00E+00	1.50E+00	1.50E+00	6.98E-08	-7.51E-03	-1.11E-07
1.80E+02	2.00E+00	1.40E+00	1.50E+00	5.59E-08	-7.51E-03	-7.52E-08
1.93E+02	2.00E+00	1.30E+00	1.50E+00	4.59E-08	-7.51E-03	-4.35E-08
2.06E+02	2.00E+00	1.20E+00	1.50E+00	4.15E-08	-7.51E-03	-1.62E-08
2.20E+02	2.00E+00	1.10E+00	1.50E+00	4.69E-08	-7.51E-03	5.18E-09
2.33E+02	2.00E+00	1.00E+00	1.50E+00	6.99E-08	-7.51E-03	1.68E-08
2.46E+02	2.00E+00	9.00E-01	1.50E+00	1.26E-07	-7.51E-03	1.01E-08
2.60E+02	2.00E+00	8.00E-01	1.50E+00	2.49E-07	-7.51E-03	-3.49E-08
2.73E+02	2.00E+00	7.00E-01	1.50E+00	5.39E-07	-7.51E-03	-1.73E-07
2.86E+02	2.00E+00	6.00E-01	1.50E+00	8.98E-07	-7.51E-03	-3.40E-07
3.00E+02	2.00E+00	5.00E-01	1.50E+00	-2.73E-07	-7.51E-03	4.50E-07
3.13E+02	2.00E+00	4.00E-01	1.50E+00	-1.73E-06	-7.51E-03	1.61E-06
3.26E+02	2.00E+00	3.00E-01	1.50E+00	-1.35E-06	-7.51E-03	1.61E-06
3.40E+02	2.00E+00	2.00E-01	1.50E+00	-7.55E-07	-7.51E-03	1.34E-06
3.53E+02	2.00E+00	1.00E-01	1.50E+00	-6.57E-07	-7.51E-03	1.45E-06
3.66E+02	2.00E+00	0.00E+00	1.50E+00	-1.39E-10	-7.51E-03	3.06E-10
3.66E+02	2.00E+00	0.00E+00	1.50E+00	-4.97E-11	-3.38E-04	1.10E-10

One lead particle falling in stagnant air, particle tracking data

Particle No.1 Diameter=8.000E-06 m Mass=2.681E-12 kg

T(s)	X(m)	Y(m)	Z(m)	U(m/s)	V(m/s)	W(m/s)
0.00E+00	2.00E+00	2.75E+00	1.50E+00	0.00E+00	0.00E+00	0.00E+00
2.62E+00	2.00E+00	2.70E+00	1.50E+00	4.17E-07	-1.91E-02	-2.59E-07
7.84E+00	2.00E+00	2.60E+00	1.50E+00	7.04E-07	-1.91E-02	-4.83E-07
1.31E+01	2.00E+00	2.50E+00	1.50E+00	6.24E-07	-1.91E-02	-4.29E-07
1.83E+01	2.00E+00	2.40E+00	1.50E+00	4.71E-07	-1.91E-02	-3.08E-07
2.35E+01	2.00E+00	2.30E+00	1.50E+00	3.56E-07	-1.91E-02	-2.14E-07
2.87E+01	2.00E+00	2.20E+00	1.50E+00	2.75E-07	-1.91E-02	-1.47E-07
3.40E+01	2.00E+00	2.10E+00	1.50E+00	2.17E-07	-1.91E-02	-1.01E-07
3.66E+01	2.00E+00	2.05E+00	1.50E+00	1.96E-07	-1.91E-02	-8.53E-08
3.92E+01	2.00E+00	2.00E+00	1.50E+00	1.74E-07	-1.91E-02	-6.92E-08
4.44E+01	2.00E+00	1.90E+00	1.50E+00	1.39E-07	-1.91E-02	-4.67E-08
4.97E+01	2.00E+00	1.80E+00	1.50E+00	1.10E-07	-1.91E-02	-3.10E-08
5.49E+01	2.00E+00	1.70E+00	1.50E+00	8.55E-08	-1.91E-02	-2.03E-08
6.01E+01	2.00E+00	1.60E+00	1.50E+00	6.32E-08	-1.91E-02	-1.31E-08
6.53E+01	2.00E+00	1.50E+00	1.50E+00	4.24E-08	-1.91E-02	-8.45E-09
7.06E+01	2.00E+00	1.40E+00	1.50E+00	2.26E-08	-1.91E-02	-5.33E-09
7.58E+01	2.00E+00	1.30E+00	1.50E+00	3.12E-09	-1.91E-02	-2.92E-09
8.10E+01	2.00E+00	1.20E+00	1.50E+00	-1.65E-08	-1.91E-02	-4.35E-10
8.62E+01	2.00E+00	1.10E+00	1.50E+00	-3.67E-08	-1.91E-02	2.94E-09
9.14E+01	2.00E+00	1.00E+00	1.50E+00	-5.82E-08	-1.91E-02	8.07E-09
9.67E+01	2.00E+00	9.00E-01	1.50E+00	-8.17E-08	-1.91E-02	1.59E-08
1.02E+02	2.00E+00	8.00E-01	1.50E+00	-1.08E-07	-1.91E-02	2.77E-08
1.07E+02	2.00E+00	7.00E-01	1.50E+00	-1.39E-07	-1.91E-02	4.49E-08
1.12E+02	2.00E+00	6.00E-01	1.50E+00	-1.77E-07	-1.91E-02	6.94E-08
1.16E+02	2.00E+00	5.33E-01	1.50E+00	-2.09E-07	-1.91E-02	9.26E-08
1.18E+02	2.00E+00	5.00E-01	1.50E+00	-2.25E-07	-1.91E-02	1.04E-07
1.23E+02	2.00E+00	4.00E-01	1.50E+00	-2.90E-07	-1.91E-02	1.54E-07
1.28E+02	2.00E+00	3.00E-01	1.50E+00	-3.79E-07	-1.91E-02	2.24E-07
1.33E+02	2.00E+00	2.00E-01	1.50E+00	-5.00E-07	-1.91E-02	3.20E-07
1.38E+02	2.00E+00	1.00E-01	1.50E+00	-6.52E-07	-1.91E-02	4.38E-07
1.44E+02	2.00E+00	0.00E+00	1.50E+00	-3.60E-10	-1.91E-02	2.42E-10
1.44E+02	2.00E+00	0.00E+00	1.50E+00	-1.39E-10	-8.48E-03	9.32E-11
1.44E+02	2.00E+00	0.00E+00	1.50E+00	-2.03E-12	-5.24E-05	1.06E-13

One lead particle falling in stagnant air, particle tracking data

Particle No.1 Diameter=1.000E-05 m Mass=5.236E-12 kg

T(s)	X(m)	Y(m)	Z(m)	U(m/s)	V(m/s)	W(m/s)
0.00E+00	2.00E+00	2.75E+00	1.50E+00	0.00E+00	0.00E+00	0.00E+00
1.68E+00	2.00E+00	2.70E+00	1.50E+00	5.21E-07	-2.98E-02	-3.23E-07
5.04E+00	2.00E+00	2.60E+00	1.50E+00	8.80E-07	-2.98E-02	-6.05E-07
8.40E+00	2.00E+00	2.50E+00	1.50E+00	7.80E-07	-2.98E-02	-5.37E-07
1.18E+01	2.00E+00	2.40E+00	1.50E+00	5.90E-07	-2.98E-02	-3.85E-07
1.51E+01	2.00E+00	2.30E+00	1.50E+00	4.46E-07	-2.98E-02	-2.67E-07
1.85E+01	2.00E+00	2.20E+00	1.50E+00	3.46E-07	-2.98E-02	-1.85E-07
2.18E+01	2.00E+00	2.10E+00	1.50E+00	2.73E-07	-2.98E-02	-1.28E-07
2.52E+01	2.00E+00	2.00E+00	1.50E+00	2.19E-07	-2.98E-02	-8.73E-08
2.85E+01	2.00E+00	1.90E+00	1.50E+00	1.76E-07	-2.98E-02	-5.91E-08
3.19E+01	2.00E+00	1.80E+00	1.50E+00	1.40E-07	-2.98E-02	-3.96E-08
3.53E+01	2.00E+00	1.70E+00	1.50E+00	1.09E-07	-2.98E-02	-2.62E-08
3.86E+01	2.00E+00	1.60E+00	1.50E+00	8.08E-08	-2.98E-02	-1.72E-08
4.20E+01	2.00E+00	1.50E+00	1.50E+00	5.49E-08	-2.98E-02	-1.14E-08
4.53E+01	2.00E+00	1.40E+00	1.50E+00	3.01E-08	-2.98E-02	-7.50E-09
4.87E+01	2.00E+00	1.30E+00	1.50E+00	5.68E-09	-2.98E-02	-4.50E-09
5.20E+01	2.00E+00	1.20E+00	1.50E+00	-1.89E-08	-2.98E-02	-1.40E-09
5.54E+01	2.00E+00	1.10E+00	1.50E+00	-4.43E-08	-2.98E-02	2.81E-09
5.88E+01	2.00E+00	1.00E+00	1.50E+00	-7.13E-08	-2.98E-02	9.25E-09
6.21E+01	2.00E+00	9.00E-01	1.50E+00	-1.01E-07	-2.98E-02	1.91E-08
6.55E+01	2.00E+00	8.00E-01	1.50E+00	-1.34E-07	-2.98E-02	3.39E-08
6.88E+01	2.00E+00	7.00E-01	1.50E+00	-1.73E-07	-2.98E-02	5.55E-08
7.22E+01	2.00E+00	6.00E-01	1.50E+00	-2.21E-07	-2.98E-02	8.65E-08
7.55E+01	2.00E+00	5.00E-01	1.50E+00	-2.82E-07	-2.98E-02	1.31E-07
7.89E+01	2.00E+00	4.00E-01	1.50E+00	-3.63E-07	-2.98E-02	1.93E-07
8.23E+01	2.00E+00	3.00E-01	1.50E+00	-4.76E-07	-2.98E-02	2.82E-07
8.56E+01	2.00E+00	2.00E-01	1.50E+00	-6.28E-07	-2.98E-02	4.02E-07
8.90E+01	2.00E+00	1.00E-01	1.50E+00	-8.21E-07	-2.98E-02	5.51E-07
9.23E+01	2.00E+00	0.00E+00	1.50E+00	-7.62E-10	-2.98E-02	5.12E-10
9.23E+01	2.00E+00	0.00E+00	1.50E+00	-3.12E-10	-1.29E-02	2.10E-10
9.23E+01	2.00E+00	0.00E+00	1.50E+00	-1.05E-11	-6.57E-03	3.14E-11
9.23E+01	2.00E+00	0.00E+00	1.50E+00	-2.12E-13	-2.02E-05	2.09E-13

One lead aprticle falling in stagnant air, particle tracking data

Particle No.1 Diameter=2.000E-05 m Mass=4.189E-11 kg

T(s)	X(m)	Y(m)	Z(m)	U(m/s)	V(m/s)	W(m/s)
0.00E+00	2.00E+00	2.75E+00	1.50E+00	0.00E+00	0.00E+00	0.00E+00
4.44E-01	2.00E+00	2.70E+00	1.50E+00	1.05E-06	-1.16E-01	-6.41E-07
1.31E+00	2.00E+00	2.60E+00	1.50E+00	1.79E-06	-1.16E-01	-1.20E-06
2.18E+00	2.00E+00	2.50E+00	1.50E+00	1.62E-06	-1.16E-01	-1.07E-06
3.04E+00	2.00E+00	2.40E+00	1.50E+00	1.25E-06	-1.16E-01	-7.58E-07
3.91E+00	2.00E+00	2.30E+00	1.50E+00	9.79E-07	-1.16E-01	-5.19E-07
4.77E+00	2.00E+00	2.20E+00	1.50E+00	7.89E-07	-1.16E-01	-3.52E-07
5.64E+00	2.00E+00	2.10E+00	1.50E+00	6.58E-07	-1.16E-01	-2.40E-07
6.50E+00	2.00E+00	2.00E+00	1.50E+00	5.66E-07	-1.16E-01	-1.67E-07
7.37E+00	2.00E+00	1.90E+00	1.50E+00	4.99E-07	-1.16E-01	-1.23E-07
8.23E+00	2.00E+00	1.80E+00	1.50E+00	4.53E-07	-1.16E-01	-1.04E-07
9.10E+00	2.00E+00	1.70E+00	1.50E+00	4.25E-07	-1.16E-01	-1.07E-07
9.97E+00	2.00E+00	1.60E+00	1.50E+00	4.16E-07	-1.16E-01	-1.31E-07
1.08E+01	2.00E+00	1.50E+00	1.50E+00	4.31E-07	-1.16E-01	-1.80E-07
1.17E+01	2.00E+00	1.40E+00	1.50E+00	4.80E-07	-1.16E-01	-2.60E-07
1.26E+01	2.00E+00	1.30E+00	1.50E+00	5.86E-07	-1.16E-01	-3.84E-07
1.34E+01	2.00E+00	1.20E+00	1.50E+00	7.87E-07	-1.16E-01	-5.81E-07
1.43E+01	2.00E+00	1.10E+00	1.50E+00	1.17E-06	-1.16E-01	-9.09E-07
1.52E+01	2.00E+00	1.00E+00	1.50E+00	1.90E-06	-1.16E-01	-1.48E-06
1.60E+01	2.00E+00	9.00E-01	1.50E+00	3.34E-06	-1.16E-01	-2.54E-06
1.63E+01	2.00E+00	8.69E-01	1.50E+00	4.46E-06	-1.16E-01	-3.30E-06
1.69E+01	2.00E+00	8.00E-01	1.50E+00	7.03E-06	-1.16E-01	-5.04E-06
1.78E+01	2.00E+00	7.00E-01	1.50E+00	1.63E-05	-1.16E-01	-1.11E-05
1.86E+01	2.00E+00	6.00E-01	1.50E+00	7.16E-06	-1.16E-01	-6.21E-06
1.95E+01	2.00E+00	5.00E-01	1.50E+00	-1.44E-05	-1.16E-01	8.76E-06
2.03E+01	2.00E+00	4.00E-01	1.50E+00	-1.52E-05	-1.16E-01	1.11E-05
2.09E+01	2.00E+00	3.39E-01	1.50E+00	-1.08E-05	-1.16E-01	7.96E-06
2.12E+01	2.00E+00	3.00E-01	1.50E+00	-7.92E-06	-1.16E-01	5.84E-06
2.21E+01	2.00E+00	2.00E-01	1.50E+00	-4.92E-06	-1.16E-01	3.57E-06
2.29E+01	2.00E+00	1.00E-01	1.50E+00	-3.41E-06	-1.16E-01	2.47E-06
2.38E+01	2.00E+00	0.00E+00	1.50E+00	-4.62E-08	-1.16E-01	3.35E-08
2.38E+01	2.00E+00	0.00E+00	1.50E+00	-1.94E-08	-4.96E-02	1.41E-08
2.38E+01	2.00E+00	0.00E+00	1.50E+00	-1.25E-08	-2.56E-03	9.08E-09
2.38E+01	2.00E+00	0.00E+00	1.50E+00	-9.83E-10	-1.41E-04	7.13E-10
2.38E+01	2.00E+00	0.00E+00	1.50E+00	-8.55E-12	-8.28E-06	6.21E-12

One lead particle falling in stagnant air, particle tracking data

Particle No.1 Diameter=3.000E-05 m Mass=1.414E-10 kg

T(s)	X(m)	Y(m)	Z(m)	U(m/s)	V(m/s)	W(m/s)
0.00E+00	2.00E+00	2.75E+00	1.50E+00	0.00E+00	0.00E+00	0.00E+00
2.26E-01	2.00E+00	2.70E+00	1.50E+00	1.53E-06	-2.48E-01	-9.46E-07
6.30E-01	2.00E+00	2.60E+00	1.50E+00	2.68E-06	-2.48E-01	-1.83E-06
1.03E+00	2.00E+00	2.50E+00	1.50E+00	2.46E-06	-2.48E-01	-1.69E-06
1.44E+00	2.00E+00	2.40E+00	1.50E+00	1.90E-06	-2.48E-01	-1.23E-06
1.84E+00	2.00E+00	2.30E+00	1.50E+00	1.45E-06	-2.48E-01	-8.66E-07
2.24E+00	2.00E+00	2.20E+00	1.50E+00	1.13E-06	-2.48E-01	-6.07E-07
2.65E+00	2.00E+00	2.10E+00	1.50E+00	9.10E-07	-2.48E-01	-4.26E-07
3.05E+00	2.00E+00	2.00E+00	1.50E+00	7.41E-07	-2.48E-01	-3.00E-07
3.46E+00	2.00E+00	1.90E+00	1.50E+00	6.08E-07	-2.48E-01	-2.12E-07
3.86E+00	2.00E+00	1.80E+00	1.50E+00	4.98E-07	-2.48E-01	-1.50E-07
4.26E+00	2.00E+00	1.70E+00	1.50E+00	4.02E-07	-2.48E-01	-1.08E-07
4.67E+00	2.00E+00	1.60E+00	1.50E+00	3.17E-07	-2.48E-01	-8.08E-08
5.07E+00	2.00E+00	1.50E+00	1.50E+00	2.37E-07	-2.48E-01	-6.31E-08
5.47E+00	2.00E+00	1.40E+00	1.50E+00	1.60E-07	-2.48E-01	-5.18E-08
5.88E+00	2.00E+00	1.30E+00	1.50E+00	8.36E-08	-2.48E-01	-4.35E-08
6.28E+00	2.00E+00	1.20E+00	1.50E+00	6.27E-09	-2.48E-01	-3.51E-08
6.68E+00	2.00E+00	1.10E+00	1.50E+00	-7.44E-08	-2.48E-01	-2.32E-08
7.09E+00	2.00E+00	1.00E+00	1.50E+00	-1.61E-07	-2.48E-01	-4.10E-09
7.49E+00	2.00E+00	9.00E-01	1.50E+00	-2.57E-07	-2.48E-01	2.66E-08
7.89E+00	2.00E+00	8.00E-01	1.50E+00	-3.67E-07	-2.48E-01	7.40E-08
8.30E+00	2.00E+00	7.00E-01	1.50E+00	-4.97E-07	-2.48E-01	1.45E-07
8.70E+00	2.00E+00	6.00E-01	1.50E+00	-6.59E-07	-2.48E-01	2.48E-07
9.10E+00	2.00E+00	5.00E-01	1.50E+00	-8.66E-07	-2.48E-01	3.97E-07
9.51E+00	2.00E+00	4.00E-01	1.50E+00	-1.15E-06	-2.48E-01	6.10E-07
9.91E+00	2.00E+00	3.00E-01	1.50E+00	-1.53E-06	-2.48E-01	9.13E-07
1.03E+01	2.00E+00	2.00E-01	1.50E+00	-2.06E-06	-2.48E-01	1.33E-06
1.07E+01	2.00E+00	1.00E-01	1.50E+00	-2.73E-06	-2.48E-01	1.84E-06
1.11E+01	2.00E+00	0.00E+00	1.50E+00	-1.74E-07	-2.48E-01	1.18E-07
1.11E+01	2.00E+00	0.00E+00	1.50E+00	-7.48E-08	-1.07E-01	5.05E-08
1.12E+01	2.00E+00	0.00E+00	1.50E+00	-4.87E-08	-5.56E-02	3.29E-08
1.12E+01	2.00E+00	0.00E+00	1.50E+00	-3.84E-09	-3.11E-03	2.60E-09
1.12E+01	2.00E+00	0.00E+00	1.50E+00	-3.37E-10	-1.71E-04	2.28E-10
1.12E+01	2.00E+00	0.00E+00	1.50E+00	-3.13E-11	-9.38E-05	2.12E-12
1.12E+01	2.00E+00	0.00E+00	1.50E+00	-3.01E-13	-4.60E-07	2.04E-13
1.12E+01	2.00E+00	0.00E+00	1.50E+00	-2.94E-15	-3.52E-08	1.99E-15

One lead particle falling in stagnant air, particle tracking data

Particle No.1 Diameter=5.000E-05 m Mass=6.545E-10 kg

T(s)	X(m)	Y(m)	Z(m)	U(m/s)	V(m/s)	W(m/s)
0.00E+00	2.00E+00	2.75E+00	1.50E+00	0.00E+00	0.00E+00	0.00E+00
1.35E-01	2.00E+00	2.70E+00	1.50E+00	2.02E-06	-5.49E-01	-1.25E-06
3.05E-01	2.00E+00	2.60E+00	1.50E+00	4.22E-06	-6.02E-01	-2.81E-06
4.71E-01	2.00E+00	2.50E+00	1.50E+00	4.58E-06	-6.05E-01	-3.11E-06
6.36E-01	2.00E+00	2.40E+00	1.50E+00	3.78E-06	-6.05E-01	-2.49E-06
8.01E-01	2.00E+00	2.30E+00	1.50E+00	2.92E-06	-6.05E-01	-1.79E-06
9.67E-01	2.00E+00	2.20E+00	1.50E+00	2.29E-06	-6.05E-01	-1.27E-06
1.13E+00	2.00E+00	2.10E+00	1.50E+00	1.84E-06	-6.05E-01	-9.00E-07
1.30E+00	2.00E+00	2.00E+00	1.50E+00	1.51E-06	-6.05E-01	-6.44E-07
1.46E+00	2.00E+00	1.90E+00	1.50E+00	1.26E-06	-6.05E-01	-4.66E-07
1.63E+00	2.00E+00	1.80E+00	1.50E+00	1.06E-06	-6.05E-01	-3.42E-07
1.79E+00	2.00E+00	1.70E+00	1.50E+00	8.84E-07	-6.05E-01	-2.59E-07
1.96E+00	2.00E+00	1.60E+00	1.50E+00	7.33E-07	-6.05E-01	-2.05E-07
2.12E+00	2.00E+00	1.50E+00	1.50E+00	5.97E-07	-6.05E-01	-1.75E-07
2.29E+00	2.00E+00	1.40E+00	1.50E+00	4.73E-07	-6.05E-01	-1.62E-07
2.45E+00	2.00E+00	1.30E+00	1.50E+00	3.57E-07	-6.05E-01	-1.63E-07
2.62E+00	2.00E+00	1.20E+00	1.50E+00	2.52E-07	-6.05E-01	-1.75E-07
2.78E+00	2.00E+00	1.10E+00	1.50E+00	1.62E-07	-6.05E-01	-1.99E-07
2.95E+00	2.00E+00	1.00E+00	1.50E+00	1.01E-07	-6.05E-01	-2.41E-07
3.12E+00	2.00E+00	9.00E-01	1.50E+00	9.99E-08	-6.05E-01	-3.21E-07
3.28E+00	2.00E+00	8.00E-01	1.50E+00	2.27E-07	-6.05E-01	-4.84E-07
3.45E+00	2.00E+00	7.00E-01	1.50E+00	6.48E-07	-6.05E-01	-8.43E-07
3.61E+00	2.00E+00	6.00E-01	1.50E+00	1.76E-06	-6.05E-01	-1.67E-06
3.78E+00	2.00E+00	5.00E-01	1.50E+00	4.63E-06	-6.05E-01	-3.69E-06
3.94E+00	2.00E+00	4.00E-01	1.50E+00	1.30E-05	-6.05E-01	-9.28E-06
4.11E+00	2.00E+00	3.00E-01	1.50E+00	4.19E-05	-6.05E-01	-2.75E-05
4.19E+00	2.00E+00	2.53E-01	1.50E+00	5.28E-05	-6.05E-01	-3.50E-05
4.27E+00	2.00E+00	2.00E-01	1.50E+00	5.77E-05	-6.05E-01	-3.96E-05
4.44E+00	2.00E+00	1.00E-01	1.50E+00	1.19E-05	-6.06E-01	-1.11E-05
4.60E+00	2.00E+00	0.00E+00	1.50E+00	-3.03E-06	-6.05E-01	7.03E-07
4.67E+00	2.00E+00	0.00E+00	1.50E+00	-1.48E-06	-2.66E-01	3.82E-07
4.70E+00	2.00E+00	0.00E+00	1.50E+00	-1.01E-07	-1.39E-02	2.64E-07
4.71E+00	2.00E+00	0.00E+00	1.50E+00	-8.11E-08	-7.72E-03	2.14E-08
4.72E+00	2.00E+00	0.00E+00	1.50E+00	-7.18E-09	-4.33E-04	1.89E-09
4.73E+00	2.00E+00	0.00E+00	1.50E+00	-6.72E-10	-2.38E-05	1.77E-10
4.73E+00	2.00E+00	0.00E+00	1.50E+00	-6.48E-11	-1.18E-06	1.71E-11
4.73E+00	2.00E+00	0.00E+00	1.50E+00	-6.37E-13	-5.96E-07	1.68E-13

One lead particle falling in stagnant air, particle tracking data

PARTICLE NO.1 Diameter=1.000E-04 m Mass=5.236E-09 kg

T(s)	X(m)	Y(m)	Z(m)	U(m/s)	V(m/s)	W(m/s)
0.00E+00	2.00E+00	2.75E+00	1.40E+00	0.00E+00	0.00E+00	0.00E+00
1.09E-01	2.00E+00	2.70E+00	1.40E+00	1.77E-06	-8.42E-01	-1.13E-06
2.03E-01	2.00E+00	2.60E+00	1.40E+00	4.65E-06	-1.25E+00	-3.15E-06
2.77E-01	2.00E+00	2.50E+00	1.40E+00	6.86E-06	-1.43E+00	-4.87E-06
3.44E-01	2.00E+00	2.40E+00	1.40E+00	7.77E-06	-1.53E+00	-5.68E-06
4.09E-01	2.00E+00	2.30E+00	1.40E+00	7.78E-06	-1.59E+00	-5.80E-06
4.71E-01	2.00E+00	2.20E+00	1.40E+00	7.34E-06	-1.64E+00	-5.56E-06
5.32E-01	2.00E+00	2.10E+00	1.40E+00	6.70E-06	-1.68E+00	-5.16E-06
5.93E-01	2.00E+00	2.00E+00	1.40E+00	6.02E-06	-1.68E+00	-4.70E-06
6.53E-01	2.00E+00	1.90E+00	1.40E+00	5.35E-06	-1.68E+00	-4.24E-06
7.13E-01	2.00E+00	1.80E+00	1.40E+00	4.73E-06	-1.68E+00	-3.81E-06
7.72E-01	2.00E+00	1.70E+00	1.40E+00	4.17E-06	-1.68E+00	-3.42E-06
8.32E-01	2.00E+00	1.60E+00	1.40E+00	3.67E-06	-1.68E+00	-3.06E-06
8.92E-01	2.00E+00	1.50E+00	1.40E+00	3.22E-06	-1.68E+00	-2.73E-06
9.51E-01	2.00E+00	1.40E+00	1.40E+00	2.82E-06	-1.68E+00	-2.43E-06
1.01E+00	2.00E+00	1.30E+00	1.40E+00	2.46E-06	-1.68E+00	-2.15E-06
1.07E+00	2.00E+00	1.20E+00	1.40E+00	2.13E-06	-1.68E+00	-1.88E-06
1.13E+00	2.00E+00	1.10E+00	1.40E+00	1.82E-06	-1.68E+00	-1.62E-06
1.19E+00	2.00E+00	1.00E+00	1.40E+00	1.52E-06	-1.68E+00	-1.36E-06
1.25E+00	2.00E+00	9.00E-01	1.40E+00	1.22E-06	-1.68E+00	-1.10E-06
1.31E+00	2.00E+00	8.00E-01	1.40E+00	9.09E-07	-1.68E+00	-8.16E-07
1.37E+00	2.00E+00	7.00E-01	1.40E+00	5.62E-07	-1.68E+00	-5.03E-07
1.43E+00	2.00E+00	6.00E-01	1.40E+00	1.49E-07	-1.68E+00	-1.38E-07
1.49E+00	2.00E+00	5.00E-01	1.40E+00	-3.88E-07	-1.68E+00	3.18E-07
1.55E+00	2.00E+00	4.00E-01	1.40E+00	-1.15E-06	-1.68E+00	9.34E-07
1.61E+00	2.00E+00	3.00E-01	1.40E+00	-2.33E-06	-1.68E+00	1.84E-06
1.67E+00	2.00E+00	2.00E-01	1.40E+00	-4.24E-06	-1.68E+00	3.26E-06
1.72E+00	2.00E+00	1.00E-01	1.40E+00	-7.27E-06	-1.68E+00	5.43E-06
1.78E+00	2.00E+00	0.00E+00	1.40E+00	-7.61E-06	-1.68E+00	5.63E-06
1.96E+00	2.00E+00	0.00E+00	1.40E+00	-5.90E-06	-7.65E-01	4.33E-06
2.05E+00	2.00E+00	0.00E+00	1.40E+00	-4.52E-06	-4.06E-01	3.32E-06
2.10E+00	2.00E+00	0.00E+00	1.40E+00	-3.84E-07	-2.28E-02	2.82E-07
2.13E+00	2.00E+00	0.00E+00	1.40E+00	-3.50E-08	-1.30E-03	2.56E-08
2.14E+00	2.00E+00	0.00E+00	1.40E+00	-3.32E-09	-7.33E-05	2.43E-09
2.15E+00	2.00E+00	0.00E+00	1.40E+00	-3.22E-10	-4.04E-07	2.36E-10
2.16E+00	2.00E+00	0.00E+00	1.40E+00	-3.17E-11	-2.02E-08	2.33E-11
2.16E+00	2.00E+00	0.00E+00	1.40E+00	-3.15E-13	-1.04E-09	2.31E-13

Appendix B Scalars, Vectors and Tensors

In all fluid dynamic problems we have to manipulate with scalars, vectors, and tensors. Scalars are entities each with a magnitude but no sense of direction. Vectors are entities each with a magnitude and a direction. Besides these properties vectors are governed by a law of addition of two vectors and a law of multiplication of a vector by a scalar. Tensors are higher order vectors and have a number of components depending on their orders and also on the dimension of the space in which they occur. Tensors of various orders either appear naturally in a derivation or can be constructed to express a natural phenomenon. In fact, every quantity can be called a tensor of a particular order. Thus a scalar is a tensor of order zero while a vector is a tensor of order one. The most important property of vector and tensor representations lies in the invariant character of physical phenomena. For example, if the velocity vector at a point in a fluid medium is **u**, then it can be represented with reference to either a rectangular Cartesian co-ordinate system or any other general curvilinear system without changing its magnitude or direction.

Let T be a tensor of order n in a space of dimension N. Then the number of components of T are N^n. Another way of looking at tensor is to represent them as an indefinite product of vectors. For example, consider two arbitrary vectors **a** and **b**. We now define a tensor T as:

$$\mathbf{T} = \mathbf{ab}, \qquad (\mathbf{ab} \neq \mathbf{ba}) \tag{B-1}$$

where **ab** is called the *dyadic product* of vectors. Equation (B-1) can also be written as:

$$\mathbf{T} = a_i b_j \mathbf{i}_i \mathbf{i}_j \tag{B-2}$$

so that the components of **T** are $a_i b_j$ and in 3-D space there are nine such components.

Tensors of various orders are usually written in their component forms, e.g., T_{ij}, T^{i}_{mn} etc. Tensors of order two are most efficiently handled by using the dyadic product of base vectors. Thus a second order tensor in rectangular Cartesian co-ordinates is written in the form of (B-2).

The tensor product of tensor A and B is defined by:

$$(A \otimes B)_{ij} = A_i B_j \tag{B-3}$$

The transpose of a second order tensor is obtained by interchanging the rows and columns of the matrix $[A_{ij}]$. In dyadic form, the transpose of **A** is:

$$A^T = \left(A^{ji}\right) \tag{B-4}$$

A second order tensor is said to be symmetric when:

$$A = A^T \tag{B-5}$$

A second order tensor is said to be skew-symmetric when:

$$\mathbf{A} = -\mathbf{A}^{T} \tag{B-6}$$

The divergence of a rank two tensor is defined by:

$$(\nabla \cdot \mathbf{S})^{i} = \frac{\partial S^{ji}}{\partial x^{j}} \tag{B-7}$$

The contraction of a second rank tensor with a vector is denoted as:

$$(\mathbf{S} \bullet \mathbf{V})^{i} = S^{ij} V_{j} \tag{B-8}$$

Appendix C Integration of the General Equation

The general equation is integrated over a finite control volume (see figure 4.2) as follows:

$$\int_V \frac{\partial}{\partial x_i}(\rho U_i \Phi)dV - \int_V \frac{\partial}{\partial x_i}\left(\Gamma_\Phi \frac{\partial \Phi}{\partial x_i}\right)dV = \int_V S_\Phi dV \qquad \text{(C-1)}$$

$$\Downarrow \qquad \Downarrow \qquad \Downarrow$$

convection diffusion source

The integration of convection terms is as follows:

$$\int_V \left[\frac{\partial}{\partial x}(\rho U\Phi) + \frac{\partial}{\partial y}(\rho V\Phi) + \frac{\partial}{\partial z}(\rho W\Phi)\right]dV =$$

$$\rho U\Phi\Big|_w^e \Delta y\Delta z + \rho V\Phi\Big|_s^n \Delta x\Delta z + \rho W\Phi\Big|_d^u \Delta x\Delta y \qquad \text{(C-2)}$$

The integration of diffusion terms can be written as below:

$$\int_V \left[\frac{\partial}{\partial x}\left(\Gamma_\Phi \frac{\partial \Phi}{\partial x}\right) + \frac{\partial}{\partial y}\left(\Gamma_\Phi \frac{\partial \Phi}{\partial y}\right) + \frac{\partial}{\partial z}\left(\Gamma_\Phi \frac{\partial \Phi}{\partial z}\right)\right]dV =$$

$$\Gamma_\Phi \frac{\Delta\Phi}{\Delta x}\Big|_w^e \Delta y\Delta z + \Gamma_\Phi \frac{\Delta\Phi}{\Delta y}\Big|_s^n \Delta x\Delta z + \Gamma_\Phi \frac{\Delta\Phi}{\Delta z}\Big|_d^u \Delta x\Delta y \qquad \text{(C-3)}$$

The integration of source term is below:

$$\int_V S_\Phi dV = \int_V (S_P \Phi_P + S_C) dV = (S_P \Phi_P + S_C) \Delta x \Delta y \Delta z \qquad \text{(C-4)}$$

In the above equations, the source term has been linearized. The assumption that Φ varies piecewise linear between the nodes is now applied, then

$$\Phi_e = \frac{1}{2}(\Phi_{i-1,j,k} + \Phi_{i,j,k}) = \frac{1}{2}(\Phi_E + \Phi_P) \qquad \text{(C-5)}$$

$$\Phi_w = \frac{1}{2}(\Phi_{i,j,k} + \Phi_{i-1,j,k}) = \frac{1}{2}(\Phi_P + \Phi_W) \qquad \text{(C-6)}$$

$$\Phi_n = \frac{1}{2}(\Phi_{i,j+1,k} + \Phi_{i,j,k}) = \frac{1}{2}(\Phi_N + \Phi_P) \qquad \text{(C-7)}$$

$$\Phi_s = \frac{1}{2}(\Phi_{i,j,k} + \Phi_{i,j-1,k}) = \frac{1}{2}(\Phi_P + \Phi_S) \qquad \text{(C-8)}$$

$$\Phi_u = \frac{1}{2}(\Phi_{i,j,k+1} + \Phi_{i,j,k}) = \frac{1}{2}(\Phi_U + \Phi_P) \qquad \text{(C-9)}$$

$$\Phi_d = \frac{1}{2}(\Phi_{i,j,k} + \Phi_{i,j,k-1}) = \frac{1}{2}(\Phi_P + \Phi_D) \qquad \text{(C-10)}$$

The discretisation equation can now be written as:

$$A_e\left[(\rho U)_e\frac{1}{2}(\Phi_E+\Phi_P)-(\Gamma_\Phi)_e\frac{(\Phi_E-\Phi_P)}{\delta_e}\right]$$

$$-A_w\left[(\rho U)_w\frac{1}{2}(\Phi_P+\Phi_W)-(\Gamma_\Phi)_w\frac{(\Phi_P-\Phi_W)}{\delta_w}\right]$$

$$+A_n\left[(\rho U)_n\frac{1}{2}(\Phi_N+\Phi_P)-(\Gamma_\Phi)_n\frac{(\Phi_N-\Phi_P)}{\delta_n}\right]$$

$$-A_s\left[(\rho U)_s\frac{1}{2}(\Phi_P+\Phi_S)-(\Gamma_\Phi)_s\frac{(\Phi_P-\Phi_S)}{\delta_s}\right]$$

$$+A_d\left[(\rho U)_d\frac{1}{2}(\Phi_D+\Phi_P)-(\Gamma_\Phi)_d\frac{(\Phi_D-\Phi_P)}{\delta_d}\right]$$

$$-A_u\left[(\rho U)_u\frac{1}{2}(\Phi_P+\Phi_U)-(\Gamma_\Phi)_u\frac{(\Phi_P-\Phi_U)}{\delta_u}\right]$$

$$=(S_P\Phi_P+S_C)\Delta x\Delta y\Delta z \qquad \text{(C-11)}$$

The equation of mass conservation is integrated over the control volume as:

$$\int_V\left[\frac{\partial}{\partial x}(\rho U)+\frac{\partial}{\partial y}(\rho V)+\frac{\partial}{\partial z}(\rho W)\right]dV=0 \qquad \text{(C-12)}$$

The mass flux over the volume face is regarded as constant, so

$$\left[(\rho U)_e-(\rho U)_w\right]\Delta y\Delta z+\left[(\rho V)_n-(\rho V)_s\right]\Delta x\Delta z$$

$$+\left[(\rho W)_d-(\rho W)_u\right]\Delta x\Delta y=0 \qquad \text{(C-13)}$$

The above equation is multiplied by Φ_P and subtracted from the general equation, and then we have:

$$\Phi_E\left[\frac{1}{2}A_e(\rho U)_e-(\Gamma_\Phi)_e\frac{A_e}{\delta_e}\right]-\Phi_W\left[\frac{1}{2}A_w(\rho U)_w+(\Gamma_\Phi)_w\frac{A_w}{\delta_w}\right]$$

$$+\Phi_N\left[\frac{1}{2}A_n(\rho U)_n-(\Gamma_\Phi)_n\frac{A_n}{\delta_n}\right]-\Phi_S\left[\frac{1}{2}A_s(\rho U)_s+(\Gamma_\Phi)_s\frac{A_s}{\delta_s}\right]$$

$$+\Phi_D\left[\frac{1}{2}A_d(\rho U)_d-(\Gamma_\Phi)_d\frac{A_d}{\delta_d}\right]-\Phi_U\left[\frac{1}{2}A_u(\rho U)_u+(\Gamma_\Phi)_u\frac{A_u}{\delta_u}\right]$$

$$+\Phi_P\left\{\left[\frac{1}{2}A_e(\rho U)_e+(\Gamma_\Phi)_e\frac{A_e}{\delta_e}-(\rho U)_e\right]-\left[\frac{1}{2}A_w(\rho U)_w+(\Gamma_\Phi)_w\frac{A_w}{\delta_w}-(\rho U)_w\right]\right\}$$

$$+\Phi_P\left\{\left[\frac{1}{2}A_s(\rho V)_s+(\Gamma_\Phi)_s\frac{A_s}{\delta_s}-(\rho V)_s\right]-\left[\frac{1}{2}A_n(\rho V)_n+(\Gamma_\Phi)_n\frac{A_n}{\delta_n}-(\rho V)_n\right]\right\}$$

$$+\Phi_P\left\{\left[\frac{1}{2}A_d(\rho W)_d+(\Gamma_\Phi)_d\frac{A_d}{\delta_d}-(\rho W)_d\right]-\left[\frac{1}{2}A_u(\rho W)_u+(\Gamma_\Phi)_u\frac{A_u}{\delta_u}-(\rho W)_u\right]\right\}$$

$$=(S_P\Phi_P+S_C)\Delta x\Delta y\Delta z \qquad \text{(C-14)}$$

The following coefficients are defined:

$$a_e=(\Gamma_\Phi)_e\frac{A_e}{\delta_e}-A_e\frac{(\rho U)_e}{2},\quad a_w=(\Gamma_\Phi)_w\frac{A_w}{\delta_w}+A_w\frac{(\rho U)_w}{2} \qquad \text{(C-15)}$$

$$a_n=(\Gamma_\Phi)_n\frac{A_n}{\delta_n}-A_n\frac{(\rho V)_n}{2},\quad a_s=(\Gamma_\Phi)_s\frac{A_s}{\delta_s}+A_s\frac{(\rho V)_s}{2} \qquad \text{(C-16)}$$

$$a_d=(\Gamma_\Phi)_d\frac{A_d}{\delta_d}-A_d\frac{(\rho W)_d}{2},\quad a_u=(\Gamma_\Phi)_u\frac{A_u}{\delta_u}+A_u\frac{(\rho W)_u}{2} \qquad \text{(C-17)}$$

The coefficients are substituted into the equation (C-14), then

$$\Phi_P\left(a_e + a_w + a_n + a_s + a_d + a_u\right) =$$

$$a_e\Phi_E + a_w\Phi_W + a_n\Phi_N + a_s\Phi_S + a_d\Phi_D + a_u\Phi_U + \left(S_P\Phi_P + S_C\right)\Delta x\Delta y\Delta z$$

$$\Rightarrow \qquad \Phi_P\left(\sum_k a_k - S_P\Delta x\Delta y\Delta z\right) = \sum_{k,K} a_k\Phi_K + S_C\Delta x\Delta y\Delta z \qquad \text{(C-18)}$$

Appendix D The Exponential Scheme

The general equation is assumed one-dimensional, with constant Γ and with no additional source term, then

$$\frac{\partial}{\partial x}(\rho U\Phi)=\frac{\partial}{\partial x}\left[\Gamma_{\Phi}\frac{\partial \Phi}{\partial x}\right] \qquad \text{(D-1)}$$

$$\Downarrow \qquad \Downarrow$$

convection diffusion

This equation can be solved exactly with the following boundary conditions:

$$\Phi|_{x=0}=\Phi_P, \qquad \Phi|_{x=\delta_e}=\Phi_E \qquad \text{(D-2)}$$

So the solution is as follows (Patankar 1980):

$$\frac{\Phi-\Phi_P}{\Phi_E-\Phi_P}=\frac{\exp\left[\frac{\rho U\delta_e}{\Gamma}\frac{x}{\delta_e}\right]-1}{\exp\left[\frac{\rho U\delta_e}{\Gamma}\right]-1} \qquad \text{(D-3)}$$

Equation (D-1) is integrated over a control volume as below:

$$\int_w^e \frac{\partial}{\partial x}(\rho U\Phi)dx = \int_w^e \frac{\partial}{\partial x}\left[\Gamma_\Phi \frac{\partial \Phi}{\partial x}\right]dx \Rightarrow$$

$$\left[\rho U\Phi - \Gamma_\Phi \frac{\partial \Phi}{\partial x}\right]_e - \left[\rho U\Phi - \Gamma_\Phi \frac{\partial \Phi}{\partial x}\right]_w = 0 \qquad \text{(D-4)}$$

If the exact solution is substituted into the integrated equation, following equation is obtained:

$$\left\{\rho U\left[\Phi_P + \frac{\Phi_P - \Phi_E}{\exp(P_e)-1}\right]\right\}_e - \left\{\rho U\left[\Phi_W + \frac{\Phi_W - \Phi_P}{\exp(P_e)-1}\right]\right\}_w = 0 \qquad \text{(D-5)}$$

Equation (D-5) can be written in the coefficient form as:

$$a_P\Phi_P = a_e\Phi_E + a_w\Phi_W \qquad \text{(D-6)}$$

where the coefficients are as follows:

$$a_e = \frac{(\rho U)_e}{\exp\left[\frac{(\rho U\delta)_e}{\Gamma_\Phi}\right]-1} = \frac{(\rho U)_e}{\exp\left[(P_e)_e\right]-1} \qquad \text{(D-7)}$$

$$a_w = \frac{(\rho U)_w \exp\left[\frac{(\rho U\delta)_w}{\Gamma_\Phi}\right]}{\exp\left[\frac{(\rho U\delta)_w}{\Gamma_\Phi}\right]-1} = \frac{(\rho U)_w \exp\left[(P_e)_w\right]}{\exp\left[(P_e)_w\right]-1} \qquad \text{(D-8)}$$

$$a_P = a_e + a_w + \left[(\rho U)_e - (\rho U)_w\right] \qquad \text{(D-9)}$$

The above is exponential scheme.

Appendix E Specification of Thermal Wall Boundary Conditions

From CIBSE Guide, the heat loss through unit area of a component slab wall (see figure 8.7) due to the temperature difference on both sides of the slab can be expressed as:

$$Q = \frac{\lambda \Delta T}{l} \left(W/m^2\right) \tag{E-1}$$

and the heat transfer through the air space is defined as

$$Q_a = h_a \Delta T \left(W/m^2\right) \tag{E-2}$$

According to energy conservation, the heat transfer through every slab and air space must be constant, therefore the following relations are obtained:

Slab 1: $$Q_1 = \frac{\lambda_1 (T_w - T_1)}{l_1} \tag{E-3}$$

Airgap: $$Q_2 = h_a (T_1 - T_2) \tag{E-4}$$

Slab 3: $$Q_3 = \frac{\lambda_3 (T_2 - T_3)}{l_3} \tag{E-5}$$

Slab 4: $$Q_4 = \frac{\lambda_4 (T_3 - T_4)}{l_4} \tag{E-6}$$

Outside air: $$Q_5 = h_\infty (T_4 - T_o) \tag{E-7}$$

Heat balance: $$Q_1 = Q_2 = Q_3 = Q_4 = Q_5 = Q_w \tag{E-8}$$

From equations (E-3) ~ (E-8), the following formula is obtained:

$$T_w + \left(\frac{1}{h_a} + \frac{l_1}{\lambda_1} + \frac{l_3}{\lambda_3} + \frac{l_4}{\lambda_4} + \frac{1}{h_{so}} \right) Q_w = T_o \qquad \text{(E-9)}$$

Comparing equation (E-9) with equation (8-7), the following formulae obtained:

$$A = 1, \qquad \text{(E-10)}$$

$$B = \frac{1}{h_a} + \frac{l_1}{\lambda_1} + \frac{l_3}{\lambda_3} + \frac{l_4}{\lambda_4} + \frac{1}{h_{so}} \qquad \text{(E-11)}$$

$$C = T_o \qquad \text{(E-12)}$$

According to CIBSE Guide, the thermal transmittance of a building element is frequently used in building engineering which is defined as below:

$$U = \frac{1}{R_{si} + R_1 + R_2 + \cdots\cdots + R_a + R_{so}} \qquad \text{(E-13)}$$

and

$$R_i = \frac{l_i}{\lambda_i}, \quad R_{so} = \frac{1}{h_{so}} \qquad \text{(E-14)}$$

Then equation (8-19) can be written as below:

$$B = \frac{1}{U} - R_{si} \qquad \text{(E-15)}$$

T_o and U-value are known from the problem definition in §8.2.1. R_{si} can be found from CIBSE Guide (1986), here choosing R_{si}=0.1 $W^{-1} \cdot m^2 \cdot K$.

By specifying the values of A, B and C using equations (E-10), (E-12) and (E-15), the CFD code can then calculate the internal surface temperature of the wall, the heat flux at the wall, and the amount of heat loss through the wall.

Ceiling:	A=1.0,	B=1.0494,	C=282.5
Floor:	A=1.0,	B=1.7818,	C=282.5
Wall 1:	A=1.0,	B=1.3085,	C=282.5
Wall 2:	A=1.0,	B=2.7571,	C=282.5
Wall 3:	A=1.0,	B=2.7571,	C=282.5
Wall 4:	A=1.0,	B=1.1821,	C=270.15
Window:	A=1.0,	B=0.2937,	C=270.15